The Calculation of Electron Collisions with Atoms and Molecules

Thomas Meltzer

A dissertation submitted in partial fulfillment

of the requirements for the degree of

Doctor of Philosophy

of

University College London.

August 10, 2020

I, Thomas Meltzer, confirm that the work presented in this thesis is my own. Where information has been derived from other sources, I confirm that this has been indicated in the work.

Abstract

In this thesis electron collisions are studied under two different scattering energy regimes. Firstly, low energy electron-molecule collisions are considered. These typically occur in interstellar medium, planetary atmospheres or industrial plasmas. Under these conditions the electrons cannot be treated classically and so a quantum mechanical approach is used. Using R-matrix theory two targets are studied: nitric oxide (NO) and molecular hydrogen (H_2). Owing to new developments in the UKRMol+ code the boundaries of previous R-matrix calculations are pushed to new limits in order to produce accurate cross-sections for electron-impact electronic excitation of H_2. This includes the use of a B-spline continuum basis, a triply-augmented target basis and a box size of 100 a_0. NO is used as a prototypical example of an open-shell molecule that exhibits mixed Rydberg-like and Valence states. Systems like this are typically difficult to solve using standard quantum chemistry approaches, and so the R-matrix with pseudo-states method is employed to produce a set of improved potential energy curves, capable of being used in further scattering calculations.

In the second regime, high energy electron-atom collisions are investigated. These types of collision take place in strongly-driven systems, e.g., atoms in intense laser fields. In this case, the *scattering* electron is provided by the neutral parent atom as it is ionised by the external field. The specific focus of this work is the phenomena of non-sequential double ionisation. A semiclassical Monte-Carlo method is used based on the three step model, which fully accounts for two active electrons, the Coulomb potential and the magnetic-field. Using this model the role of magnetic-field effects in strong-field physics are investigated.

Impact Statement

The research conducted in this thesis concerns mostly fundamental physics. Therefore, the impact to society is somewhat less immediate. Nevertheless, this research has implications for the academic community that will no doubt influence society further along the line.

Electron collisions are important for understanding the world around us, whether they occur in natural environments, such as, planetary aurora, lightning strikes or interstellar medium. Or whether they occur in man-made environments like those found in the plasma etching industry, lasers or nuclear fusion reactors. Furthermore, research conducted in the strong-field regime has already revolutionised physics by providing access to high intensity, ultrafast laser pulses. Now it is possible to observe electrons, atoms and molecules with unprecedented levels of accuracy and detail.

The R-matrix calculations presented in this thesis are intended as a proof-of-concept. They push the limits of previous R-matrix studies and provide an example of the capabilities of the new UKRMol+ code. It is hoped that many more calculations like these will be carried out in future for a wide range of molecules, to satisfy the demand for accurate cross-section data.

Finally, the studies of non-sequential double ionisation, presented in this thesis, have identified important magnetic-field effects that were previously assumed to be negligible. This body of work predominantly focussed on linearly-polarised laser fields but given the flexibility of the theory it could be readily adapted to describe more intricate experiments, such as those that employ two-colour lasers or pump-probe beam experiments.

Acknowledgements

When I sat down to write this thesis, I had no idea that it would actually be harder to thank all of the people that helped me get here in the first place. To that end, I want to start first and foremost with my family. Mum and Dad, thanks for all of your unending support, encouragement and love – I would not be here without you. To my twin Betty, thanks for putting me in my place on numerous occasions. Without you telling me to stop playing video games I would probably have never made it past my A-levels. It was a privilege to share my progress through education with you every step of the way. To my brother Pete, you have been a constant source of inspiration to me, your dedication to learning and your ability to do anything you put your mind to has never ceased to amaze me. To my sister Issy, thanks for showing me that there's more to life than physics. Your appreciation of art, music and pottery painting have most definitely rubbed off on me over the years. To my partner Emma, you have taken the rough end of the stick over the last four and a half (nine?) years and I cannot thank you enough. You have selflessly supported me in all of my endeavours, no matter what. You have helped me navigate the rocky and emotional terrain of PhD research, and you have never once complained about it – for that, I am eternally grateful.

PhD supervisors can be good, bad and ugly. It turns out I lucked out with my supervisor, Prof Jonathan Tennyson, and the ExoMol group. Jonathan leads by example and in doing so he has crafted generations of successful academics. It is both intimidating and inspiring to see just how successful his mentoring has been – whilst former students and postdocs merit their own success, clearly Jonathan is doing something right. Personally, his ability to provide just the right amount

of guidance has allowed me to develop self-confidence and independence, whilst ensuring I never strayed too far from the path. Thank you for taking me in.

I would like to thank all of my collaborators throughout the PhD, in particular Dr Zdeněk Mašín for allowing me to use his DCS code and for his helpful suggestions with the UKRMol+ code. I would also like to thank Dr Mark Zammit, Liam Scarlett, Prof Dmitry Fursa and Prof Igor Bray for providing their MCCC data and useful discussions on the molecular hydrogen project. I thank Prof Paul Corkum for his insightful contributions to our non-dipole recollision gating project. Additionally, I thank Jakub Benda for his valuable help in debugging the UKRMol+ code.

I would like to thank all of the past and present members of ExoMol for welcoming me into the group and making me feel at home, with special thanks to: Sergey Yurchenko for his enthusiasm and constant supply of memes; Tony Lynas-Gray for his infectious kindness and Friday evening whiskies; and Victoria Clark for being the heart of the ExoMol group and a great friend. I would also like to thank the members of my former group, whom without, I would have given up long before the end, i.e., Harry Banks, Arnau Casanovas and Ahai Chen.

I would like to thank all my former office mates for helping the days fly by: Carlo Sparaciari, Tom Galley, Lorenzo Catani, Mike Staddon, Alex Paraschiv and Eryn Spinlove. In addition, I also want to thank everyone who made UCL special for me including: Jacob Lang, Erika Aranas, Andy Maxwell, Katy Chubb, Diana Serbanescu and Duncan Little.

Finally, thanks to my "physics friends": Simon Hind, Tom Vice (Kennelly) and Josh Kettlewell*.

*also a mini shout-out to Bram Moolenaar et al. for making my life easier – `vim <3`

Publications

1. A. Emmanouilidou and T. Meltzer. Recollision as a probe of magnetic-field effects in nonsequential double ionization. *Phys. Rev. A*, 95:033405, 2017. doi:10.1103/PhysRevA.95.033405.

2. A. Emmanouilidou, T. Meltzer, and P. B. Corkum. Non-dipole recollision-gated double ionization and observable effects. *J. Phys. B: At. Mol. Opt. Phys.*, 50:225602, 2017. doi:10.1088/1361-6455/aa90e9.

3. T. Meltzer, J. Tennyson, Z. Mašín, M. C. Zammit, L. H. Scarlett, D. V. Fursa, and I. Bray. Benchmark calculations of electron impact electronic excitation of the hydrogen molecule. *J. Phys. B At. Mol. Opt. Phys.*, 53:145204, 2020. doi:10.1088/1361-6455/ab8c58.

Contents

List of Figures

List of Tables

Chapter 1

Introduction

"A very familiar example of scattering theory is called *looking at things*" – Tong (2017).

1.1 Overview

Scattering theory is vital to our understanding of the universe. It has played an important role in many discoveries from the mapping of DNA's internal structure to the first successful detection of the Higgs boson. The general idea is to bounce projectiles off of an object that you wish to know more about. By measuring the scattered projectiles many interesting properties of the target can be inferred. The information that you can obtain is dictated by the choice of projectile. In this thesis collisions of electrons with atoms and molecules will be considered.

Electron collisions are crucial for modelling man-made plasmas, astrophysical processes and planetary atmospheres (Bartschat and Kushner, 2016). They also have direct implications for society via applications in medical physics, such as proton beam therapy (Gorfinkiel and Ptasinska, 2017), and nuclear power generation via the Joint European Torus (JET) (Darby-Lewis et al., 2018). Furthermore, in the presence of strong laser fields, electron collisions can lead to High-Harmonic Generation (HHG) and Non-Sequential Double Ionisation (NSDI) (Krausz and Ivanov, 2009). HHG led to the invention of high intensity, ultrafast laser pulses which has, in turn, opened up an entire field of research allowing angstrom and attosecond spatiotemporal resolution to probe the structure of atoms and molecules on their

intrinsic time and length-scales (Bruner et al., 2015).

Table 1.1 gives a list of the atomic and molecular processes covered in this thesis. This is by no means an exhaustive or complete list. For example, neither rovibrational excitations in molecules nor dissociative effects are explicitly investigated. The table is in approximate energy order from lowest energy collisions up to intermediate and higher energy scattering. The molecular processes are considered in field-free environments, whereas the atomic processes will be studied in the presence of strong laser fields.

Table 1.1 | List of processes that will be discussed in this thesis for atomic, A, and molecular, AB, targets.

Description	Process
Molecular	
Elastic Scattering	$AB + e^- \rightarrow AB + e^-$
Electronic Excitation	$AB + e^- \rightarrow AB^* + e^-$
Single Ionisation	$AB + e^- \rightarrow AB^+ + 2e^-$
Atomic	
Single Ionisation	$A + h\nu \rightarrow A^+ + e^-$
Double Ionisation (NSDI)	$A + h\nu \rightarrow (A^+ + e^-) + h\nu$
	$(A^+ + e^-) + h\nu \rightarrow A^{2+} + 2e^-$
Double Ionisation (sequential)	$A + h\nu \rightarrow A^{2+} + 2e^-$

In this thesis, two contrasting theoretical approaches will be employed – high-level, *ab initio* theory and more approximate methods that allow for analytical insight. If accuracy is required often fully-quantum, large-scale numerical calculations are the only way to go. However, to gain physical insight it can be preferential to use approximate, semiclassical techniques that retain more analytical character. This trade-off is highlighted in the recent review of strong-field processes, see Amini et al. (2019). In the best case scenario, both techniques can be used, leading to a deeper understanding. Although, this is often not possible.

This thesis has two main objectives. The first objective is to push the boundaries of previous R-matrix calculations by harnessing the latest features of the recently released UKRMol+ code (Mašín et al., 2020). R-matrix calculations will be carried out for two different targets, molecular hydrogen (H_2) and nitric oxide

(NO), in the low to intermediate scattering energy regime. These calculations are intended as a proof-of-concept. H_2 is one of the most widely studied molecules and therefore it will provide a stringent test of the recently developed code and molecular R-matrix theory in general. Studies carried out on NO move towards a more realistic use case with a higher number of electrons. NO has specifically been chosen due to its complicated electronic structure i.e., mixed low-lying Rydberg-like and valence states. Hybrid state systems cannot be easily represented in scattering calculations using traditional quantum chemistry approaches.

The second objective is to develop more analytical methods that can be used to describe the phenomena observed in strong-field physics. That is, with the advent of table-top, high-power lasers, strong-field experiments are rapidly becoming more accessible. Theory is somewhat playing catchup and there is a gap in the understanding of some of the most fundamental processes in atoms and molecules. Whilst *ab initio* quantum-mechanical models are capable of providing extremely accurate comparisons with experiment, semiclassical methods are sought that can provide more physical intuition behind the phenomena being observed in experiment.

1.2 Low Energy Scattering

At low scattering energies, i.e., below the first ionisation threshold $E \lesssim I_p$, the theoretical treatment of electron scattering is difficult. This is due to the complex interactions that can take place between the projectile electron and electrons contained within the target, such as exchange and polarisation (Burke, 2011). In order to provide an accurate description of the physics, any theoretical framework has to take these effects into account. For this reason, at low scattering energies, if accuracy is required then *ab initio* fully-quantum theories are the only realistic option. Whilst there are many successful perturbative approaches, these do not typically become valid until larger scattering energies. As a result, discussion of perturbative approaches will be reserved for intermediate scattering energies.

At low scattering energies, most theories rely on a close-coupling expansion

which is carried out in order to model exchange and polarisation effects. This includes: the Kohn variational principle (Rescigno et al., 1995); the Schwinger variational principle (Huo, 1995); the R-matrix method (Burke, 2011); and the Convergent Close-Coupling (CCC) method (Bray and Stelbovics, 1992). In the mid 1980s a numerical benchmark was carried out using the Kohn (Schneider and Collins, 1985), Schwinger (Lima et al., 1985) and R-matrix (Baluja et al., 1985) methods for electron-H_2 collisions and it was found that the three methods produced consistent results. Similar benchmarks have also been run for electron-atom collisions including comparisons to the atomic CCC method (Bartschat et al., 1996a; Lange et al., 2006; Bartschat et al., 2010). As yet, a benchmark comparison of the molecular CCC (MCCC) method has not been carried out, however this will be addressed in chapter 3.

Whilst there are similarities between the above methods, the R-matrix method has one unique advantage that the others do not. That is, in the R-matrix method configuration space is divided into two distinct regions. In the outer region, the scattering electron is treated as being distinguishable from the N target electrons and it is propagated in a simplified potential. Whereas, in the inner region all $N+1$ electrons are treated on equal footing (Burke, 2011). Due to the separation of space the inner region, which requires the diagonalisation of a computationally expensive $N+1$-electron Hamiltonian, is computed only once, i.e., independently of the scattering energy (Tennyson, 2010). This allows an arbitrarily-fine energy grid to be calculated in the outer region, which is crucial for reproducing narrow resonances that could be otherwise missed.

Since early work carried out by Burke et al. (1971), the R-matrix method has since been deployed on a large number of electron-atom and electron-molecule scattering calculations, e.g., Branchett et al. (1990b), Zatsarinny et al. (2006) and Little and Tennyson (2014) to name a few. For electron-molecule collisions, most of the calculations were produced using the diatomic or polyatomic UKRMol codes (Morgan et al., 1998; Carr et al., 2012). The UKRMol project has a long running history and over the years many incremental changes have been contributed by a

plethora of authors. Recently, however, a substantial re-write of the integrals code was carried out by Mašín et al. (2020) and this has led to a new version of the code called UKRMol+. This newly developed code introduces B-spline type orbitals for use in the continuum. The inclusion of a mixed B-spline type orbital (BTO) and Gaussian type orbital (GTO) continuum orbitals allows for larger scale scattering calculations.

Historically, electron-polyatomic-molecule calculations used GTO-only continua. GTO functions have analytic integrals, making them faster and more accurate to compute. However, the continuum must be orthogonalised to the target, which is also typically expanded in GTOs, and without due care this leads to linear dependence (Tennyson, 2010). This places a limitation on the maximum scattering energy that can be calculated, as the maximum supported scattering energy is proportional to the number of continuum GTOs. Furthermore, the R-matrix radius also affects the completeness of the continuum basis. Larger radii require more GTOs to represent the same maximum scattering energy. Therefore, it was difficult to use diffuse target basis sets – which are required for Rydberg-like states – because the target orbitals began to leak outside of the R-matrix sphere. As a result R-matrix radii, for electron-molecule calculations, were typically between 10 and 15 a.u. BTOs, however, essentially eliminate the issue of linear dependence and therefore allow much bigger R-matrix radii to be used – although, it must be said, they come with an increase in computational cost.

Modelling of Rydberg states is not just essential to improve the accuracy of electron scattering calculations, which depend heavily on the target description, but also because they are interesting in their own right. Rydberg states are often produced and studied in experiments and they can even be used to control the nuclear dynamics of the constituent atoms. For example, work carried out by Minns et al. (2003) and Kirrander et al. (2007) demonstrated that time-delayed, coherent laser pulses could be used to control the dissociation pathways of NO and H_2 respectively.

1.3 Intermediate Energy Scattering

Intermediate scattering energies, $E \gtrsim I_p$, present a challenge for theory. At this energy range fully-quantum *ab initio* approaches become computationally intractable, due to the increased number of open channels and higher angular momenta. Moreover, the scattering energy is not quite high enough to use approximate methods such as, perturbative or semi-empirical models that neglect the necessarily complicated electron correlation effects. However, in lieu of a method that is tractable and highly-accurate, both types of method have been used in literature to address the demand for theoretical data.

Firstly, approximate methods such as the optical model potential (OMP) (Jain, 1986) and complex optical potential (COP) (Lee and Iga, 1999) have been used to study a range of different electron-molecule collisions. These methods are capable of providing elastic, inelastic and ionisation cross-sections but they cannot resolve the contributions from individual excitations. Instead the inelastic cross-section is a sum over all inelastic channels. Next up, there are the semi-empirical binary encounter (BEB) method of Kim and Rudd (1994) and the scaled BEB variants of Tanaka et al. (2016). These methods use empirical data and fitting of experimental oscillator strengths to obtain accurate ionisation cross-sections, and similarly to the COP and OMP methods, they are also not capable of providing state-resolved inelastic cross-sections. Unfortunately, these methods are not suitable for plasma modelling because state-resolved cross-sections are required as inputs for collisional radiative models (Bartschat, 2013). One approximate method that is state-resolved is the semiclassical impact parameter approach of Celiberto and Rescigno (1993), based on earlier work by Hazi (1981). In this approach the target is treated quantum-mechanically but the scattering electron is classical. Therefore exchange effects are ignored and the method can only be applied to spin-allowed transitions (Hazi, 1981).

Moving on, there are several notable theories in the non-perturbative regime that have tackled electron-atom and electron-molecule collisions. These include: the intermediate energy R-matrix method (IERM) (Burke et al., 1987); the molec-

ular convergent close-coupling (MCCC) method (Zammit et al., 2017b), which is based on the atomic CCC method (Bray and Stelbovics, 1992); and the R-matrix with pseudostates method (RMPS) introduced by Bartschat et al. (1996b) for use in electron-atom collisions and subsequently extended to molecules by Gorfinkiel and Tennyson (2004). The IERM approach was capable of describing single and double ionisation however it was difficult to generalise to larger targets. Similarly, the MCCC approach is good at producing accurate, converged cross-sections at essentially any scattering energy required, however, it also restricted in application to one and two-active electron targets (Zammit et al., 2017a). The RMPS, on the other hand, has proved to be widely applicable as it builds upon the generalisability of the underlying R-matrix method (e.g., see Gorfinkiel and Tennyson (2005), Halmová and Tennyson (2008) and Brigg et al. (2014)). In this approach, pseudostates are added to the inner region solution which allow for the improved description of target states, improved convergence of the polarisability and also they represent ionisation channels in the infinite but discrete continuum (Bartschat et al., 1996b).

1.4 High Energy Scattering

In strong field physics, the strength of the laser's electric field approaches that of the atom. This means that the potential experienced by a bound electron is significantly perturbed. In what is known as the three step model (Corkum, 1993), this forms the first step of the process. Essentially, a bound electron tunnels through the modified atomic potential into the continuum. Once the bound electron is liberated from the core it is initially driven away by the oscillating laser field until a subsequent half-cycle when it comes crashing back. Upon recolliding with the core, the electron can either recombine with the parent atom, emitting a photon – this is known as High-Harmonic Generation (HHG) – or it can collide with other bound electrons to induce double or multiple ionisation. When double ionisation occurs, this is referred to as Non-Sequential Double Ionisation (NSDI). It was shown by Fittinghoff (1994) and others (e.g., (Walker et al., 1994)) that it is recollisions that govern the NSDI mechanism, by comparing measurements obtained in linearly-polarised light

with those of elliptically and circularly-polarised light. Hence, the situation can be viewed as an electron-atom collision where the projectile electron is provided by the parent atom.

When scattering energies exceed the first ionisation potential, i.e., in the region of $2 - 5\ I_p$ and above, the divide between the quantum and classical physics contracts. Scattering electrons with high kinetic energy start to exhibit classical behaviour. This opens up the possibility of solving physical systems with increasingly approximate methods whilst still yielding sensible results. In fact, these approximations are not just necessary to reduce the computational cost of fully-quantum methods, but they can also offer more insight into the underlying physics.

Theoretical approaches to NSDI can be split into three main categories. Firstly, there is the brute-force approach of numerically solving the Time-Dependent Schrödinger Equation (TDSE) on a grid. These calculations are extremely expensive, and as a result they were often carried out with reduced dimensionality, e.g., see work by Eberly et al. (1989) and Grobe and Eberly (1992). However, in the late 1990s Taylor and collaborators developed a code based on the R-matrix method, HELIUM, which was one of the first codes to solve the TDSE in full dimensionality for more than one electron (Dundas et al., 1999; Parker et al., 2003, 2006). Furthermore, this work was recently extended to provide a more accurate description of the two ionised electrons in the continuum (Wragg et al., 2015). Going back to grid based methods, Ruiz et al. (2006) managed to solve the two electron TDSE by restricting the motion of the atomic nucleus to the polarisation axis, which appears to be near the limit of what is currently achievable. Another approach to solving the TDSE numerically is that of (Feist et al., 2008) who used a time-dependent close-coupling method to investigate non-sequential two-photon double ionization of helium. However, most of these approaches are not extendable to larger atomic systems and especially not molecules. That being said, this lack of generality has since been addressed by another R-matrix based method, R-matrix with Time-Dependence (RMT). This method exploits the benefits of the R-matrix method to describe complicated multi-electron atomic targets (e.g., see (Hassouneh

et al., 2014; Clarke et al., 2018)) and, most recently, molecular targets (Brown et al., 2020) in a more general fashion.

Moving one rung up the semiclassical ladder, the next category includes the Strong Field Approximation (SFA) methods. SFA has a long history dating back to original work by Keldysh (1965), which was extended via separate efforts by Faisal (1973) and Reiss (1980) to become Keldysh-Faisal-Reiss (KFR) theory. Initial work by Lewenstein et al. (1994) and Becker et al. (1995) demonstrated that KFR-type theories were capable of describing strong-field phenomena. Then, subsequent developments by Popruzhenko et al. (2002) and Liu and Figueira de Morisson Faria (2004) extended this work to look at two electron processes, such as NSDI. One great difficulty of the SFA approach has been the inclusion of Coulomb effects as, typically, the residual Coulombic potential of the ionised atom is neglected in the continuum. However, this has recently been addressed in work carried out by Yan and Bauer (2012) and Maxwell et al. (2017), who used Coulomb-corrected SFA theory to investigate above-threshold ionisation (ATI) interference patterns. That being said, so far these corrections have only been applied in the case of single active electrons which is insufficient to model two electron phenomena such as NSDI, for instance, that can also be sensitive to the long-range Coulomb potential.

The third category concerns semiclassical trajectory methods. These methods are arguable the most approximate, however they can display surprisingly good agreement with experimental and theoretical data e.g., see (Emmanouilidou et al., 2011; Shvetsov-Shilovski et al., 2016). Monte-Carlo trajectory methods, for use in strong-field physics, were first popularised by Leopold and Percival (1978) who used this theoretical framework to describe ionisation of atoms in microwave fields. In early work the initial conditions were governed by a classical microcanonical distribution (Grochmalicki et al., 1991), however in later years Ammosov–Delone–Krainov (ADK) theory became the standard approach (Ammosov et al., 1986). That is, after the widespread adoption of the three-step model (Corkum, 1993), it was assumed that the least bound electron could be accurately described as an electron born into the continuum with a position, momentum and ionisation rate governed by

ADK theory. This approach was successfully demonstrated by Chen et al. (2000) who investigated the momentum distribution of recoil ions resulting from NSDI. One of the additional benefits of trajectory methods is the ability to perform detailed analysis on the trajectories that lead to a specific observable e.g., double ionisation, which can provide valuable insights. For example, by analysing trajectories Yudin and Ivanov (2001) and Bhardwaj et al. (2001) calculated the effect of the Coulomb potential and pulse duration on the DI rate and Emmanouilidou et al. (2011) investigated the contribution of different ionisation pathways to NSDI at different laser intensities.

1.5 Outline of the Thesis

The work presented in this thesis falls largely into two categories based on the scattering energy of the projectile electron. As such, the remainder of this thesis is separated into two parts. Part I concerns low and intermediate energy electron collisions, whilst part II concerns higher energy collisions that occur in strongly-driven systems. In chapter 2, R-matrix theory will be discussed in the context of low and intermediate scattering energies. This is followed by the results obtained from R-matrix calculations for molecular hydrogen and nitric oxide, chapters 3 and 4 respectively. Part II focuses on higher scattering energies such as those induced in strong laser fields opening with chapter 5 which introduces a semiclassical theory based on the three-step model. The results of this theory are presented in chapters 6 and 7, which investigate the effect of the magnetic-field on electron-atom collisions, specifically in the context of non-sequential double ionisation. Finally, conclusions drawn from the entire thesis are presented in chapter 8.

Part I

Low to Intermediate Energy Electron Collisions with Molecules

Chapter 2

R-matrix Theory

This thesis is concerned with the interaction of electrons with atom and molecules. Therefore, it is judicious to work on the energy scale of the atom. The classical Bohr model of hydrogen provides a useful reference point. In this simplified picture the classical radius of the bound electron is $a_0 = 0.529$ Å and the ground state energy, which is equivalent to the ionisation potential, is $I_p = 0.5$ Hartree. Low energy collisions will describe energies that are smaller than the ionisation potential of the atom or molecule i.e., $E \leq I_p$. High energy pertains to collisions where the scattering energy is much greater then the ionisation potential i.e., $E \gg I_p$. The intermediate region is transition between the two regimes.

Atomic units will be used throughout this thesis unless otherwise stated. In atomic units the electron mass m_e, fundamental charge e, Plank's constant $\hbar$ and Coulomb's constant $k_e = 4\pi\epsilon_0$ are all set to one.

This chapter will develop the theory behind electron-molecule scattering at low to intermediate energies – specifically, for molecular processes such as those listed in Table 1.1. Molecules have many additional degrees of freedom that are simply not present in atoms. For example, in addition to the electronic degrees of freedom, molecules can undergo rovibrational excitation owing to the motion of their constituent atoms. This greatly increases the difficulty of solving the time-independent Schrödinger equation (TISE). However, due to the large mass ratio between the nuclei and the electrons, the problem can be split into two more manageable parts. The nuclear wavefunction, which contains rovibrational effects, and the electronic

wavefunction that deals with electronic excitation. This is the Born-Oppenheimer (BO) approximation (Born and Oppenheimer, 1927). The approximation is valid when the time scale of the electron motion is much faster than that of the nuclei. For electron-molecule collisions this is generally true but it tends to break down near resonances or excitation thresholds, where the scattering electron spends more time in the presence of the nuclei (Morrison, 1988).

Using the BO approximation, R-matrix theory will be developed in the Fixed-Nuclei (FN) approximation, where the nuclear degrees of freedom are frozen. This approach neglects the rovibrational motion, however, these effects can be recuperated in the Adiabatic-Nuclei (AN) approximation, as will be discussed in section 2.2.

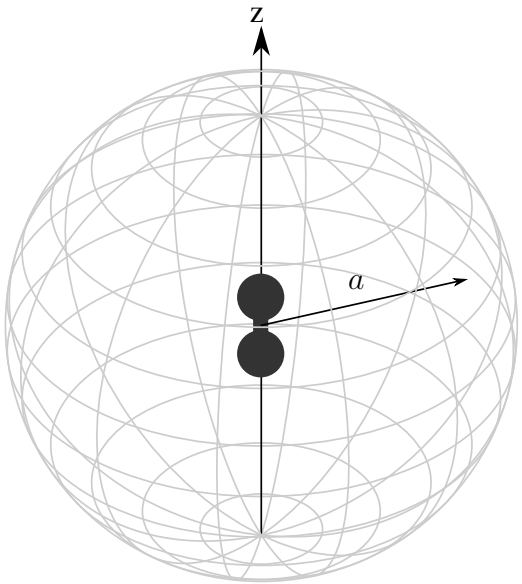

Figure 2.1 | The R-matrix sphere of radius a separates configuration space into an inner and outer region.

Electron collisions with molecules can be described by the time-independent Schrödinger equation.

$$H_{N+1}\Psi = E\Psi, \tag{2.1}$$

where H_{N+1} is the non-relativistic Hamiltonian and E is the total energy. The exact

form of H_{N+1} will be detailed later in this section. To solve equation 2.1 the R-matrix approach is employed. The R-matrix method relies on the principle that configuration space can be separated into two parts; an inner region and an outer region. In the inner region the scattering electron is treated identically as the other N target electrons – taking into account exchange and correlation effects analogous to quantum chemistry methods. But outside this region, in the outer region, all the complicated exchange and correlation effects can be neglected. In the outer region, the scattering electron moves in a simplified potential that is determined by the properties of the target. In the following *target* refers to the solitary molecule that is contained within the inner region.

For scattering in three dimensions a sphere is usually the most sensible choice. Figure 2.1 shows the typical setup for a diatomic molecule. The sphere is centred on the molecule's centre-of-mass (although there are other options (Fandreyer et al., 1993)). The radius of the R-matrix sphere a is selected so that the charge density of the molecule tends towards zero at the boundary. That is, outside the sphere the scattering electron is treated as being distinguishable from the target electrons. If the R-matrix sphere is not big enough then this approximation is no longer valid.

In order to simplify the theory it is preferential to use a body-fixed coordinate system (Burke, 2011). In this coordinate system the molecule itself becomes the frame of reference. It is typical convention to align the z-axis to the molecular axis as shown in Fig. 2.2.

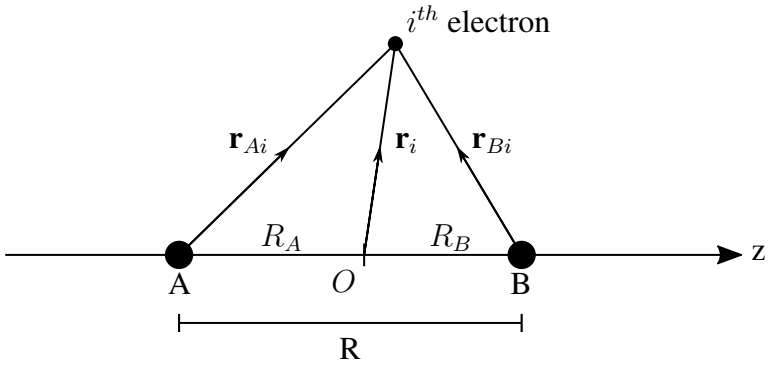

Figure 2.2 | Body-Fixed reference frame for a diatomic molecule AB that is aligned along the z-axis.

In Figure 2.2 $R = R_A + R_B$ is the internuclear separation between the con-

stituent atoms, A and B, with nuclear charge Z_A and Z_B respectively. $\mathbf{r}_i$ is the position of the i^{th} electron with respect to the molecular centre-of-mass, O. Similarly, $\mathbf{r}_{Xi}$ is the position of the i^{th} electron with respect to atom A or B.

2.1 Fixed Nuclei Approximation

2.1.1 Outer Region

The R-matrix method used in this work can be summarised as follows. First, equation 2.1 is solved inside the R-matrix sphere, $r < a$. Then, the inner region solution is used to construct the R-matrix at the boundary $r = a$. Equation 2.1 is then solved in the outer region, $r > a$, in order to propagate the R-matrix to the asymptotic limit, $r \to \infty$, where the solutions can be matched to asymptotic expressions. It is the matching of asymptotic expressions that allows K-matrices, S-matrices and cross-sections to be determined. The theory presented in this section is based on the derivations presented in Burke (2011).

Outside the sphere i.e., for $r > a$ the Hamiltonian is

$$H_{N+1} = -\frac{1}{2}\nabla^2_{N+1} + \sum_{i=1}^{N}\frac{1}{r_{iN+1}} - \frac{Z_A}{r_{AN+1}} - \frac{Z_B}{r_{BN+1}} + \frac{Z_A + Z_B - N}{r_{N+1}}, \tag{2.2}$$

$$H_{N+1} = -\frac{1}{2}\nabla^2_{N+1} + V(r_{N+1}), \tag{2.3}$$

where r_{iN+1} is the distance between the i^{th} and $N + 1^{th}$ electrons and r_{XN+1} is the distance between the $N + 1^{th}$ electron and the atomic nuclei $X = A$ or B. Here $V(r_{N+1})$ is used to represent the potential experienced by the $N + 1^{th}$ electron. In the outer region, using the Hamiltonian given by Eq. 2.3, the solution of equation 2.1 can be expanded in the following way (Burke, 2011)

$$\Psi^{\Delta}_j(E;R) = \sum_{i=1}^{n}\Phi^{\Delta}_i(\mathbf{X}_N;\hat{\mathbf{r}}_{N+1}\sigma_{N+1})\frac{F^{\Delta}_{ij}(r_{N+1})}{r_{N+1}}. \tag{2.4}$$

where the subscript j denotes the set of linearly independent solutions and E is the total energy. $\Phi^{\Delta}_i(\mathbf{X}_N;\hat{\mathbf{r}}_{N+1}\sigma_{N+1})$ are channel functions which depend on the spin-space coordinates of the N target electrons and the angular position $\hat{\mathbf{r}}_{N+1}$ and spin

σ_{N+1} of the scattering electron. The radial dependence of the scattering electron is contained in the reduced radial function $F_{ij}^{\Delta}(r_{N+1})$.

Applying equation 2.3 to equation 2.4 and projecting onto the channel functions $\Phi_i^{\Delta}(\mathbf{X}_N;\hat{\mathbf{r}}_{N+1}\sigma_{N+1})$ leads to the following set of coupled differential equations (Burke, 2011),

$$\left(\frac{d^2}{dr_{N+1}^2} - \frac{\ell_i(\ell_i+1)}{r_{N+1}^2} + \frac{2(Z_A+Z_B-N)}{r_{N+1}} + k_i^2\right) F_{ij}^{\Delta} = 2\sum_{i'=1}^{n} V_{ii'}(r_{N+1}) F_{i'j}^{\Delta}, \tag{2.5}$$

where $i = 1,\ldots,n$ runs over the number of channel functions, Δ is a set of conserved quantum numbers that describe the total scattering state and ℓ_i is the scattering electron's orbital angular momentum. The wavevector, k_i, of a given channel is defined as

$$k_i^2 = 2(E - E_i^N), \tag{2.6}$$

where E is the total energy as before and E_i^N is the energy of a specific target state coupled to that channel. Using a multipole expansion, $V_{ii'}(r_{N+1})$ is given by (Burke, 2011)

$$V_{ii'}^{\Delta}(r_{N+1}) = \sum_{\lambda=0}^{\infty} \frac{\alpha_{ii'\lambda}^{\Delta}}{r_{N+1}^{\lambda+1}}. \tag{2.7}$$

$\alpha_{ii'\lambda}$ are long-range potential coefficients and their form is given in Tennyson (2010). Typically only the first few terms in λ are needed to achieve convergence. $\lambda = 0$ is the static potential and is important for charged targets, otherwise for neutral molecules the dipole $\lambda = 1$ and quadrupole $\lambda = 2$ potentials make the most significant contributions.

2.1.2 Inner Region

Inside the sphere, $0 < r < a$, the Hamiltonian H_{N+1} treats all $N+1$ electrons on equal footing. It can be written as follows (Burke, 2011)

$$H_{N+1} = \sum_{i=1}^{N+1} \left(-\frac{1}{2}\nabla_i^2 - \frac{Z_A}{r_{Ai}} - \frac{Z_B}{r_{Bi}} \right) + \sum_{i>j=1}^{N+1} \frac{1}{r_{ij}} + \frac{Z_A Z_B}{R}, \tag{2.8}$$

where r_{ij} is the distance between the i^{th} and j^{th} electrons and $-\frac{1}{2}\nabla_i^2$ is the kinetic energy operator, in position-space, for the i^{th} electron. The solution of the TISE, equation 2.1, in the inner region is expanded in a set of basis functions ψ_k^Δ (Burke, 2011)

$$\Psi_j^\Delta(E) = \sum_k \psi_k^\Delta(\mathbf{X}_{N+1}; R) A_{kj}^\Delta(E), \tag{2.9}$$

where $A_{kj}^\Delta(E)$ are energy-dependent expansion coefficients, which depend on the asymptotic boundary conditions satisfied by the wave function $\Psi_j^\Delta(E)$ at a given energy E (Burke, 2011). The choice of basis function ψ_k^Δ is flexible and can be altered depending on the purpose of the calculation. In general they are written in this form

$$\psi_k^\Delta = \mathcal{A} \sum_{i=1}^{n} \sum_{j=1}^{n_c} \Phi_i^\Delta(\mathbf{X}_N; \hat{\mathbf{r}}_{N+1}\sigma_{N+1}) \frac{u_{ij}(r_{N+1})}{r_{N+1}} a_{ijk}^\Delta + \sum_i^{n_L} \chi_i^\Delta(\mathbf{X}_{N+1}) b_{ik}^\Delta. \tag{2.10}$$

k runs over the total number of linearly independent basis functions $nn_c + n_L$, n and n_c are the number of channels and continuum functions retained in the expansion respectively and n_L is the number of L-squared functions. $\mathcal{A}$ is the antisymmetric operator that ensures the wavefunction remains antisymmetric under the exchange of two electrons. Φ_i^Δ are channel functions created by coupling the eigenstates of the target to the spin-angle functions of the scattering electron (Burke, 2011). u_{ij} are continuum functions which are centred on the molecular centre-of-mass. In the UKRMol+ codes these continuum functions can be either Gaussian-Type Orbitals (GTOs), B-Spline-Type Orbitals (BTOs) or a combination of both depending on

the requirements of the calculation (Mašín et al., 2020). In each case, they are centred on the molecular centre-of-mass and at the boundary $r = a$ they have, in general, a non-zero amplitude. These non-zero boundary amplitudes form the link between the inner and outer region calculations via the R-matrix. χ_i^Δ are L-squared functions that have vanishing amplitudes at the boundary $r = a$. They represent short-range polarisation and correlation effects. a_{ijk}^Δ and b_{ik}^Δ are expansion coefficients determined by the construction and diagonalisation of the inner region Hamiltonian, $H_{N+1} + L_{N+1}$, in a basis given by 2.10.

$$\langle \psi_k^\Delta | H_{N+1} + L_{N+1} | \psi_k^\Delta \rangle = E_{kk'}^\Delta \delta_{kk'}. \tag{2.11}$$

Unlike the outer region, the inner region is constrained by the R-matrix sphere. In order to keep the Hamiltonian Hermitian an additional Bloch term L_{N+1} is required (Bloch, 1957). The Bloch operator takes the form

$$L_{N+1} = \sum_{i=1}^{N+1} \frac{1}{2} \delta(r_i - a) \left(\frac{d}{dr_i} - \frac{b-1}{r_i} \right). \tag{2.12}$$

b is an arbitrary constant and in this work it is set to zero. This leads to a modified form Eq. 2.1.

$$(H_{N+1} + L_{N+1} - E)\Psi_j^\Delta(E) = L_{N+1}\Psi_j^\Delta(E). \tag{2.13}$$

The solution of this equation is

$$\Psi_j^\Delta(E) = (H_{N+1} + L_{N+1} - E)^{-1} L_{N+1} \Psi_j^\Delta(E), \tag{2.14}$$

$$\Psi_j^\Delta(E) = G_{N+1} L_{N+1} \Psi_j^\Delta(E), \tag{2.15}$$

where G_{N+1} is a Green's function. G_{N+1} can be spectrally decomposed into the R-matrix basis functions ψ_k^Δ which are defined by Eq. 2.10, giving

$$|\Psi_j^\Delta(E)\rangle = \sum_{k=1}^{n_t} \frac{|\psi_k^\Delta\rangle \langle \psi_k^\Delta | L_{N+1} | \Psi_j^\Delta(E)\rangle}{E_k^\Delta - E}. \tag{2.16}$$

This solution is valid for radial distances within the R-matrix sphere i.e., $0 < r \leq a$. By projecting Eq. 2.16 onto the channel functions Φ_i^Δ and evaluating at the boundary $r_{N+1} = a$ it is possible to link the inner and outer region wavefunctions (Burke, 2011).

$$\langle \Phi_i^\Delta r_{N+1}^{-1} | \Psi_{j,\text{in}}^\Delta(E) \rangle |_{r=a} = \sum_{k=1}^{n_t} \left. \frac{\langle \Phi_i^\Delta r_{N+1}^{-1} | \psi_k^\Delta \rangle \langle \psi_k^\Delta | L_{N+1} | \Psi_{j,\text{out}}^\Delta(E) \rangle}{E_k^\Delta - E} \right|_{r=a}, \quad (2.17)$$

$$F_{ij}^\Delta(a, E) = \sum_{i'=1}^{n} R_{ii'}^\Delta(a, E) \left(a \frac{dF_{i'j}^\Delta}{dr} \right). \quad (2.18)$$

where the reduced radial functions F_{ij}^Δ are the same as those in equation 2.4. Equation 2.18 provides the link between the inner and outer region solutions. $R_{ii'}^\Delta$ is the R-matrix which is defined by

$$R_{ii'}^\Delta(a, E) = \frac{1}{2a} \sum_{k=1}^{n_t} \frac{w_{ik}^\Delta w_{i'k}^\Delta}{E_k^\Delta - E}. \quad (2.19)$$

The channel reduced radial functions $F_{ij}^\Delta(a, E)$ are given by

$$F_{ij}^\Delta(a, E) = \langle \Phi_i^\Delta r_{N+1}^{-1} | \Psi_j^\Delta(E) \rangle. \quad (2.20)$$

$w_{i'k}^\Delta$ are boundary amplitudes and they are defined by

$$w_{i'k}^\Delta = \langle \Phi_i^\Delta r_{N+1}^{-1} | \psi_k^\Delta \rangle |_{r=a}, \quad (2.21)$$

$$= \sum_{j=1}^{n_c} u_{ij}(a) a_{ijk}^\Delta. \quad (2.22)$$

The integrals in equations 2.20 and 2.21 are carried out over all of the $N + 1$ spin-space coordinates $\mathbf{X}_{N+1}$ except for the radial coordinate of the scattering electron r_{N+1}. The final step required to obtain scattering amplitudes is to match outer region solutions with their asymptotic counterparts. Generally, the R-matrix sphere is of the order of 10 a_0 and as such, this is not sufficiently far enough away from the molecule to be considered asymptotic. Therefore the R-matrix must be propagated radially outwards e.g., using Light-Walker (Light and Walker, 1976) or BBM

(Baluja et al., 1982) propagators, until the dipole and quadrupole potentials of the molecule vanish. Typically propagation to 100 a_0 is sufficient.

2.1.3 Asymptotic Region

Assuming that the R-matrix has been propagated to the asymptotic limit it is now possible to match with asymptotic solutions. One approach is to use an asymptotic expansion such as that of Gailitis (1976) which has been previously implemented into R-matrix codes by (Noble and Nesbet, 1984). In the asymptotic limit i.e., $r \to \infty$, the solution is (Burke, 2011)

$$F_{ij}^{\Delta}(r) \underset{r\to\infty}{\sim} \frac{1}{\sqrt{k_i}}(\sin\theta_i + \cos\theta_i K_{ij}^{\Delta}), \qquad \text{(open)} \tag{2.23}$$

$$F_{ij}^{\Delta}(r) \underset{r\to\infty}{\sim} 0. \qquad \text{(closed)} \tag{2.24}$$

where k_i is defined by equation 2.6. A channel is open if $k_i^2 \geq 0$ and closed if $k_i^2 < 0$. For electronic excitation, channels are closed below threshold i.e., if $E - E_i^N < 0$. For neutral molecules, such as those studied in this thesis, θ_i are diagonal matrix elements defined by

$$\theta_i = k_i r - \frac{1}{2}\ell_i \pi \tag{2.25}$$

Equation 2.23 enables the construction of the K-matrix, $\mathbf{K}^{\Delta}$, with elements K_{ij}^{Δ}. The K-matrix is a symmetric matrix of size $n_o \times n_o$ where n_o is the number of open channels. All the scattering observables of interest, such as integrated and differential cross-sections, can be derived from the K-matrix. For example the scattering matrix (S-matrix) is given by

$$\mathbf{S}^{\Delta} = \frac{\mathbf{I} + i\mathbf{K}^{\Delta}}{\mathbf{I} - i\mathbf{K}^{\Delta}}, \tag{2.26}$$

and the T-matrix is

$$\mathbf{T}^{\Delta} = \mathbf{S}^{\Delta} - \mathbf{I}. \tag{2.27}$$

The differential cross-section $\frac{d\sigma}{d\Omega}$ for a molecule to transition from initial state i to a final state j is given by (Burke, 2011)

$$\frac{d\sigma_{i\to j}}{d\Omega} = \frac{k_j}{k_i}|f_{ji}(\theta,\phi)|^2. \tag{2.28}$$

k_i and k_j are the channel wavevectors as defined in equation 2.6 and f_{ji} is the scattering amplitude (as defined in Burke (2011) p.565) for the transition $i \to j$.

The integrated cross-section σ for scattering from an initial state i to a final state j is obtained integrating over the scattering angles θ and ϕ. It is directly proportional to the modulus squared of the T-matrix element T_{ji}. The integrated cross-section can be written (Burke, 2011)

$$\sigma_{i\to j} = \frac{1}{2k_i^2(2S_i+1)} \sum_{\Lambda S\pi} \sum_{\ell_i m_{\ell_i} \ell_j m_{\ell_j}} (2S+1)|T_{ji}|^2, \tag{2.29}$$

where Λ is the projection of the total orbital angular momentum of the electron-molecule system onto the molecule axis and S is the total spin angular momentum. π is the parity and is only conserved for diatomic homonuclear (or symmetric linear polyatomic) molecules. ℓ_i and m_{ℓ_i} correspond to the orbital angular momentum and magnetic sublevel of the scattering electron. The first sum is carried out over intermediate states, the second sum is over initial and final channels that contribute to a given transition.

2.2 Adiabatic Nuclei Approximation

In the Born-Oppenheimer approximation the electronic and nuclear degrees of freedom are separated. This principle is used in the Adiabatic-Nuclei approximation. First, the electronic problem is solved with the nuclei fixed in place i.e., the FN approximation. Then, using the vibrational wavefunctions, the nuclear motion effects are recovered by averaging across FN calculations obtained at a range of different geometries. Following the approach of Lane (1980) the vibrationally resolved

cross-section is

$$\sigma^{\mathrm{AN}}_{i,\nu_i\to j,\nu_j} = \frac{1}{2k_i^2(2S_i+1)} \sum_{\Lambda S\pi} \sum_{\ell_i m_{\ell_i} \ell_j m_{\ell_j}} (2S+1) |\langle \nu_j | T_{ji}(R) | \nu_i \rangle|^2, \tag{2.30}$$

where the symbols have the same meaning as equation 2.29. However, if vibrational resolution of the final state is not required then the following is obtained (Lane, 1980)

$$\sigma^{\mathrm{AN}}_{i,\nu_i\to j} = \frac{1}{2k_i^2(2S_i+1)} \sum_{\Lambda S\pi} \sum_{\ell_i m_{\ell_i} \ell_j m_{\ell_j}} (2S+1) \langle \nu_i | | T_{ji}(R) |^2 | \nu_i \rangle, \tag{2.31}$$

$$= \langle \nu_i | \sigma^{\mathrm{FN}}_{i\to j}(R) | \nu_i \rangle, \tag{2.32}$$

where the closure property has been used to sum over all final states ν_j. The AN approximation is valid when the collision time is short compared to the period for vibrational motion. This is predominantly true for high energy scattering and away from resonances (Burke, 2011).

2.3 Scattering Models

The key to a successful R-matrix calculation depends heavily on the functions ψ_k^Δ used to expand the solutions Ψ_j^Δ. Equation 2.10 details the form of these functions ψ_k^Δ, which are solutions to the inner region Hamiltonian (equation 2.11). The first term corresponds to placing N electrons into target orbitals Φ_i^Δ with the $(N+1)^{th}$ electron placed in a space-spin symmetry coupled continuum orbital u_{ij}. The second term consists of L-squared functions that represent all $N+1$ electrons occupying the molecular orbitals (MOs) of the target. Different approaches for constructing these inner region solutions are grouped into categories which correspond to different scattering models.

Before the $N+1$ electron-molecule system is discussed, it is important to select a model to describe the target. The target description relies on standard quantum chemistry approaches that are well described in literature such as Szabo and Ostlund (1989). Knowledge of these methods is assumed for brevity. For com-

patibility with the UKRMol+ code the target can either be described by a Hartree-Fock (HF) model, complete active space configuration interaction (CASCI) model or full configuration interaction (FCI) model. This choice is largely influenced by the number of electrons in the target molecule N. For small targets, $N < 4$, FCI may be tractable however for anything bigger FCI quickly becomes computationally unfeasible. Depending on the choice, target models will contain the following configurations

$$(core)^N, \qquad \text{(HF)}$$
$$(core)^{N_c}(\text{CAS})^{N_a}, \qquad \text{(CASCI)}$$
$$(\text{CAS})^N, \qquad \text{(FCI)}$$

where N_c and N_a represent the number of electrons in the core (i.e., frozen MOs) and the active space MOs respectively. The size of the CAS i.e., the number of MOs available in the active space, will also depend on the number of electrons. Generally, the bigger the CAS the more accurate the calculation – however, careful selection of fewer but more appropriate orbitals can be more effective. Choice of CAS is extremely context specific and a whole field of its own (Tennyson, 1996b). For efficiency it is best to *freeze* as many of the core electrons N_c as possible leaving only the minimum required N_a to capture the correct physics. The choice of target model is dependent on the scattering model employed. Types of scattering model include; static exchange (SE) and static exchange plus polarisation (SEP) which both depend on HF targets; and close-coupling (CC) which can be used with either a CASCI or FCI target depending on the size of the calculation (Tennyson, 2010). For this work, only CC has been used. CC consists of configurations of the type

$$(target)^N(continuum)^1,$$
$$(target)^{N+1},$$
$$(target)^{N-1}(virtual)^1(continuum)^1, \qquad \text{(CASCI only)}$$
$$(target)^{N-1}(virtual)^2, \qquad \text{(CASCI only)}$$

where $target$ represents one of the target models described previously e.g., FCI. $virtual$ corresponds to target MOs that are part of the basis set but not used in the CAS and $continuum$ corresponds to the continuum MOs. When FCI is used the last two configurations (marked CASCI only) are redundant as they will be included in the FCI expansion.

2.4 UKRMol+ Code

The results presented later in this thesis, Chapters 3 and 4, have been obtained using the recently developed UKRMol+ codes which are based on the well established UKRMol codes (Carr et al., 2012). The UKRMol+ code offers new functionality – most notably that B-splines can now be used to represent the continuum. That is, the continuum can now be represented by either a GTO only, GTO+BTO or BTO basis set. The addition of B-splines has played a crucial role in removing the issues associated with linear-dependence which tends to manifest as oscillatory behaviour in the eigenphases.

The code release paper (Mašín et al., 2020) provides a detailed description of the UKRMol+ codes. Therefore only the key points relevant to this thesis will be included in this section.

2.4.1 UKRMol+ Inner

The workflow of a typical UKRMol+ inner region run is summarised in Fig. 2.3. The starting point of any R-matrix scattering calculation is to obtain a *molden* file which is typically generated by the third-party program MOLPRO (Werner et al., 2012). This file contains preliminary molecular data such as the geometry, the target basis set and the target molecular orbitals. This information is fed into `scatci_integrals` which generates all of the 1- and 2-electron integrals that are used in the remaining programs.

The configuration state functions (CSFs) are generated in `congen`. These CSFs are required by `scatci`, the program that builds and diagonalises the Hamiltonian matrix. Both `congen` and `scatci` are run twice, once for the N-electron target and the second time for the $N + 1$-electron complex. It's worth noting that

most of the physics takes place in the construction of the $N+1$-electron wavefunction (Eq. 2.10) and this is determined by configurations generated in `congen`.

`denprop` is used to generate target properties, such as the transition dipole and quadrupole moments in addition to compiling the target states. The target states, along with molecular integrals are used in the second run of `congen` and `scatci`. This generates the inner region scattering states that are required to build the R-matrix on the boundary, in addition to the boundary amplitudes and target properties obtained previously. The generation of the R-matrix is carried out by an interface program `swinterf` which is part of the outer region code suite UKRMol-out.

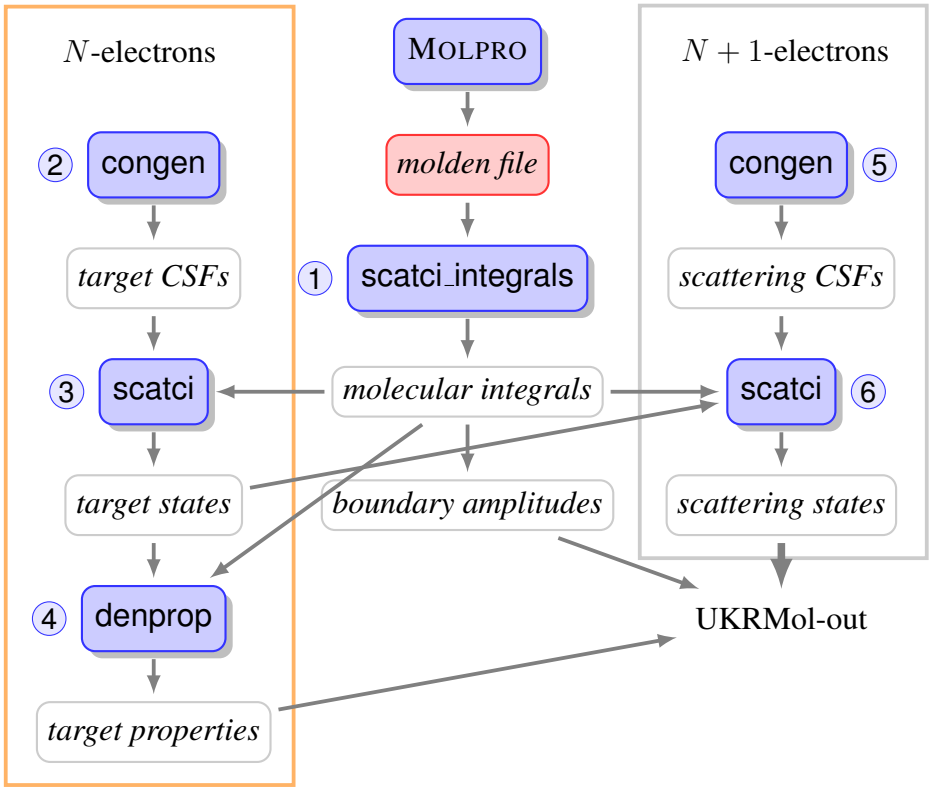

Figure 2.3 | UKRMol+ Process Flowchart for the inner region. Adapted from Mašín et al. (2020) (see text for full description). On the left-hand side `congen` and `scatci` are first run to solve the N-electron problem. Then, on the right-hand side, these two programs are used again but now including the $N+1^{th}$ scattering electron.

2.4.2 UKRMol+ Outer

The workflow of a typical UKRMol+ outer region run is summarised in Fig. 2.4. Carrying on from the inner region, `swinterf` is used to generate channel and R-

matrix data which is input into `rsolve`. `rsolve` is responsible for propagating the R-matrix from the R-matrix sphere radius $r = a$ to the asymptotic limit $r \to \infty$ (Light and Walker, 1976; Baluja et al., 1982). At the asymptotic limit the open channels are matched to asymptotic solutions, thus providing the K-matrices (Noble and Nesbet, 1984). From the K-matrices it is possible to obtain eigenphases (`eigenp`), resonances (`reson`) and T-matrices (`tmatrx`). The T-matrices are required to calculate the differential and integrated cross-sections using the programs `dcs` and `ixsecs` respectively.

In addition to `reson`, `timedel(n)` is also capable of providing resonance parameters and `bound` can be used to find bound states. However none of these programs were used to obtain the results presented in this thesis.

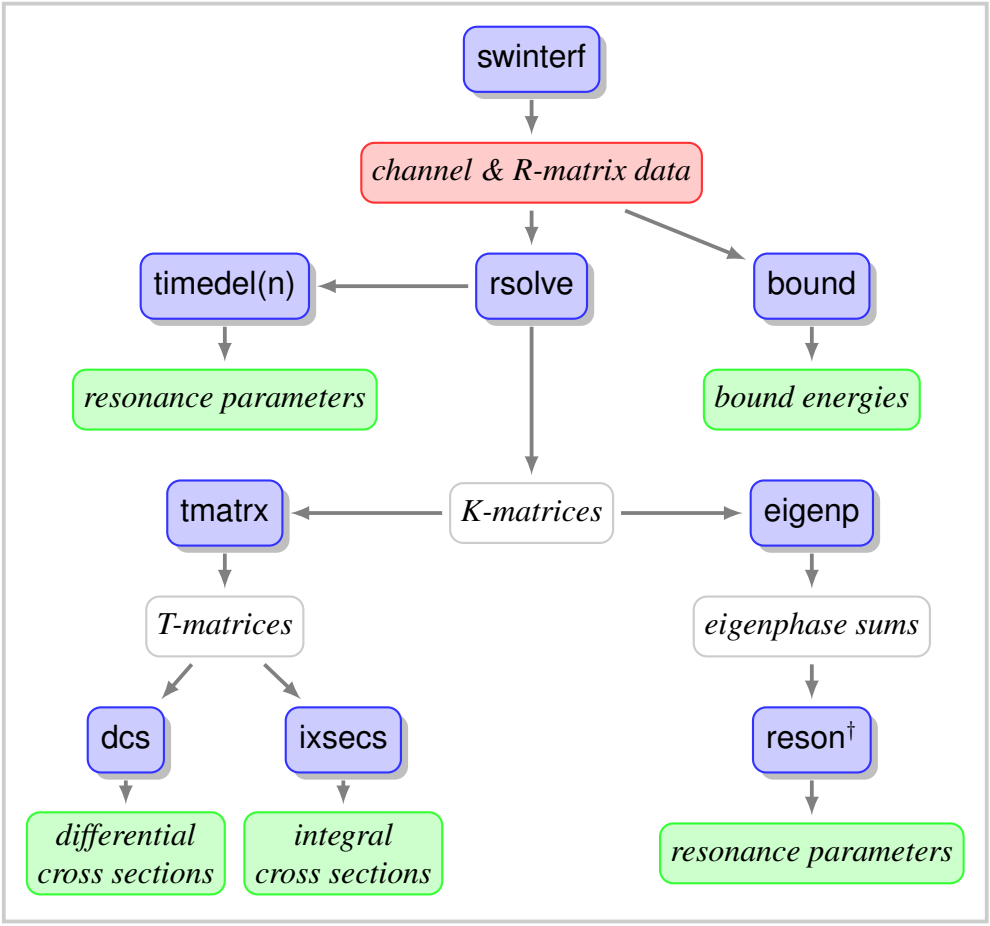

Figure 2.4 | UKRMol+ Process Flowchart for the outer region. Adapted from Mašín et al. (2020) (see text for full description). †reson recursively calls rsolve.

Chapter 3

Benchmark Calculations of Electron Impact Electronic Excitation of the Hydrogen Molecule

This chapter is adapted from published work (Meltzer, Tennyson, Mašín, Zammit, Scarlett, Fursa, and Bray, 2020).

Part I of this thesis investigates low energy electron collisions with molecules before moving onto higher energy collisions with atoms in laser fields in Part II. In this chapter electron collisions with molecular hydrogen are studied in order to produce benchmark cross-section data. The work in this chapter and the next takes place in the absence of any external fields.

The MCCC calculations contained in this chapter were carried out by Zammit, Scarlett, Fursa and Bray.

3.1 Introduction

Molecular hydrogen is one of the simplest, most abundant molecules in the Universe. Understanding of how it interacts with its surroundings is of vital importance for a large variety of physical systems, both naturally occurring and man-made e.g., fusion plasmas, planetary atmospheres and interstellar medium. In these environments, H_2 molecules are subject to frequent collisions with low to high-energy electrons.

The equations that govern electron-molecule collisions are well understood; however, accurate and reliable cross-sections for the different processes that can occur are few and far between. Several recommended cross-section datasets for H_2 have been assembled and published (Tawara et al., 1990; Yoon et al., 2008; Pitchford et al., 2017), and yet, in their most recent review, Anzai et al. (2012) note that benchmark cross-sections are still not available for a variety of cases. Thus far the vast majority of recommended H_2 data are based on experimental results. However, due to practical reasons these data can not always be obtained via experiment. For example, the required target may be unstable (short-lived), or hazardous, or both e.g., T_2.

Furthermore, it is often difficult to obtain *complete* sets of data that contain all the cross-sections of interest across the required energy ranges. Therefore theory must often be relied upon to provide this information. In addition, if cross-sections are required from an initial state other than the ground state then theory is presently the only realistic option. For example, electron impact cross-section data for electronic excitation from metastable excited states is of great interest for the modelling of industrial and astrophysical plasmas, as outlined by Marinković et al. (2007).

In this work molecular convergent close-coupling (MCCC) theory and R-matrix theory are used to produce a set of high-accuracy, benchmark cross-sections for electron impact electronic excitation. This is similar in spirit to the convergent close-coupling (CCC) and R-matrix comparisons for 1 and 2 (active) electron atomic systems namely H (Bartschat et al., 1996a), He (Lange et al., 2006) and Mg (Bartschat et al., 2010). A similar theoretical benchmark for total cross-sections for excitation to the $b\ ^3\Sigma_u^+$ state was performed using the Schwinger variational (Lima et al., 1985), linear algebraic approach (Schneider and Collins, 1985) and R-matrix (Baluja et al., 1985) approaches. It is important to note that this benchmark was a theoretical benchmark of a two-state close-coupling calculation, and was not intended to produce convergent cross-sections. The previous R-matrix calculation was extended by a series of authors; Branchett et al. (1990a) expanded the target model to include the first six excited electronic states, giving an improved integrated

cross-section and subsequently differential cross-sections (Branchett et al., 1991); Stibbe and Tennyson (1998) added adiabatic nuclei effects to study near-threshold electron impact dissociation; and Trevisan and Tennyson (2002) then applied these methods to other isotopes of hydrogen, namely deuterium and tritium.

The R-matrix method used in this work is well established and tested. On the other hand, MCCC theory is more recent in its development (Zammit et al., 2014), although it is based on the atomic CCC approach (Bray and Stelbovics, 1992) which has been rigorously tested since its inception in the early 1990's. A tutorial summarising the MCCC theory is provided by Zammit et al. (2017a) and the theory pertaining to the R-matrix method has been covered in chapter 2. Therefore, below only the features of each theory that are relevant for this work are discussed.

Where data are available, theoretical calculations obtained in this work are compared with experiment. For example, there are integrated and differential cross-sections available for some of the lower-lying excited states at intermediate (14 eV to 17.5 eV) (Hargreaves et al., 2017) and higher energies (17.5 eV to 30 eV) (Wrkich et al., 2002). As well as work carried out by Muse et al. (2008) which provides elastic cross-sections from 1 eV up to 30 eV. Also, in a recent comparison between theory and experiment, Zawadzki et al. (2018) provides cross-sections for the $X\ ^1\Sigma_g^+ \rightarrow b\ ^3\Sigma_u^+$ transition.

3.2 Method

3.2.1 R-Matrix

For the R-matrix calculations, the UKRMol+ suite of codes (Mašín et al., 2020) has been utilised. This new and improved version of the former UKRMol codes has been successfully used for a variety of molecular targets such as BeH (Darby-Lewis et al., 2017), CO (Zawadzki et al., 2020) and pyrimidine (Regeta et al., 2016). The most notable difference between UKRMol+ and UKRMol is the implementation of B-spline type orbital (BTO) basis functions allowing the user to select a Gaussian type orbital (GTO) only, mixed BTO/GTO or BTO only representation of the continuum. Use of BTOs greatly extends the range of possible R-matrix radii. The

calculations in this work use a BTO-only continuum, a large molecular R-matrix radius of $a = 100\ a_0$ and a triply-augmented target basis set especially designed for Rydberg-like orbitals.

3.2.1.1 Target Model

The R-matrix method relies on a balanced description of the target and scattering wavefunctions, N and $N + 1$ respectively (Tennyson, 1996b), where N is the number of electrons in the target. Molecular hydrogen is a two electron system. Therefore the aim is to use the most comprehensive models available in each case. Full-CI is the hallmark of accuracy in electronic structure methods and it provides an exact solution to the Schrödinger equation within a given finite-sized one-electron basis set (Knowles and Handy, 1984). This method is used with an augmented Dunning basis set, especially designed to describe Rydberg-type excitations in molecules, x-aug-cc-pVXZ (Dunning, 1989; Woon and Dunning, 1994). x-aug signifies that the basis set is doubly, triply, quadruply-augmented where x = d, t, q, etc. Triply augmented means that three additional, even-tempered basis functions are added for each angular symmetry available in the original cc-pVXZ set. Traditional Dunning basis sets, cc-pVXZ, are correlation consistent and hence provide a systematic way of approaching the complete basis set limit as the number, X, of zeta functions is increased – although they are largely designed for optimisation of the ground state.

Preliminary work found that moving from a singly augmented basis set to a triply augmented basis set had a more profound effect on the target description than increasing the number of zeta functions i.e., pVXZ for X = D, T, Q, etc. Figure 3.1 shows the convergence of different basis sets; the standard Dunning basis sets, cc-pVXZ; and the augmented Dunning basis sets, x-aug-cc-pVXZ for an individual hydrogen atom. The hydrogenic target states should be degenerate for a given shell, n. The standard Dunning basis sets fail to produce degenerate states even for the first excited state of H i.e., $n = 2$. The standard Dunning basis sets do show improvement as more zeta functions are added but they are clearly not sufficient. As for the augmented Dunning basis sets, the situation is much better. The singly augmented aug-cc-pVTZ basis set shows a marked improvement across all target

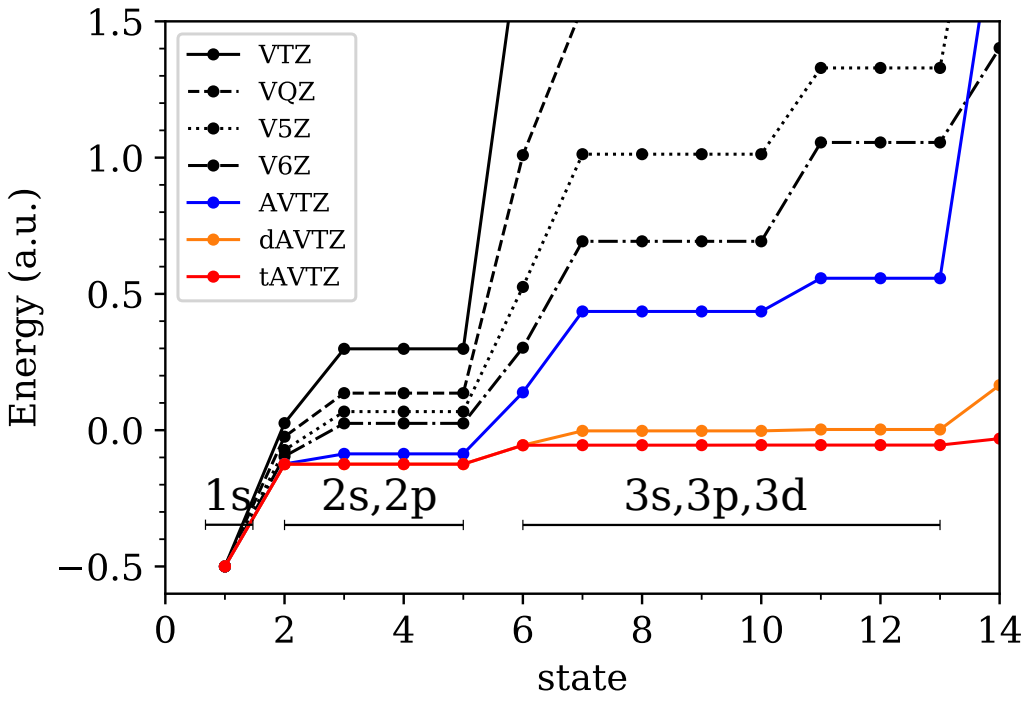

Figure 3.1 | Convergence of H atom basis set for; Dunning basis sets, cc-pVXZ, where X = T (solid), Q (dashed), 5 (dotted) and 6 (dot-dashed); and augmented Dunning basis sets, x-aug-cc-pVXZ where X = T and x = s (blue), d (orange), t (red).

states for the H atom, even though the $n = 2$ level is not degenerate. The doubly-augmented basis set d-aug-cc-pVTZ provides degenerate $n = 2$ states and finally the triply-augmented basis set, t-aug-cc-pVTZ (tAVTZ hereafter), produces degenerate states up to $n = 4$ which are required for this work, where excitations of H_2 for $n \leq 3$ are considered. Hence, for this work tAVTZ was found to be the optimal choice (see Fig. 3.2).

As mentioned previously, this calculation will use Full-CI and the tAVTZ basis set. Therefore, the target model, in D_{2h} symmetry[1], can be expressed as $(19, 9, 9, 4, 19, 9, 9, 4)^2$. This notation is used to represent two electrons occupying any spin-space symmetry allowed combination of Molecular Orbitals (MOs), where the UKRMol+ code has the convention of ordering the MOs in terms of the eight irreducible representation as follows, (A_g, B_{3u}, B_{2u}, B_{1g}, B_{1u}, B_{2g}, B_{3g}, A_u). Using

[1]The polyatomic UKRMol and UKRMol+ codes work in Abelian symmetry. Therefore D_{2h} is used instead of $D_{\infty h}$, however it is possible to convert between the two point group symmetries as and when required.

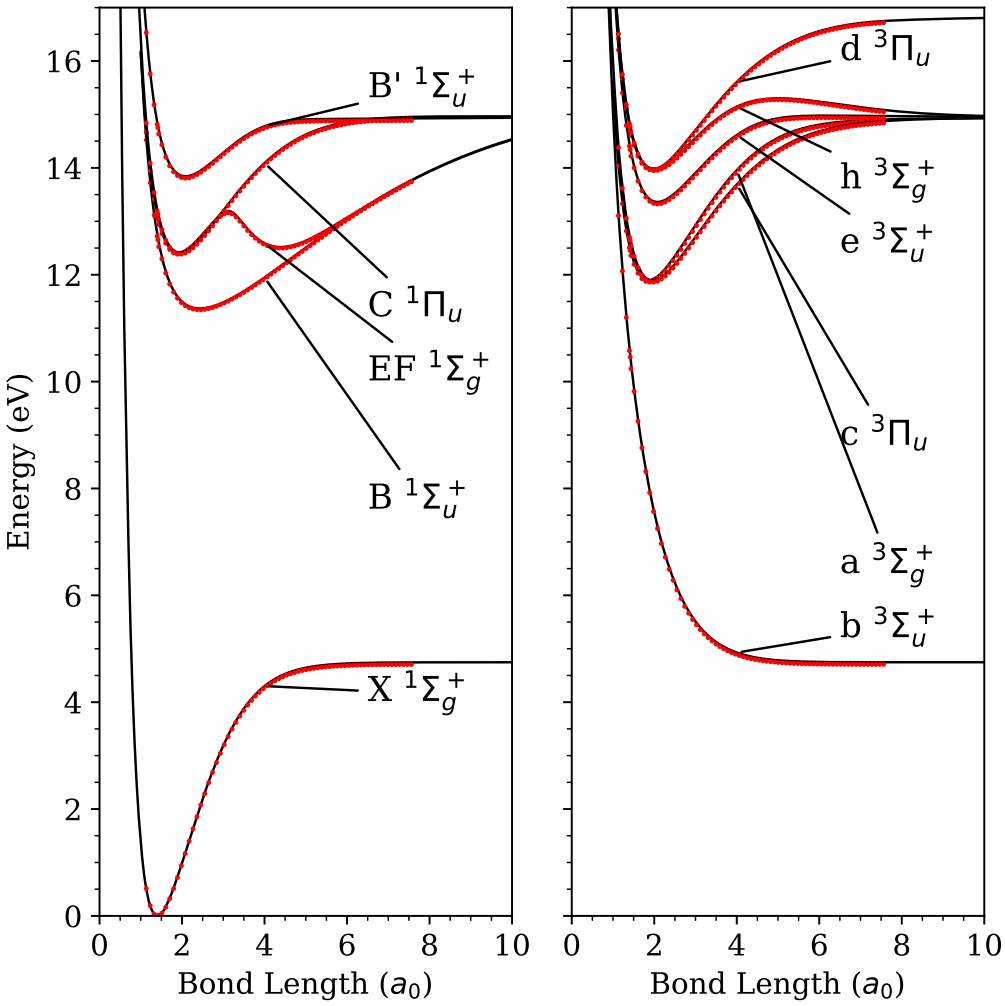

Figure 3.2 | Potential energy curves for the ground state and the lower-lying excited states. Reference data (black) from Kolos et al. (1986), Staszewska and Wolniewicz (1999), Staszewska and Wolniewicz (2002), Wolniewicz and Dressler (1994) and Wolniewicz and Staszewska (2003). UKRMol+ calculation (red) produced in this work using the tAVTZ basis set and the Full-CI method.

this model, the N-electron problem can be solved in order to calculate target state energies (on average, 400 configuration state functions are generated per molecular spin-space symmetry). Target state energies were calculated at the equilibrium geometry $R_e = 1.40\ a_0$ to compare with accurate structure calculations of Kolos et al. (1986), Staszewska and Wolniewicz (1999), Staszewska and Wolniewicz (2002), Wolniewicz and Dressler (1994), Wolniewicz and Staszewska (2003) and the MCCC calculations of Zammit et al. (2017b) (see Table 3.1). Potential energy curves from the aforementioned references are compared with our calculations in Fig. 3.2.

For the excited states considered in this work, the R-matrix method produces more accurate target states than the spherical MCCC method. This is due to the difference in how the target is expanded in the two methods. MCCC uses single centre expansion, which performs worse for lower target states, however it quickly improves for the higher lying, Rydberg-like states. The R-matrix method however uses a linear combination of atom-centred GTOs. This generally performs better for the ground and low-lying excited states and in this work it performs well for all the states listed in Table 3.1.

3.2.1.2 Scattering Model

In the R-matrix method the electronic density of the target must be contained within the R-matrix sphere, which is of radius a. Therefore, for a given target basis set the radial charge density of each of the MOs should be negligible at the boundary. It was found in this work that 1×10^{-10} was a suitable threshold. For a doubly-augmented basis set (d-aug-cc-pVTZ) this means an R-matrix radius of size $a = 45$ a_0 is required, whilst for the tAVTZ basis set used here a radius of $a = 100\ a_0$ is sufficient. Free-particle scattering provides a useful tool to validate the R-matrix radius for a given target. It was found that radii that did not meet the criteria above suffered from unphysical behaviour i.e., negative eigenvalues of the kinetic energy matrix.

Up until now, an R-matrix sphere of size $a = 100\ a_0$ would have been impossible, as the continuum basis set required to fill the space would suffer from severe

Table 3.1 | Absolute target energies, E (a.u.), at the equilibrium bond length $R_e = 1.40\ a_0$ compared to accurate electronic structure calculations.

	E (a.u.)		
state	Ref	RM[f]	MCCC[g]
$X\ ^1\Sigma_g^+$	-1.174[a]	-1.173	-1.162
$b\ ^3\Sigma_u^+$	-0.784[b]	-0.784	-0.770
$a\ ^3\Sigma_g^+$	-0.714[b]	-0.713	-0.710
$B\ ^1\Sigma_u^+$	-0.706[c]	-0.705	-0.697
$c\ ^3\Pi_u$	-0.707[b]	-0.706	-0.701
$EF\ ^1\Sigma_g^+$	-0.692[d]	-0.691	-0.687
$C\ ^1\Pi_u$	-0.689[e]	-0.688	-0.683
$e\ ^3\Sigma_u^+$	-0.644[b]	-0.643	-0.640
$h\ ^3\Sigma_g^+$	-0.630[b]	-0.630	-0.628
$d\ ^3\Pi_u$	-0.629[b]	-0.628	-0.626
$B'\ ^1\Sigma_u^+$	-0.629[c]	-0.628	-0.625

[a]Kolos et al. (1986); [b]Staszewska and Wolniewicz (1999); [c]Staszewska and Wolniewicz (2002); [d]Wolniewicz and Dressler (1994); [e]Wolniewicz and Staszewska (2003); [f]This work; [g]Zammit et al. (2017b).

linear dependence. However, as mentioned previously, the new UKRMol+ codes allow the use of BTOs which are numerically stable regardless of the size of the R-matrix sphere. It was found that, for molecular hydrogen, using a BTO only continuum basis not only removed linear dependence issues but it also gave a better description of the continuum. Moreover, the wall-clock time required to compute continuum integrals was reduced for a BTO-only continuum compared to that of the mixed BTO/GTO continuum. Details of the continuum basis can be found in Table 3.2.

Table 3.2 | Parameters used for the continuum basis.

Property	Value
Number of B-Splines (per L)	75
B-spline Order	9
L_{max}	6

The convergence of scattering observables also depends on $L_{\max}$, the maximum number of partial waves included. In principle, the higher the cut-off the better. However, as will be discussed in section 3.3.3 this becomes computationally intractable very quickly. For this calculation, $L_{\max} = 6$ provided the best compromise between computational resources and accuracy.

It is found that a relatively large number of continuum BTOs are required and this is due to two reasons. Firstly, an R-matrix sphere of $100\ a_0$ has been used in order to contain the charge density of the target. Secondly, integrated cross-sections (ICS) are required up to scattering energies of 30 eV. Higher scattering energies require more basis functions in order to converge. The convergence of the continuum basis is verified by free-particle scattering. In free-particle scattering the target potential is completely neglected, therefore the scattering electron experiences no phase-shift. This means that the eigenphase sum, across the energy range considered, should be zero. Figure 3.3 shows how the convergence of the BTO continuum basis set varies as a function of the number of B-splines. The eigenphase sum is plotted for the A_g symmetry. It was found that satisfactory convergence is achieved with 75 B-splines per angular symmetry.

A close-coupling expansion is employed to solve the scattering problem. This is necessary for describing exchange and polarisation effects in addition to modelling electronic excitation. To ensure balance between the $N + 1$ and N-electron contributions in the close-coupling expansion, a similar treatment is required in the $N + 1$ electron system as that used for the target. Two types of configuration state function (CSF) are adopted in the $N+1$ system. There are those where one electron occupies a continuum orbital, and those where all of the $N+1$ electrons occupy the target molecular orbitals. This amounts to;

$$(target)^2(continuum)^1,$$
$$(target)^3,$$

where $target$ stands for the complete set of target molecular orbitals. Note that in the first configuration step it is necessary to couple the target electrons to the appro-

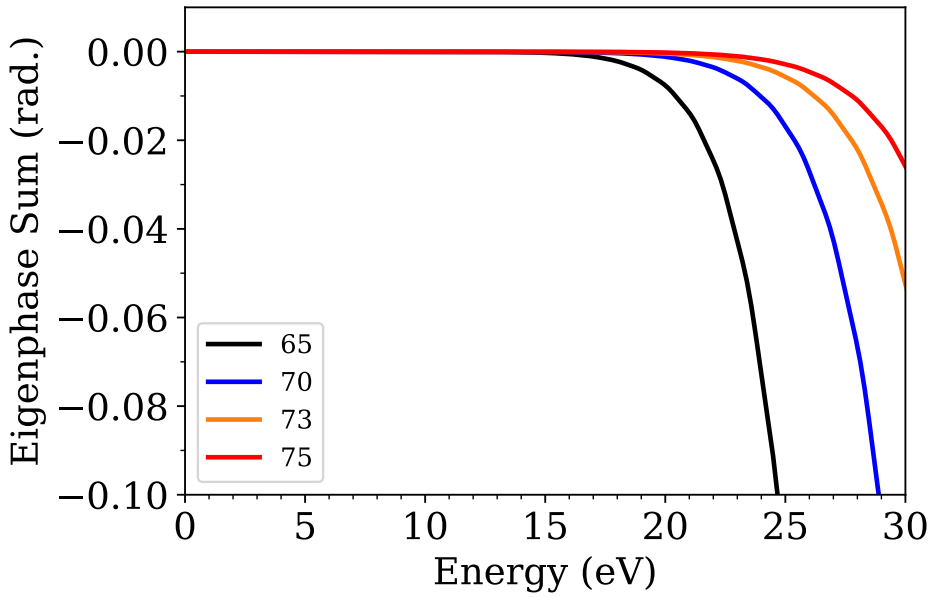

Figure 3.3 | Eigenphase sum for a free scattering electron in the A_g symmetry computed with a continuum basis of 65 (black), 70 (blue), 73 (orange) and 75 (red) b-splines per angular symmetry.

priate symmetry, in order to facilitate the identification of the correct target states (Tennyson, 1996a). However, there are no such constraints on the "L^2" configurations generated in the second step. Using this model, all the target states below 30 eV vertical excitation energy are retained – which for this calculation is 98 states. This generates an average of 65,000 CSFs per molecular symmetry. Preliminary tests were carried out using fewer states e.g., all states up to 20 eV, however, it was found that all the states below the scattering energy of interest must be included in order to get accurate results. Past the energy of the last state included the scattering cross-sections are incorrectly enhanced as there are fewer open channels.

As discussed in sec. 2.4.1, the construction of the $N + 1$ Hamiltonian is carried out by the program `scatci` (Al-Refaie and Tennyson, 2017) which is based on an earlier version written by Tennyson (1996a). A dramatic time-saving is gained by re-using the target states already generated in the N-electron diagonalisation. However, in preliminary studies it was found that there was a phase-inconsistency (Tennyson, 1997) between the target states generated in the N and $N + 1$ calculations. This problem was resolved by reading in the CI vectors generated in the

N-electron calculation.

In the scattering calculation, after the R-matrix has been constructed it must be propagated outwards, as discussed in the theory section (sec. 2.1.3). For smaller R-matrix radii, $a \sim 10\ a_0$, the asymptotic limit is usually taken to be $r_{\text{asym}} = 100\ a_0$. However, in this work the R-matrix radius is already $a = 100\ a_0$. As an initial test, calculations were run without any propagation at all but this lead to spurious resonances in the ICSs at the higher scattering energies. These resonances were eliminated by increasing the asymptotic limit from $r_{\text{asym}} = 100\ a_0$ to $r_{\text{asym}} = 200\ a_0$. To check convergence a further test was run with an asymptotic limit of $r_{\text{asym}} = 300\ a_0$ which displayed no differences to the $r_{\text{asym}} = 200\ a_0$ calculation. For this work, the results obtained with the asymptotic limit $r_{\text{asym}} = 300\ a_0$ are presented.

Up to now differential cross-sections obtained from UKRMol and UKRMol+ calculations were generated using the program POLYDCS (Sanna and Gianturco, 1998) which includes rotational excitation of the molecule but is limited to electronically elastic transitions. Therefore a new program has been developed for the calculation of differential cross-sections (DCS) which includes only orientational averaging of the molecule but is applicable to electronically inelastic transitions and optionally employs the standard top-up procedure based on the first Born approximation for inelastic dipolar scattering. This will be discussed later in sec. 3.3.3.

3.2.2 Molecular convergent close-coupling

The MCCC method is a momentum-space formulation of the close-coupling theory. The target spectrum is represented by a set of (pseudo)states generated by diagonalising the target electronic Hamiltonian in a basis of Sturmian (Laguerre) functions. For a suitable choice of basis the resulting states provide a sufficiently accurate representation of the low-lying discrete spectrum and a discretisation of the continuous spectrum, which allows the effects of coupling to ionisation channels to be modelled. Expanding the total scattering wave function in terms of the target pseudostates and performing a partial-wave expansion of the projectile wave function leads to a set of linear integral equations for the partial-wave T-matrix elements,

which are solved using standard techniques. The strength of the MCCC method is the ability to perform calculations with very large close-coupling expansions, allowing for the explicit demonstration of convergence in the scattering quantities of interest with respect to the number of target states included in the calculations and the size of the projectile partial-wave expansion.

The MCCC method has been implemented for electron and positron scattering on diatomic molecules in both spherical and spheroidal coordinates. The spherical implementation is simpler and provides an adequate description of the molecular structure at the mean internuclear separation of the H_2 ground state. The spherical MCCC method has been used for detailed convergence studies and the calculation of elastic, excitation, ionisation, and grand-total cross-sections over a wide range of incident energies. Spheroidal coordinates are a more natural system for describing the electronic structure at larger R, where the target wave functions become more diffuse. The spheroidal MCCC method has been utilised to calculate vibrationally-resolved cross-sections for excitation of a number of low-lying states of H_2, including scattering on all bound vibrational levels of the ground electronic state (Scarlett et al., 2020, submitted). This has allowed detailed studies to be performed for dissociation of H_2 in the ground and vibrationally-excited states (Scarlett et al., 2019a; Tapley et al., 2018b,a; Scarlett et al., 2018), and vibrational excitation of the $X\ ^1\Sigma_g^+$ state via electronic excitation and radiative decay (Scarlett et al., 2019b). For clarity of presentation, in the present work only the spherical MCCC results are used. For details of the spheroidal MCCC method and comparisons of the spherical and spheroidal MCCC cross-sections see Scarlett et al. (2020).

3.2.2.1 Target Model

The MCCC target structure is obtained using a CI calculation. The basis for the CI expansion consists of two-electron configurations formed by products $(n\ell, n'\ell')$ of one-electron Laguerre-based orbitals. To reduce the number of two-electron states generated, one of the target electrons is allowed to occupy any one-electron orbital, while the other is restricted to the $1s$, $2s$, and $2p$ orbitals. The largest target structure calculation performed in this work utilises a Laguerre basis of $N_\ell = 17-\ell$ functions

with $\ell \leq 3$, which generates a total of 491 states. To improve the accuracy of the $X\ ^1\Sigma_g^+$ and $b\ ^3\Sigma_u^+$ states, where the multicentre effects are strongest, the $1s$ Laguerre function is replaced with an accurate H_2^+ $1s\sigma_g$ state obtained via diagonalisation of the H_2^+ Hamiltonian in a basis with $N_\ell = 60 - \ell$ functions for $\ell \leq 8$.

3.2.2.2 Scattering Models

Fixed-Nuclei MCCC calculations were performed at $R = 1.448\ a_0$ using a number of scattering models, ranging from 9 to 491 states included in the close-coupling expansion. This allowed for a detailed investigation of convergence and the effects of including various reaction channels (see Zammit et al. (2017b) for details). The MCCC results presented here were obtained from the 491-state model, which yielded convergent cross-sections for each of the transitions of interest. With regards to the partial-wave expansion of the projectile wave function, angular momenta up to $L_{\text{max}} = 8$ have been included, as well as all total angular momentum projections up to $M_{\text{max}} = L_{\text{max}}$. To account for the contributions from higher partial waves an analytical Born subtraction (ABS) technique is utilised, which is equivalent to replacing the $L > L_{\text{max}}$ cross-sections with their respective partial-wave Born cross-sections. It is found that the partial-wave expansion with $L_{\text{max}} = 8$ produces convergent integrated cross-sections for all transitions considered here when used in conjunction with the ABS technique. For dipole-allowed transitions, the partial-wave convergence of the DCS can be considerably slower than it is for the ICS. The method adopted to resolve this issue is discussed in Zammit et al. (2017b). For the $X\ ^1\Sigma_g^+ \rightarrow b\ ^3\Sigma_u^+$ transition, adiabatic-nuclei calculations have been performed at low incident energies using a model consisting of 12 target states which yields convergent cross-sections for the $b\ ^3\Sigma_u^+$ state below approximately 15 eV. These calculations are described in Scarlett et al. (2017).

3.3 Results

In this section, FN ICS and DCS for elastic and inelastic processes are presented. For inelastic processes the first ten electronic excited states are considered. In the second section the AN approximation is used to introduce nuclear motion effects

which are particularly important close to threshold.

Table 3.3 | Absolute target energies, E (a.u.), and vertical excitation energies, ΔE (eV), at the mean vibrational bond length $R_0 = 1.448\ a_0$. RM data are from UKRMol+ (this work) and MCCC from Zammit et al. (2017b).

	E (a.u.)		ΔE (eV)	
State	RM	MCCC	RM	MCCC
$X\ ^1\Sigma_g^+$	-1.172	-1.161	-	-
$b\ ^3\Sigma_u^+$	-0.796	-0.782	10.23	10.31
$a\ ^3\Sigma_g^+$	-0.718	-0.715	12.35	12.14
$B\ ^1\Sigma_u^+$	-0.712	-0.704	12.52	12.44
$c\ ^3\Pi_u$	-0.712	-0.707	12.52	12.35
$EF\ ^1\Sigma_g^+$	-0.697	-0.693	12.93	12.73
$C\ ^1\Pi_u$	-0.694	-0.693	13.02	12.73
$e\ ^3\Sigma_u^+$	-0.650	-0.647	14.21	13.99
$h\ ^3\Sigma_g^+$	-0.636	-0.634	14.60	14.34
$B'\ ^1\Sigma_u^+$	-0.635	-0.631	14.63	14.42
$d\ ^3\Pi_u$	-0.634	-0.632	14.65	14.39

The scattering calculations that follow were carried out at the mean vibrational bond length, $R_0 = 1.448\ a_0$, to provide the best comparison to experiment, within the FN approximation. Table 3.3 lists the target states and the vertical excitation energies obtained for both methods. Similarly, compared to Table 3.1, the R-matrix target energies are more accurate than the MCCC method, as they are lower in energy (note that both methods are variational). However, it should be noted that the absolute energy is of less significance for this work, and that the vertical excitation energies (relative to the ground state) are in good agreement.

3.3.1 Fixed-Nuclei Cross-Sections

ICS and DCS for the first ten target states (see Table 3.3); $X\ ^1\Sigma_g^+$, $b\ ^3\Sigma_u^+$, $a\ ^3\Sigma_g^+$, $B\ ^1\Sigma_u^+$, $c\ ^3\Pi_u$, $EF\ ^1\Sigma_g^+$, $C\ ^1\Pi_u$, $e\ ^3\Sigma_u^+$, $h\ ^3\Sigma_g^+$, $B'\ ^1\Sigma_u^+$ and $d\ ^3\Pi_u$ are presented in the following section. Where available, previously recommended cross-sections and experimental results are plotted against the two theoretical calculations.

3.3.1.1 Elastic Cross-Sections

The elastic ICS (Fig. 3.4) demonstrates good agreement between MCCC and R-matrix theory. The calculated data lie within the error bars of the experiment conducted by Muse et al. (2008). For the DCS (Fig. 3.5) at scattering angles exceeding 15° the two theories essentially overlap. At energies greater than 15 eV the R-matrix calculations have a diminished forward peak and this is due to a lack of convergence of the partial wave expansion. Due to computational constraints $L_{\max} = 6$ for the R-matrix calculations. This compares to $L_{\max} = 8$ for the MCCC calculation, which also employs the analytical Born subtraction technique. Nevertheless, scattering angles close to $\theta = 0$ or $\theta = 180$ do not contribute as much to the ICS due to a $\sin\theta$ term in the integrand. Therefore, despite the differences in the DCSs the resulting ICSs are similar.

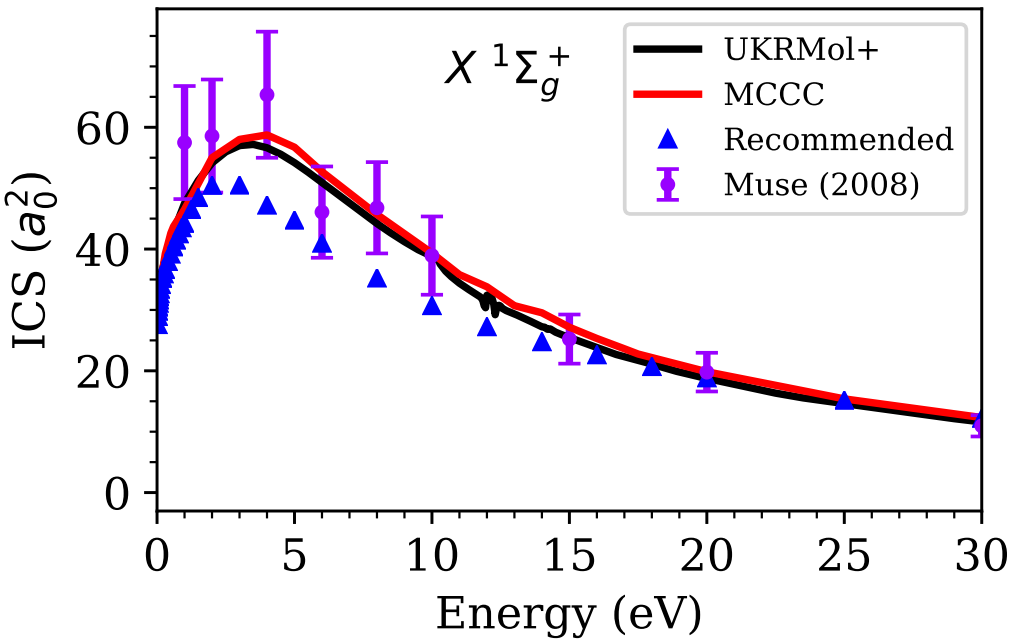

Figure 3.4 | ICS for elastic collisions. Comparison of the UKRMol+ and MCCC calculations with the measurements of Muse et al. (2008) and recommended data of Yoon et al. (2008).

The recommended data of Yoon et al. (2008) for the ICS are noticeably lower than those obtained from the R-matrix and MCCC calculations (Fig. 3.4). Whilst they are within their specified margin of error ($\pm 20\%$), due to the excellent agree-

ment between both theories and experiment for the DCS (Fig. 3.5), it is believed that the recommended data should be revised upwards.

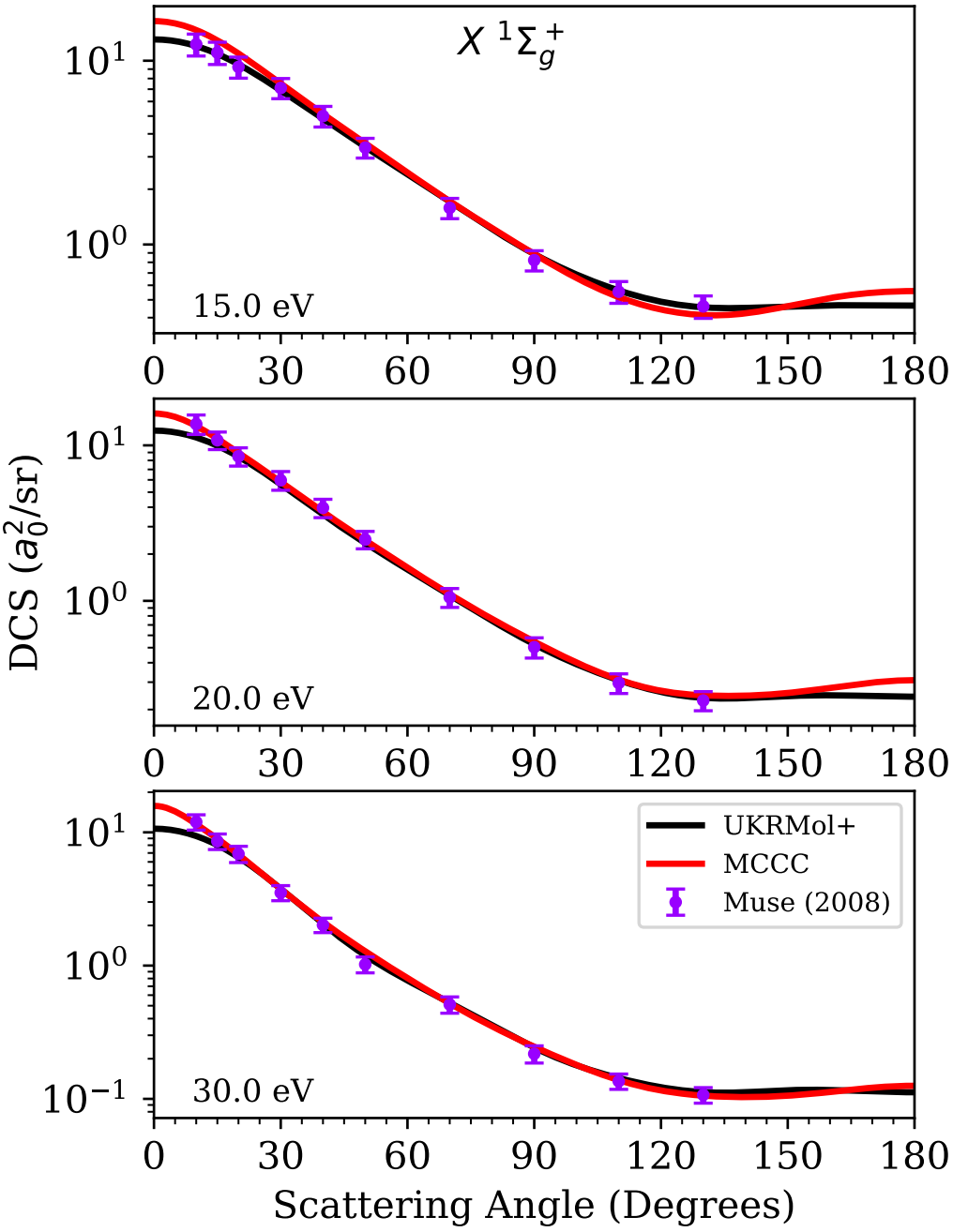

Figure 3.5 | DCS for elastic collisions. Comparison of the UKRMol+ and MCCC calculations with the measurements of Muse et al. (2008).

3.3.1.2 Triplet States

The first excited electronic state is $b\,^3\Sigma_u^+$. For this state a fine energy grid has been used for both the MCCC and UKRMol+ calculations. This allows an accurate comparison of the two ICSs. In Fig. 3.6 prominent resonance structures are observed near 12 eV. Across the energy range considered the two calculations agree.

The current recommended cross-sections agree at low energy but from 15 eV to 20 eV they appear to overestimate the cross-section. The newer experiment from Zawadzki et al. (2018) is much closer to the two theories. The DCSs (Fig. 3.7) also agree closely with these experimental data. The R-matrix calculations are a little higher than the MCCC calculations for angles exceeding 135° but, again, the effect of this on the ICS is insignificant.

For higher excited states i.e., those energetically above $b\,^3\Sigma_u^+$, MCCC results are presented on a coarser energy grid. Therefore, narrow resonant structures cannot be compared. The ICSs for states $a\,^3\Sigma_g^+$, $c\,^3\Pi_u$ and $e\,^3\Sigma_u^+$ (Figs. 3.8, 3.10 and 3.12 respectively) show good agreement between the MCCC and R-matrix theories.

The recommended data points are based on the EELS (Electron Energy Loss Spectroscopy) experiment of Wrkich et al. (2002). The data points are sparse so it is hard to quantitatively compare against the two theory calculations. However, given agreement between the two theoretical calculations and more recent experiments, it is proposed that the recommended cross-sections should be revised for all of the triplet states considered so far.

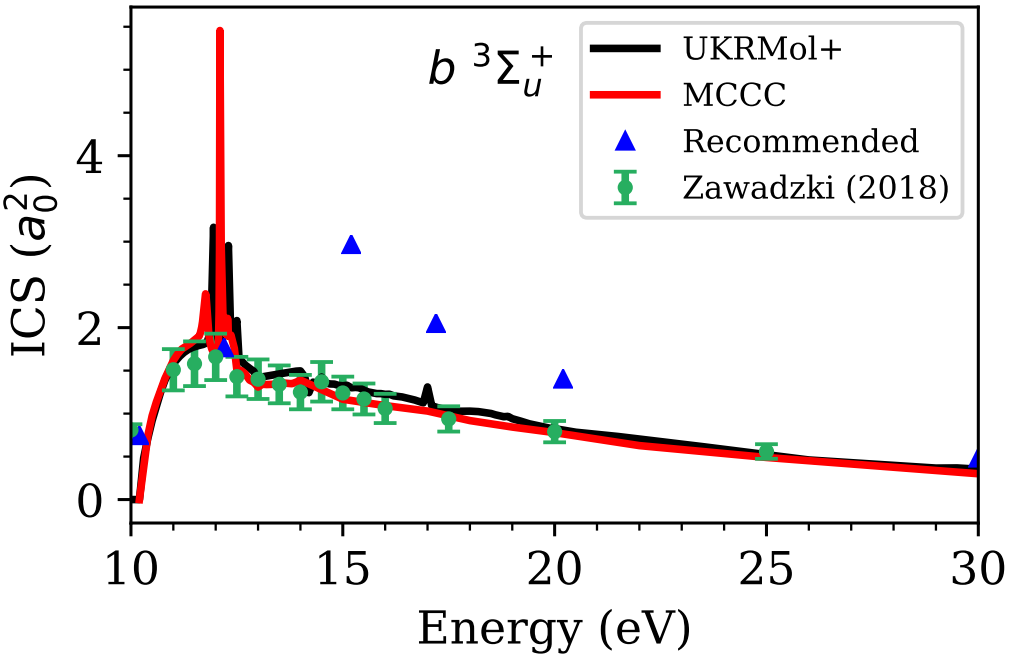

Figure 3.6 | ICS for the $X\ ^1\Sigma_g^+ \rightarrow b\ ^3\Sigma_u^+$ transition. Comparison of the UKRMol+ and MCCC calculations with the measurements of Zawadzki et al. (2018) and recommended data of Yoon et al. (2008).

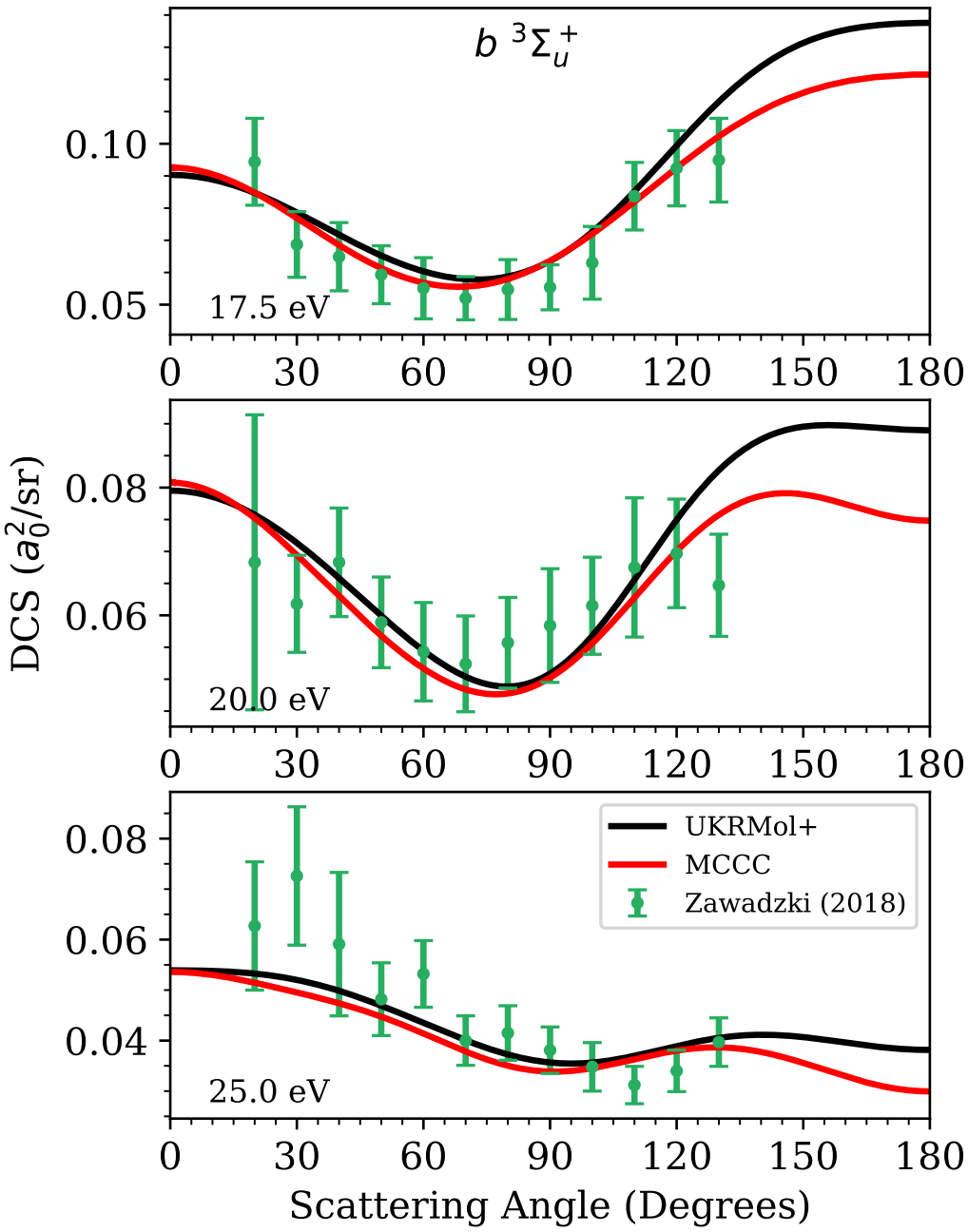

Figure 3.7 | DCS for the $X\ ^1\Sigma_g^+ \rightarrow b\ ^3\Sigma_u^+$ transition. Comparison of the UKRMol+ and MCCC calculations with the measurements of Zawadzki et al. (2018).

The DCSs shed more light on the comparison. Fig. 3.9 shows the $a\ ^3\Sigma_g^+$ state. Agreement is best for 17.5 eV and 30 eV. The general shape is present at all three energies. That is, the cross-section dips around 60° and 120°. However, for intermediate angles the magnitude of the DCS is higher (especially for 20 eV) than the theoretical calculations. EELS experiments are hard to conduct for excited states of H_2 because the states overlap in the spectra and the individual components have to be deconvoluted. Based on the difficulty of these type of experiments for highly-excited states it is postulated that the calculations are more reliable.

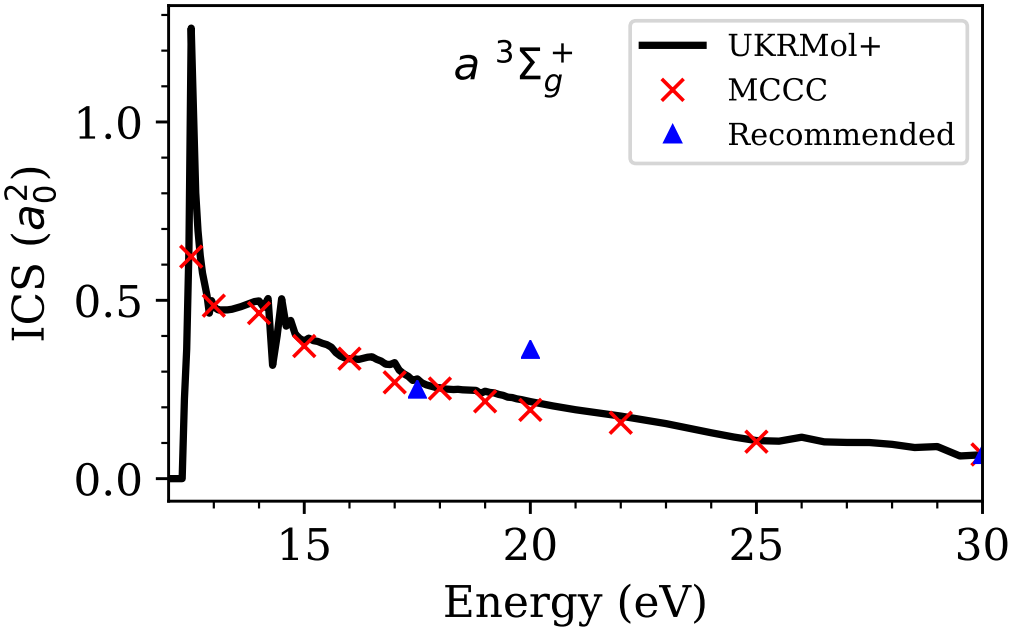

Figure 3.8 | ICS for the $X\ ^1\Sigma_g^+ \rightarrow a\ ^3\Sigma_g^+$ transition. Comparison of the UKRMol+ and MCCC calculations with the recommended data of Yoon et al. (2008).

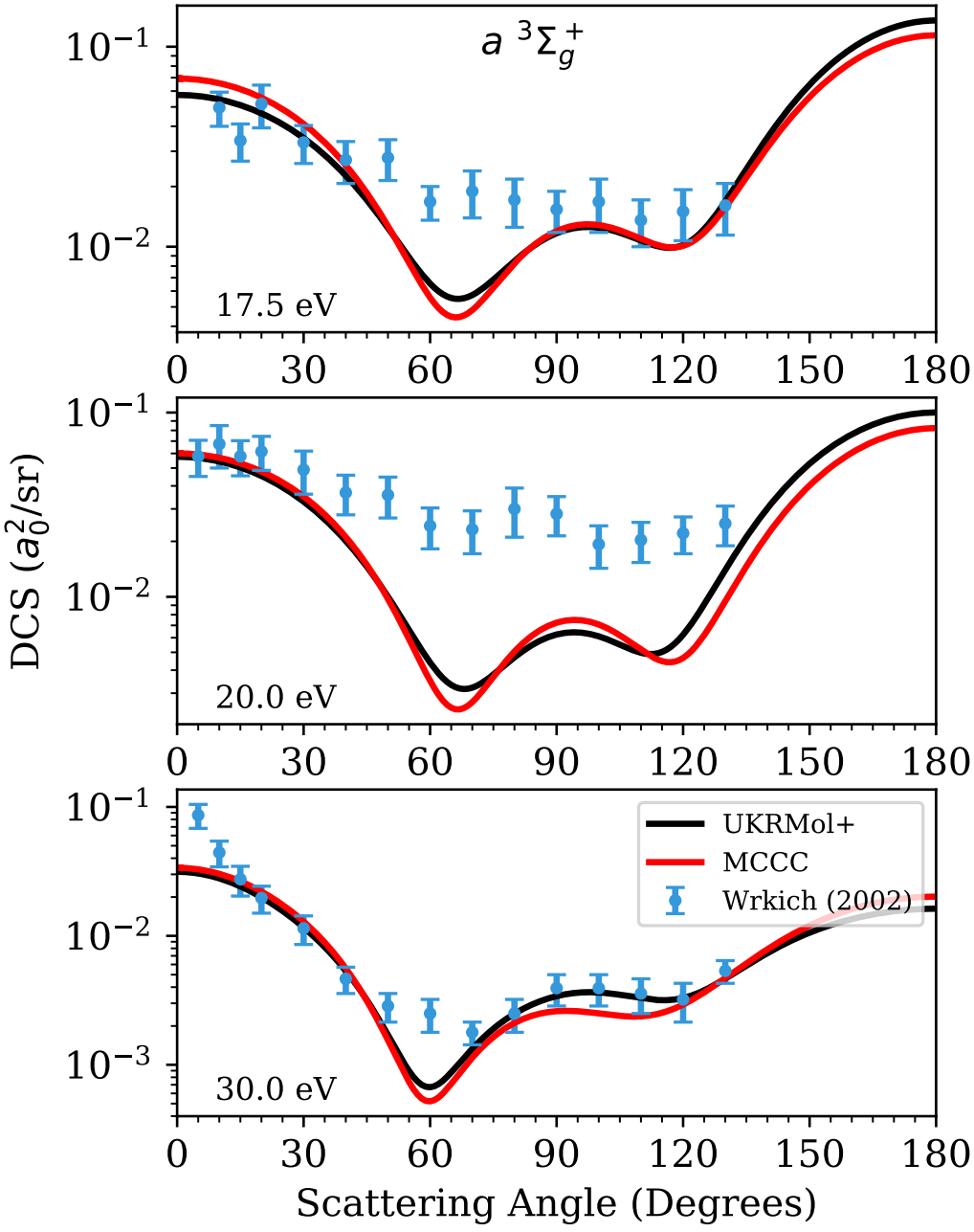

Figure 3.9 | DCS for the $X\ ^1\Sigma_g^+ \rightarrow a\ ^3\Sigma_g^+$ transition. Comparison of the UKRMol+ and MCCC calculations with the measurements of Wrkich et al. (2002).

For the $c\,^3\Pi_u$ state (Fig. 3.11) the situation is similar to the $a\,^3\Sigma_g^+$ state. There is a slight downward slope towards higher scattering angles that is present in both the calculation and the experiment. However, the experimental DCS at 20 eV is approximately an order of magnitude higher.

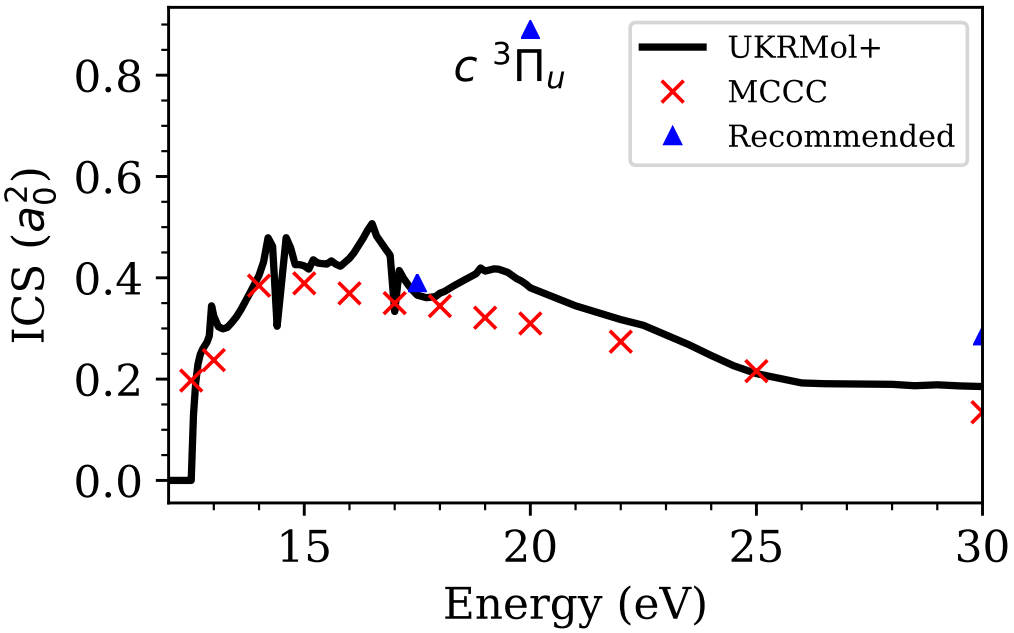

Figure 3.10 | ICS for the $X\,^1\Sigma_g^+ \rightarrow c\,^3\Pi_u$ transition. Comparison of the UKRMol+ and MCCC calculations with the recommended data of Yoon et al. (2008).

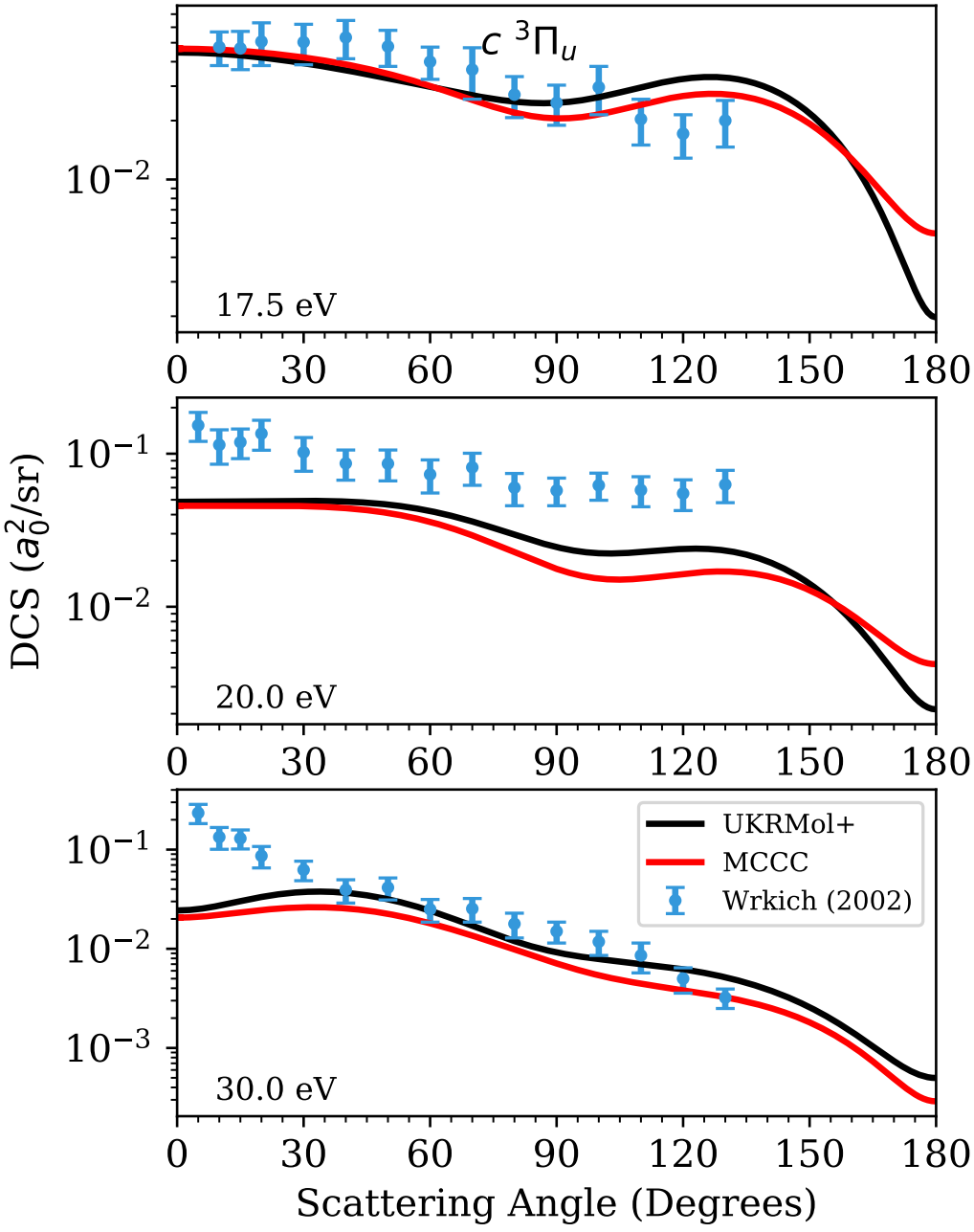

Figure 3.11 | DCS for the $X\ ^1\Sigma_g^+ \rightarrow c\ ^3\Pi_u$ transition. Comparison of the UKRMol+ and MCCC calculations with the measurements of Wrkich et al. (2002).

For the $e\ ^3\Sigma_u^+$ state there is no qualitative agreement between theory and experiment. At all three energies (shown in Fig. 3.13) there are large discrepancies for low angle scattering i.e., below 30°. This is not too surprising though as low and high angle scattering is difficult to measure due to the physical constraints of the experimental setup.

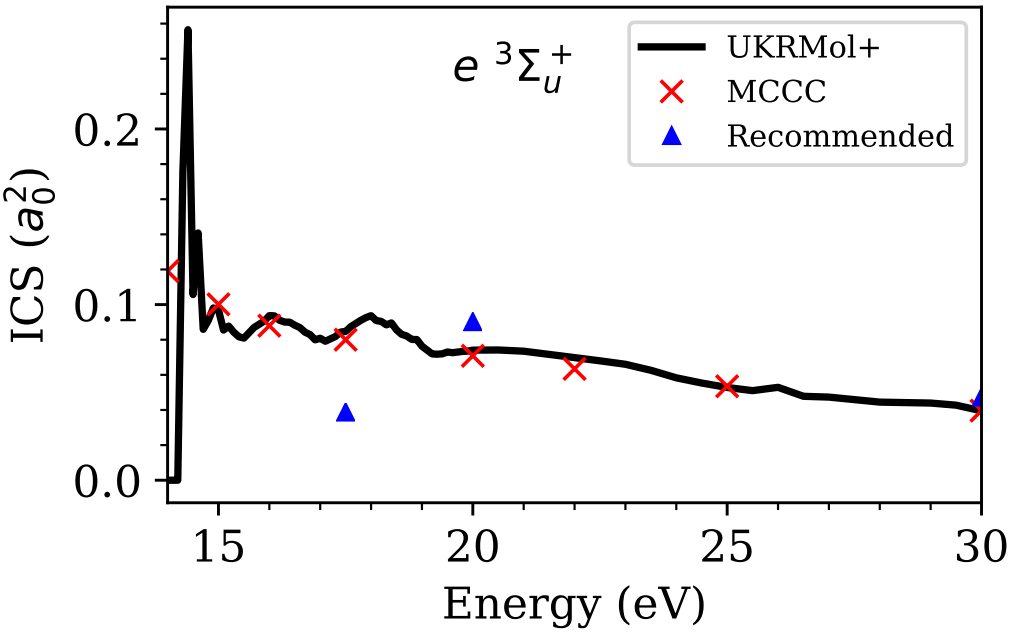

Figure 3.12 | ICS for the $X\ ^1\Sigma_g^+ \rightarrow e\ ^3\Sigma_u^+$ transition. Comparison of the UKRMol+ and MCCC calculations with the recommended data of Yoon et al. (2008).

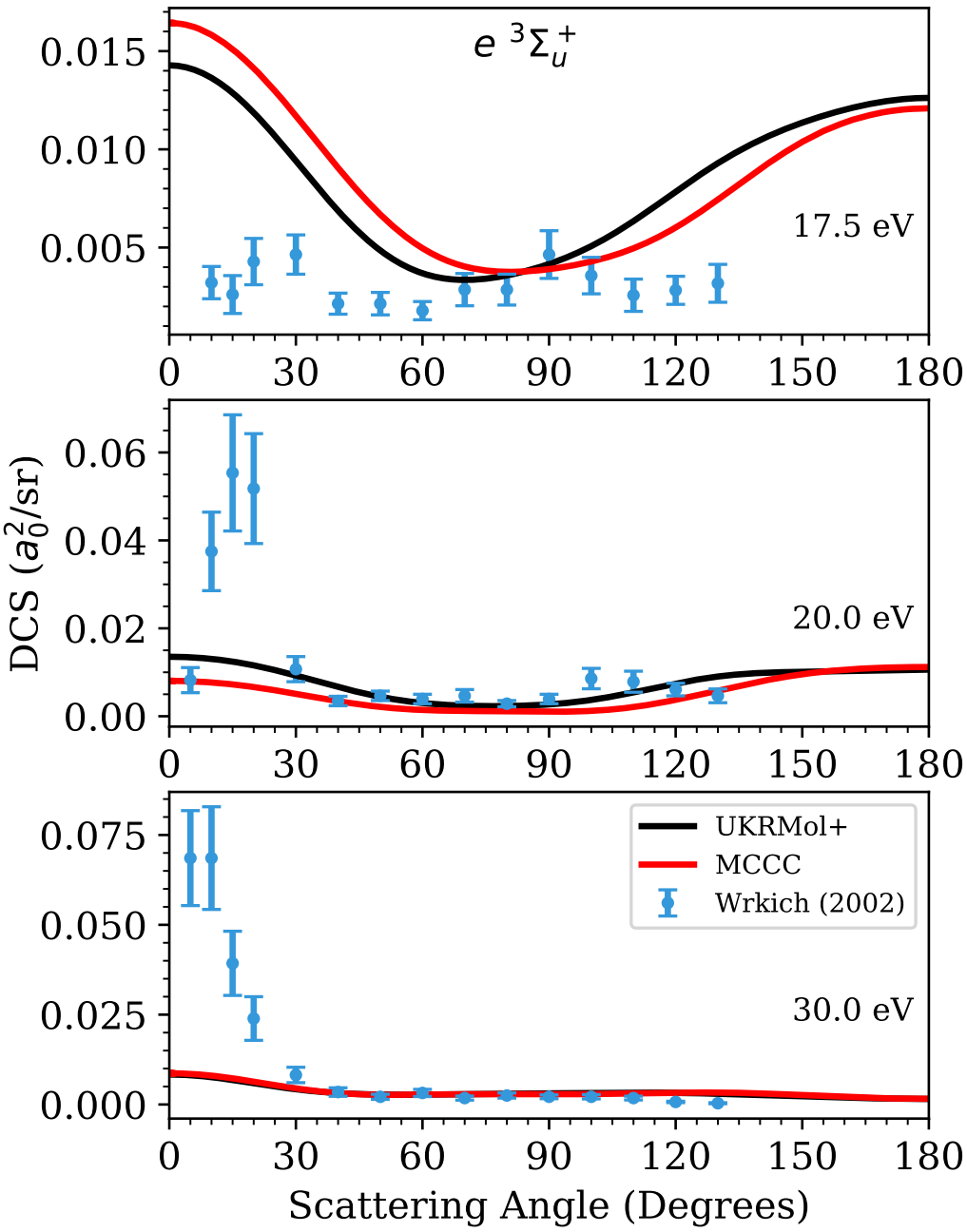

Figure 3.13 | DCS for the $X\ ^1\Sigma_g^+ \rightarrow e\ ^3\Sigma_u^+$ transition. Comparison of the UKRMol+ and MCCC calculations with the measurements of Wrkich et al. (2002).

The ICSs for states $h\ ^3\Sigma_g^+$ and $d\ ^3\Pi_u$ (Figs. 3.14 and 3.15) show agreement between the two theories. However, the R-matrix calculation exhibits pronounced features around 16 eV and 19 eV. In the standard R-matrix approach used in this work, ionisation effects are not included. States above the ionisation threshold are included but pseudostates are not explicitly included. To model ionisation, pseudostates are required as implemented in the R-matrix with pseudostates (RMPS) method (Gorfinkiel and Tennyson, 2005). As a result, the cross-section is overestimated above ionisation threshold. This behaviour was demonstrated previously in MCCC calculations when only the bound states were used (Zammit et al., 2017b). In addition, weak transitions can also suffer from small oscillations, but the impact is reduced as the size of the close-coupling expansion increases. Therefore, the enhanced R-matrix cross-section is likely due to missing ionisation channels.

The DCSs for state $h\ ^3\Sigma_g^+$ (Fig. 3.16) show broad agreement with the MCCC data. There are no recommended data for either the $h\ ^3\Sigma_g^+$ or $d\ ^3\Pi_u$ states. For the $d\ ^3\Pi_u$ state (Fig. 3.17) there are more significant differences between the two theories. As the target excitation increases, typically less agreement between the two theories is expected. Higher excited states tend to be less accurately described by the electronic structure calculations used in this work.

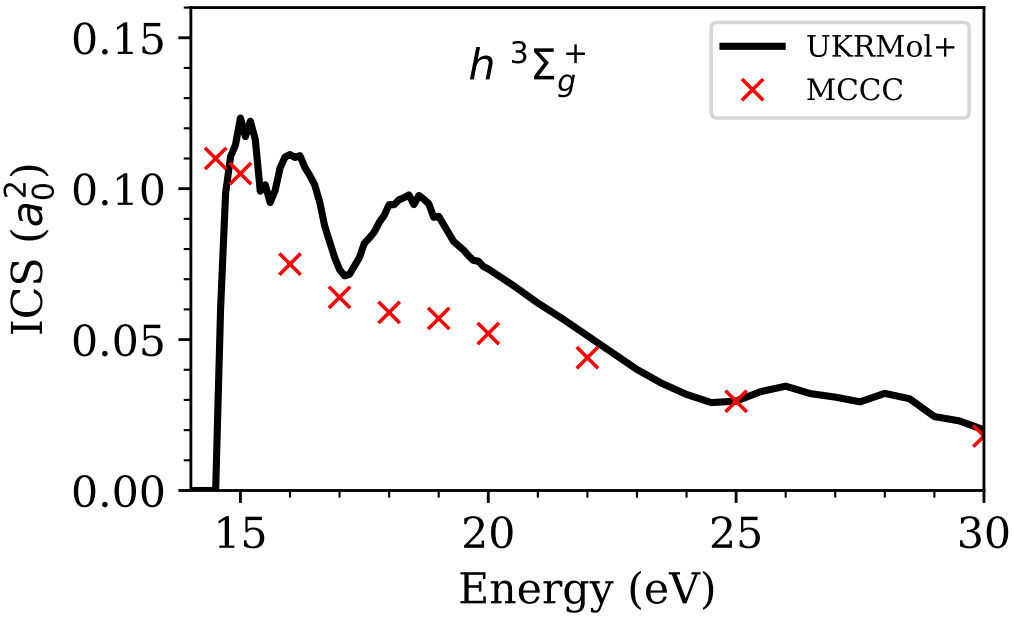

Figure 3.14 | ICS for the $X\ ^1\Sigma_g^+ \rightarrow h\ ^3\Sigma_g^+$ transition. Comparison of the UKRMol+ and MCCC calculations.

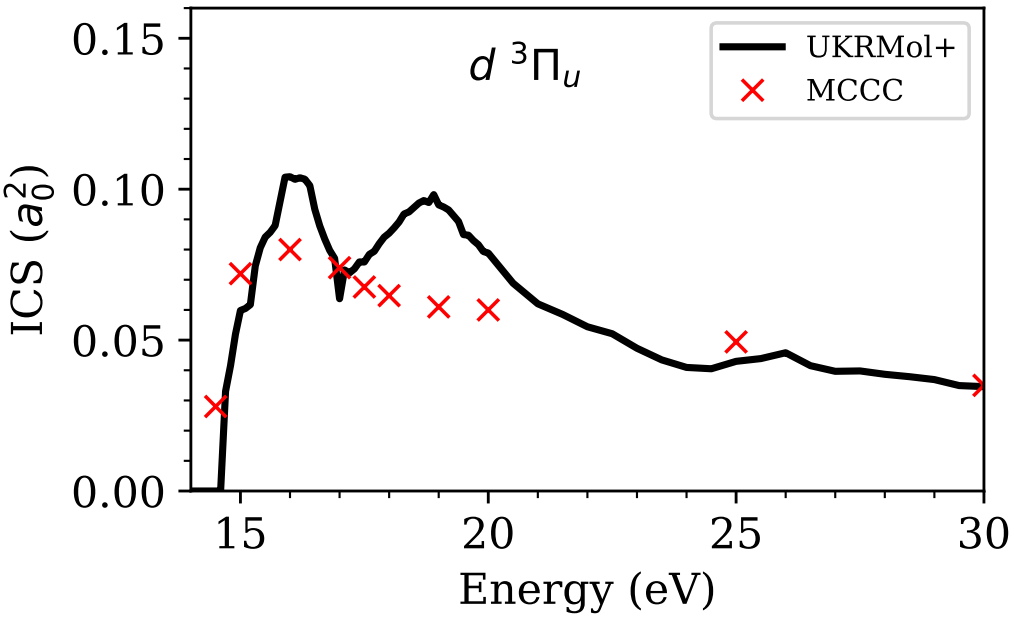

Figure 3.15 | ICS for the $X\ ^1\Sigma_g^+ \rightarrow d\ ^3\Pi_u$ transition. Comparison of the UKRMol+ and MCCC calculations.

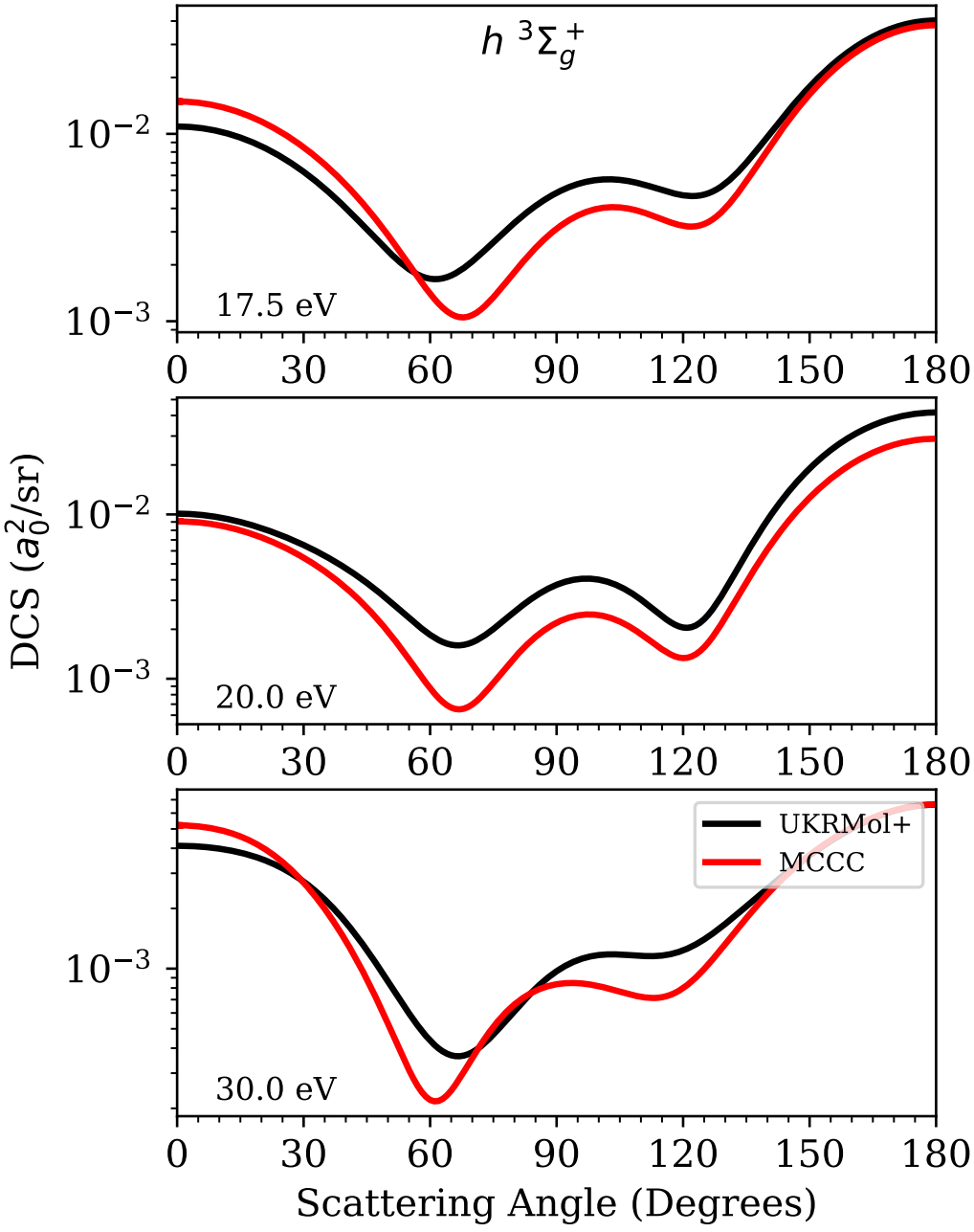

Figure 3.16 | DCS for the $X\ ^1\Sigma_g^+ \rightarrow h\ ^3\Sigma_g^+$ transition. Comparison of the UKRMol+ and MCCC calculations.

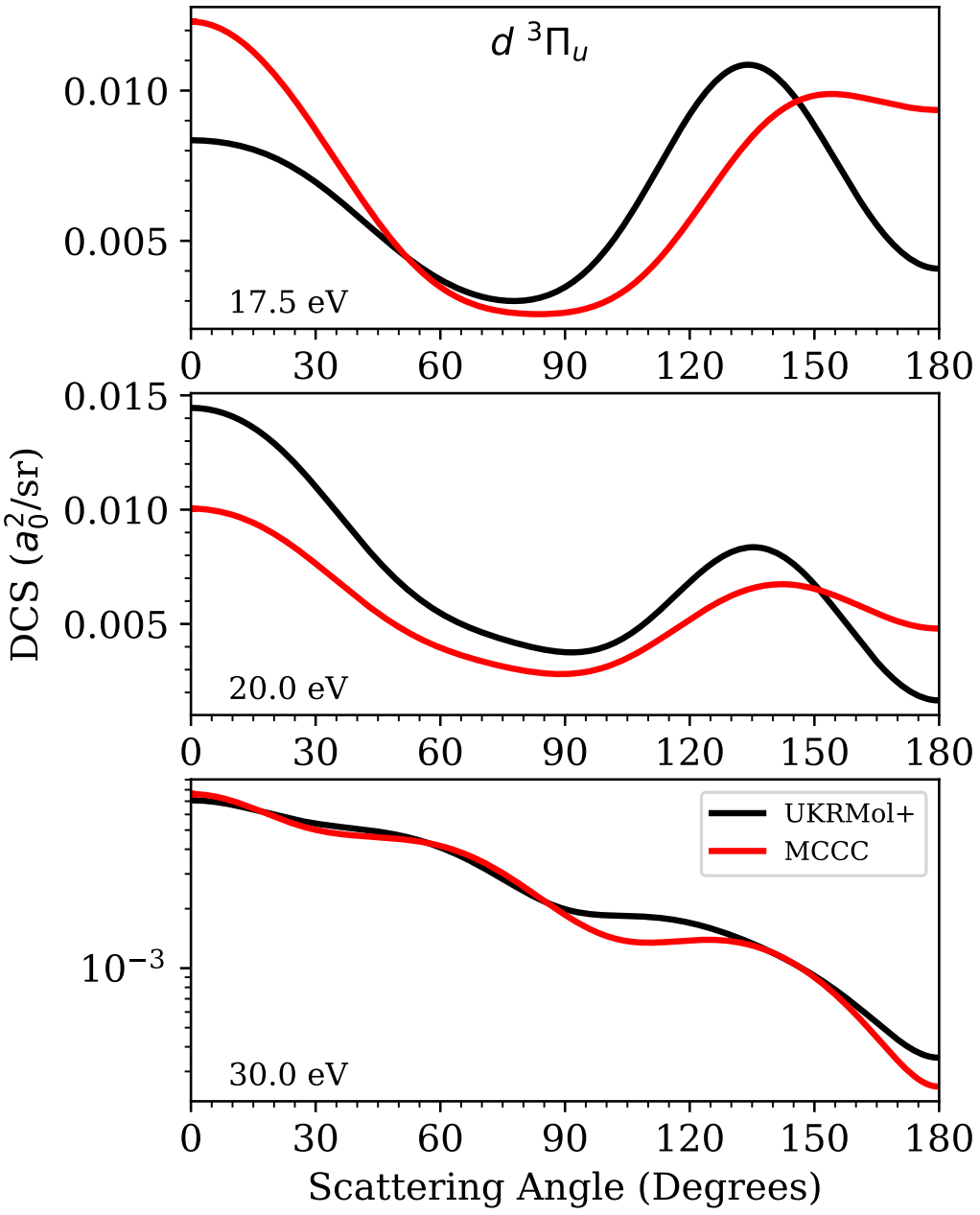

Figure 3.17 | DCS for the $X\ ^1\Sigma_g^+ \rightarrow d\ ^3\Pi_u$ transition. Comparison of the UKRMol+ and MCCC calculations.

3.3.1.3 Singlet States

Next the singlet target states are considered. ICSs for three dipole-allowed states, $B\ ^1\Sigma_u^+$, $C\ ^1\Pi_u$ and $B'\ ^1\Sigma_u^+$, are shown in Figs. 3.18, 3.19 and 3.20 respectively. All three ICSs show excellent agreement between MCCC and R-matrix theory. Furthermore, agreement with the recommended data, which is available for the $B\ ^1\Sigma_u^+$ and $C\ ^1\Pi_u$ states, is extremely good at the energies considered here. Contrary to the previous EELS experimental data, these recommended data were measured from the optical emission of the electron impact electronically excited B and C states (Liu et al., 1998).

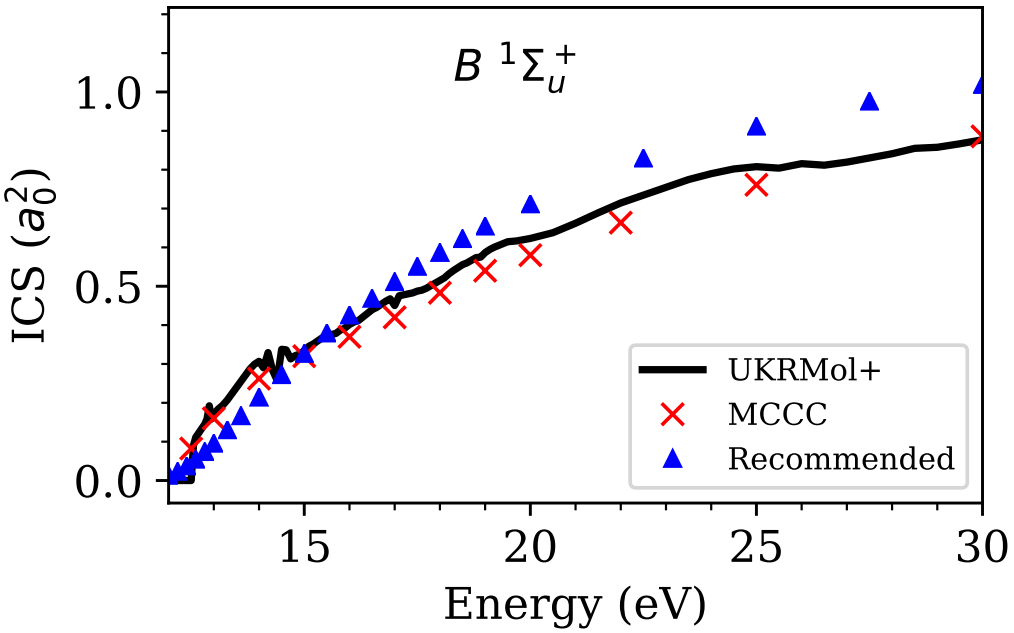

Figure 3.18 | ICS for the $X\ ^1\Sigma_g^+ \rightarrow B\ ^1\Sigma_u^+$ transition. Comparison of the UKRMol+ and MCCC calculations with the recommended data of Yoon et al. (2008).

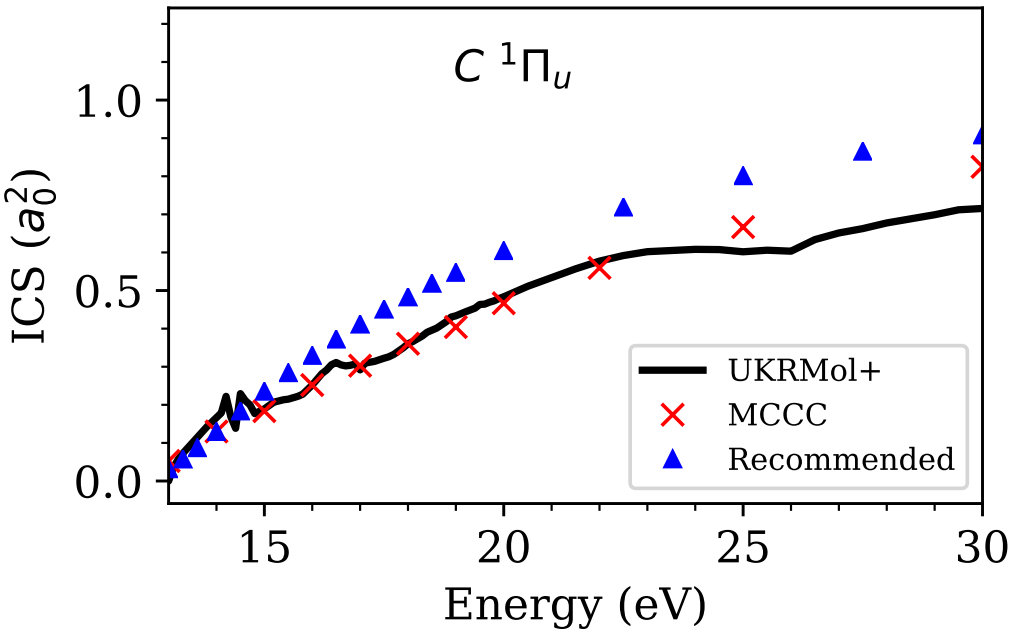

Figure 3.19 | ICS for the $X\ ^1\Sigma_g^+ \rightarrow C\ ^1\Pi_u$ transition. Comparison of the UKRMol+ and MCCC calculations with the recommended data of Yoon et al. (2008).

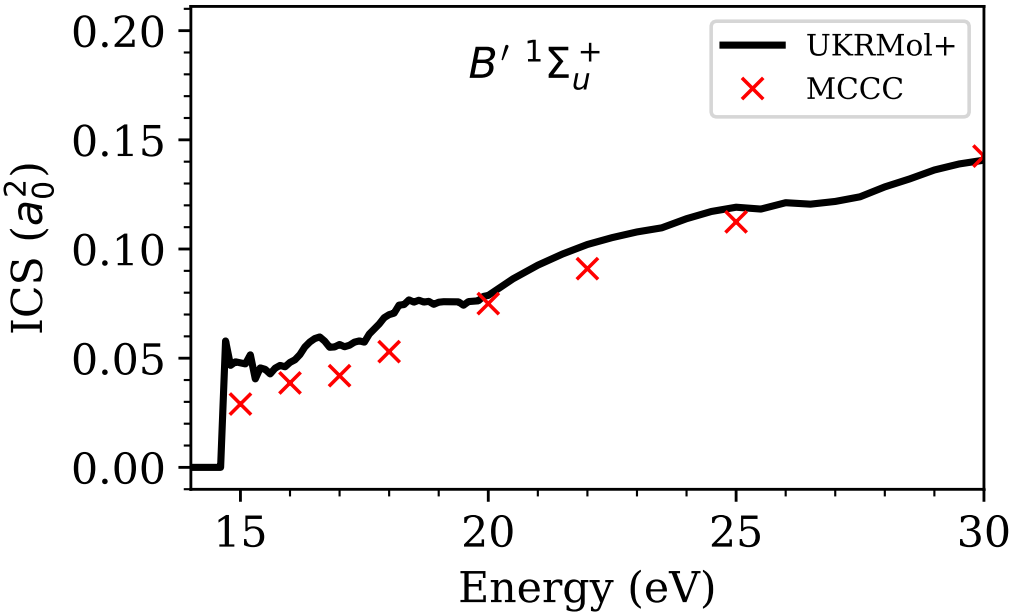

Figure 3.20 | ICS for the $X\ ^1\Sigma_g^+ \rightarrow B'\ ^1\Sigma_u^+$ transition. Comparison of the UKRMol+ and MCCC calculations.

DCSs could not be determined in the emission experiments of Liu et al. (1998). However, Wrkich et al. (2002) produced a set of EELS DCS which have been plotted in Figs. 3.21 and 3.22. For the $B\ ^1\Sigma_u^+$ state the agreement with experiment is good. At 30 eV however the R-matrix calculation displays oscillations that are not present in the MCCC Calculation. This is due to a lack of convergence in the partial-wave expansion. Typically a Born correction would be applied to dipole allowed transitions. However, in the present work this has not been possible. The Born top-up requires a sufficiently converged cross-section, up to some intermediate number of partial waves, $\bar{L}_{\text{max}}$. For MCCC this is found to be $\bar{L}_{\text{max}} = 25$, or more, depending on the scattering energy (Zammit et al., 2017b). A similar approach was attempted for the R-matrix calculation. Although this was not tractable given currently available software and computational power (see sec. 3.3.3).

Similarly, the oscillations observed for the $B\ ^1\Sigma_u^+$ state at higher energies are also observed in states $C\ ^1\Pi_u$ and $B'\ ^1\Sigma_u^+$ (Figs. 3.22 and 3.23). Furthermore, in all of the singlet state DCSs, Figs. 3.21, 3.22, 3.23 and 3.25, the R-matrix calculation has a lower forward peak. This is attributed, as in the elastic scattering case, to a lack of convergence in the number of partial waves used. Regardless, forward and backward scattering only make a small contribution to the total ICS. Therefore the differences caused by the oscillatory behaviour and lower forward peak are lost upon integration. This highlights the importance of using DCSs as a stringent test of theories. Two theories may produce the same ICS but have different angular profiles.

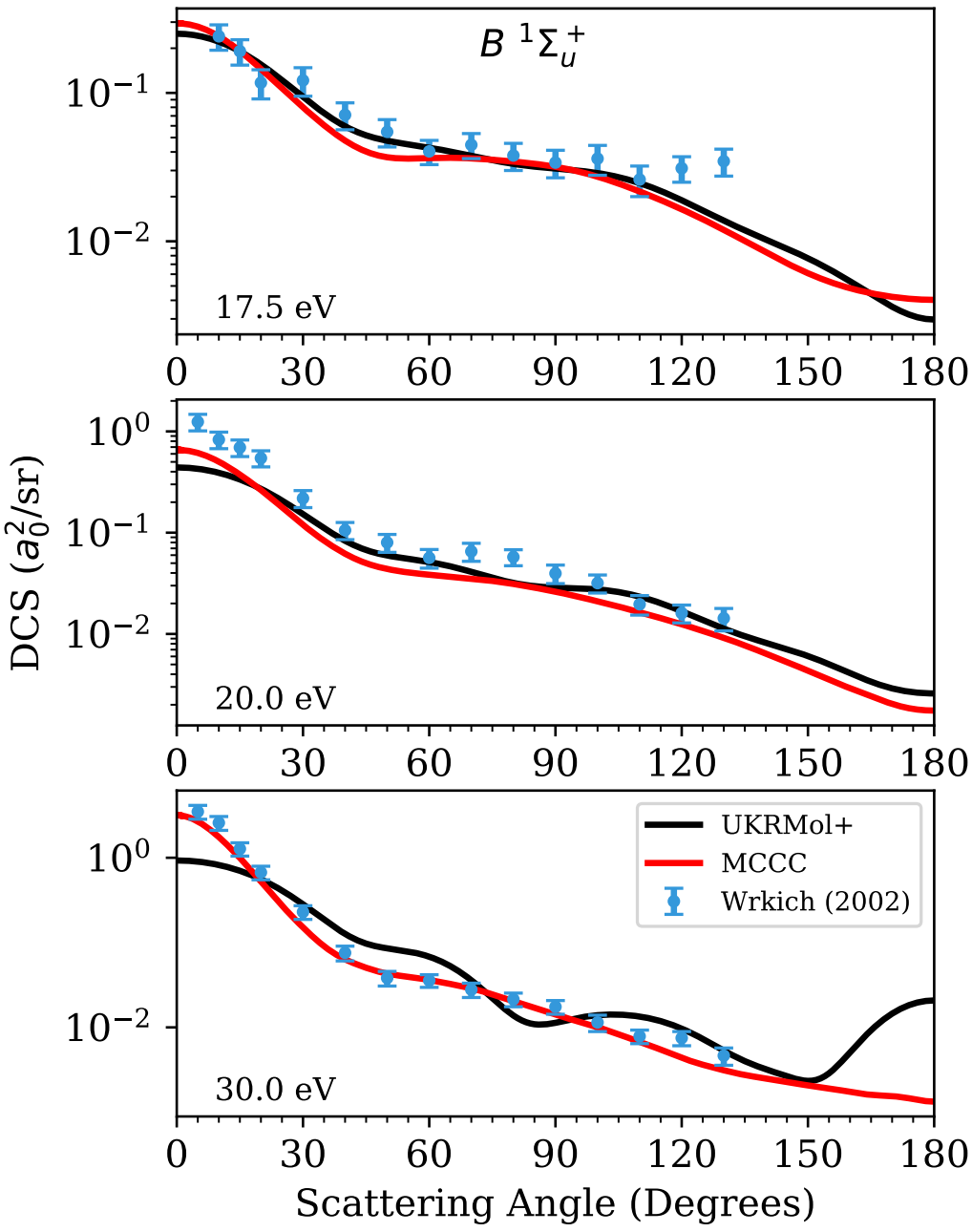

Figure 3.21 | DCS for the $X\ ^1\Sigma_g^+ \rightarrow B\ ^1\Sigma_u^+$ transition. Comparison of the UKRMol+ and MCCC calculations with the measurements of Wrkich et al. (2002).

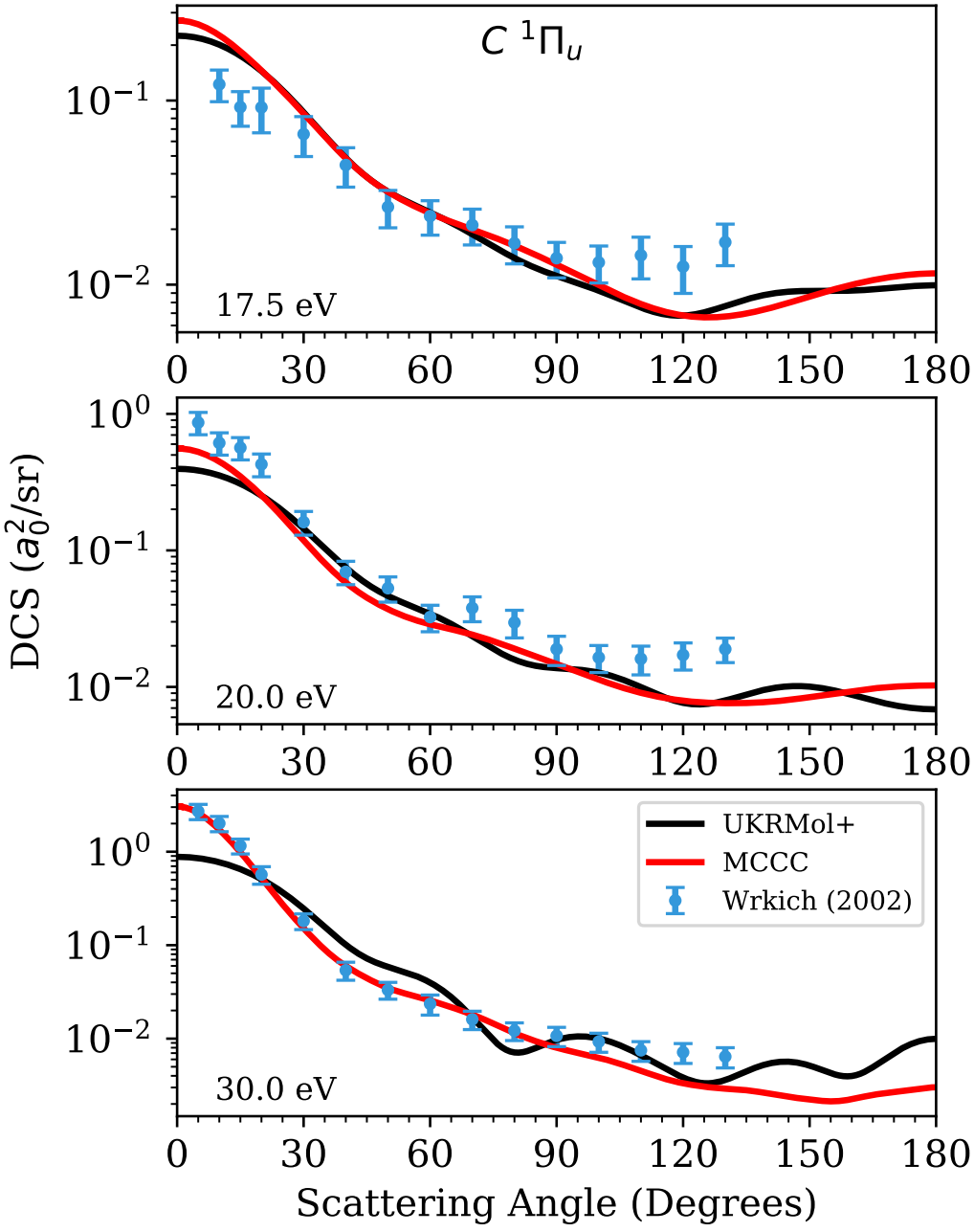

Figure 3.22 | DCS for the $X\ ^1\Sigma_g^+ \rightarrow C\ ^1\Pi_u$ transition. Comparison of the UKRMol+ and MCCC calculations with the measurements of Wrkich et al. (2002).

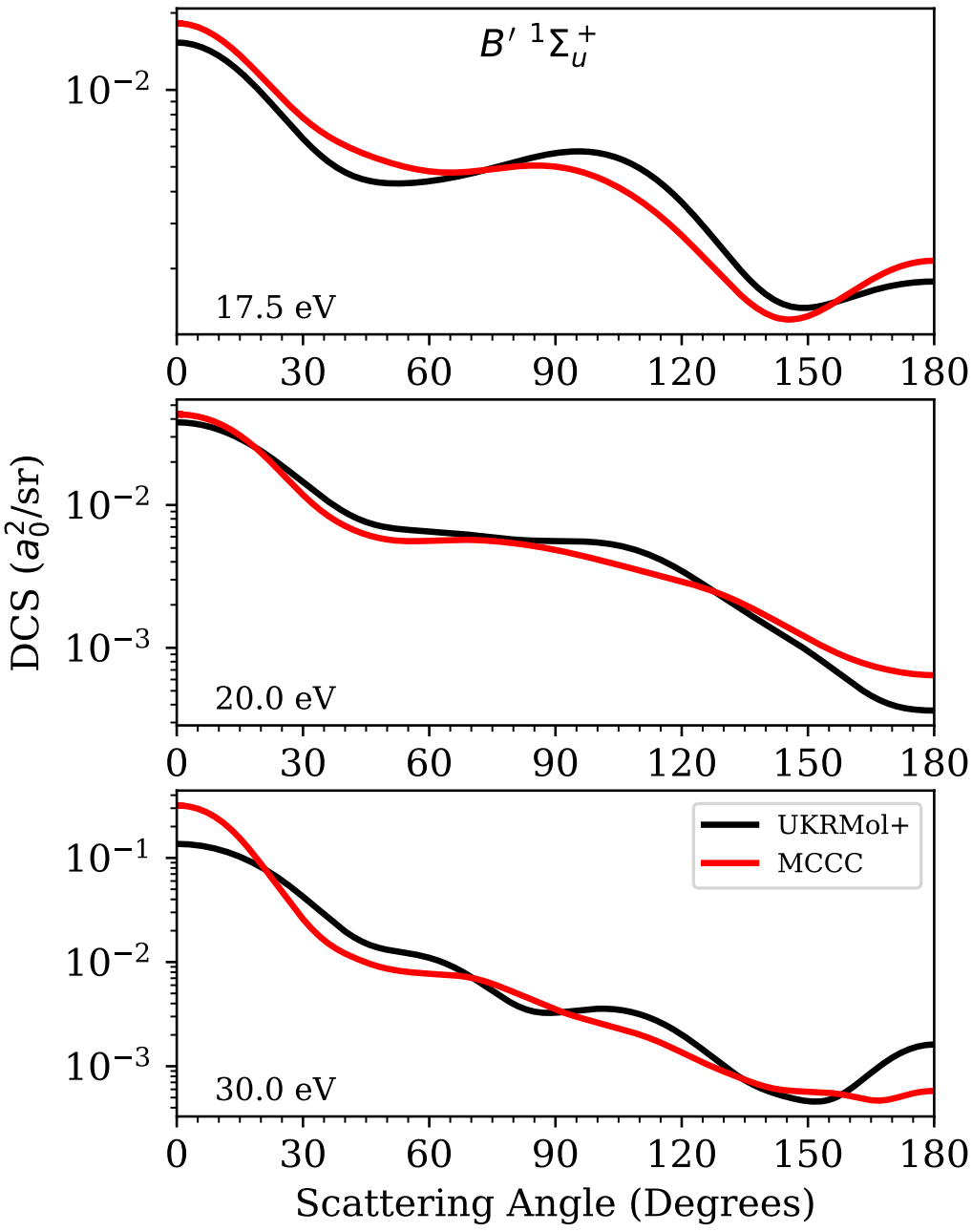

Figure 3.23 | DCS for the $X\ ^1\Sigma_g^+ \rightarrow B'\ ^1\Sigma_u^+$ transition. Comparison of the UKRMol+ and MCCC calculations.

In contrast to the dipole-allowed singlet states, the forbidden $EF\ ^1\Sigma_g^+$ state DCS (Fig. 3.25) is not as sensitive to higher partial-waves. Agreement between the two theories is good. The agreement between theory and experiment is acceptable, except for the scattering angles from 60° to 100° at 20 eV where the experiment gives a larger cross-section, which could be due to the analysis of the measured EELS.

Comparing the ICS (Fig. 3.24) between the two theories, the R-matrix calculation is consistently above the MCCC data. Again, this is due to the absence of ionisation channels in the R-matrix close-coupling expansion that leads to an overestimated cross-section.

The recommended data are based on an emission experiment carried out by Liu et al. (2003). Whilst the $EF\ ^1\Sigma_g^+$ state is dipole-forbidden, the cross-section can be inferred using a combination of theoretical and experimental considerations. There is a difference in threshold for experiment, which occurs near 15 eV as opposed to 13 eV for the FN MCCC and R-matrix calculations. However the magnitude and qualitative shape agree with theory.

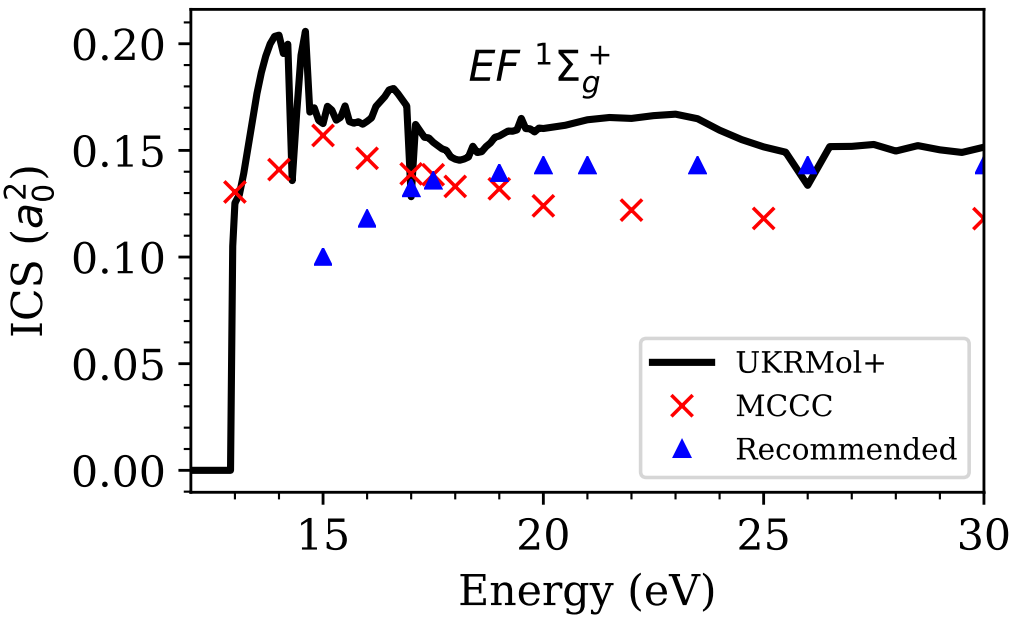

Figure 3.24 | ICS for the $X\ ^1\Sigma_g^+ \rightarrow EF\ ^1\Sigma_g^+$ transition. Comparison of the UKRMol+ and MCCC calculations with the recommended data of Yoon et al. (2008).

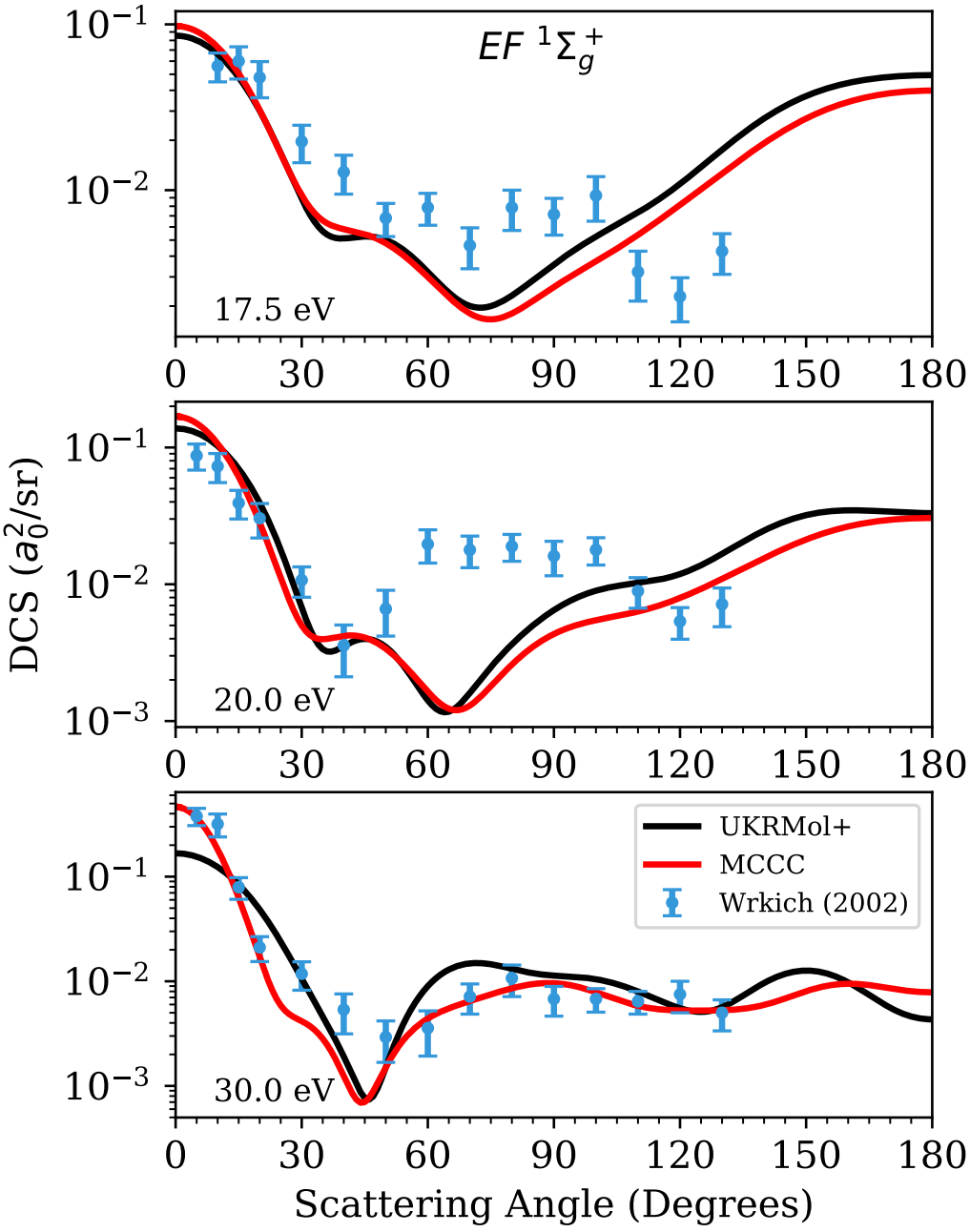

Figure 3.25 | DCS for the $X\ ^1\Sigma_g^+ \rightarrow EF\ ^1\Sigma_g^+$ transition. Comparison of the UKRMol+ and MCCC calculations with the measurements of Wrkich et al. (2002).

3.3.2 Adiabatic-Nuclei Cross-Sections

In reality, the molecular geometry is not fixed and experiment effectively samples a range of initial and final states. This will have an impact on both the integrated and differential cross-sections. This behaviour is most notable near threshold (Stibbe and Tennyson, 1998). At higher scattering energies, away from the threshold, the two approximations converge as nuclear motion effects become less significant. The AN approximation was introduced earlier in section 2.2 to address this issue and it has been recently demonstrated by Scarlett et al. (2017) on molecular hydrogen. In this work the ground vibrational wavefunction is used to vibrationally average multiple FN calculations, carried out at a range of different nuclear geometries (see equation 2.32). Although, in general, this method can also be used to produce vibrationally resolved cross-sections as shown in equation 2.30.

In Fig. 3.26 both FN (dot-dashed line) and AN calculations (solid line) are shown side-by-side for electronic excitation to the first excited state ($X\ ^1\Sigma_g^+ \rightarrow b\ ^3\Sigma_u^+$). For both the MCCC (red) and UKRMol+ (black) calculations there are two main differences. The first is that resonant structures are washed-out and the second is that the sharp turn-on near the vertical excitation threshold (10 eV) is smoothed into a ramp. This is due to the vibrational averaging over different molecular geometries. The threshold for the $X\ ^1\Sigma_g^+ \rightarrow b\ ^3\Sigma_u^+$ transition is essentially the vertical excitation energy. For some geometries this will be lower than 10 eV and for others it will be greater. The average is weighted by the square of the ground vibrational wavefunction, which means the largest contributions occur at the maximum of the wavefunction i.e., about R_0. This is why the FN calculation at $R = R_0$ and the AN calculation are broadly similar. Adiabatic effects have consequences for near-threshold electron impact dissociation of H_2 (Stibbe and Tennyson, 1998).

The AN approximation requires FN calculations to be performed across a grid of different internuclear bond separations. For this work, a grid size of $\Delta R = 0.05$ a.u. was used for $0.95 < R < 1.95$ a.u., with a finer grid of $\Delta R = 0.01$ a.u. used in the region closer to the mean vibrational bond length, $1.35 < R < 1.55$ a.u. Due to the large number of FN calculations required it was not possible to use

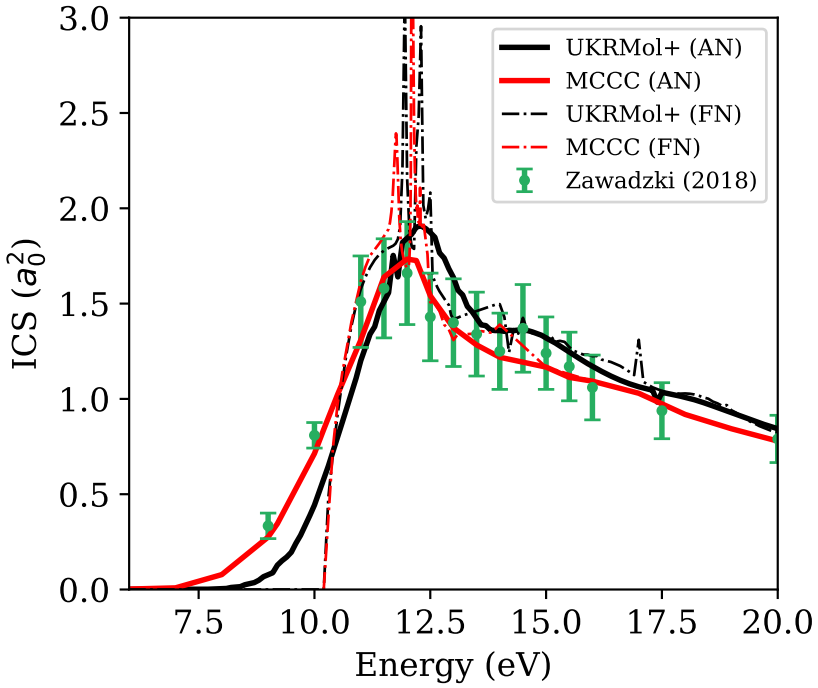

Figure 3.26 | Integrated cross-section for the $X\ ^1\Sigma_g^+ \rightarrow b\ ^3\Sigma_u^+$ transition using the AN approximation. (black) UKRMol+, (red) MCCC, (green dots) experiment from Zawadzki et al. (2018).

the full model described previously (sec. 3.2.1). Therefore a smaller model was used which featured a singly augmented aug-cc-pVTZ basis set and an R-matrix radius $a = 25$ a.u. Due to the smaller radius, the continuum representation can be simplified to 22 BTOs per angular momentum symmetry with $L_{\max} = 4$ without sacrificing completeness. This model works well for the first excited state but due to the simplified target description it cannot represent higher-excited states. As before, all the target states below 30 eV are included which gives a 59-state model.

3.3.3 Including Higher Partial Waves

To include higher partial waves, specifically for dipole-allowed transitions, a top-up procedure is required. A typical approach is to use a Born correction as suggested by Norcross and Padial (1982). Its form applied to DCS is

$$\frac{d\sigma}{d\Omega} = \left(\frac{d\sigma}{d\Omega}\right)_{\text{Born}} + \sum_{\lambda=0}^{\lambda_{\max}} (A_\lambda - A_\lambda^{\text{Born}}) P_\lambda(\cos\theta), \tag{3.1}$$

where the first term on the right hand side is the DCS calculated for inelastic dipolar scattering in the first Born approximation and the second term includes the contribution of the lower partial waves A_λ calculated with close-coupling and subtraction of the corresponding Born partial waves A_λ^{Born}. Only orientational averaging of the molecule is taken into account. This approach was used in previous R-matrix calculations for inelastic collisions, but only for ICSs (Baluja et al., 2000; Kaur et al., 2008; Mašín et al., 2012), which tend to converge quicker than DCSs. Recently, Zawadzki et al. (2020) employed the Born correction described above for the electronically inelastic DCS of CO. This method, however, requires a sufficiently high partial wave cut-off, $L_{\max}$. At lower partial waves the analytic Born method is less accurate and can overestimate the cross-section, leading to unphysical negative cross-sections.

Born corrections have been successfully applied to DCSs for elastic collisions, see e.g., Zhang et al. (2009) and Mašín et al. (2012). However, these cross-sections are usually an order of magnitude larger than those for dipole-allowed inelastic transitions. Hence, they are less susceptible to the oscillatory behaviour seen in inelastic DCSs.

Figure 3.27 shows the DCS for the dipole-allowed $B\ ^1\Sigma_u^+$ state. In solid black the original R-matrix calculation without the Born correction is shown. If the Born correction is applied to the DCS the dotted line is obtained. At 17.5 eV, the Born corrected DCS displays unphysical behaviour around 150° where it becomes negative. The situation worsens for higher energies. This is due to an incomplete convergence of the partial-wave Born contribution $\sum_\lambda A_\lambda^{Born} P_\lambda(\cos\theta)$.

To resolve this issue, the MCCC approach (Zammit et al., 2017b) has been to run a smaller-sized calculation but with a higher cut-off e.g., $\bar{L}_{\max} = 25$. The results of this calculation are then used to augment the T-matrices of the more expensive calculation. This allows the DCS contributions from higher partial waves to be calculated with the more accurate MCCC theory before including the additional contributions from the Born procedure.

A similar approach has been adopted in the R-matrix calculations, however

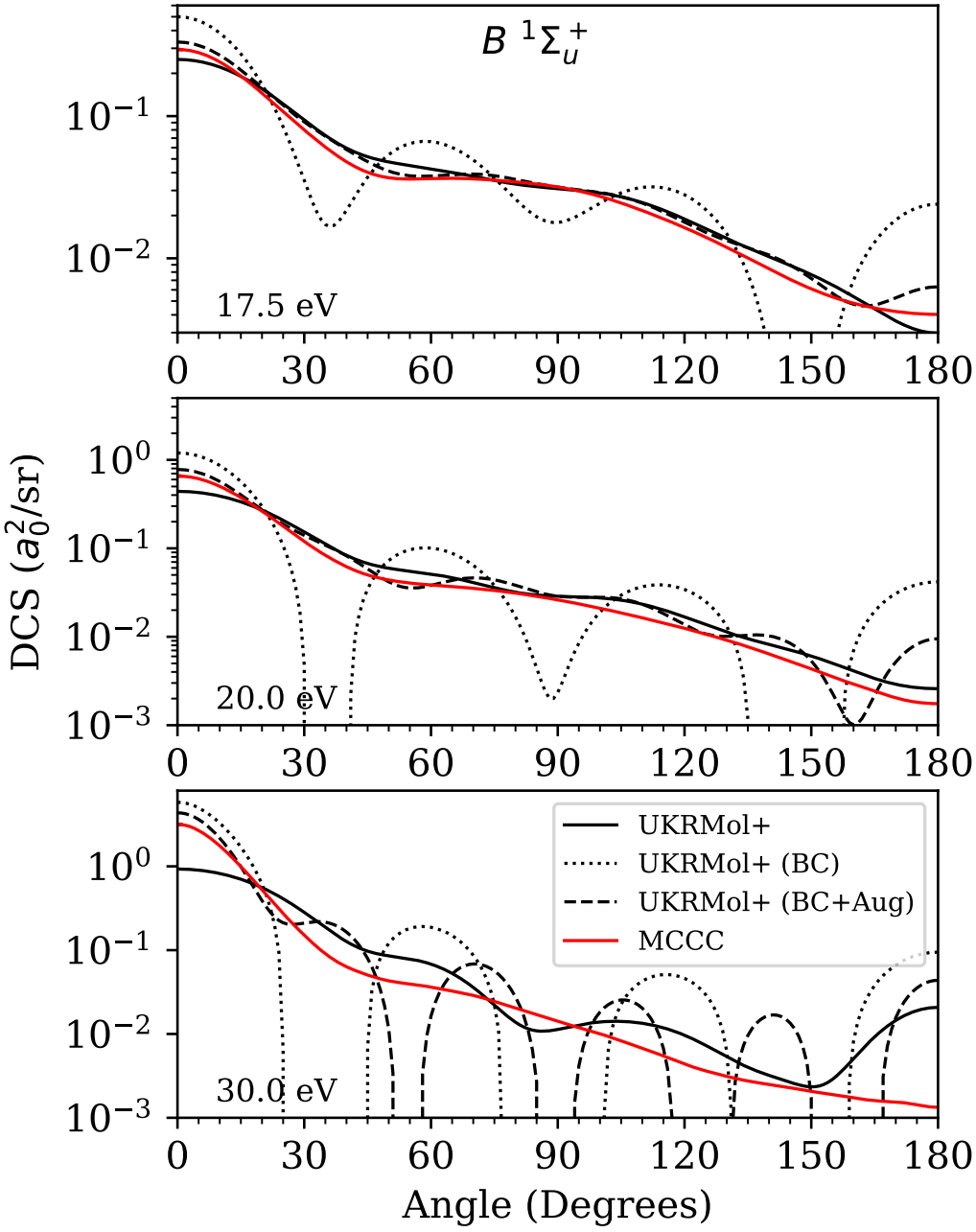

Figure 3.27 | DCS for the $B\ ^1\Sigma_u^+$ state calculated using the R-matrix method, with $L_{\max} = 6$ (black) and the MCCC method (red). The Born top-up was applied to the original calculation before (dotted) and after (dashed) the T-matrix elements were augmented with a cheaper $L_{\max} = 10$ calculation.

$\bar{L}_{\text{max}} = 25$ is currently not computationally feasible with the UKRMol+ codes. Calculations using a smaller model, but with $\bar{L}_{\text{max}} = 10$, have been computed and these were used to augment the T-matrices of the accurate R-matrix calculation with $L_{\text{max}} = 6$. When augmenting the T-matrix elements, care must be taken to phase-match the two calculations. This can be achieved by comparing the transition dipole moments of the target states involved in each transition.

The result of augmenting the T-matrices and applying the Born correction is shown as the dashed line in Fig. 3.27. For the lowest scattering energy shown, 17.5 eV, the oscillatory behaviour is greatly reduced and the Born correction improves the quality of agreement between the MCCC and R-matrix calculations. At 20 eV Born-corrected DCS is improved but it still shows oscillatory behaviour that is characteristic of a lack of convergence. At 30 eV, even with the augmented T-matrix elements the DCS remains oscillatory when the Born correction is applied.

In theory, an approach similar to the MCCC method can be developed for the R-matrix calculations but there are two factors that currently inhibit further improvement. The first is that the target states from cheaper calculations need to be shifted to the more accurate values from the expensive calculation. In this work the energies were shifted in the outer region. This is not ideal and instead the energy shift should be implemented in the $N + 1$ scattering calculation, similar to the approach used successfully by Stibbe and Tennyson (1997). Secondly, the outer region quickly dominates the computational resources required, both physical RAM and CPU-time, as a large number of channels are generated for higher partial waves. As a result a sophisticated approach would need to be implemented in the outer region to reduce the number of states included in the calculation.

As an alternative approach, a top-up to the DCS using a more basic method was also attempted (Fig. 3.28). Two cheaper calculations with small basis sets, as described in sec. 3.3.2 but using $L_{\text{max}} = 6$ and $L_{\text{max}} = 10$ were carried out. Then, the difference between the two DCSs was computed and used to top-up the expensive calculation. This approach does help to capture the forward peak scattering but it was too susceptible to unphysical negative cross-sections when the differences

between the cheap calculations became negative. This method behaved particularly poorly in regions where the cross-section is small.

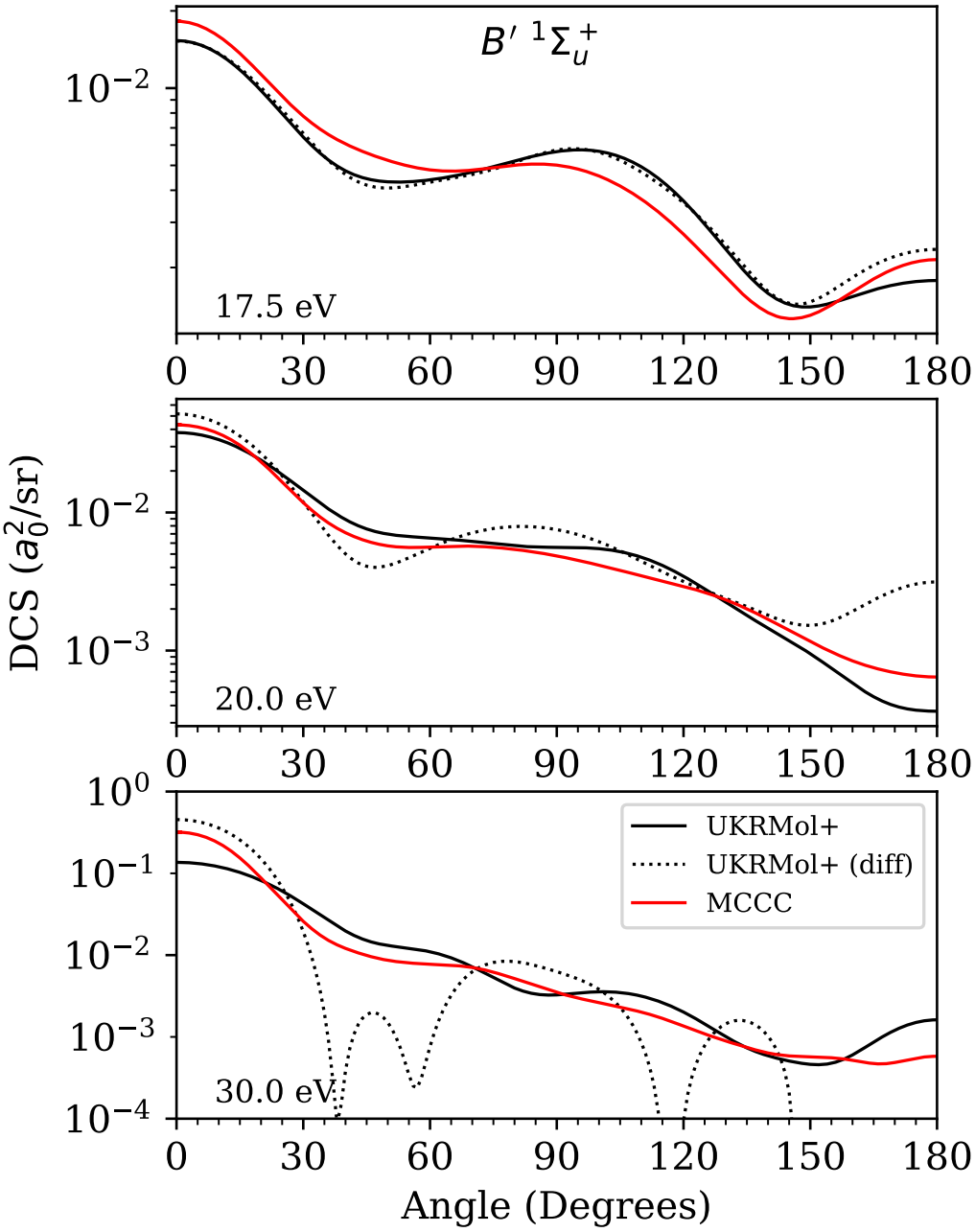

Figure 3.28 | DCS for the $B'\ ^1\Sigma_u^+$ state calculated using the R-matrix method, with $L_{\max} = 6$ (black) and the MCCC method (red). The difference between two smaller calculations with $L_{\max} = 6$ and $L_{\max} = 10$ was computed and added to the ICS of the full calculation (dotted).

In summary, the MCCC approach to the Born top-up appears to be the most sensible way forward, however there is still work to be done before it can be imple-

mented in R-matrix calculations.

3.4 Conclusion

In this work good agreement with recent experimental data has been demonstrated, validated by two independent theories. There is less agreement with recommended data, predominantly for the triplet states but this is believed to be due to the difficulties associated with the underlying experiments. Furthermore, any significant differences between the two theories and experiments are well understood.

This is the first time the MCCC and R-matrix theories have been verified for a molecular target. This work presents one of the largest molecular R-matrix calculations to date. Many novel features have been exploited for the first time: a triply-augmented target basis set, a box size of 100 a.u. and the first B-spline only continuum for a molecular target. This shows that both MCCC and R-matrix method can be used to perform large-scale, high-accuracy close-coupling calculations.

Both fixed-nuclei and adiabatic-nuclei calculations have been compared. For FN calculations, dipole-forbidden states generally show better agreement in the DCSs. Whereas, for dipole-allowed states the R-matrix calculations show oscillatory behaviour but this could be eliminated by using a higher cut-off in the number of partial-waves. However, this is currently not tractable given currently available hardware and software. All of the ICSs show good agreement between the two theories with the exclusion of weak transitions that are more sensitive to the absence of ionisation channels in the R-matrix calculations, leading to slightly enhanced cross-sections. The AN ICS for the first excited state shows excellent agreement between the two theories and the recent experimental data.

There are several directions for future work. Firstly, it would be interesting to compare the effect of target model used in the MCCC calculations i.e., spherical versus spheroidal. Preliminary results for the $EF\ ^1\Sigma_g^+$ state suggest that the use of a spheroidal model could improve the agreement between both theories.

Secondly, in order to accurately describe ionisation effects in the R-matrix method the RMPS method would need to be employed. Whilst the RMPS method

is implemented in UKRMol+, the calculations for this system are currently too expensive. Following this, further developments to the UKRMol+ integrals code are required to reduce the computational cost of calculations, both in terms of wall-clock time and RAM. The calculations presented in this work for molecular hydrogen, a two-electron system, required 1.5 Tb of RAM and 15 hours on a 36-core machine. In order to study larger polyatomics, the UKRMol+ integral code requires substantial optimisation.

Additionally, for the R-matrix calculations presented in this work it has not been possible to carry out systematic, quantitative analysis of the uncertainties. This is a common problem across the field for theoretical calculations (Chung et al., 2016). A tractable approach that is capable of providing uncertainties for the data calculated in this chapter would be the subject of future work.

Finally, a general approach for handling Born top-ups, similar to the ABS method used in MCCC calculations would be desirable for the UKRMol+ calculations in order to reach convergence where larger numbers of partial-waves are required (as discussed in sec. 3.3.3).

Chapter 4

Intermediate Energy Collisions

In this chapter, the R-matrix with Pseudostates (RMPS) method is used to investigate the potential energy curves of nitric oxide, which display a complicated mixture of Rydberg-like and valence-type states. Typically, producing continuous and accurate curves for mixed valence and Rydberg state systems is a challenge for standard quantum chemistry approaches. The RMPS method can also be used to investigate intermediate energy electron collisions with molecules – extending the validity of the traditional R-matrix approach.

4.1 Introduction

Intermediate energy collisions present a unique problem for many theoretical approaches as they bridge the realm between quantum and classical mechanics. High energy scattering is typically harder to converge for *ab initio* approaches and semi-classical, empirical or perturbative methods lack validity in the lower energy limit. The later group includes techniques such as; binary encounter Bethe (BEB) (Kim and Rudd, 1994; Khare et al., 1999); scaled BEB variants (Tanaka et al., 2016); Deutsch-Märk (Deutsch et al., 2000); semiclassical impact parameter (Hazi, 1981; Celiberto and Rescigno, 1993); and spherical complex optical potential (Jain, 1986). At intermediate energies, this situation is even worse as the target can be ionised and/or electronically excited. Therefore, in order to provide an accurate physical description, the theory must be capable of representing both of these effects (Burke, 2011). This means that fully quantum *ab initio* methods must be used when accu-

racy at intermediate energies is required.

For electron-atom collisions, several *ab initio* methods have been developed to tackle this issue. The intermediate energy R-matrix (IERM) method was introduced by Burke et al. (1987), however, this was only applicable to hydrogenic targets. The Convergent Close-Coupling (CCC) method, discussed in the previous chapter (chapter 3), was initially developed for electron collisions with atomic hydrogen (Bray and Stelbovics, 1992) although more recently it has been applied to many electron atoms (Bray et al., 2015) and few electron molecular (MCCC) targets (Zammit et al., 2017b), albeit under the two-active electron approximation. The RMPS method, developed by Bartschat et al. (1996b), was one of the first methods that was capable of producing accurate and converged cross-sections, whilst also retaining broad applicability to a range of different targets. Although initially developed for electron-atom collisions, the RMPS method was later extended to molecular targets by Gorfinkiel and Tennyson (2004, 2005). It has been successfully demonstrated on a range of different molecules e.g., H_2 and H_3^+ (Gorfinkiel and Tennyson, 2005), C_2^- (Halmová and Tennyson, 2008; Halmová et al., 2008) and methane (Brigg et al., 2014). Furthermore it has also been adapted to investigate positron collisions with H_2 (Zhang et al., 2011a) and acetylene (Zhang et al., 2011b).

The key feature of the RMPS method, as the name suggests, is the addition of pseudostates via a set of pseudo-orbitals. The role of these pseudo-orbitals is threefold (Bartschat et al., 1996b). Firstly, they can be used to obtain more accurate target states which, for a variational calculation, is reflected by lower (more negative) target state energies. Secondly, they also generate pseudostates that are essential for converging properties such as the polarisability (Jones and Tennyson, 2010). In fact, Castillejo et al. (1960) found that even for atomic hydrogen the sum over all of the infinite target states still only accounts for 81.4% of the polarisability. The remaining 18.6% is provided by continuum terms. Finally, pseudo-orbitals can be used to represent the highly excited states of the target or the infinite, but discrete, continuum states that exist inside of the R-matrix sphere (Bartschat et al., 1996b). The work in this chapter will take advantage of these features to improve the target

states for the open-shell radical nitric oxide (NO).

NO is the simplest known thermally stable radical (Polák and Fišer, 2004). It is found in the Earth's atmosphere (although in minor abundance) either from anthropogenic sources or natural sources such as lightning (Murray, 2016). NO is a catalyst for ozone destruction (Schappe et al., 2002) and it plays a vital role in the chemistry of the thermosphere and auroral activity Cartwright et al. (2000). Furthermore it is an important biomolecule – serving as a messenger molecule in the human cardiovascular, nervous and immune systems – and it is found in the atmospheres of Venus and Mars, as well as in interstellar medium (Nagano and Yoshimura (2002) and references therein). Accurate electron impact cross-sections are required for collisional-radiative modelling of NO in aurora (Cartwright et al., 2000).

NO is a 15-electron molecule and in its ground state the unpaired electron occupies a degenerate, anti-bonding π^*-orbital. This can be represented as follows,

$$(1\sigma^2 1\sigma^{*2} 2\sigma^2 2\sigma^{*2} 3\sigma^2 1\pi^4 1\pi^*).$$

The unpaired electron manifests as a mixture of low-lying Rydberg-like and valence states, which typically lead to discontinuous potential energy curves. The theoretical treatment of these two different types of state is of great difficulty for standard quantum chemistry approaches as noted by numerous authors that have investigated NO (De Vivie and Peyerimhoff, 1988; Polák and Fišer, 2003; Shi and East, 2006). Typical strategies to mitigate these difficulties include, optimising different sets of MOs and or constructing different target models, to compute a specific subsection of target states. However, contrary to standard electronic structure calculations, scattering calculations require that the target ansatz is constructed from a single set of MOs and single target model. In addition, scattering calculations require both the doublet and quartet target states as they can both couple to triplet scattering states. This rules out the previous approaches and therefore a new method of calculating target states for mixed Rydberg-like and valence type systems is sought. This forms the principle aim of this work which is to generate accurate target states that are

compatible for use in scattering calculations.

Electron impact cross-section data for nitric oxide are few and far between, although recommended data have been compiled by Song et al. (2019), which encompass both experimental and theoretical sources. Of these sources the most complete are the electronically inelastic cross-section data measured by Brunger et al. (2000a) for DCS and Brunger et al. (2000b) for ICS. Recent theoretical endeavours include; da Paixão et al. (1996) who use the Schwinger Multichannel Channel method to calculate elastic DCS and ICS; Fujimoto and Lee (2000) who use a complex optical potential to calculate absorption cross-sections, elastic ICS and DCS; Trevisan et al. (2005) and Laporta et al. (2012) who study electronically elastic scattering from 0 to 2 eV and 0 to 10 eV respectively; and Joshipura et al. (2007) who use the "complex scattering potential-ionisation contribution" method to produce ΣQ_{inel} ICS which is the summed cross-section over all electronically excited states of NO. As far as is known, the only work to calculate electronically-excited state-resolved cross-sections is Laricchiuta et al. (2017) who use the similarity approach to produce ICS for the $X\ ^2\Pi \rightarrow B\ ^2\Pi$ and $X\ ^2\Pi \rightarrow C\ ^2\Pi$ transitions. There has been one former R-matrix investigation, carried out by Tennyson and Noble (1986), which employed a 6-state CC calculation to compute the resonance positions and widths for the three lowest-lying resonances of the NO^- anion but no cross-section data were calculated.

4.2 Method

The methodology used in this chapter builds upon the theory presented in chapter 2. Here the theory will be expanded to include pseudostates in the theoretical framework. The RMPS method was initially developed for electron-atom collisions and the theory is detailed in (Bartschat et al., 1996b) and Burke (2011). RMPS was extended to molecules by Gorfinkiel and Tennyson (2004) with theory detailed therein, in addition to Gorfinkiel and Tennyson (2005) and Tennyson (2010). The following description is adapted from Gorfinkiel and Tennyson (2005).

4.2.1 R-matrix with Pseudostates

The basic idea of the RMPS method is to add pseudostates, Φ_i^{Δ}, into the close-coupling expansion, equation 2.10. These pseudostates are obtained by diagonalising the target Hamiltonian in a basis of configurations that contain both the target MOs, ϕ_i, (Hartree-Fock or CASCI) and pseudo-orbitals, $\bar{\phi}_i$, also known as pseudo continuum orbitals (PCOs). The choice of PCO is not unique but due to computational reasons GTOs have historically been favoured for electron-molecule collisions. The idea is that these PCOs are capable of representing polarised states of the target or states of the positively charged parent ion. As such, they are typically centred about the molecule's centre-of-mass. Gorfinkiel and Tennyson (2004) found that even-tempered GTOs (Schmidt and Ruedenberg, 1979) were ideal for application to polyatomic targets for two reasons. Firstly, as you increase the number of PCOs they approach *completeness*. Secondly, the exponents, α_i, are systematically generated by the control of two parameters, α_0 and β.

$$\alpha_i = \alpha_0 \beta^{(i-1)} \qquad i = 1, \ldots, n_L. \tag{4.1}$$

where, α_0 specifies the effective width of the widest PCO and β determines the spread of PCOs i.e., how closely grouped they are, as shown in Fig. 4.1. n_L is the maximum number of PCOs included in each partial wave L. As noted by Gorfinkiel and Tennyson (2005) the choice of β is dictated by two opposing constraints. Small values of β i.e., close to one, lead to a better distribution of pseudostates but they also increase the likelihood of linear dependence caused by numerical instability. The choice of α_0 will be dependent on the target and/or quantities that are being optimised. However, a basic requirement is that the PCOs – like the target MOs – are contained within the R-matrix sphere which means that their amplitude on the boundary must be negligible. Smaller values of α_0 lead to more diffuse PCOs (see Fig. 4.1).

PCOs are included into the close-coupling expansion via the following target

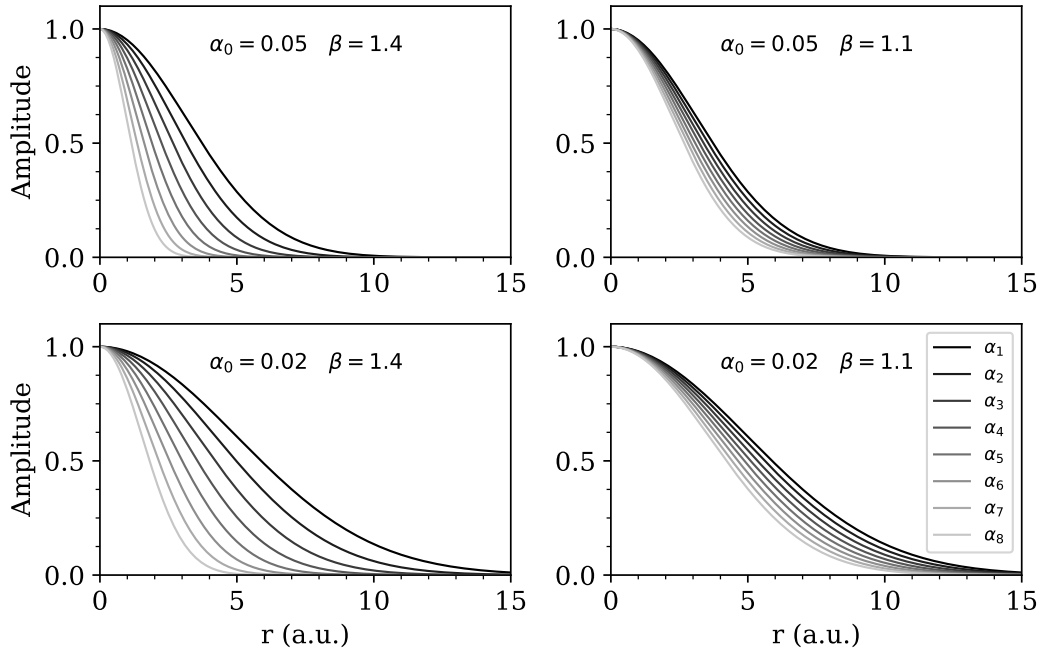

Figure 4.1 | Even-tempered GTOs, $\exp(-\alpha_i r^2)$, for use as a PCO basis set, as a function of the two parameters α_0 and β.

configurations:

$$(core)^{N_c}(CAS)^{N_a}, \qquad \text{(CASCI)}$$

$$(core)^{N_c}(CAS)^{N_a-1}(PCO)^1, \qquad \text{(CASCI+PCO)}$$

The CASCI configuration is the same as before (sec. 2.3), but now new configurations, CASCI+PCO, are included that allow one target electron to occupy a PCO. The new configurations provide a natural representation of Rydberg-like states, whilst the original CASCI configurations generally describe valences states. In the scattering model PCOs are included as follows,

$$(core)^{N_c}(CAS)^{N_a}(continuum)^1,$$
$$(core)^{N_c}(CAS)^{N_a-1}(PCO)^1(continuum)^1,$$
$$(core)^{N_c}(CAS)^{N_a+1},$$
$$(core)^{N_c}(CAS)^{N_a}(PCO)^1,$$
$$(core)^{N_c}(CAS)^{N_a-1}(PCO)^2,$$

The key difference between this scattering model and the ones presented in sec. 2.3 is the addition of two electron excitation into either the PCOs or a PCO and a continuum orbital. These types of configuration essentially model the scattering and ionised electrons both being in the (pseudo)continuum, which is necessary in order to model the effects of ionisation and polarisation at intermediate scattering energies. The choice of scattering model is not unique and it can have a pronounced effect on both the tractability and accuracy of the calculation. This situation is discussed in great detail by Halmová et al. (2008), who investigated the effect of eight different scattering models on the C_2^- anion.

4.2.2 Mixed Rydberg and valence states

Accurate *ab initio* potential energy curves, that take into account both types of state (Rydberg-like and valence), were first attempted by De Vivie and Peyerimhoff (1988) who used a Multi-Reference Double Excitation Configuration Interaction (MRDCI) method to generate curves for the lower excited states. Data calculated using their model were fit using a spline method in order to produce smooth curves. Further work was carried out by Polák and Fišer (2003) who investigated the four lowest-lying $^2\Sigma^+$ states of NO. They used a different MRCI variant that is internally contracted (icMRCI) and for their four-state calculation they obtained smooth curves but only for the $^2\Sigma^+$ states. Shi and East (2006) improved upon the results of De Vivie and Peyerimhoff (1988) by including more terms in the CI expansion but they only targeted the doublet states of NO. Shi and East (2006) use state-averaged CASCI calculations in order to obtain curves however they suffer from discontinuities due to a change in the selection of states being averaged at different bond lengths (Shi and East, 2006). To remedy this they employed a weight extrapolation technique to smooth the curves but this method treats each of the target states independently. Gilmore (1965) used the Rydberg-Klein method to obtain numerical curves from published spectroscopic data, which are widely used across the literature. The curves were not provided as supplementary data, however, data have been extracted from this work using a plot digitiser (Rohatgi, 2017). The extracted curves are shown in Fig. 4.2 for reference.

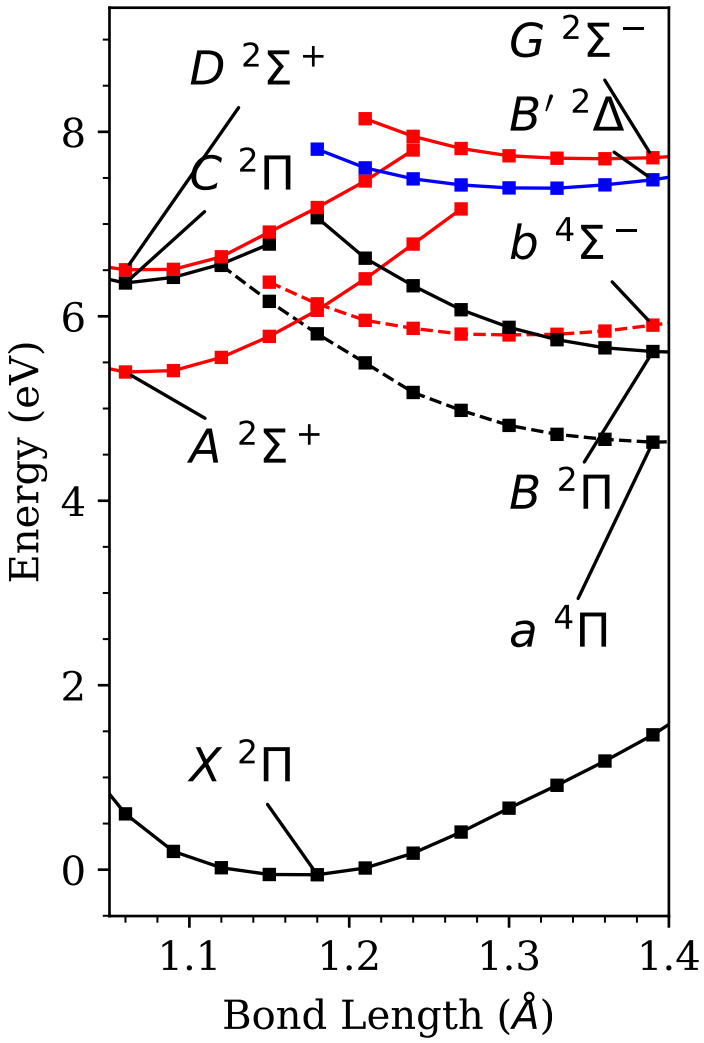

Figure 4.2 | Potential energy curves for NO derived from spectroscopic data using Rydberg-Klein method. Data were extracted using a plot digitiser from Gilmore (1965).

The UKRMol code requires one target model and one set of optimised molecular orbitals that are capable of describing both the Rydberg and valence-type states of the target. This rules out the Multi-Reference calculations of De Vivie and Peyerimhoff (1988) and Polák and Fišer (2003) because the MRCI method must be run separately for each spin-space symmetry. Therefore it is not possible to obtain one set of orbitals for all of the target states required. The CASCI approach of Shi and East (2006) does indeed produce smooth curves but by manually averaging separate calculations, with different numbers of states, which again is not possible for the current work. Therefore a new approach is investigated that takes advantage of

pseudo-orbitals and the RMPS method to obtain smooth PECs that also represent the mixed Rydberg and valence-type states of NO.

4.3 Results

In the following section, PECs obtained via three different approaches will be presented; independent geometry CASCI, dependent geometry CASCI and dependent geometry CASCI with the addition of pseudostates. Dependent geometry refers to CASCI calculations that have been calculated based on MOs optimised from the previous geometry, where as independent geometry calculations use no prior knowledge. The aim of this work is to produce accurate PECs for the ground and first six excited states of NO, namely, $X\ ^2\Pi$, $a\ ^4\Pi$, $b\ ^4\Sigma^-$, $A\ ^2\Sigma^+$, $B\ ^2\Pi$, $C\ ^2\Pi$ and $D\ ^2\Sigma^+$ (see Fig. 4.2).

Producing a balanced R-matrix calculation using the RMPS method is a difficult challenge. If care is not taken, the target model and scattering model can quickly become overwhelmingly large (Halmová et al., 2008). Therefore, the target model considered in this work must be able to support a balanced $N + 1$-electron treatment when the scattering electron is included. For this reason the target model, for RMPS calculations, will use two types of configurations. The first, Type I, will be the same as those used in the standard R-matrix CASCI calculations i.e., not using the RMPS method. Here, target states are generated from a series of configurations, using a CAS of (4,3,3,0) in C_{2v} symmetry.

$$(4,0,0,0)^8(4,3,3,0)^7. \qquad \text{(Type I)}$$

To include pseudostates, an additional set of configurations (Type II) is used. Due to the large number of configurations generated by adding an additional basis set, the CAS is reduced to (2,2,2,0).

$$(4,0,0,0)^8(2,2,2,0)^6(26,13,13,6)^1. \qquad \text{(Type II)}$$

In both cases the same core configuration is used, in which the first 4 σ orbitals

will be double occupied, which corresponds to freezing electrons in the first two s-orbitals of each atomic site. The PCOs included in the second set of configurations, Type II, were generated using $\alpha_0 = 0.05$, $\beta = 1.4$ and $n_L = 8, 8, 6$ for $L = 0, 1, 2$ leading to (26,13,13,6) PCOs in C_{2v} symmetry. For a standard CASCI calculations i.e., not including pseudostates, only configurations of Type I will be used. For RMPS target calculations, both Type I and Type II configurations will be used to generate target (pseudo)states.

Figure 4.3 shows the PECs generated using a CASCI target model, where only Type I configurations are included. For the target MOs a correlation-consistent Dunning basis set, aug-cc-pVQZ (AVQZ hereafter) (Dunning, 1989; Kendall et al., 1992), was used. The singly-augmented basis set contains additional diffuse basis functions that are better at describing Rydberg-like states. Each geometry was calculated independently of the neighbouring geometries and it can be seen that the curves are strongly discontinuous (see Fig. 4.3).

For geometries below the equilibrium, $R < R_e = 1.15$ Å, the lower-lying excited states are generally Rydberg-like. As the lower states transition, from predominantly Rydberg-like, to valence-type character (near R=1.18 Å) the ground state, $X\ ^2\Pi$, jumps. This sudden change occurs because the character of the target MOs has switched from Rydberg-like to valence, which leads to a better description of the ground state (Shi and East, 2006). This is a common issue with CASCI calculations, but the effects can be mitigated by using MOs optimised in the previous geometry. Using the previous geometry's MOs as a starting point allows a smoother transition between calculations at different geometries, thus leading to more continuous PECs.

There are several sensible choices for using previously optimised MOs. For example, the starting point can be selected as the shortest or longest bond length required – in this case either $R = 1.05$ Å or $R = 1.40$ Å respectively. In theory starting from $R = 1.05$ Å provides a better description of the Rydberg-like states but initial tests showed that calculations of this type suffered from severe discontinuities. Discontinuities arose as the bond length increased, passing through re-

gions where state crossings and avoided crossings occur. Calculations which started from larger bond lengths, working inwards, demonstrated much better behaviour as shown in Figure 4.4. This figure shows continuous curves across the full range of bond lengths considered. This has clearly come at the cost of the Rydberg-like states, which have nearly all but disappeared, with the exception of the $A\ ^2\Sigma^+$ excited state. Although the aforementioned PECs are not sufficient for a complete study of the NO molecule, they do at least provide a foundation on which to build.

It is already known that the RMPS method is capable of converging target properties such as the polarisability and, in addition, that it can provide an improved description of the target states (Bartschat et al., 1996b; Gorfinkiel and Tennyson, 2005). Here the RMPS method is employed to improve the description of the target – specifically for the Rydberg-like states which have been poorly represented by the previous CASCI calculations (using Type I only configurations). In the RMPS method additional states, pseudostates, are introduced to the calculation by allowing both Type I and Type II configurations.

Figure 4.5 shows the PECs generated by the RMPS method, which also use MOs generated from the previous geometry. Compared to the previous CASCI calculation (Fig. 4.4) these curves are also continuous, but now, at smaller internuclear distances, the Rydberg-like states are partially recovered. That is, at small bond lengths the $C\ ^2\Pi$ and $D\ ^2\Sigma^+$ states regain their Rydberg-like character, although they are approximately 2 eV too high in energy. This is a significant improvement over the previous two calculations. The $A\ ^2\Sigma^+$ Rydberg-like state is lowered slightly in energy, relative to the ground state compared to Fig. 4.4. This indicates that the $A\ ^2\Sigma^+$ state might be over-represented by the basis set compared to say the valence states, however, the effect is small. The other excited states, $a\ ^4\Pi$, $b\ ^4\Sigma^-$ and $B\ ^2\Pi$ are largely unaffected by the introduction of pseudostates, which is expected as they are valence states.

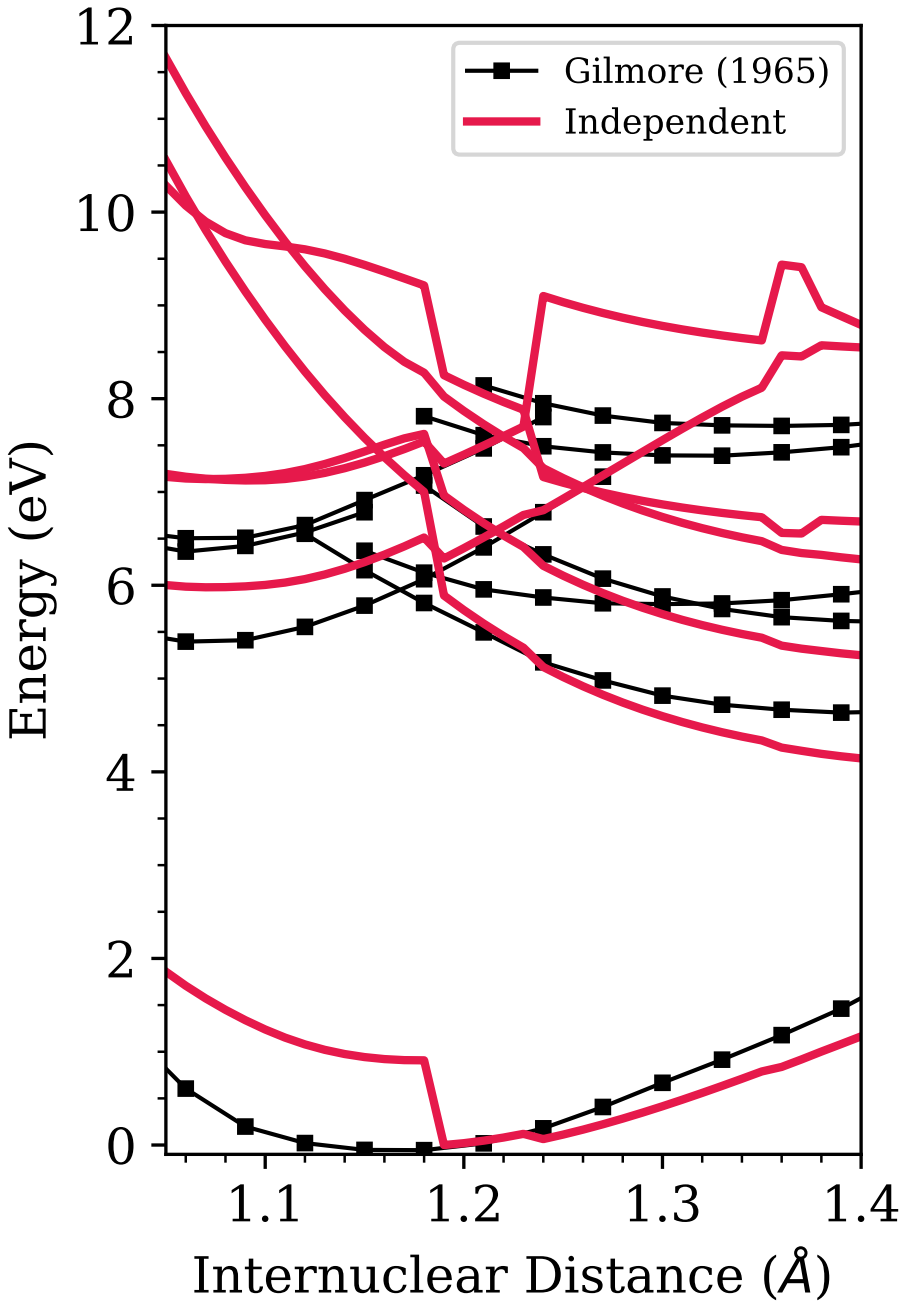

Figure 4.3 | Independent geometry CASCI PECs for NO using the AVQZ basis set. Data from Gilmore (1965) are provided as a reference.

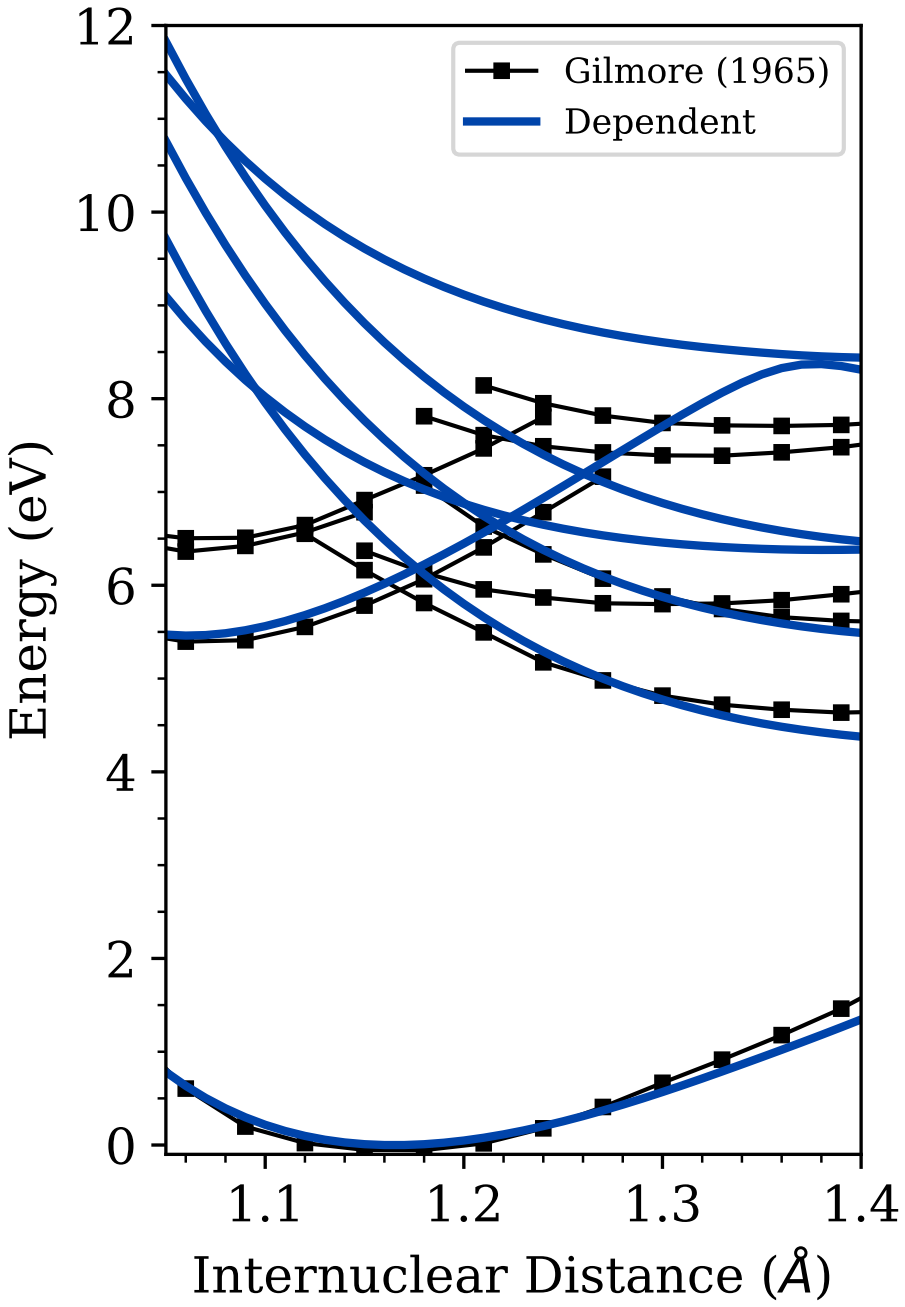

Figure 4.4 | Dependent geometry CASCI PECs for NO using the AVQZ basis set. Data from Gilmore (1965) are provided as a reference.

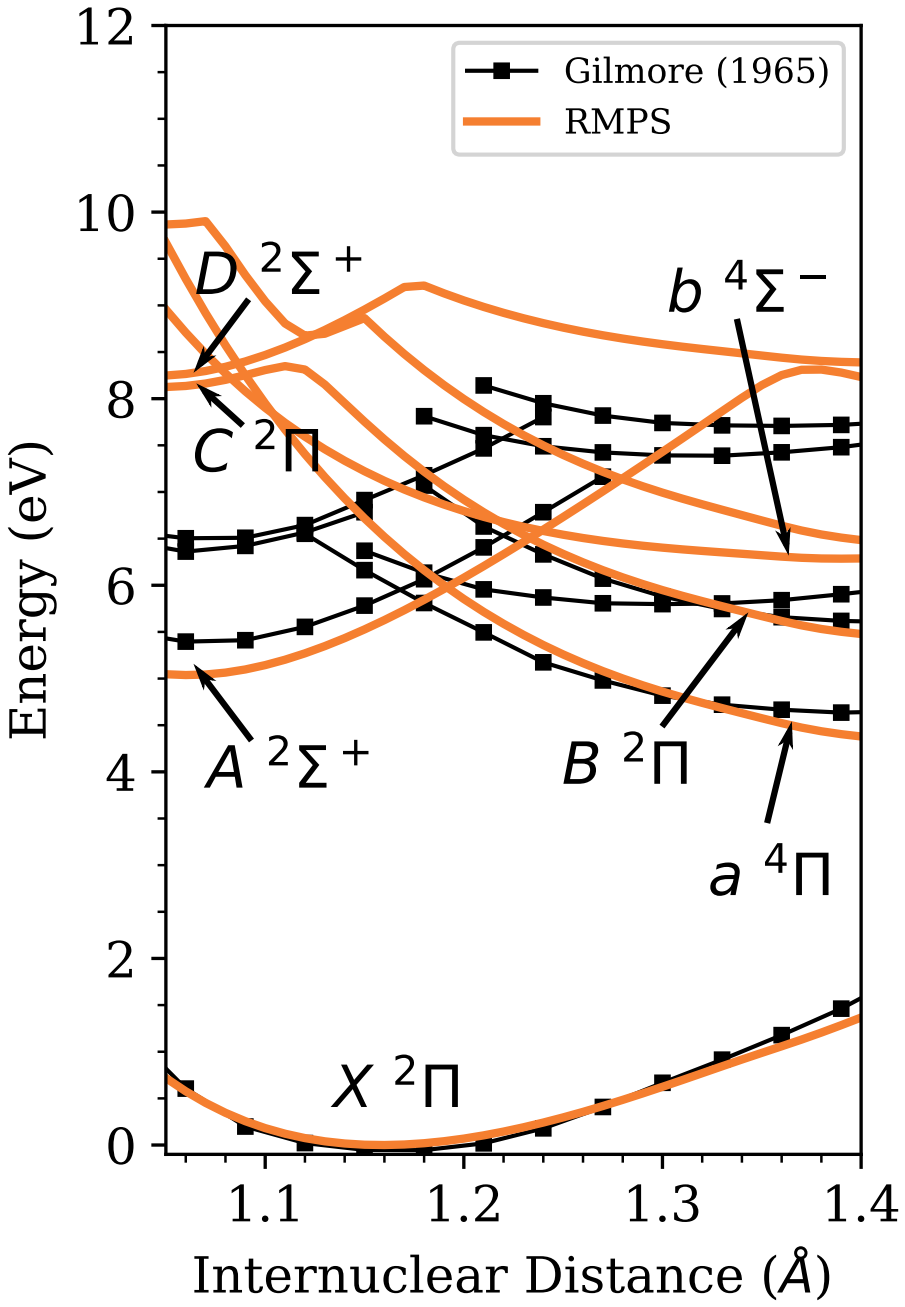

Figure 4.5 | Dependent geometry CASCI PECs for NO using the AVQZ basis set with additional pseudostates added via the RMPS method. Data from Gilmore (1965) are provided as a reference.

4.4 Conclusion and Further Work

The target description is arguably one of the most important factors of a scattering calculation, which is often over-looked as remarked by Bartschat (2013). Sophisticated, large-scale calculations based on an inadequate target will still give incorrect results. Therefore the aim of this work was to resolve the outstanding issues associated with modelling mixed Rydberg-like and valence state targets, before moving on to the $N + 1$ scattering complex. To an extent, it has been shown in this work that it is possible to model both Rydberg-like and valence states with a single set of CASCI MOs and a unified target model that is not state dependent, as opposed to MRCI calculations (see Fig. 4.5). Furthermore, this target model is compatible with existing UKRMol and UKRMol+ codes that rely on the aforementioned properties i.e., a single set of orbitals and a single target model.

Whilst a full scattering calculation has not been demonstrated yet for this target model, preliminary tests show that it should be possible with current computational resources. The $N + 1$ Hamiltonians generated in test calculations have dimensions of the order 10^5 per scattering symmetry. The size of the $N + 1$ matrix is indicative of the computational cost of the scattering calculation, as matrix diagonalisation typically consumes a significant proportion of the total compute time and RAM. The other major contribution comes from propagating large numbers of channels, as was the case for previous work on molecular hydrogen (chapter 3). For the study of H_2, calculations were restricted to $L_{\text{max}} = 6$ to limit the number of channels that needed to be propagated through the outer region.

Traditionally, the standard R-matrix and RMPS methods utilise all of the $N+1$ eigenvalues in order to construct the R-matrix (see Eq. 2.19). This presents an issue as the size of the Hamiltonian rapidly increases commensurate with the size of the scattering model. However, this problem can be alleviated by adopting the partitioned R-matrix approach (Tennyson, 2004), as successfully demonstrated by Halmová et al. (2008) and Dora et al. (2009). In fact, Dora et al. (2009) carried out one of the largest calculations to date, on the molecule uracil, in which they utilised the partitioned R-matrix approach to diagonalise a matrix of dimension 218064,

where only a small subset (less than 10%) of the eigenvalues were required. So, with the application of the partitioned R-matrix approach and RMPS, electron-impact electronic excitation of NO should be within reach of future theoretical work.

Part II

High Energy Electron Collisions with Atoms in Strong Laser Fields

Chapter 5

Strong-Field Theory

So far electron collisions have been considered in the absence of external electromagnetic fields, where the scattering energies have been small compared to the ionisation potential I_p. In strongly driven systems however, the scattering energies can quickly exceed this limit and the R-matrix approach becomes impractical and or invalid. There are two main reasons for this. Firstly, even with the addition of pseudo-states there is no way to accurately represent double (or multiple) ionisation. Secondly, the R-matrix method becomes computationally intractable due to the large number of channels and target states required. That being said, the aforementioned HELIUM code (Dundas et al., 1999) was capable of representing double ionisation, however, as implied by the name it was only applicable to helium. In an attempt to improve the applicability, Wragg et al. (2015) successfully adapted the mixed finite difference and basis set approach used in the HELIUM code and applied it to R-matrix with time-dependence (RMT) calculations. However, as yet, the two-electron continuum RMT approach has only been applied to helium (Wragg and van der Hart, 2016). For single ionisation however, the situation is somewhat improved. RMT has been successfully demonstrated for single ionisation of molecular hydrogen in weaker fields i.e., $I = 10^{12} - 10^{13}$ W cm^{-2} (Brown et al., 2020) and again, in theory, this can be extended to other molecules in a more general fashion.

In this chapter, semiclassical techniques are introduced that explore single and double ionisation of atomic targets in the presence of strong-laser fields i.e., intensities of the order $I = 10^{14} - 10^{15}$ W cm^{-2}.

5.1 Three Step Model

The cornerstone of many strong-field physics theories is the *three step model*. It provides a simplified picture of the underlying processes (Corkum, 1993). In step one, a strong external electric field manipulates the atomic potential creating a potential barrier through which the outermost electron can tunnel (see Fig. 5.1). In the second step, the tunnel-ionised electron then propagates with its motion largely dictated by the strong electric field. Initially the electric field will lead the electron away from its parent ion. However, as the oscillating electric field changes direction the electron is driven back towards its parent ion. Thus leading to the third step, where the energetic, recolliding electron can scatter from the parent ion or interact with other bound electrons to give rise to multiple ionisation. For elliptically and circularly polarised (CP) light the first two steps are essentially the same, but the likelihood of recollision (step 3) is significantly decreased due to the other components of the electric field pushing the electron off course. This explains the suppression of non-sequential double ionisation as seen by Fittinghoff (1994).

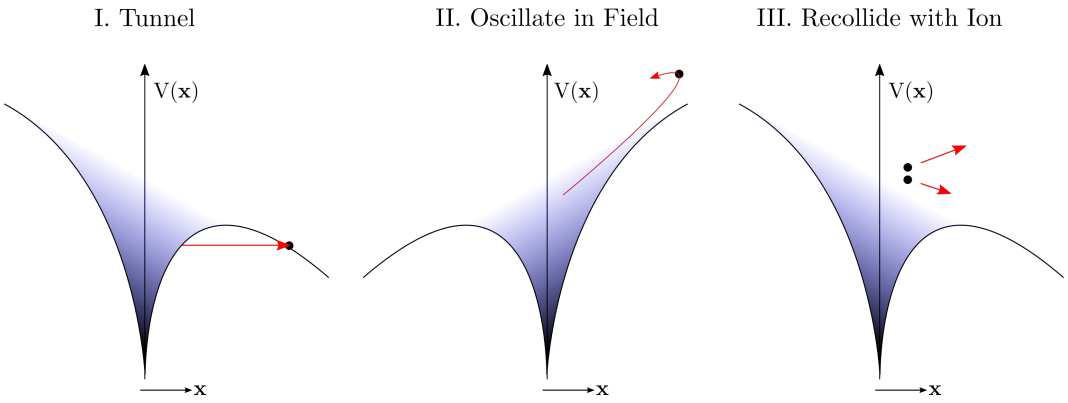

Figure 5.1 | In step I the atomic potential is modified by the presence of an external electric field. This creates a barrier through which the electron can tunnel. In step II the electron oscillates, with its motion dictated largely by the external electric field. As the electric field changes direction the electron is sent back towards the parent ion. Finally, step III, the electron returns to the ion and in this example ionises a second electron, leading to double ionisation.

5.2 Initial Conditions

5.2.1 Tunnel Exit

The three step model begins with a continuum electron. There are different ways of selecting the initial conditions for the continuum electron. They can either be selected from a classical micro-canonical ensemble e.g., Grochmalicki et al. (1991) or by solving the Schrödinger equation for hydrogen-like system in a static field e.g., Chen et al. (2000). Here the latter method is used.

The presence of an electric field alters the atomic potential. This can be seen from the Hamiltonian below, given for a hydrogenic atom in a linearly polarised laser field acting in the z-direction.

$$H = -\frac{1}{2}\nabla^2 + V_{\text{eff}}, \quad \text{where} \quad V_{\text{eff}} = -\frac{Z}{r} + zE, \tag{5.1}$$

where $-\frac{1}{2}\nabla^2$ is the kinetic energy operator, r is the magnitude of the electron's displacement, z is the component of the electron's position in the z-direction, E is the electric field strength and Z is the atomic number. The atomic potential is tilted becoming lower on one side and higher on the other. This creates a barrier through which the electron can tunnel (see Fig. 5.1). The exact tunnel exit can be calculated by solving Schrödinger's equation for the Hamiltonian above i.e., $H\psi = \epsilon\psi$. However, it is necessary to first transform from Cartesian to parabolic coordinates (Landau and Lifshitz, 1965),

$$\xi = r + z, \quad \eta = r - z, \quad r = \frac{1}{2}(\xi + \eta) \quad and \quad z = \frac{1}{2}(\xi - \eta). \tag{5.2}$$

ξ and η range from 0 to ∞. In parabolic coordinates it is possible to separate variables i.e., $\psi = \psi_1(\eta)\psi_2(\xi)$. This leads to the following equation,

$$\frac{\partial^2\psi_1}{\partial\eta^2} + \left(-\frac{I_p}{2} + \frac{1}{2\eta} + \frac{1}{4\eta^2} + \frac{1}{4}E\eta\right)\psi_1 = 0, \tag{5.3}$$

where I_p is the ionisation potential. Equation 5.3 represents states that tunnel. There is a corresponding equation for $\psi_2(\xi)$ but this relates to states that are bound. Equa-

tion 5.3 has the form of a simple time-independent Schrödinger equation,

$$-\frac{1}{2}\frac{\partial^2\psi}{\partial\eta^2} + (V-\epsilon)\psi = 0, \tag{5.4}$$

where,

$$V = -\frac{1}{4\eta} - \frac{1}{8\eta^2} - \frac{1}{8}E\eta \quad \text{and} \quad \epsilon = -\frac{I_p}{4}. \tag{5.5}$$

The tunnel exit is found when $V - \epsilon = 0$. This equation is cubic in terms of η and can be solved analytically. The exit point in Cartesian coordinates in recovered with the expression $z = -\eta/2$.

5.2.2 Tunnelling Rate

The tunnelling rate of an electron is calculated using Ammosov–Delone–Krainov (ADK) theory (Ammosov et al., 1986). The ADK rate w_{adk} is valid for laser fields with photon energy $\hbar\omega \ll I_p$ and electric field strength $E_0 \ll E_a$, where the characteristic field strength of the atom is $E_a = (2I_p)^{3/2}$. For linearly polarised light it can be written as follows

$$w_{adk} = C\left(\frac{1}{|\mathbf{E}(t_0,0)|}\right)^{2n_{\text{eff}}-1}\exp\left(\frac{-2(2I_p)^{3/2}}{3|\mathbf{E}(t_0,0)|}\right). \tag{5.6}$$

C is a constant which can be found in Ammosov et al. (1986) but for this work it is set to $C = 1$ (this does not affect the physics). The effective quantum number is $n_{\text{eff}} = Z_{\text{eff}}(2I_p)^{-\frac{1}{2}}$ and $|\mathbf{E}(t_0,0)|$ is the magnitude of the electric field at the time of tunnelling t_0 and position $y = 0$. For circularly polarised light the above formula still holds because at any given instant the field can be considered linear. Note that the spatial dependence of the electric field is ignored for the tunnelling rate. This is valid for two reasons. Firstly, it is assumed that the electron is initially bound i.e., close to the origin. Hence, the y-position will be close to zero. Secondly, the spatial dependence of the laser field is a factor of $1/c$ smaller than the time dependence.

The initial velocity of the ionised electron is zero in the direction of the electric field and the transverse velocity v_t is governed by a Gaussian probability distribu-

tion, w_v (Fu et al., 2001).

$$w_v = \frac{v_t}{|\mathbf{E}(t_0,0)|} \exp\left(-v_t^2 \frac{\sqrt{2I_p}}{|\mathbf{E}(t_0,0)|}\right). \tag{5.7}$$

5.2.3 Microcanonical Distribution

For two (active) electron atoms, the initial conditions of the first electron (tunnel-ionised electron) have already been discussed. However, there exists also a bound electron (initially bound) that must be described. To model the initially bound electron, a microcanonical distribution can be used (Abrines and Percival, 1966). The initial state of the bound electron can be approximated as a hydrogenic system, in the absence of any external fields, with the binding energy $-I_p^B$. The Hamiltonian is

$$H = \frac{\mathbf{p}^2}{2} - \frac{Z}{|\mathbf{r}|} = -I_p^B. \tag{5.8}$$

A pseudo-random position $\mathbf{r}$ and momentum $\mathbf{p}$ are selected that satisfy the microcanonical condition,

$$w_{micro} = K\delta(-I_p - H(\mathbf{p},\mathbf{r})), \tag{5.9}$$

where K is a normalisation constant (Abrines and Percival, 1966).

5.2.4 Importance Sampling

In Monte-Carlo simulations, large numbers of trajectories must be propagated. This can be computationally expensive if improbable events $w_{adk} \approx 0$ are propagated. For example, in Fig. 5.2 (a) the ADK rate is plotted as a function of time. There are regions of the laser field where $w_{adk} \approx 0$ and others where w_{adk} is large i.e., at the peaks of the electric field. If samples are drawn from a uniform distribution, there will be large numbers of trajectories propagated that do not appreciably contribute to the final result.

The efficiency can be greatly improved by implementing importance sampling.

In this approach, a new probability distribution function is selected from which the samples are drawn. A good choice is one that increases the likelihood of samples in regions where the integrand is large or rapidly varying (Kalos and Whitlock, 2008). For this work, a good choice is the function (see Fig. 5.2 (b)).

$$W(t) = \int_{t_i}^{t} w_{adk}(t)\, dt. \tag{5.10}$$

Uniform samples from this distribution i.e., $W_x \sim [0, W_{max}]$ correspond to biased distributions in time. W_{max} is the maximum value of the function as calculated from the start t_i to the end of the laser field t_f i.e., $W_{max} = \int_{t_i}^{t_f} w_{adk}\, dt$. To remove this bias of importance sampling, each trajectory must be divided by its corresponding rate $w_{adk}(t_x)$. Hence the new weight is given by

$$w_x = 1/w_{adk}(t_x). \tag{5.11}$$

The randomly generated tunnel time t_x is obtained by solving

$$W_x(t_x) = \int_{t_i}^{t_x} w_{adk}(t)\, dt. \tag{5.12}$$

The probability of a certain process e.g., single ionisation (SI) can be calculated as follows

$$P(\mathrm{SI}) = \frac{\sum_{i=1}^{N(\mathrm{SI})} w_x^i w_{adk}^i}{\sum_{j=1}^{N(\mathrm{All})} w_x^j w_{adk}^j} = \frac{N(\mathrm{SI})}{N(\mathrm{All})}. \tag{5.13}$$

$N(\mathrm{All})$ is the total number of trajectories that propagated successfully and $N(\mathrm{SI})$ is the number of trajectories that produced single ionisation.

5.3 Non-Dipole Effects

In order to realise efficient simulations, often systems are modelled in the dipole approximation. This is a restriction on the laser field which neglects the spatial component of the vector potential, which in general is a function of time and space i.e., $\mathbf{A}(\mathbf{r}, t) \rightarrow \mathbf{A}(t)$. This approximation is extensively used in strong field physics

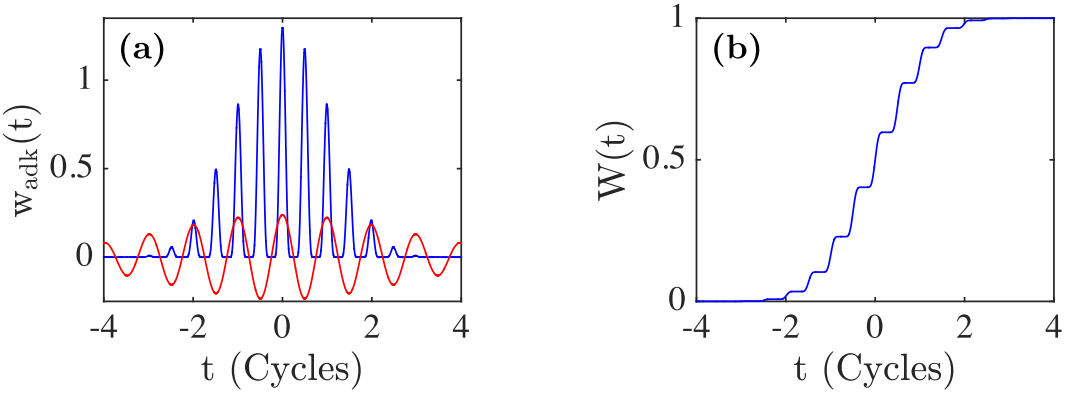

Figure 5.2 | (a) The ADK rate w_{adk} (blue) scaled to unit area with the electric field $E(t, 0)$ (red) as a reference. The tunnelling rate is for a He atom in an 800 nm, $I = 2.0 \times 10^{15}$ W cm^{-2}, FWHM = 12 fs laser field. (b) The sampling function $W(t) = \int_{t_i}^{t} w_{adk}(t)\, dt$.

and has been successfully deployed in a large number of quantum and classical simulations (Parker et al., 2006; Staudte et al., 2007; Emmanouilidou, 2008). Its validity relies on the fact that the wavelength of the electric field is significantly larger than the intrinsic length scale of the atom (Ludwig et al., 2014).

The electric **E** and magnetic **B** fields are derived from the vector potential in the following manner

$$\mathbf{E} = -\partial_t \mathbf{A}, \tag{5.14}$$

$$\mathbf{B} = \nabla \times \mathbf{A}. \tag{5.15}$$

From equation 5.15 it follows that if the spatial dependence of the vector potential is neglected, then the magnetic field is effectively set to zero i.e., $\mathbf{B} = 0$. This approximation therefore ignores magnetic field effects. For the most part this is a reasonable assumption, as the magnetic field is two orders of magnitude smaller than the electric field. However, there are circumstances where this approximation is no longer valid.

The dipole approximation is valid when the laser's wavelength is sufficiently larger than the length scale of the atomic target. Hence this creates, as expected, a lower bound when using shorter and shorter wavelengths. There is, however, a less obvious limit. To explain this, it is useful to first introduce a quantity called the *ponderomotive energy* U_p. The ponderomotive energy is the cycle-averaged energy

of a *free* electron in a laser field. For linearly polarised, monochromatic light acting in the x-direction the force on an electron is,

$$\begin{aligned}\mathbf{F} &= -\mathbf{E}, \\ &= -E_0 \cos(\omega t)\, \hat{\mathbf{x}}. \end{aligned} \tag{5.16}$$

Note that in the dipole approximation the magnetic component of the Lorentz force is zero. Integrating with respect to time (and dividing by the unit mass) gives the velocity.

$$\mathbf{v} = -\frac{E_0}{\omega} \sin(\omega t)\, \hat{\mathbf{x}}. \tag{5.17}$$

The ponderomotive energy is the average energy gained in one period of the laser, T.

$$\begin{aligned} U_p &= \frac{1}{2} \left\langle \mathbf{v}^2 \right\rangle, \\ &= \frac{1}{T} \frac{E_0^2}{2\omega^2} \int_0^T \sin^2(\omega t)\, dt, \\ &= \frac{E_0^2}{4\omega^2}. \end{aligned} \tag{5.18}$$

From equation 5.18 it follows that this energy is directly proportional to the square of the wavelength i.e., $U_p \propto \lambda^2$. Therefore an increase in wavelength means that the electron will gain more kinetic energy from the field and reach higher velocities. This is where the second limit comes in. For sufficiently large velocities, relativistic effects must be accounted for. This occurs in the following limit (in atomic units $m_e = 1$ but it is shown for clarity) (Reiss, 2008, 2014).

$$2U_p = m_e c^2 \quad \text{(Relativistic Limit)}, \tag{5.19}$$

where c is the speed of light. However, even before this limit is reached the dipole approximation will in fact breakdown due to magnetic field effects. The Lorentz

force acting on an electron in a laser field is,

$$\mathbf{F} = -(\mathbf{E} + \mathbf{v} \times \mathbf{B}), \tag{5.20}$$

where $\mathbf{v}$ is the velocity of the electron. Previously (see Eq. 5.16), the second term was neglected because the electric field is much larger than the magnetic field – in fact $|\mathbf{E}| = c|\mathbf{B}|$. However, as the velocity increases the effect of the magnetic field increases. Quantitatively, it is accepted that magnetic field effects become important when the electron's displacement β_0 caused by the magnetic field approaches 1 a.u. (Reiss, 2008, 2014).

$$\beta_0 \approx \frac{U_p}{2\omega c} = 1.0 \quad \text{(Magnetic Field Effect Limit)}. \tag{5.21}$$

Recent experiments have been carried out in proximity to the above limit (Eq. 5.21). For example, Smeenk et al. (2011) investigated the effect of circularly polarised light on Ne and Ar atoms. In the latter work two laser fields are used, $\lambda = 800$ nm and $\lambda = 1400$ nm, across a range of intensities, $I = 10^{14} - 10^{15}$ W cm^{-2}. It was shown that the average electron momentum in the direction of laser propagation was greater than zero and increased with intensity and wavelength. This is contrary to the dipole approximation which assumes no net momentum gain in the direction of propagation. Ludwig et al. (2014) used longer wavelengths still ($\lambda = 3400\ nm$) to investigate the effect of linearly-polarised light on a variety of noble gas atom. This work however focused on the peak offset in the momentum distribution, not the average. It was shown that the peak offset was negative in all cases and that the effect increased with intensity. This is a surprising result. A naive assumption would predict that the offset would be positive due to the magnetic component of the Lorentz force, $\mathbf{F}_B = -\mathbf{v} \times \mathbf{B}$. However, it was identified that the negative offset is likely the result of the Coulomb interaction, thus, reinforcing the importance of modelling the ion's potential accurately.

5.4 Equations of Motion

In this work, magnetic field effects are fully accounted for by modelling the laser field as follows. To simulate the laser field a vector potential with a Gaussian envelope is used, propagating in the y-direction. For elliptically-polarised light the vector potential $\mathbf{A}(t, y)$ can be written,

$$\mathbf{A}(t,y) = -\frac{E_0}{\omega} e^{-\left(\frac{ct-y}{c\tau}\right)^2} \begin{pmatrix} \sin(\omega t - ky) \\ 0 \\ \chi \cos(\omega t - ky) \end{pmatrix}. \tag{5.22}$$

Where χ is used here as an ellipticity parameter. The light is linearly polarised for $\chi = 0$, circularly polarised for $\chi = \pm 1$ and elliptically polarised for values in between. E_0 is the electric field strength, ω is the frequency, $\tau = \text{FWHM}/\sqrt{\ln 4}$ (where FWHM is the intensity full-width half-maximum) and $k = \omega/c$ is the magnitude of the wavevector.

The electric $\mathbf{E}(t, y)$ and magnetic $\mathbf{B}(t, y)$ fields can be derived from the vector potential using equations 5.14 and 5.15 respectively.

$$\mathbf{E}(t,y) = \quad E_0 e^{-\left(\frac{ct-y}{c\tau}\right)^2} \begin{pmatrix} \cos(\omega t - ky) - \frac{2}{\omega\tau}\left(\frac{ct-y}{c\tau}\right)\sin(\omega t - ky) \\ 0 \\ -\chi\left[\sin(\omega t - ky) + \frac{2}{\omega\tau}\left(\frac{ct-y}{c\tau}\right)\cos(\omega t - ky)\right] \end{pmatrix}, \tag{5.23}$$

$$\mathbf{B}(t,y) = -\frac{E_0}{c} e^{-\left(\frac{ct-y}{c\tau}\right)^2} \begin{pmatrix} \chi\left[\sin(\omega t - ky) + \frac{2}{\omega\tau}\left(\frac{ct-y}{c\tau}\right)\cos(\omega t - ky)\right] \\ 0 \\ \cos(\omega t - ky) - \frac{2}{\omega\tau}\left(\frac{ct-y}{c\tau}\right)\sin(\omega t - ky) \end{pmatrix}. \tag{5.24}$$

For linearly-polarised ($\chi = 0$) light this simplifies to,

$$\mathbf{A}(t,y) = -\frac{E_0}{\omega} e^{-\left(\frac{ct-y}{c\tau}\right)^2} \sin(\omega t - ky)\, \hat{\mathbf{x}}, \tag{5.25}$$

$$\mathbf{E}(t,y) = \quad E_0 e^{-\left(\frac{ct-y}{c\tau}\right)^2} \left[\cos(\omega t - ky) - \frac{2}{\omega\tau}\left(\frac{ct-y}{c\tau}\right)\sin(\omega t - ky)\right] \hat{\mathbf{x}}, \tag{5.26}$$

$$\mathbf{B}(t,y) = -\frac{E_0}{c} e^{-\left(\frac{ct-y}{c\tau}\right)^2} \left[\cos(\omega t - ky) - \frac{2}{\omega\tau}\left(\frac{ct-y}{c\tau}\right)\sin(\omega t - ky)\right] \hat{\mathbf{z}}. \tag{5.27}$$

The path of a particular trajectory is governed by the classical equations of motion. These can be derived from the Hamiltonian, which is in turn derived from the Lagrangian.

In everything that follows, the subscripts 1 and 2 will be used to represent the tunnelling and initially bound electrons respectively. The Lagrangian for a fixed nucleus, two (active) electron atom can be written as follows (Goldstein, 1980),

$$L(\mathbf{q}_i, \dot{\mathbf{q}}_i, t) = \frac{\dot{\mathbf{q}}_1^2}{2} + \frac{\dot{\mathbf{q}}_2^2}{2} + \frac{Z}{|\mathbf{q}_1|} + \frac{Z}{|\mathbf{q}_2|} - \frac{1}{|\mathbf{q}_1 - \mathbf{q}_2|} - \dot{\mathbf{q}}_1 \cdot \mathbf{A}(\mathbf{q}_1, t) - \dot{\mathbf{q}}_2 \cdot \mathbf{A}(\mathbf{q}_2, t), \tag{5.28}$$

where $\mathbf{q}_i$ and $\dot{\mathbf{q}}_i$ are the position and velocity respectively. Note that the nucleus is frozen. This is a suitable approximation as the nucleus is considerably massive compared to the electrons. The Hamiltonian $H(\mathbf{q}_i, \mathbf{p}_i, t)$, is obtained using,

$$H(\mathbf{q}_i, \mathbf{p}_i, t) = \sum \dot{\mathbf{q}}_i \mathbf{p}_i - L(\mathbf{q}_i, \dot{\mathbf{q}}_i, t). \tag{5.29}$$

The conjugate momentum $\mathbf{p}_i$ is defined as $\mathbf{p}_i \equiv \frac{\partial L}{\partial \dot{\mathbf{q}}_i}$.

$$\mathbf{p}_1 = \dot{\mathbf{q}}_1 - \mathbf{A}_1, \tag{5.30}$$

$$\mathbf{p}_2 = \dot{\mathbf{q}}_2 - \mathbf{A}_2, \tag{5.31}$$

where $\mathbf{A}_1 = \mathbf{A}(\mathbf{q}_1, t)$ and $\mathbf{A}_2 = \mathbf{A}(\mathbf{q}_2, t)$. Therefore the Hamiltonian is,

$$H(\mathbf{q}_i, \mathbf{p}_i, t) = \frac{(\mathbf{p}_1 + \mathbf{A}_1)^2}{2} + \frac{(\mathbf{p}_2 + \mathbf{A}_2)^2}{2} - \frac{Z}{|\mathbf{q}_1|} - \frac{Z}{|\mathbf{q}_2|} + \frac{1}{|\mathbf{q}_1 - \mathbf{q}_2|}. \quad (5.32)$$

For computational efficiency it is necessary to transform the generalised coordinates via a KS-transformation (Stiefel and Kustaanheimo, 1965). The KS-transformations are as follows,

$$(\mathbf{q}_i, 0)^\intercal = \mathbf{M}_i \mathbf{Q}_i \quad \text{and} \quad (\mathbf{p}_i, 0)^\intercal = \frac{\mathbf{M}_i \mathbf{P}_i}{2Q_i^2}, \quad (5.33)$$

where,

$$\mathbf{Q}_i = \begin{pmatrix} Q_{i1} \\ Q_{i2} \\ Q_{i3} \\ Q_{i4} \end{pmatrix} \quad \text{and} \quad \mathbf{M}_i = \begin{pmatrix} Q_{i1} & -Q_{i2} & -Q_{i3} & Q_{i4} \\ Q_{i2} & Q_{i1} & -Q_{i4} & -Q_{i3} \\ Q_{i3} & Q_{i4} & Q_{i1} & Q_{i2} \\ Q_{i4} & -Q_{i3} & Q_{i2} & -Q_{i1} \end{pmatrix}. \quad (5.34)$$

Applying these transformations (equation 5.33) to the Hamiltonian (equation 5.32) yields,

$$H(\mathbf{Q}_i, \mathbf{P}_i, t) = \frac{1}{2}\left(\frac{\mathbf{M}_1\mathbf{P}_1}{2Q_1^2} + \mathbf{A}_1\right)^2 + \frac{1}{2}\left(\frac{\mathbf{M}_2\mathbf{P}_2}{2Q_2^2} + \mathbf{A}_2\right)^2 - \frac{Z}{|\mathbf{M}_1\mathbf{Q}_1|} - \frac{Z}{|\mathbf{M}_2\mathbf{Q}_2|} + \frac{1}{|\mathbf{M}_1\mathbf{Q}_1 - \mathbf{M}_2\mathbf{Q}_2|}. \quad (5.35)$$

But now the vector fields are defined as $\mathbf{A}_1 = \mathbf{A}(\mathbf{M}_1\mathbf{Q}_1, t)$ and $\mathbf{A}_2 = \mathbf{A}(\mathbf{M}_2\mathbf{Q}_2, t)$. To regularise the Hamiltonian two new coordinates $Q_3 = t$ and $P_3 = -H(\mathbf{Q}_i(t), \mathbf{P}_i(t), t) \equiv -E(t)$ are introduced (Szebehely, 1967). The new Hamiltonian $\Gamma(\mathbf{Q}_i, \mathbf{P}_i, t)$ can be written as,

$$\Gamma(\mathbf{Q}_i, \mathbf{P}_i, t) = H(\mathbf{Q}_i, \mathbf{P}_i, t) - E(t). \quad (5.36)$$

In this extended phase-space the energy $\Gamma(\mathbf{Q}_i, \mathbf{P}_i, t)$ will be conserved. Notice that

time t has now become one of the coordinates. A new fictitious time τ is introduced, which can be scaled by a factor of g i.e., $dt = gd\tau$. For this problem, a sensible choice of scaling factor is,

$$g = \frac{Q_1^2 Q_2^2}{Q_1^2 + Q_2^2}. \tag{5.37}$$

The regularised Hamiltonian is given by $\Gamma^* = g\Gamma$.

$$\Gamma^* = g\Bigg\{\frac{1}{2}\left(\frac{\mathbf{M}_1\mathbf{P}_1}{2Q_1^2} + \mathbf{A}_1\right)^2 + \frac{1}{2}\left(\frac{\mathbf{M}_2\mathbf{P}_2}{2Q_2^2} + \mathbf{A}_2\right)^2 - \frac{Z}{|\mathbf{M}_1\mathbf{Q}_1|} - \frac{Z}{|\mathbf{M}_2\mathbf{Q}_2|} + \frac{1}{|\mathbf{M}_1\mathbf{Q}_1 - \mathbf{M}_2\mathbf{Q}_2|} - E\Bigg\}, \tag{5.38}$$

$$= \frac{1}{Q_1^2 + Q_2^2}\Bigg\{\frac{Q_2^2 P_1^2}{8} + \frac{Q_1^2 P_2^2}{8} + \frac{Q_2^2 \mathbf{P}_1^\intercal \mathbf{M}_1^\intercal}{2}\mathbf{A}_1 + \frac{Q_1^2 \mathbf{P}_2^\intercal \mathbf{M}_2^\intercal}{2}\mathbf{A}_2 + \frac{Q_1^2 Q_2^2}{2}(A_1^2 + A_2^2) - Q_2^2 Z - Q_1^2 Z + \frac{Q_1^2 Q_2^2}{|\mathbf{M}_1\mathbf{Q}_1 - \mathbf{M}_2\mathbf{Q}_2|} - Q_1^2 Q_2^2 E\Bigg\}. \tag{5.39}$$

The equations of motion are found in the usual way.

$$\dot{\mathbf{Q}}_i = \frac{\partial \Gamma^*}{\partial P_i}, \qquad \dot{\mathbf{P}}_i = -\frac{\partial \Gamma^*}{\partial \mathbf{Q}_i}, \qquad \text{where} \qquad i = 1, 2, 3. \tag{5.40}$$

Recall that $Q_3 = t$ and $P_3 = -E(t)$. Hence, the equations of motion are,

$$\dot{\mathbf{Q}}_1 = \frac{Q_2^2}{Q_1^2 + Q_2^2}\left\{\frac{\mathbf{P}_1}{4} + \frac{\mathbf{M}_1^\intercal \cdot \mathbf{A}_1}{2}\right\}, \tag{5.41}$$

$$\dot{\mathbf{Q}}_2 = \frac{Q_1^2}{Q_1^2 + Q_2^2}\left\{\frac{\mathbf{P}_2}{4} + \frac{\mathbf{M}_2^\intercal \cdot \mathbf{A}_2}{2}\right\}, \tag{5.42}$$

$$\dot{t} = \frac{Q_1^2 Q_2^2}{Q_1^2 + Q_2^2}, \tag{5.43}$$

$$\begin{aligned}\dot{\mathbf{P}}_1 = \frac{-1}{Q_1^2+Q_2^2}\Bigg\{ & 2\mathbf{Q}_1 \\ & \times \left[\frac{P_2^2}{8} + \frac{\mathbf{M}_2\mathbf{P}_2}{2}\cdot\mathbf{A}_2 + \frac{Q_2^2}{2}\left(A_1^2+A_2^2\right) - Z - Q_2^2 E + \frac{Q_2^2}{|\mathbf{M}_1\mathbf{Q}_1 - \mathbf{M}_2\mathbf{Q}_2|}\right] \\ & \quad + \frac{Q_2^2}{2}\mathbf{A}_1\cdot\frac{\partial \mathbf{M}_1\mathbf{P}_1}{\partial \mathbf{Q}_1} + Q_2^2\left(\frac{\mathbf{M}_1\mathbf{P}_1}{2} + Q_1^2\mathbf{A}_1\right)\cdot\frac{\partial \mathbf{A}_1}{\partial \mathbf{Q}_1} \\ & \quad - \frac{2Q_1^2Q_2^2\mathbf{M}_1^{\intercal}\cdot(\mathbf{M}_1\mathbf{Q}_1 - \mathbf{M}_2\mathbf{Q}_2)}{|\mathbf{M}_1\mathbf{Q}_1 - \mathbf{M}_2\mathbf{Q}_2|(\mathbf{M}_1\mathbf{Q}_1 - \mathbf{M}_2\mathbf{Q}_2)^2}\Bigg\}, \end{aligned} \tag{5.44}$$

$$\begin{aligned}\dot{\mathbf{P}}_2 = \frac{-1}{Q_1^2+Q_2^2}\Bigg\{ & 2\mathbf{Q}_2 \\ & \times \left[\frac{P_1^2}{8} + \frac{\mathbf{M}_1\mathbf{P}_1}{2}\cdot\mathbf{A}_1 + \frac{Q_1^2}{2}\left(A_1^2+A_2^2\right) - Z - Q_1^2 E + \frac{Q_1^2}{|\mathbf{M}_1\mathbf{Q}_1 - \mathbf{M}_2\mathbf{Q}_2|}\right] \\ & \quad + \frac{Q_1^2}{2}\mathbf{A}_2\cdot\frac{\partial \mathbf{M}_2\mathbf{P}_2}{\partial \mathbf{Q}_2} + Q_1^2\left(\frac{\mathbf{M}_2\mathbf{P}_2}{2} + Q_2^2\mathbf{A}_2\right)\cdot\frac{\partial \mathbf{A}_2}{\partial \mathbf{Q}_2} \\ & \quad + \frac{2Q_1^2Q_2^2\mathbf{M}_2^{\intercal}\cdot(\mathbf{M}_1\mathbf{Q}_1 - \mathbf{M}_2\mathbf{Q}_2)}{|\mathbf{M}_1\mathbf{Q}_1 - \mathbf{M}_2\mathbf{Q}_2|(\mathbf{M}_1\mathbf{Q}_1 - \mathbf{M}_2\mathbf{Q}_2)^2}\Bigg\}, \end{aligned} \tag{5.45}$$

$$\dot{E} = \frac{1}{Q_1^2+Q_2^2}\left\{Q_2^2\left(\frac{\mathbf{M}_1\mathbf{P}_1}{2} + Q_1^2\mathbf{A}_1\right)\frac{\partial \mathbf{A}_1}{\partial t} + Q_1^2\left(\frac{\mathbf{M}_2\mathbf{P}_2}{2} + Q_2^2\mathbf{A}_2\right)\frac{\partial \mathbf{A}_2}{\partial t}\right\}. \tag{5.46}$$

Using the initial conditions discussed in section 5.2 and the equations of motion given above, it is possible to carry out a Monte-Carlo simulation. Using the statistics generated over millions of classically propagated trajectories it is possible to calculate observables of interest such as double ionisation rates and momentum distributions.

Chapter 6

Magnetic-Field Effects

This chapter is adapted from published work (Emmanouilidou and Meltzer, 2017).

As mentioned previously, this part of the thesis is concerned with higher-energy electron collisions with atoms in strong laser fields. In contrast with part I, the scattering electrons described here originate from the atom itself. Whereas, for the electron-molecule scattering considered in the first part, the scattering electron was considered *free* beforehand.

The main effect considered in the following two chapters is non-sequential double ionisation (NSDI). As discussed in the theory, sec. 5.1, NSDI can be most easily understood using the three step model. Whilst this simplified model does not capture all of the physics it does describe a number of the observed phenomena. In the first step one of the target atom's electrons tunnel ionises to the continuum. Next, this continuum electron is driven back to the parent atom's nucleus by the field where, finally, it can lead to subsequent ionisation of a second electron.

In this chapter, magnetic field effects are investigated to challenge the use of the commonly employed dipole approximation. In the following chapter (chapter 7) the mechanisms behind NSDI and magnetic field effects are explored in greater detail.

6.1 Introduction

Non-sequential double ionisation in multiple-electron atoms is a fundamental process that explores electron-electron correlation in strong fields. As such, it has at-

tracted a lot of interest in the field of light-matter interactions in recent years (Becker et al., 2005; Taylor et al., 2007). The majority of theoretical studies on NSDI are delivered in the framework of the dipole approximation, particularly the studies involving the commonly used near-infrared laser fields and intensities (Milosevic et al., 2006).

As discussed in section 5.3, when the dipole approximation is applied the vector potential $\mathbf{A}$ of the laser field no longer depends on space. Therefore, magnetic field effects are automatically neglected, since the magnetic field component of the laser field $\mathbf{B} = \nabla \times \mathbf{A}(t)$ is zero. However, in the general case where $\mathbf{A}(\mathbf{r}, t)$ depends both on space and time, an electron experiences a Lorentz force whose magnetic field component $\mathbf{F}_B$ increases with increasing electron velocity, since $\mathbf{F}_B = \mathbf{v} \times \mathbf{B}$. Due to scattering and recollision processes in the presence of strong laser fields, high velocity electrons are readily produced. Therefore it is important to account for magnetic field effects as the magnitude of electron velocity increases.

Criteria for the onset of magnetic field effects both in the relativistic and the non-relativistic limit have already been formulated (Reiss, 2008, 2014), as discussed in sec. 5.3. In the non-relativistic limit, where this work focuses, magnetic field effects are expected to arise when the amplitude of the electron motion, β_0, due to the magnetic field component of the Lorentz force becomes 1 a.u. (see equation 5.21).

Studies addressing magnetic field effects include work by Palaniyappan et al. (2005), who used a 3D semiclassical rescattering model that accounts for $\mathbf{F}_B$ to successfully describe the observed ionisation of Ne^{n+} ($n \leq 8$) in ultra-strong fields. Moreover, non-dipole effects were addressed in theoretical studies of; stabilisation (Keitel and Knight, 1995); high-order harmonic generation by neglecting the Coulomb potential (Chirilă et al., 2002) with a first order expansion of the vector potential (Walser et al., 2000); and by using a Monte-Carlo simulation (Emelin and Ryabikin, 2014). In recent studies of single ionisation (SI), the electron momentum distribution along the propagation direction of the laser field was computed using different quantum mechanical approaches (Chelkowski et al., 2014, 2015; Titi and

Drake, 2012; Ivanov, 2015). For example, for H interacting with a 3400 nm laser field at intensities ranging from 0.5 $\times 10^{14}$ W cm^{-2} to 1$\times 10^{14}$ W cm^{-2} the average momentum along the propagation direction of the laser field was found to increase from 0.003 a.u. to 0.006 a.u. as the intensity increases (Chelkowski et al., 2015). Thus, for single ionisation, the average momentum along the propagation direction of the laser field increases with increasing β_0, given $\beta_0 \approx I/(8\omega^3 c)$ (Chelkowski et al., 2015; Smeenk et al., 2011). If magnetic field effects are not accounted for, then this momentum component averages to zero. The motivation for these theoretical studies was a recent experimental measurement of the average momentum in the propagation direction of the laser field (Smeenk et al., 2011).

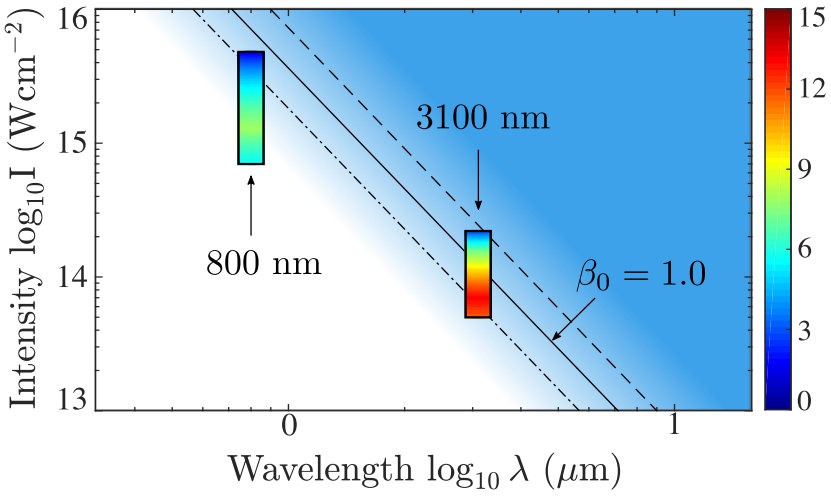

Figure 6.1 | Range of validity of the dipole approximation and momentum in double ionisation. The white area indicates the range of intensities and wavelengths where the dipole approximation is valid. $\beta_0 = 0.5$ a.u. (dot-dash line), $\beta_0 = 1$ a.u. (solid line) and $\beta_0 = 2$ a.u. (dash line). The arrows mark the 800 nm and the 3100 nm wavelengths driving He and Xe, respectively. At these wavelengths, for a range of intensities, the colour bars indicate the ratio of the average sum of the electron momenta along the direction of $\mathbf{F}_B$ for double ionisation with twice the respective electron momentum for single ionisation $\langle p_y^1 + p_y^2 \rangle_{\mathrm{DI}} / (2 \langle p_y \rangle_{\mathrm{SI}})$.

The work presented in this chapter reveals another aspect of non-sequential double ionisation (NSDI) which has not been previously addressed. The strong electron-electron correlation in NSDI is identified as a probe of magnetic field effects both for near-infrared and mid-infrared intense laser fields. Specifically, the intensities considered are around 10^{15} W cm^{-2} for He at 800 nm and around 10^{14}

W cm^{-2} for Xe at 3100 nm where the rescattering mechanism underlies double ionisation (Corkum, 1993). For these intensities, it is found that the average sum of the two electron momenta along the propagation direction of the laser field is unexpectedly large. It is roughly an order of magnitude larger than twice the average of the respective electron momentum for single ionisation. This average sum of the momenta for double ionisation (DI) is shown to be maximum at intensities smaller than the intensities satisfying the criterion for the onset of magnetic field effects $\beta_0 \approx 1$ a.u. (Reiss, 2008, 2014). This is illustrated in Fig. 6.1 for He driven by a near-infrared (800 nm) laser field and for Xe driven by a mid-infrared (3100 nm) laser field. The motivation for choosing near-infrared laser fields is that they are very common in strong field studies. Mid-infrared laser-fields are chosen because magnetic field effects set in for small intensities, see Fig. 6.1, attracting a lot of interest in recent years (Ludwig et al., 2014; Wolter et al., 2015).

6.2 Method

In this chapter a semiclassical trajectory model is used, referred to as the 3D-SMND (3-Dimensional Semiclassical Monte-Carlo including Non-Dipole effects) model, based on the theory presented in chapter 5. This is similar to the 3D-SMD (3-Dimensional Semiclassical Monte-Carlo Dipole approximation) model used by Emmanouilidou (2008), Emmanouilidou et al. (2011) and Chen et al. (2017) except that non-dipole effects are now included. One further addition to the 3D-SMND model is that the field can have arbitrary polarisation. However, this feature is not used for the current work. The former 3D-SMD model was used previously to identify the mechanism responsible for the finger-like structure observed in the 2D correlated momentum distributions parallel to the polarisation axis (Emmanouilidou, 2008), which was predicted theoretically (Parker et al., 2006) and observed experimentally for He driven by 800 nm laser fields (Staudte et al., 2007; Rudenko et al., 2007). It was also used to investigate direct versus delayed pathways of NSDI for He driven by a 400 nm laser field while achieving excellent agreement with fully *ab initio* quantum mechanical calculations (Emmanouilidou et al., 2011). And most

recently, the 3D-SMD model was used to identify the underlying mechanisms for the carrier-envelope phase effects observed experimentally in NSDI of Ar driven by an 800 nm laser field at a range of intensities (Kübel et al., 2016; Chen et al., 2017).

The following Hamiltonian is used,

$$H(\mathbf{q}_i, \mathbf{p}_i, t) = \frac{(\mathbf{p}_1 + \mathbf{A}_1)^2}{2} + \frac{(\mathbf{p}_2 + \mathbf{A}_2)^2}{2} - c_1 \frac{Z}{|\mathbf{q}_1|} - c_2 \frac{Z}{|\mathbf{q}_2|} + \frac{c_3}{|\mathbf{q}_1 - \mathbf{q}_2|}. \quad (6.1)$$

This Hamiltonian is similar to Eq. 5.32 however, three parameters c_1, c_2 and c_3 have been introduced. These parameters can be set to one (zero) and they are used to selectively turn on (off) the Coulomb interaction between the parent nucleus and electrons 1 and 2 or the electron-electron interaction respectively. For example, to neglect only the electron-electron interaction the parameters would be $c_1 = c_2 = 1$ and $c_3 = 0$.

The vector potential experienced by electron i, $\mathbf{A}_i \equiv \mathbf{A}(\mathbf{q}_i, t)$, has the same form as that given by Eq. 5.25 for a linearly-polarised laser field propagating in the y-direction. The fact that the spatial dependence of the laser field is included allows the model to fully account for non-dipole effects during the time propagation. Following equations 5.14 and 5.15 **E** and **B** are along the x- and z-axis, respectively. Unless otherwise stated, all Coulomb forces as well as the electric and the magnetic field are fully accounted for during time propagation.

The initial state in the 3D-SMND model is taken to be the same as in the 3D-SMD model (Emmanouilidou, 2008) as discussed earlier in sec. 5.2. However this approach ignores the effect of the magnetic field on the initial conditions for the tunnelling electron because equations 5.1, 5.6 and 5.7 have been derived in the dipole approximation. Yakaboylu et al. (2013) showed that if non-dipole effects were accounted for in the ADK rate (Ammosov–Delone–Krainov rate, see section 5.2.2) then the most probable transverse velocity, along the laser's propagation direction, ranges from 0.33 I_p/c to almost zero with increasing barrier suppression ratio E_0/E_a, where $E_a = (2I_p)^{3/2}$ and I_p is the ionisation energy of the tunnelling electron. This is shown in Fig. 6.2.

In this work, the smallest intensities considered are 5×10^{13} W cm^{-2} for Xe and

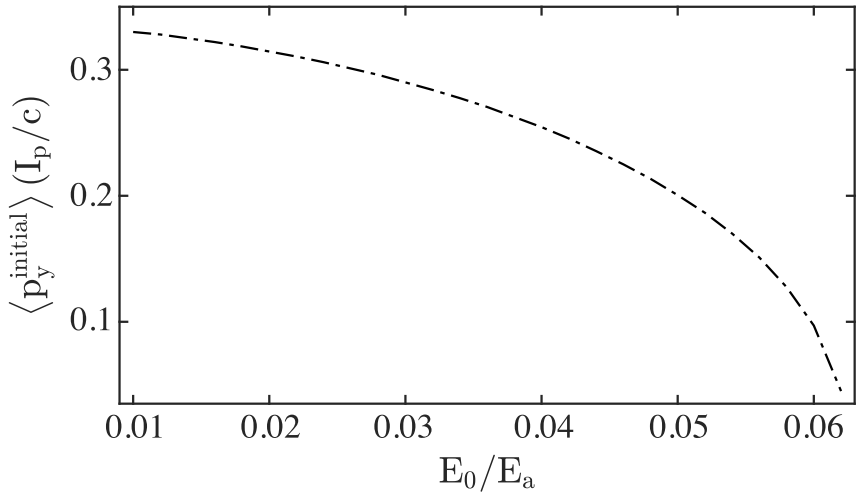

Figure 6.2 | Average y-component of the initial transverse momentum in the direction of laser propagation $\langle p_y^{\text{initial}} \rangle$ as a function of the barrier suppression ratio E_0/E_a.

7×10^{14} W cm^{-2} for He. At these intensities, if non-dipole effects are accounted for in the ADK rate, the transverse velocity of the tunnelling electron is centred around 0.17 I_p^{Xe}/c for Xe which is 5.5×10^{-4} a.u. (I_p^{Xe} =0.446 a.u.) and 0.12 I_p^{He}/c for He which is 7.9×10^{-4} a.u. (I_p^{He} =0.904 a.u.). These values are significantly smaller than the values of the average momenta along the propagation direction of the laser field, which are presented in what follows. Thus, using the non-relativistic ADK rate is a good approximation for the quantities addressed in this work. In what follows, the tunnelling and bound electron are denoted as electrons 1 and 2, respectively.

6.3 Results

6.3.1 Momentum Offset for SI of Xe and H

The accuracy of the 3D-SMND model is established by computing the momentum distribution along the propagation direction of the laser field, p_y, for single ionisation (SI) and by comparing it with available experimental and theoretical results. Ludwig et al. (2014) showed that the peak of the p_y distribution was observed to shift in the direction opposite to the magnetic field component of the Lorentz force, $\mathbf{F}_B$, for intensities of the order of 10^{13} W cm^{-2}. This shift, p_y^{offset}, was attributed to the combined effect of the magnetic field and the Coulomb attraction of the nu-

cleus (Ludwig et al., 2014). To compare with these experimental results, the shift of the peak of the y-momentum distribution is computed for Xe interacting with a 3400 nm and a 44 fs FWHM laser field as the intensity increases from 3-6$\times 10^{13}$ W cm^{-2}. In Fig. 6.3 the shift of the peak of the p_y distribution is found to vary from -0.0055 a.u. to -0.012 a.u. These results are in agreement with the simulations and experimental results obtained by Ludwig et al. (2014).

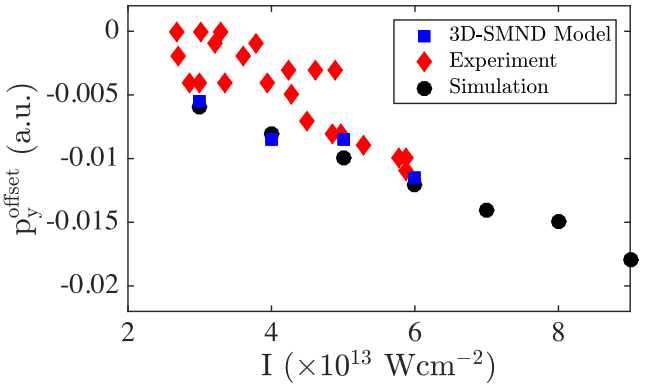

Figure 6.3 | The peak of the momentum distribution, in the direction of laser propagation p_y^{offset} is given for Xe in a 3400 nm, 44 fs FWHM laser field. The experimental (red diamond) and theoretical results (black circle) of Ludwig et al. (2014) plotted alongside the results of the 3D-SMND model (blue square) described in this work.

Moreover, to compare with the results of Chelkowski et al. (2015), the average of the momentum $\langle p_y \rangle_{\text{SI}}$ is computed for H driven by a 3400 nm and a 16 fs FWHM laser field for intensities 0.5-1$\times 10^{14}$ W cm^{-2}. Using the 3D-SMND model, $\langle p_y \rangle_{\text{SI}}$ is found to vary from 0.0022 a.u. to 0.0046 a.u. (see Fig. 6.4(a)). These values differ by 27% from the results obtained by Chelkowski et al. (2015) and are thus in reasonable agreement. The difference may be due to non-dipole effects not accounted for in the ADK rate in the 3D-SMND model. In addition, the quantum calculation used by Chelkowski et al. (2015) employs a 2D soft-core potential while a full 3D potential is employed by the 3D-SMND model. The peak momentum offset, p_y^{offset}, was also computed, as shown in Fig. 6.4(b). The momentum offset obtained by the 3D-SMND model is roughly half that of the 2D quantum calculation. Both models experience the same trend of increasingly negative momentum offsets, similar to the results obtained by Ludwig et al. (2014). The single ionisation results obtained in this work were computed with at least 4$\times 10^5$ events and therefore the statistical

error introduced is very small.

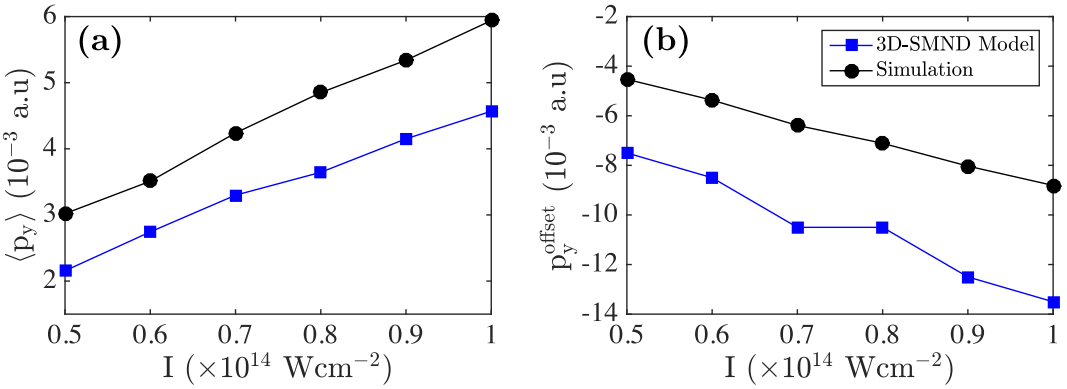

Figure 6.4 | (a) The average $\langle p_y \rangle$ and (b) the peak p_y^{offset} of the momentum distribution in the direction of laser propagation is calculated. Model parameters are for H in a 3400 nm, 16 fs FWHM laser field. The 2D quantum results (black circle) of (Chelkowski et al., 2015) are plotted against the 3D-SMND model (blue square) described in this work.

6.3.2 Average Momentum for SI of He and Xe

The 3D-SMND model is now employed to compute $\langle p_y \rangle_{\text{SI}}$ for He driven by an 800 nm, 12 fs FWHM laser field and for Xe driven by a 3100 nm, 44 fs FWHM laser field; the two laser fields have roughly the same number of cycles. First an analytic expression is obtained relating $\langle p_y \rangle_{\text{SI}}$ with the average electron kinetic energy $\langle E_k \rangle_{\text{SI}}$ (Smeenk et al., 2011; Chelkowski et al., 2014). When an electron interacts with an electromagnetic field with all the Coulomb forces switched-off, i.e., $c_1 = c_2 = c_3 = 0$ in Eq. 6.1, the Lorentz force is given by,

$$\dot{\mathbf{p}} = -(\mathbf{E} + \mathbf{v} \times \mathbf{B}). \tag{6.2}$$

To first order in $1/c$ this can be written,

$$\dot{p}_x = -E_x \qquad \text{and} \qquad \dot{p}_y = v_x B_z. \tag{6.3}$$

For an electron (in atomic units) $v_x = p_x$ and inspecting equations 5.26 and 5.27 gives $B_z = -E_x/c$. Therefore,

$$p_y = \int \dot{p}_y \, dt, \tag{6.4}$$

$$p_y = \frac{1}{c} \int p_x \dot{p}_x \, dt, \tag{6.5}$$

$$p_y = \frac{p_x^2}{2c}. \tag{6.6}$$

So now, the change in y-momentum is given by,

$$p_y - p_{y,0} = \frac{p_x^2}{2c} - \frac{p_{x,0}^2}{2c}, \tag{6.7}$$

where p_y is the final momentum and $p_{y,0}$ is the initial. Recall that the ADK tunnelling rate assumes that the initial momentum in the direction of polarisation, which in this case is the x-direction, is equal to zero. Hence,

$$p_y = p_{y,0} + p_x^2/2c \tag{6.8}$$

Taking the average gives,

$$\langle p_y \rangle = \langle p_{y,0} \rangle + \frac{1}{2c} \langle p_x^2 \rangle . \tag{6.9}$$

As discussed in section 6.2, the initial momentum in the direction of propagation of the laser field is in general non-zero. In fact it was shown to be $\langle p_{y,0} \rangle \approx 0.33 \; I_p/c$ for small intensities diminishing towards zero for larger intensities (see Fig. 6.2). For the parameters used in this section the initial momentum is typically of the order 10^{-4} a.u. and so to a good approximation this can be neglected.

$$\langle p_y \rangle = \frac{1}{2c} \langle p_x^2 \rangle \approx \frac{1}{c} \langle E_k \rangle . \tag{6.10}$$

Comparing $\langle p_y \rangle$ and $\langle E_k/c \rangle$ from table 6.1, for the simplified model ($c_{1,2,3}$=0) it is found that the above relation holds i.e., $\langle p_y \rangle = \langle E_k/c \rangle$.

Table 6.1 | Single ionisation results for Xe and He.

		SI Z=2		SI		SI Z=2	
		$c_{1,2,3}$=1		$c_{1,2,3}$=0		c_1=0,$c_{2,3}$=1	
I ($\times 10^{15}$ W cm^{-2})		$\langle p_y \rangle^a$	$\langle E_k/c \rangle^a$	$\langle p_y \rangle^a$	$\langle E_k/c \rangle^a$	$\langle p_y \rangle^a$	$\langle E_k/c \rangle^a$
	0.7	3.5	2.3	1.5	1.5	1.8	2.2
He	1.3	6.0	4.4	3.4	3.4	3.4	4.4
	4.8	28	32	19	19	19	21
	0.05	3.2	1.6	1.3	1.3	1.8	1.6
Xe	0.07	3.5	2.5	2.1	2.1	2.4	2.4
	0.22	11	12	9.9	9.9	9.1	11

[a] Average momentum and kinetic energy given in $\times 10^{-3}$ a.u.

Next, $\langle p_y \rangle_{\text{SI}}$ and $\langle E_k \rangle_{\text{SI}}$ are computed with the 3D-SMND model fully accounting for all Coulomb forces and the presence of the initially bound electron in driven He and Xe, i.e., $c_1 = c_2 = c_3 = 1$ with $Z = 2$. The tunnelling electron is the one that is mostly singly ionising. Figure 6.5(a) shows that, for He, $\langle p_y \rangle_{\text{SI}}$ varies from 0.0035 a.u. to 0.028 a.u. at intensities 0.7-4.8$\times 10^{15}$ W cm^{-2}. For Xe (Fig. 6.5(b)), $\langle p_y \rangle_{\text{SI}}$ varies from 0.0032 a.u. to 0.011 a.u. at intensities 0.5-2.2$\times 10^{14}$ W cm^{-2}.

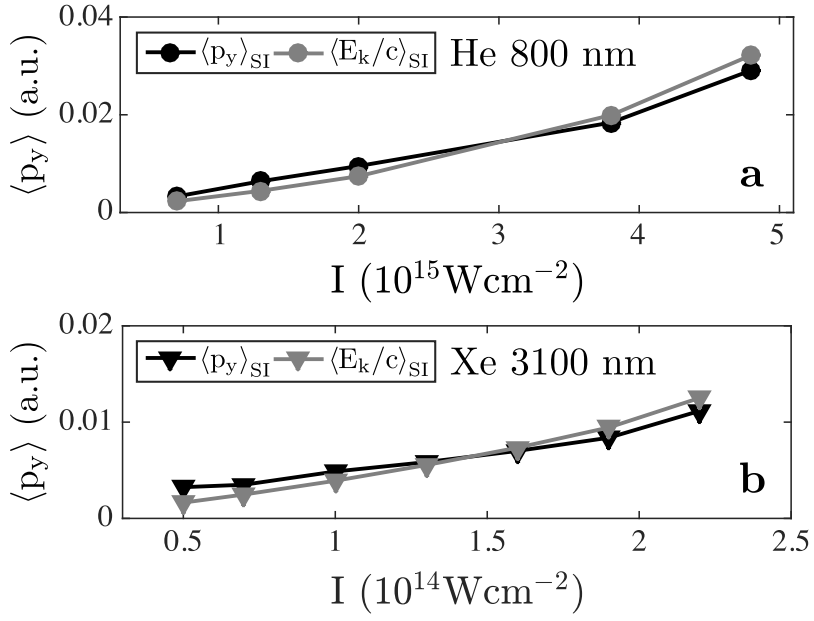

Figure 6.5 | $\langle p_y \rangle_{\text{SI}}$ and $\langle E_k \rangle_{\text{SI}}/c$ are plotted as a function of intensity in (a) for He driven by an 800 nm laser field and in (b) for Xe driven by a 3100 nm laser field.

In Table 6.1, it is shown that $\langle p_y \rangle_{\text{SI}}$ and $\langle E_k \rangle_{\text{SI}} / c$, when obtained with the full model, do not differ by more than a factor of 3 from the values obtained when all Coulomb forces are switched-off. Thus, the simple model yields the correct order of magnitude for $\langle p_y \rangle_{\text{SI}}$. It is also shown in Table 6.1, that with all Coulomb forces accounted for, $\langle p_y \rangle_{\text{SI}}$ is no longer equal to $\langle E_k \rangle_{\text{SI}} / c$ both for driven He and for driven Xe. For the full model, $\langle E_k \rangle_{\text{SI}}$ is no longer just the drift kinetic energy, mainly due to the interaction of the tunnelling electron with the nucleus. Indeed, using the 3D-SMND model with this interaction switched off, i.e., $c_1 = 0$ and $c_2 = c_3 = 1$, $\langle p_y \rangle_{\text{SI}}$ is roughly equal to $\langle E_k \rangle_{\text{SI}} / c$, see Table 6.1. $\langle p_y \rangle_{\text{SI}}$ is also shown in Table 6.1 to be more sensitive than $\langle E_k \rangle_{\text{SI}}$ to the interaction of the tunnelling electron with the nucleus. Summarising the results for single ionisation, propagating classical trajectories with initial times determined by the ADK rate and all Coulomb forces switched-off yields the correct order of magnitude for $\langle p_y \rangle_{\text{SI}}$.

6.3.3 Average Momentum for DI of He and Xe

For double ionisation, the average of the sum of the electron momenta along the propagation direction of the laser field, $\langle p_y^1 + p_y^2 \rangle_{\text{DI}}$, is computed for He driven by an 800 nm laser field and for Xe driven by a 3100 nm laser field. Henceforth, superscripts e.g., the i in p_y^i and E_k^i, are used to indicate electron 1 or 2 – as opposed to an exponent. The parameters of the laser fields are the same as the ones employed in the single ionisation section for He and Xe. The double ionisation results obtained in this work were computed with at least $2{\times}10^5$ events and therefore the statistical error introduced is very small.

The results are plotted in Fig. 6.6(a) for He at intensities 0.7-4.8$\times 10^{15}$ W cm^{-2} and in Fig. 6.6(b) for Xe at intensities 0.5-2.2$\times 10^{14}$ W cm^{-2}. The values obtained for $\langle p_y^1 + p_y^2 \rangle_{\text{DI}}$ are quite unexpected. Specifically, $\langle p_y^1 + p_y^2 \rangle_{\text{DI}}$ is found to be roughly an order of magnitude larger than twice $\langle p_y \rangle_{\text{SI}}$, with $\langle p_y \rangle_{\text{SI}}$ computed in the previous section. For comparison, both $\langle p_y^1 + p_y^2 \rangle_{\text{DI}}$ and $2\langle p_y \rangle_{\text{SI}}$ are displayed in Fig. 6.6. It is shown that $\langle p_y^1 + p_y^2 \rangle_{\text{DI}} \approx 8 \times 2 \langle p_y \rangle_{\text{SI}}$ for He at $1.3{\times}10^{15}$ W cm^{-2}, while $\langle p_y^1 + p_y^2 \rangle_{\text{DI}} \approx 13 \times 2 \langle p_y \rangle_{\text{SI}}$ for Xe at $7{\times}10^{13}$ W cm^{-2}. For $1.3{\times}10^{15}$ W cm^{-2} and 800 nm $\beta_0 = 0.18$ a.u., while for $7{\times}10^{13}$ W cm^{-2} and 3100 nm $\beta_0 = 0.58$

a.u. Thus, $\left\langle p_y^1 + p_y^2 \right\rangle_{\mathrm{DI}} / 2 \left\langle p_y \right\rangle_{\mathrm{SI}}$ is found to be maximum at intensities considerably smaller than the intensities corresponding to $\beta_0 \approx 1$ a.u., i.e., the criterion for the onset of magnetic field effects (Reiss, 2008, 2014). This is shown in Fig. 6.1.

Moreover, unlike $\left\langle p_y \right\rangle_{\mathrm{SI}}$ which increases with increasing intensity as expected (Chelkowski et al., 2015), $\left\langle p_y^1 + p_y^2 \right\rangle_{\mathrm{DI}}$ after reaching a maximum decreases with increasing intensity for the range of intensities currently considered (Fig. 6.6(a,b)). The mechanism behind this unexpected behaviour will be explored in the following section.

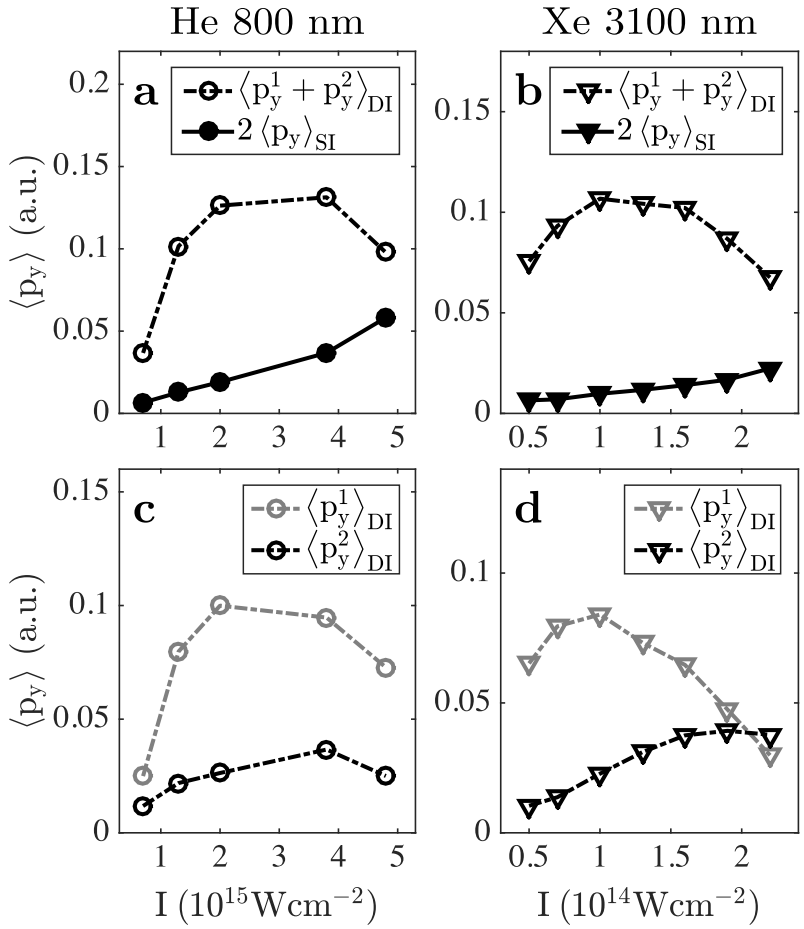

Figure 6.6 | $\left\langle p_y^1 + p_y^2 \right\rangle_{\mathrm{DI}}$ and $2\langle p_y \rangle_{\mathrm{SI}}$ are plotted as a function of intensity in (a) for He driven by an 800 nm laser field and in (b) for Xe driven by a 3100 nm laser field. $\left\langle p_y^1 \right\rangle_{\mathrm{DI}}$ and $\left\langle p_y^2 \right\rangle_{\mathrm{DI}}$ are plotted as a function of intensity in (c) for He driven by an 800 nm laser field and in (d) for Xe driven by a 3100 nm laser field.

6.3.4 Recollision Probing Magnetic Field Effects

The average electron momentum along the propagation direction is non-zero when the magnetic field component of the Lorentz force $\mathbf{F}_B$ is accounted for. This force increases with increasing intensity, increasing strength of the magnetic field, and with increasing velocity along the direction of the electric field. $\left\langle p_y^1 + p_y^2 \right\rangle_{\text{DI}} / 2 \left\langle p_y \right\rangle_{\text{SI}}$ is found to be maximum at 1.3×10^{15} W cm^{-2} for 800 nm and at 7×10^{13} W cm^{-2} for 3100 nm, intensities where the strength of the magnetic field is not large. It then follows that it must be the velocities of the two escaping electrons that are large at these intensities. Large electron velocities at intermediate intensities are a result of strong electron-electron correlation, i.e., of the rescattering mechanism (Corkum, 1993). In the rescattering scenario after electron 1 tunnels in the field-lowered Coulomb potential it accelerates in the strong laser field and can return to the core and undergo a collision with the remaining electron (Corkum, 1993).

In the following, evidence is provided that the large values of the momentum ratio $\left\langle p_y^1 + p_y^2 \right\rangle_{\text{DI}} / 2 \left\langle p_y \right\rangle_{\text{SI}}$ are due to recollisions. Specifically, it is shown that recollisions are strong resulting in overall large kinetic energies compared to the ponderomotive energy U_p, which is given by Eq. 5.18, roughly at the intensities where $\left\langle p_y^1 + p_y^2 \right\rangle_{\text{DI}} / 2 \left\langle p_y \right\rangle_{\text{SI}}$ is maximum. It is also shown that recollisions are soft resulting in overall smaller kinetic energies compared to the ponderomotive energy U_p at higher intensities where $\left\langle p_y^1 + p_y^2 \right\rangle_{\text{DI}} / 2 \left\langle p_y \right\rangle_{\text{SI}}$ is found to be smaller.

This transition from strong to soft recollisions is demonstrated in the context of He driven by an 800 nm laser field at intensities 0.7×10^{15} W cm^{-2}, 2.0×10^{15} W cm^{-2} and 3.8×10^{15} W cm^{-2}. To do so, an analysis of the doubly ionising events is performed. It is noted that a similar analysis was found to hold for Xe (not shown) where strong recollisions prevail at intensities 0.7×10^{14} W cm^{-2} and 1.0×10^{14} W cm^{-2} while soft ones prevail at 2.2×10^{14} W cm^{-2}. Focusing on He, in Fig. 6.7, the distribution of the tunnelling and recollision times is plotted. For the intensities 0.7×10^{15} W cm^{-2}, 2.0×10^{15} W cm^{-2} and 3.8×10^{15} W cm^{-2} considered in Fig. 6.7 the ponderomotive energy U_p is equal to 1.54 a.u., 4.39 a.u. and 8.35

a.u., respectively. Thus, the maximum recollision energies 3.17 U_p (Corkum, 1993) are well above the second ionisation energy of He, which is 2 a.u. As expected, for the smaller intensities (Fig. 6.7(a1,b1)), electron 1 tunnel-ionises at times around the extrema of the laser field. For 3.8×10^{15} W cm^{-2} (Fig. 6.7(c1)) the electric field is sufficiently strong so that electron 1 can tunnel-ionise at times other than the extrema of the field.

The recollision time is identified for each double ionising trajectory as the time that the electron-electron potential energy, $V_{ee} = 1/|\mathbf{r}_1 - \mathbf{r}_2|$, as a function of time is maximum. For the smaller intensities the recollision times are centred roughly around $\pm 2nT/3$, with n an integer and T the period of the laser field, as expected from the rescattering model (Corkum, 1993) (Fig. 6.7(a2,b2)). At 3.8×10^{15} W cm^{-2} the recollision times shift and are centred around the extrema of the laser field (Fig. 6.7(c2)). This shift of the recollision times signals a transition from strong to soft recollisions (Emmanouilidou and Staudte, 2009).

This transition from strong to soft recollisions is further corroborated by the average kinetic energy of each electron, $\left\langle E_k^{1,2}\right\rangle$, plotted in Fig. 6.7 as a function of time – zero time is set equal to the recollision time of each double ionising trajectory. For smaller intensities, $\left\langle E_k^{1,2}\right\rangle$ changes sharply at the recollision time (Fig. 6.7(a3,b3)). The change in $\left\langle E_k^{1,2}\right\rangle$ compared to the ponderomotive energy, U_p, is much smaller at 3.8×10^{15} W cm^{-2} (Fig. 6.7(c3)). The above results show that for the smaller intensities electron 1 tunnel-ionises around the extrema of the field. It then returns to the core, roughly when the electric field is small, with large velocity and undergoes a recollision with electron 2 transferring a large amount of energy (strong recollision). The strong recollisions result in higher asymptotic (in time) kinetic energies of the electrons compared to U_p. The ratios $\left\langle E_{k,x}^1\right\rangle/U_p$ and $\left\langle E_{k,x}^2\right\rangle/U_p$, where $\left\langle E_{k,x}^{1,2}\right\rangle$ are the asymptotic (in time) average kinetic energies of electrons 1 and 2 along the polarisation direction of the laser field, are 117% and 104% for an intensity of 0.7×10^{15} W cm^{-2} and 50% and 77% for an intensity of 2.0×10^{15} W cm^{-2}.

The velocities of both electrons, along the direction of the electric field, are

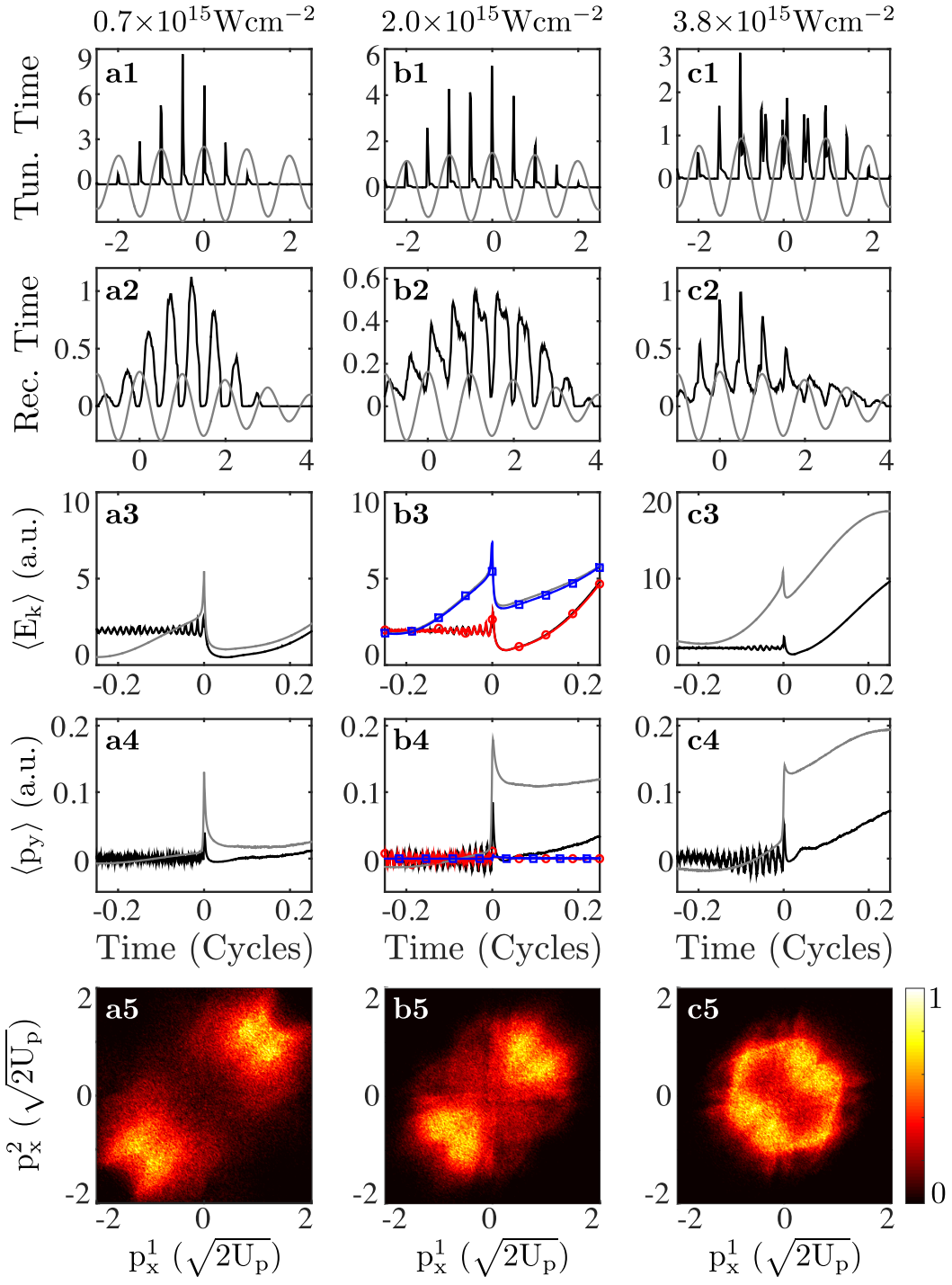

Figure 6.7 | Recollision underlying double ionisation of He driven at 800 nm. The intensities considered are (a) 0.7×10^{15} W cm^{-2}, (b) 2.0×10^{15} W cm^{-2} and (c) 3.8×10^{15} W cm^{-2}. The distribution of tunnelling times (black line) are plotted in row 1. The distribution of recollision times (black line) are plotted in row 2. The electric field is denoted as a grey line in the plots of the tunnelling and recollision times. $\langle E_k^1 \rangle$ (grey line) and $\langle E_k^2 \rangle$ (black line) are plotted as a function of time in row 3 with time zero set equal to the recollision time of each double ionising event. For 2.0×10^{15} W cm^{-2}, $\langle E_k^1 \rangle$ (blue line) and $\langle E_k^2 \rangle$ (red line) are also plotted in the absence of the magnetic field. $\langle p_y^1 \rangle$ (grey line) and $\langle p_y^2 \rangle$ (black line) are plotted as a function of time in row 4 with time zero set equal to the recollision time of each double ionising event. For 2.0×10^{15} W cm^{-2}, $\langle p_y^1 \rangle$ (blue line) and $\langle p_2^2 \rangle$ (red line) are also plotted in the absence of the magnetic field. Correlated momenta along the direction of the electric field are plotted in row 5.

determined mainly by the vector potential at the recollision time. Thus, both electrons escape mainly either parallel or antiparallel to the electric field. Indeed, this is the pattern seen in the plots of the correlated momenta along the direction of the electric field in Fig. 6.7(a5,b5) where the highest density is in the first and third quadrants. The correlated momenta are plotted in units of $\sqrt{2U_p}$. These patterns of the correlated momenta are consistent with direct double ionisation, that is, with both electrons ionising shortly after recollision takes place (Feuerstein et al., 2001).

Indeed, analysing the double ionising events it is found that for He at 0.7×10^{15} W cm^{-2} direct double ionisation contributes 70%. Delayed double ionisation events contribute 30%. In delayed double ionisation, also known as recollision-induced excitation with subsequent field ionisation (RESI) (Kopold et al., 2000; Feuerstein et al., 2001), one electron ionises soon after recollision takes place, while the other electron ionises with a delay (Emmanouilidou et al., 2011).

In contrast, at the higher intensity of 3.8×10^{15} W cm^{-2}, electron 1 tunnel-ionises after the extrema of the laser field. It then follows a short trajectory and returns to the core when the electric field is maximum with small velocity. Electron 1 transfers a small amount of energy to electron 2 (soft recollision). Indeed, the ratios $\left\langle E^1_{k,x}\right\rangle/U_p$ and $\left\langle E^2_{k,x}\right\rangle/U_p$ are 35% and 52% for an intensity of 3.8×10^{15} W cm^{-2} and are smaller than the respective ratios for the smaller intensities.

The velocities of electron 1 and 2 along the direction of the electric field are determined mostly by the values of the vector potential at the tunnelling and recollision times, respectively. As a result, the two electrons can escape in opposite directions to each other, along the direction of the electric field. This pattern is indeed observed for the plots of the correlated momenta in Fig. 6.7(c5) with high density in the second and fourth quadrants. This antiparallel pattern was predicted in the context of strongly-driven N_2 with fixed nuclei (Emmanouilidou and Staudte, 2009). It was also seen in the case of Ar driven by intense ultra-short laser fields (Chen et al., 2017) in agreement with experiment (Kübel et al., 2016).

For single ionisation of He and Xe, it was shown that using the tunnelling times as the starting point, the 3D-SMND with all Coulomb forces switched-off

i.e., $c_1 = c_2 = c_3 = 0$, yields the correct order of magnitude for $\langle p_y^1 \rangle_{\text{SI}}$. For double ionisation of He and Xe, using the 3D-SMND model with all Coulomb forces switched-off and with initial conditions taken to be the recollision times and velocities, $\langle p_y^1 \rangle_{\text{DI}}$ and $\langle p_y^2 \rangle_{\text{DI}}$ are obtained and presented in Table 6.2. These values of $\langle p_y^1 \rangle_{\text{DI}}$ and $\langle p_y^2 \rangle_{\text{DI}}$ agree very well with the values obtained using the 3D-SMND model with all Coulomb forces accounted for, see Table 6.2. This agreement further supports that recollision is the main factor determining $\langle p_y^1 + p_y^2 \rangle_{\text{DI}}$.

Table 6.2 | Double ionisation results for Xe and He.

		NSDI[b] $c_{1,2,3}$=1, Z=2[b]				**NSDI**[b] $c_{1,2,3}$=0 $t_0 = t_{\text{rec}}, p_0^1 = p_{\text{rec}}^1, p_0^2 = p_{\text{rec}}^2$			
Intensity[a]		$\langle p_y^2 \rangle$	$\langle E_k^2/c \rangle$	$\langle p_y^1 \rangle$	$\langle E_k^1/c \rangle$	$\langle p_y^2 \rangle$	$\langle E_k^2/c \rangle$	$\langle p_y^1 \rangle$	$\langle E_k^1/c \rangle$
	0.7	12	14	25	16	13	15	25	16
He	1.3	22	22	80	21	24	24	82	20
	4.8	25	32	73	47	33	37	74	43
	0.05	10	11	65	9	11	11	67	8
Xe	0.07	14	13	80	10	15	14	81	9
	0.22	38	27	30	17	45	34	30	16

[a] Intensity given in $\times 10^{15}$ W cm^{-2}

[b] Average momentum and kinetic energy given in $\times 10^{-3}$ a.u.

Finally, the electron that contributes the most to the maximum value of $\langle p_y^1 + p_y^2 \rangle_{\text{DI}}$ is identified both for driven He and Xe. The average y-momenta for each electron, $\langle p_y^1 \rangle_{\text{DI}}$ and $\langle p_y^2 \rangle_{\text{DI}}$, are plotted as a function of time in Fig. 6.7, with time zero set equal to the recollision time of each double ionising trajectory. It is shown in Fig. 6.7(a4,b4,c4) that it is mainly $\langle p_y^1 \rangle_{\text{DI}}$ that changes significantly at the recollision time. This change is more pronounced for the smaller intensities (Fig. 6.7a4,b4). In Fig. 6.7(b4), at intensity 2.0×10^{15} W cm^{-2}, it is also illustrated that in the absence of the magnetic field both $\langle p_y^1 \rangle_{\text{DI}}$ and $\langle p_y^2 \rangle_{\text{DI}}$ tend to zero with time, as expected. In addition, in Fig. 6.6(c,d), for driven He and Xe, respectively, $\langle p_y^1 \rangle_{\text{DI}}$ and $\langle p_y^2 \rangle_{\text{DI}}$ are plotted as a function of intensity. It is seen that $\langle p_y^1 \rangle_{\text{DI}}$ and $\langle p_y^1 + p_y^2 \rangle_{\text{DI}}$ have maxima around the same intensities. At these intensities $\langle p_y^1 \rangle_{\text{DI}}$

is significantly larger than $\langle p_y^2 \rangle_{\rm DI}$. Moreover, it is shown in Fig. 6.6(c,d), that once $\langle p_y^1 \rangle_{\rm DI}$ reaches a maximum at 2×10^{15} W cm^{-2} for He and at 10^{14} W cm^{-2} for Xe it then decreases with increasing intensity, for the intensities considered. Thus the average momentum of the tunnelling electron, $\langle p_y^1 \rangle_{\rm DI}$, is the one most affected by strong recollisions.

6.4 Conclusion

In this chapter it was shown that the average sum of the electron momenta along the propagation direction of the laser field, $\langle p_y^1 + p_y^2 \rangle_{\rm DI}$, has large values at intensities where strong recollisions underlie double ionisation. This is an unexpected result. For He driven by a near-infrared laser field and for Xe driven by a mid-infrared laser field, the intensities where the average sum of the electron momenta along the propagation direction of the laser field is maximum are smaller than the intensities where magnetic field effects are predicted to be large. Thus, recollisions probe magnetic field effects at smaller intensities than expected. However, it can also be stated that a magnetic field probes strong recollisions through the measurement of the sum of the electron momenta along the propagation direction of the laser field.

In order to investigate magnetic field effects, only the y-component of momentum has been considered in this work. However, the Lorentz force for a linearly-polarised magnetic field in the z-direction has two components in the x and y-direction respectively. This means that the x-momentum should also be affected. Indeed it will be, however, due to the large electron velocities in the x-direction, caused by the electric field, these effects are not easily observed. That is, the motion due to the magnetic field is a factor of $c \approx 137$ smaller than the motion caused by the electric field. Another consideration is that, in the analysis presented in this chapter, the tunnelling and initially bound electron have been treated as distinguishable. However, in an experiment this separation is not possible and so, observables must be modified to reflect the indistinguishability of electrons. The average sum momentum in the y-direction is obviously unaffected by this statement, but, for example, the average tunnelling electron momentum in the y-direction $\langle p_y^1 \rangle_{\rm DI}$ is not

accessible to an experiment. This will be discussed in more detail in the following chapter.

This chapter has identified a novel phenomena that has not previously been addressed in the literature. However, the underlying mechanism has not been investigated. In the following chapter the mechanism behind this effect will be studied in greater detail. Owing to the semiclassical trajectory-based approach, it is possible to dig deeper into the results. By analysing the ensembles of trajectories that give rise to specific double ionisation observables, it is possible to develop an understanding of the mechanism and explain why magnetic field effects are more important than previously expected.

Chapter 7

Recollision Gating

This chapter is adapted from published work (Emmanouilidou, Meltzer, and Corkum, 2017).

In the previous chapter (chapter 6) magnetic field effects were investigated and found to be non-negligible under previously accepted criteria (Reiss, 2008, 2014). In this chapter the mechanism responsible for the larger-than-expected magnetic field effect is explored in greater detail.

7.1 Introduction

In this work, it will be shown that, for NSDI, the magnetic field in conjunction with the recollision acts as a gate. This gate selects a subset of the initial tunnelling-electron momenta along the propagation direction of the laser field. Only this subset of initial momenta lead to double ionisation. Phase-space is extremely sensitive to the initial conditions and hence the specific subset of initial momenta strongly influence the results obtained.

This recollision-gating mechanism is studied in the context of He when driven by an 800 nm laser field at intensities 1.3×10^{15} W cm^{-2}, 2×10^{15} W cm^{-2} and 3.8×10^{15} W cm^{-2}. This gating is particularly pronounced at the smaller intensities of 1.3×10^{15} W cm^{-2} and 2×10^{15} W cm^{-2} with $\beta_0 \approx U_p/(2\omega c) = 0.18$ a.u. and $\beta_0 = 0.28$ a.u., respectively. Therefore recollision-gating is important at intensities well below those that satisfy the criterion for the onset of magnetic field effects, i.e., $\beta_0 \approx$1 a.u. (Reiss, 2008, 2014).

The propagation direction of the laser field is the same as the direction of the $\mathbf{F}_B$ force (to first order) which, in the current formulation, is along the $+y$-axis. The tunnelling electron is the electron that initially tunnels in the field-lowered Coulomb potential. When non-dipole effects are fully accounted for during the propagation in time, it is shown that the y-component of the initial momentum of the tunnelling-electron is mostly negative for events leading to double ionisation. In the dipole approximation, the initial momentum of the tunnelling-electron that is transverse to the direction of the electric field is symmetric with respect to zero.

The term *non-dipole recollision-gated ionisation* is adopted to describe ionisation resulting from an asymmetric distribution of the transverse tunnelling-electron initial momentum due to the combined effect of the recollision and the magnetic field. Non-dipole recollision-gated ionisation is a general phenomenon. It is found that this mechanism underlies double electron escape in atoms driven by linearly and slightly-elliptically polarised laser fields.

Moreover, it is found that non-dipole recollision-gated ionisation results in an asymmetry in the following double ionisation observable. Let $\phi \in [0^\circ, 180^\circ]$ denote the angle of the final ($t \to \infty$) momentum of each escaping electron with respect to the propagation axis of the laser field. The observable in question is

$$P^{\mathrm{DI}}_{\mathrm{asym}}(\phi) = P^{\mathrm{DI}}(\phi) - P^{\mathrm{DI}}(180^\circ - \phi), \tag{7.1}$$

where $P^{\mathrm{DI}}(\phi)$ is the probability of either one of the two electrons to escape with an angle ϕ. $P^{\mathrm{DI}}(\phi)$ and $P^{\mathrm{DI}}_{\mathrm{asym}}(\phi)$ are accessible by kinematically complete experiments. In the dipole approximation, $P^{\mathrm{DI}}_{\mathrm{asym}}(\phi) = 0$. When non-dipole effects are accounted for, it is shown that $P^{\mathrm{DI}}_{\mathrm{asym}}(\phi) > 0$, for $\phi \in [0^\circ, 90^\circ]$. This is in accord with the effect of $\mathbf{F}_B$.

It is also found that $P^{\mathrm{DI}}_{\mathrm{asym}}(\phi)$ has consistently non-zero values over a wide interval of angles at lower intensities. This latter feature is an unexpected one. For the intensities considered the $\mathbf{F}_B$ force has small magnitude that increases with intensity. Thus, one would expect the distribution $P^{\mathrm{DI}}_{\mathrm{asym}}(\phi)$ to be very narrowly peaked around 90° with values increasing with intensity.

7.2 Method

In this work, ionisation in strongly-driven He is investigated using the same three-dimensional semiclassical model – the 3D-SMND model described in chapter 6 – that fully accounts for the magnetic field during time propagation. The Hamiltonian describing the interaction of the fixed nucleus two-electron atom with the laser field is given, as in chapter 6, by equation 6.1, and the vector potential, **A**, is given by equation 5.22. All Coulomb forces are accounted for by setting $c_1 = c_2 = c_3 = 1$.

The laser fields considered in the current work are either linearly polarised, $\chi = 0$, or have a small ellipticity of $\chi = 0.05$. For **A** given by equation 5.22, the electric, **E**, and magnetic, **B**, components of the laser field lie along the x- and z-axis, respectively, and for $\chi = 0.05$ there are small additional components along the z- and x-axis, respectively (see equations 5.23 and 5.24). The propagation direction of the laser field and the direction of $\mathbf{F}_B$ are mainly along the y-axis.

Unless otherwise stated, all Coulomb forces as well as the electric and the magnetic field are fully accounted for during time propagation. To switch-off a Coulomb interaction, the appropriate constant is set equal to zero. For example, to switch off the interaction of electron 1 with the nucleus, c_1 is set equal to zero. The initial state in the 3D-SMND model is setup in exactly the same way as the previous chapter (chapter 6) and again in this work, the tunnelling and bound electrons are denoted as electrons 1 and 2, respectively.

7.3 Results

The following results are obtained for He when driven by an 800 nm, 12 fs FWHM laser field that is; linearly polarised at intensities $1.3{\times}10^{15}$ W cm^{-2}, $2{\times}10^{15}$ W cm^{-2} and $3.8{\times}10^{15}$ W cm^{-2}; and slightly elliptically polarised with $\chi = 0.05$ at $2{\times}10^{15}$ W cm^{-2}. At these intensities the ponderomotive energies are $U_p = 2.86$ a.u., $U_p = 4.39$ a.u. and $U_p = 8.35$ a.u., respectively. Thus, the maximum energy of electron 1, which is approximately $E_k^1 \approx 3.17\ U_p$ (Krause et al., 1992), is above the energy needed to ionise He^+.

7.3.1 Asymmetry Due to the Magnetic Field

First, it is shown that the magnetic field causes an asymmetry in the double ionisation probability of electron i to ionise with an angle ϕ, which is denoted by $P_i^{\rm DI}(\phi)$ with $i = 1, 2$ for electrons 1 and 2. $P^{\rm SI}(\phi)$ is the corresponding probability in single ionisation. ϕ is the angle of the final momentum of electron i with respect to the propagation axis of the laser field, i.e.,

$$\cos\phi = \mathbf{p}^i \cdot \hat{\mathbf{y}}/|\mathbf{p}^i|. \tag{7.2}$$

The y-component of the electron momentum is parallel to the propagation direction of the laser field and to $\mathbf{F}_B$.

To highlight this asymmetry the angular distributions, $P_1^{\rm DI}(\phi)$, of the initially tunnel-ionised electron and, $P_2^{\rm DI}(\phi)$, of the initially bound electron are shown in Fig. 7.1(a) and (c), respectively, whilst $P^{\rm SI}(\phi)$ is shown in Fig. 7.1(e). These plots are at an intensity of $2{\times}10^{15}$ W cm^{-2} with the magnetic field switched-on and off. When the magnetic field is switched-on, the probability distributions are asymmetric with respect to $\phi = 90^\circ$. This asymmetry is due to the magnetic field. Indeed, when the magnetic field is switched-off all distributions are shown to be symmetric with respect to $\phi = 90^\circ$. The latter is expected, since there is no preferred direction of electron escape on the plane that is perpendicular to the x-axis (polarisation direction).

With the magnetic field switched-on the angular probability distributions are asymmetric i.e., $P_i^{\rm DI}(\phi) > P_i^{\rm DI}(180^\circ - \phi)$ and $P^{\rm SI}(\phi) > P^{\rm SI}(180^\circ - \phi)$ for $\phi \in [0^\circ, 90^\circ]$. Equivalently, the angular asymmetries are positive, $P_{i,\rm asym}^{\rm DI}(\phi) > 0$ and $P_{\rm asym}^{\rm SI}(\phi) > 0$ for $\phi \in [0^\circ, 90^\circ]$, where the asymmetry is defined more generally (compared to equation 7.1) as

$$P_{\rm asym}^{\alpha}(\phi) = P^{\alpha}(\phi) - P^{\alpha}(180^\circ - \phi), \tag{7.3}$$

where α can be single (SI) or double (DI) ionisation. This positive asymmetry is consistent with the gain of momentum due to the $\mathbf{F}_B$ force being along the $+y$-axis.

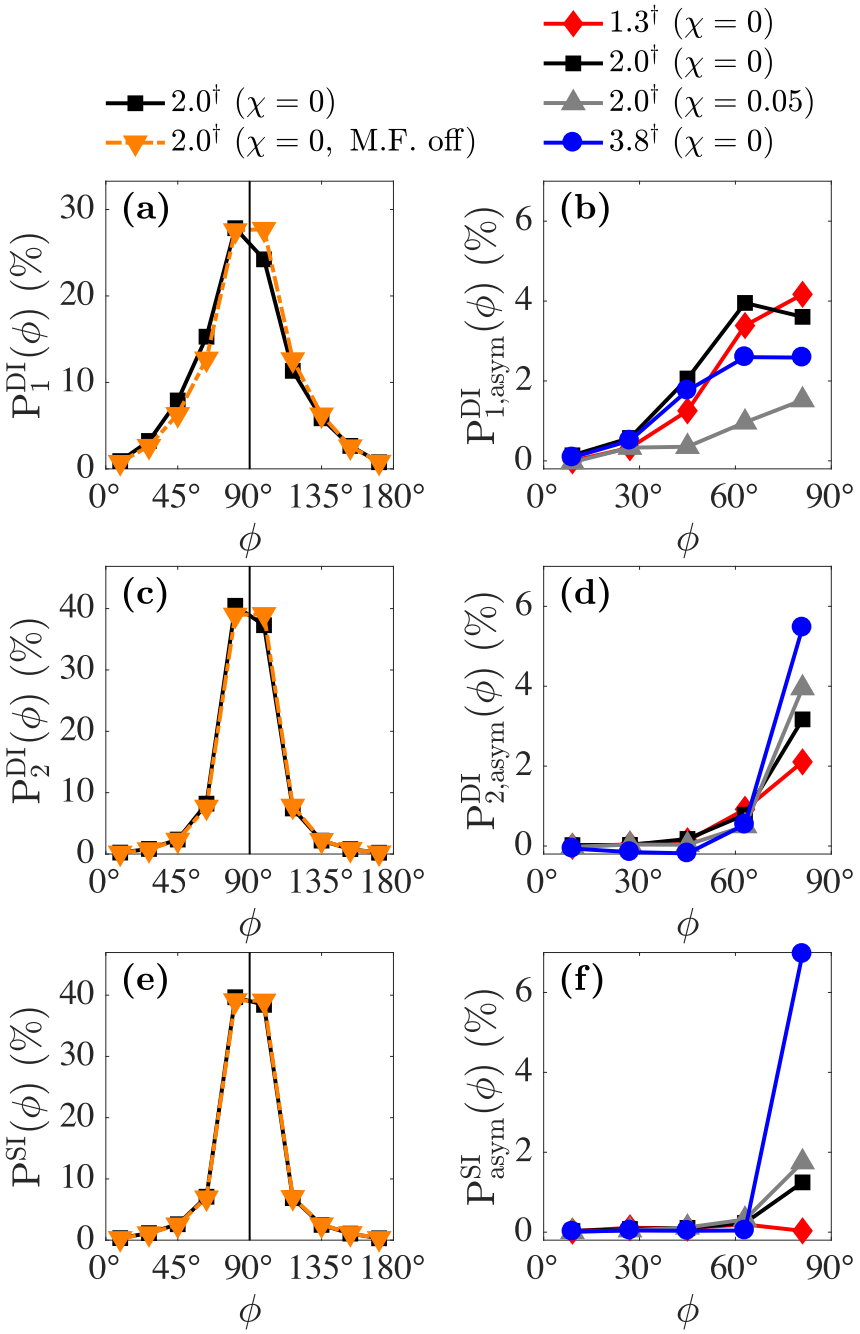

Figure 7.1 | Angular distributions of (a) the tunnelling electron, $P_1^{\mathrm{DI}}(\phi)$, (c) the initially bound electron, $P_2^{\mathrm{DI}}(\phi)$ and (e) the ionised electron, $P^{\mathrm{SI}}(\phi)$, from single ionisation events are plotted as a function of ϕ at 2 $\times 10^{15}$ W cm^{-2}, with the magnetic field switched-on and off. The asymmetries (b) $P_{1,\mathrm{asym}}^{\mathrm{DI}}(\phi)$ of the tunnelling electron, (d) $P_{2,\mathrm{asym}}^{\mathrm{DI}}(\phi)$ of the initially bound electron and (f) $P_{\mathrm{asym}}^{\mathrm{SI}}(\phi)$ in single ionisation are plotted as a function of ϕ at three intensities with $\chi = 0$ and at one intensity with $\chi = 0.05$. ϕ is binned in intervals of 18°. †Intensity in units of 10^{15} W cm^{-2}.

That is, an electron is more likely to ionise with a positive rather than a negative y-component of the final momentum.

The asymmetry with respect to $\phi = 90^\circ$ is better illustrated in Fig. 7.1, where $P^{\text{DI}}_{i,\text{asym}}(\phi)$ and $P^{\text{SI}}_{\text{asym}}(\phi)$ are plotted as a function of ϕ at $1.3{\times}10^{15}$ W cm^{-2}, $2{\times}10^{15}$ W cm^{-2} and $3.8{\times}10^{15}$ W cm^{-2} and at $2{\times}10^{15}$ W cm^{-2} with $\chi = 0.05$. Starting with single ionisation, $P^{\text{SI}}_{\text{asym}}(\phi)$ is almost zero at $1.3{\times}10^{15}$ W cm^{-2}. At the higher intensity of $3.8{\times}10^{15}$ W cm^{-2}, $P^{\text{SI}}_{\text{asym}}(\phi)$ is sharply centred around 90° reaching roughly 7%, see Fig. 7.1(f). These features of $P^{\text{SI}}(\phi)$ are in accord with the effect of the $\mathbf{F}_B$ force. $\mathbf{F}_B$ is small for the intensities considered. Therefore, $\mathbf{F}_B$ has an observable effect mostly when the y-component of the electron momentum is small as well, i.e., for an angle of escape $\phi = 90^\circ$. In addition, $|\mathbf{F}_B|$ is three times larger for the higher intensity compared to the smaller one. As a result $P^{\text{SI}}_{\text{asym}}(\phi)$ has larger values at higher intensities.

In double ionisation, the asymmetry of the initially bound electron, $P^{\text{DI}}_{2,\text{asym}}(\phi)$, is plotted in Fig. 7.1(d). It is shown that this asymmetry most closely resembles the corresponding asymmetry for single ionisation, $P^{\text{SI}}_{\text{asym}}(\phi)$, rather than $P^{\text{DI}}_{1,\text{asym}}(\phi)$ in Fig. 7.1(b). Indeed, $P^{\text{DI}}_{2,\text{asym}}(\phi)$ has larger values for higher intensities, as is the case for $P^{\text{SI}}_{\text{asym}}(\phi)$, reaching roughly 5.5% at $3.8{\times}10^{15}$ W cm^{-2}. Conversely, it is found that the asymmetry of the tunnelling electron, $P^{\text{DI}}_{1,\text{asym}}(\phi)$, exhibits different behaviour to the SI asymmetry comparing Fig. 7.1(b) with Fig. 7.1(f). That is, $P^{\text{DI}}_{1,\text{asym}}(\phi)$ is much wider than $P^{\text{SI}}_{\text{asym}}(\phi)$. Also, for $\phi \in [45^\circ, 90^\circ]$, $P^{\text{DI}}_{1,\text{asym}}(\phi)$ has higher values for the intensity $2{\times}10^{15}$ W cm^{-2} compared to $3.8{\times}10^{15}$ W cm^{-2} with 4% and 2.5%, respectively.

In chapter 6 it was shown that strong recollisions (Corkum, 1993) prevail for strongly-driven He at 800 nm at intensities of $1.3{\times}10^{15}$ W cm^{-2} and $2{\times}10^{15}$ W cm^{-2}, while soft ones prevail at $3.8{\times}10^{15}$ W cm^{-2}. It then follows that the asymmetry for the tunnelling electron, $P^{\text{DI}}_{1,\text{asym}}(\phi)$, has higher values for strong recollisions. This is also supported by the small values of $P^{\text{DI}}_{1,\text{asym}}(\phi)$ at $2{\times}10^{15}$ W cm^{-2} for a laser pulse with a small ellipticity of $\chi = 0.05$, see Fig. 7.1(b). In Fig. 7.2 the tunnel time and recollision time distributions are shown as well as the correlated

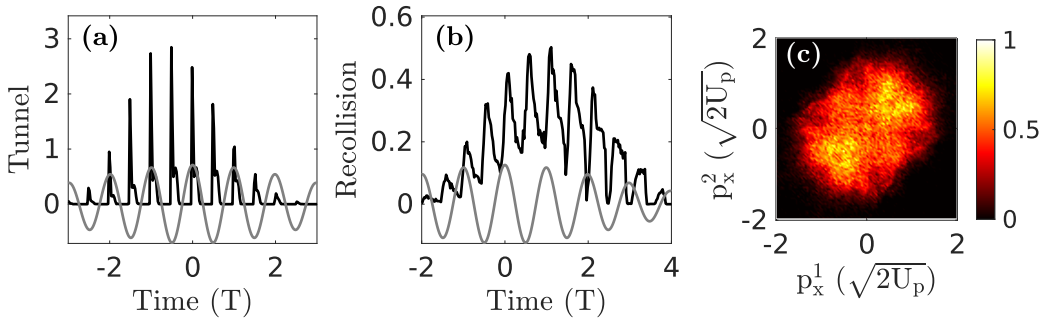

Figure 7.2 | (a) The distribution of tunnelling times (black line) and (b) the distribution of recollision times (black line) with the x-component of the electric field denoted as a grey line. (c) Correlated momenta along the x-direction.

momenta of the two electrons, Figs. 7.2(a), 7.2(b) and 7.2(c) respectively. Comparing these plots to Fig. 6.7(b1, b2 and b5) it is found that the recollisions are marginally softer at $2{\times}10^{15}$ W cm^{-2} for a laser pulse with $\chi = 0.05$ compared to that of linearly-polarised light. The difference is not so clear for in the tunnelling times but comparing Figs. 7.2(b) and 6.7(b2) it is clear that the recollision times are broader for $\chi = 0.05$. For strong recollisions the time of recollision corresponds roughly to zeros of the laser field, whilst for soft recollisions the time of recollision corresponds to extrema of the laser field, as shown previously in Fig. 6.7(b1,c1) (Emmanouilidou and Staudte, 2009). Moreover, comparing Figs. 7.2(c) and 6.7(b5), there is a slight increase in the top left and the bottom right quadrants (antiparallel) for $\chi = 0.05$ and a corresponding drop in the other two quadrants (parallel). As discussed in section 6.3, antiparallel events are related to delayed ionisation events that occur with softer recollisions.

Experimentally electron 1 can not be distinguished from electron 2. Therefore, the angular probability distributions of electrons 1 and 2, $P_1^{\mathrm{DI}}(\phi)$ (Fig. 7.1(a)) and $P_2^{\mathrm{DI}}(\phi)$ (Fig. 7.1(c)), respectively, are not experimentally accessible. However, in a kinematically complete experiment, for each doubly-ionised event, the angle ϕ of each ionising electron can be measured. Then, the probability distribution for any one of the two electrons to ionise with an angle ϕ, $P^{\mathrm{DI}}(\phi)$, can be obtained, for $\phi \in [0°, 180°]$. In Fig. 7.3 the experimentally accessible DI asymmetry, $P_{\mathrm{asym}}^{\mathrm{DI}}(\phi)$, is plotted as a function of ϕ.

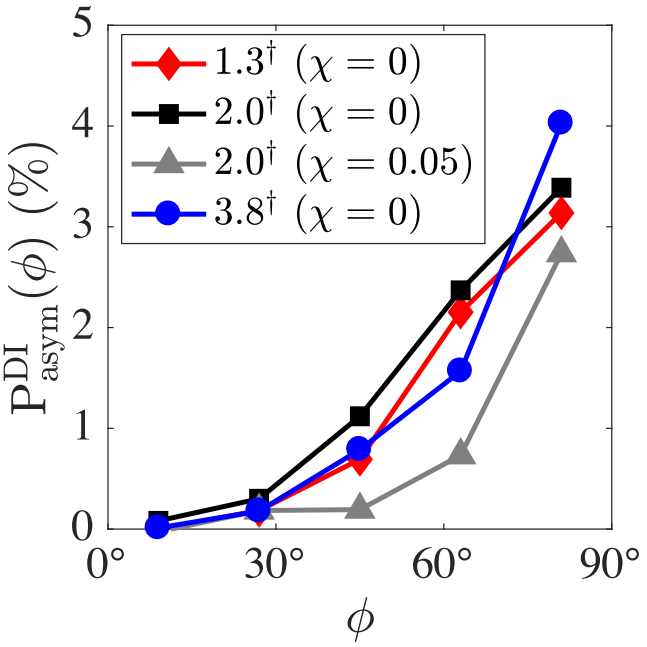

Figure 7.3 | Experimentally observable DI asymmetry, $P^{\mathrm{DI}}_{\mathrm{asym}}(\phi)$, for the two escaping electrons as a function of ϕ. Three intensities are considered and ϕ is binned in intervals of 18°. †Intensity in units of 10^{15} W cm^{-2}.

$P^{\mathrm{DI}}_{\mathrm{asym}}(\phi)$ is found to have significant values at smaller intensities over the same wide range of ϕ as $P^{\mathrm{DI}}_{1,\mathrm{asym}}(\phi)$ does. However, $P^{\mathrm{DI}}_{\mathrm{asym}}(\phi) < P^{\mathrm{DI}}_{1,\mathrm{asym}}(\phi)$ at the smaller intensities. Moreover, at 3.8×10^{15} W cm^{-2} and at 2×10^{15} W cm^{-2} with $\chi = 0.05$, $P^{\mathrm{DI}}_{\mathrm{asym}}(\phi) > P^{\mathrm{DI}}_{1,\mathrm{asym}}(\phi)$ at $\phi = 81°$ but has non zero values for a wider range of ϕ compared to $P^{\mathrm{DI}}_{2,\mathrm{asym}}(\phi)$. These features are expected since $P^{\mathrm{DI}}_{\mathrm{asym}}(\phi)$ accounts for both the tunnelling and the initially bound electron. However, the features of the experimentally accessible $P^{\mathrm{DI}}_{\mathrm{asym}}(\phi)$ still capture the main features of $P^{\mathrm{DI}}_{1,\mathrm{asym}}(\phi)$.

In order to compare directly with future experiments, the computations presented here would need to account for intensity averaging over the focal volume (Wang et al., 2005). Using the current results for intensities from 0.7×10^{15} W cm^{-2} to 3.8×10^{15} W cm^{-2} it is possible to estimate how intensity averaging affects the distribution $P^{\mathrm{DI}}_{\mathrm{asym}}(\phi)$. However, for a more accurate estimate, results at more intensities than currently considered would be required. Experimentally, the peak laser intensity is not necessarily the average intensity experienced by the target atoms. Typically, apparatus along the beam line e.g., splitters and polarisers, will attenuate the laser field reducing the intensity. Therefore, to crude approximation it is ex-

pected that $P^{\text{DI}}_{\text{asym}}(\phi)$ at 1.3×10^{15} W cm^{-2} and 2×10^{15} W cm^{-2} would be reduced compared to the distributions presented in Fig. 7.3. Although, despite a reduction due to focal averaging effects, the resulting DI asymmetries, $P^{\text{DI}}_{\text{asym}}(\phi)$, still have non zero values for a wide range of ϕ. To experimentally observe the transition shown in Fig. 7.3, where the distribution $P^{\text{DI}}_{\text{asym}}(\phi)$ at 3.8×10^{15} W cm^{-2} has smaller values over a less wide range of ϕ compared to its values at 1.3×10^{15} W cm^{-2} and 2×10^{15} W cm^{-2} intensities higher than 3.8×10^{15} W cm^{-2} would have to be considered.

7.3.2 Asymmetric Transverse Initial Momentum

In the following sections, the mechanism responsible for the features of $P^{\text{DI}}_{\text{1,asym}}(\phi)$ will be discussed which relate to the features of the observable $P^{\text{DI}}_{\text{asym}}(\phi)$. It is found that this mechanism is a signature of recollision exclusive to non-dipole effects. Furthermore, the magnetic field and the recollision act together as a gate that selects only a subset of transverse initial momenta of the tunnelling electron that lead to double ionisation.

For linearly polarised light, this gating is illustrated in Fig. 7.4(a1) and (a2) at an intensity of 2×10^{15} W cm^{-2} with the magnetic field switched-on and off, respectively. These plots show the probability distribution, $P(p^1_{y,t_0})$, of electron 1 to tunnel-ionise with a y-component of the initial momentum equal to p^1_{y,t_0} (note that these plots only include trajectories that lead to double ionisation). It is found that $P(p^1_{y,t_0})$ is asymmetric when the magnetic field is switched-on. Specifically, it is more likely for electron 1 to tunnel-ionise with a negative rather than a positive y-component of the initial momentum. In addition, $P(p^1_{y,t_0})$ peaks around small negative values of the momentum of electron 1. Instead, $P(p^1_{y,t_0})$ is symmetric when the magnetic field is switched-off. Furthermore, the distribution of momentum in the z-direction, $P(p^1_{z,t_0})$, is symmetric around zero when the magnetic field is switched-on and off (see Fig. 7.5(a)). This is expected since there is no force acting along the z-axis due to the laser field. Figures 7.5(a) and (b) show $P(p^i_{z,t_0})$ for electrons 1 and 2 respectively. For the tunnelling electron, electron 1, there is a slight difference in the peak about zero. The distribution is marginally wider with the magnetic-field switch-off. Trajectories with larger initial momentum in the

transverse direction are less likely to return to the core when the magnetic field is switched-on and so, trajectories with smaller transverse momentum are more likely to lead to DI. The initially bound electron is less affected as seen in Figure 7.5(b).

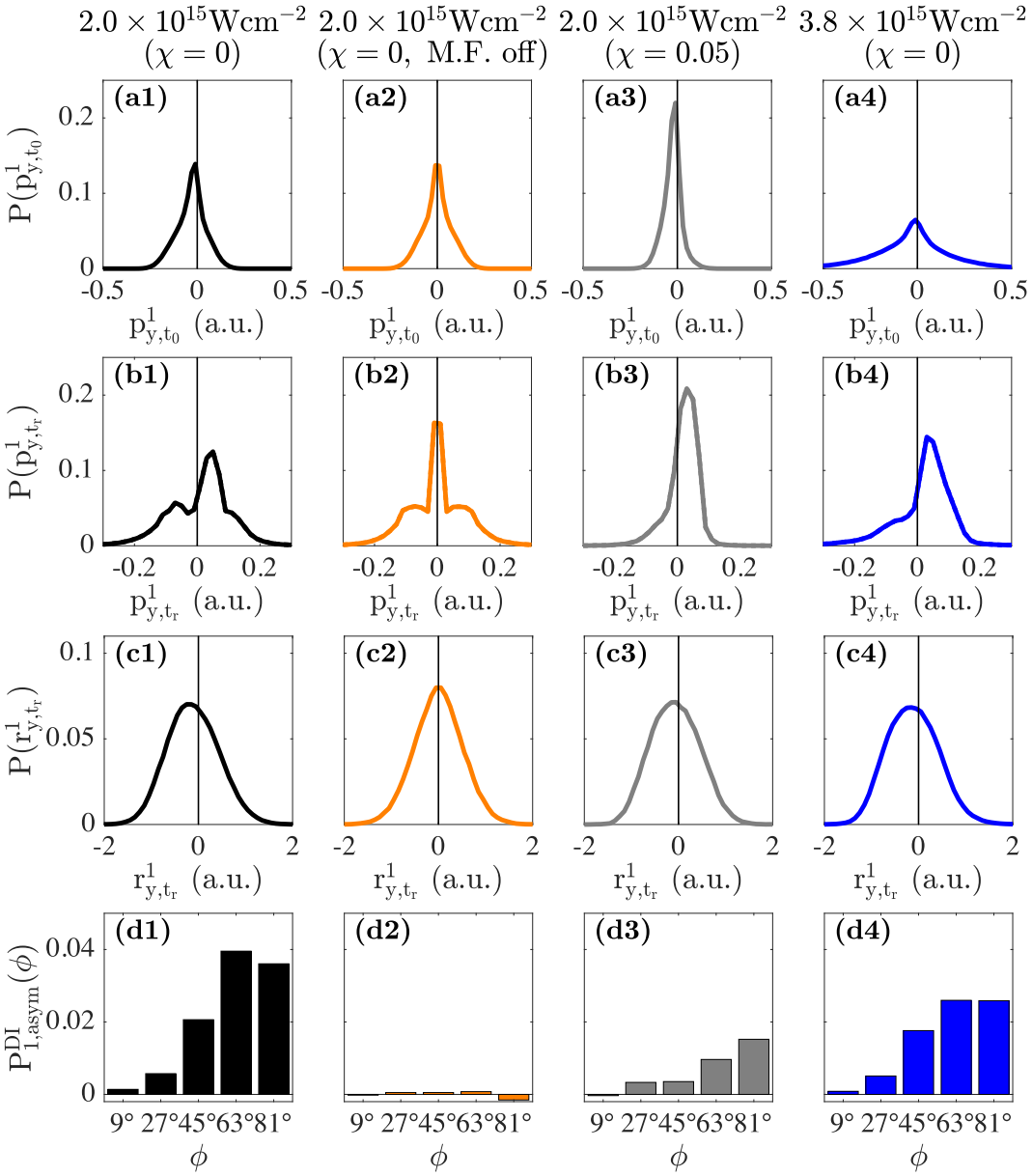

Figure 7.4 | For events that lead to double ionisation, the distributions of the y-component of the electron 1 momentum at two different times are plotted; (a1)-(a4) at the time electron 1 tunnel-ionises (momentum p^1_{y,t_0}); (b1)-(b4) at the time just before the time of recollision (momentum p^1_{y,t_r}).The distributions of the y-component of the electron 1 position are plotted (c1)-(c4) at the time just before the time of recollision (position r^1_{y,t_r}). $P^{\mathrm{DI}}_{1,\mathrm{asym}}(\phi)$ is plotted in panels (d1)-(d4) for better comparison of its features with the features of $P(p^1_{y,t_r})$. Panels (d1), (d3) and (d4) use the data shown in Fig. 7.1(b) but have been plotted separately for clarity.

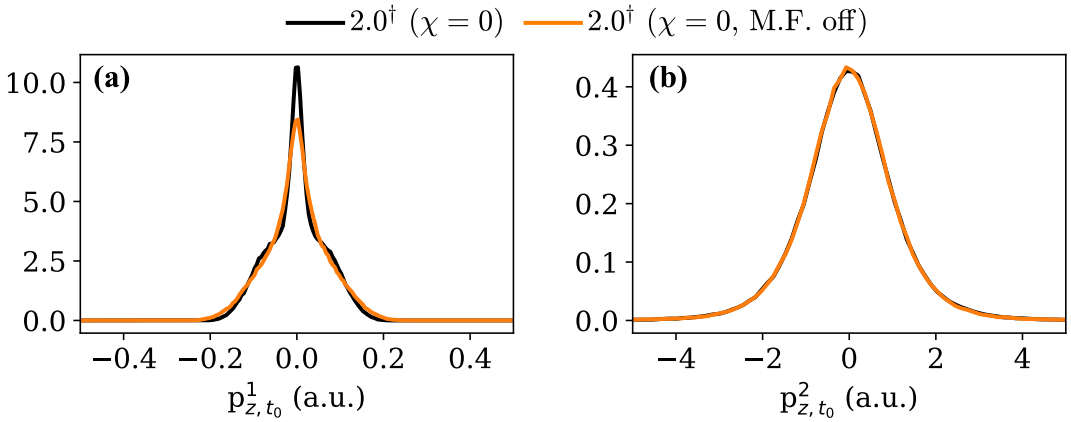

Figure 7.5 | Momentum distributions for electrons (a) 1 and (b) 2 in the z-direction calculated at the time electron 1 tunnel-ionises. The black (orange) line shows $P(p^i_{z,t_0})$ with the magnetic field switched-on (off) at an intensity of 2×10^{15} W cm^{-2}.
†Intensity in units of 10^{15} W cm^{-2}.

This asymmetry in $P(p^1_{y,t_0})$ persists even at a higher intensity of 3.8×10^{15} W cm^{-2} for linearly polarised light (Fig. 7.4(a4)) and at 2×10^{15} W cm^{-2} for a laser pulse with a small ellipticity of $\chi = 0.05$ (Fig. 7.4(a3)). In contrast, for all the above cases, the initially bound electron has a symmetric distribution $P(p^2_{y,t_0})$ at the time electron 1 tunnel-ionises and just before the time of recollision. In this work, the recollision time is identified for each double ionising trajectory as the time that the electron-electron potential energy $1/|\mathbf{r}_1 - \mathbf{r}_2|$ as a function of time is maximum. Moreover, in single ionisation the escaping electron has a symmetric distribution $P(p_{y,t_0})$ at the time this electron tunnel-ionises.

7.3.3 Asymmetric Transverse Recollision Momentum

In single ionisation, the features of $P^{\text{SI}}_{\text{asym}}(\phi)$ can be understood largely based on the distribution $P(p^1_{y,t_0})$ at the time electron 1 tunnel-ionises alone. This was discussed in the previous chapter (chapter 6, sec. 6.3.2). To recap, the y-component of the escaping electron's momentum was computed both with all Coulomb forces switched-off and with all Coulomb forces accounted for. In both cases it was shown that the average y-component of the electron 1 momentum is roughly the same. At the time electron 1 tunnel-ionises, the y-component of the transverse momentum of electron 1 is roughly symmetric around zero. This initial momentum distribution, combined with the $\mathbf{F}_B$ force, gives rise to the electron ionising mostly with ϕ

slightly less than 90°, which in turn leads to a sharply peaked distribution $P^{\text{SI}}_{\text{asym}}(\phi)$ (Fig. 7.1(f)).

In double ionisation, to understand the features of $P^{\text{DI}}_{1,\text{asym}}(\phi)$, first, the distribution $P(p^1_{y,t_r})$ of the y-component of the electron 1 momentum shortly before the time of recollision must be obtained. Then, the effect of the recollision itself on the distribution $P(p^1_{y,t_r})$ must be investigated. This was discussed previously in chapter 6, sec. 6.3.4. In summary, the y-component of the momentum of electrons 1 and 2 were propagated from the time electron 1 tunnel-ionises up to the time of recollision. This was computed using the full 3D-SMND model with all Coulomb forces accounted for. Next, using the momenta of electrons 1 and 2 shortly after the time of recollision as initial conditions, the equations of motion were propagated from the time of recollision onwards with all Coulomb forces and the magnetic field switched-off. The final average y-component of the momentum of electron 1 is roughly equal in both cases. That is, comparing $\langle p^1_y \rangle$ obtained via full propagation, with all forces accounted for, against $\langle p^1_y \rangle$ obtained using the modified propagation discussed above (see Table 6.2). The same comparison holds for electron 2. Therefore, the decisive time in double ionisation is the time of recollision.

Given the above, $P(p^1_{y,t_r})$ is computed just before the time of recollision. This is done by extracting, from the full 3D-SMND model, the distribution of the y-component of the electron 1 momentum at a time just before the recollision, for instance at $t_{\text{bef}} = t_r - 1/50T$. t_{bef} was selected such as to avoid the sharp change of the momenta which occurs at t_r, e.g., see Fig. 6.7(a4,b4,c4). At all intensities considered here a positive rather than negative y-component of electron 1 momentum is favoured, shortly before the time of recollision. This is shown at intensities of $2{\times}10^{15}$ W cm^{-2} and $3.8{\times}10^{15}$ W cm^{-2} for linearly polarised light in Fig. 7.4(b1) and (b4), respectively, and at $2{\times}10^{15}$ W cm^{-2} for elliptically polarised light with $\chi = 0.05$ in Fig. 7.4(b3). In contrast, when the magnetic field is switched-off the distribution $P(p^1_{y,t_r})$ is symmetric with respect to zero as illustrated for an intensity of $2{\times}10^{15}$ W cm^{-2} in Fig. 7.4(b2). Therefore, it is now established that the shift towards negative momenta of $P(p^1_{y,t_0})$ at the time electron 1 tunnel-ionises maps to

a shift towards positive momenta of $P(p^1_{y,t_r})$ just before the time of recollision.

The width is another interesting feature of the distribution $P(p^1_{y,t_0})$ and, by extension, of the distribution $P(p^1_{y,t_r})$. From Fig. 7.4(b1)-(b4), it is found that the width of $P(p^1_{y,t_r})$ at $2{\times}10^{15}$ W cm^{-2} with linearly polarised light is the largest one, while the width of $P(p^1_{y,t_r})$ at $2{\times}10^{15}$ W cm^{-2} with $\chi = 0.05$ is the smallest one. Moreover, the width of $P(p^1_{y,t_0})$ is comparable with the width of $P(p^1_{y,t_r})$ for both the linear and the elliptical laser field at $2{\times}10^{15}$ W cm^{-2}. However, the width of $P(p^1_{y,t_0})$ is larger than the width of $P(p^1_{y,t_r})$ at an intensity of $3.8{\times}10^{15}$ W cm^{-2}.

The widths of $P(p^1_{y,t_0})$ and $P(p^1_{y,t_r})$ are consistent with Coulomb focusing which mainly refers to multiple returns of electron 1 to the core (Brabec et al., 1996; Comtois et al., 2005). In addition, for the higher intensity of $3.8{\times}10^{15}$ W cm^{-2}, the widths are also consistent with a larger effect of the Coulomb potential of the ion on electron 1. The latter effect is not due to multiple returns of electron 1 to the core but rather due to electron 1 tunnel-ionising closer to the nucleus at higher intensities.

Table 7.1 | Number of returns to the core of electron 1 for doubly-ionised events.

	$2.0^\dagger$ ($\chi = 0$)	$2.0^\dagger$ ($\chi = 0$ M.F. off)	$2.0^\dagger$ ($\chi = 0.05$)	$3.8^\dagger$ ($\chi = 0$)
1 Return	27%	24%	53%	57%
2 Returns	24%	24%	10%	16%
3 Returns	27%	27%	19%	14%
>3 Returns	21%	25%	18%	12%

† Intensity in units of $\times 10^{15}$ W cm^{-2}

Table 7.1 details the number of returns electron 1 makes to the core, before it finally escapes. It is shown that electron 1 returns more times to the core at $2{\times}10^{15}$ W cm^{-2}. In fact, electron 1 escapes with only one return to the core in 27% of doubly-ionised events, implying that most DI events are the result of two or more returns. Also, at $2{\times}10^{15}$ W cm^{-2} with $\chi = 0.05$ and at $3.8{\times}10^{15}$ W cm^{-2} the number of returns is roughly the same. In these two latter cases, electron 1 escapes with only one return to the core in more than 50% of doubly-ionised events. It is also found that the width of the distributions $P(p^1_{y,t_0})$ and $P(p^1_{y,t_r})$ increases

with increasing number of returns to the core for all laser fields considered, which is shown in Figures 7.6(a) and (b), respectively, for the field intensity of 2×10^{15} W cm^{-2} with the magnetic field switched-on. The above features are consistent with Coulomb focusing. Thus, Coulomb focusing explains why the width of $P(p^1_{y,t_0})$ at 2×10^{15} W cm^{-2} is larger than the width of $P(p^1_{y,t_0})$ at 2×10^{15} W cm^{-2} with $\chi = 0.05$.

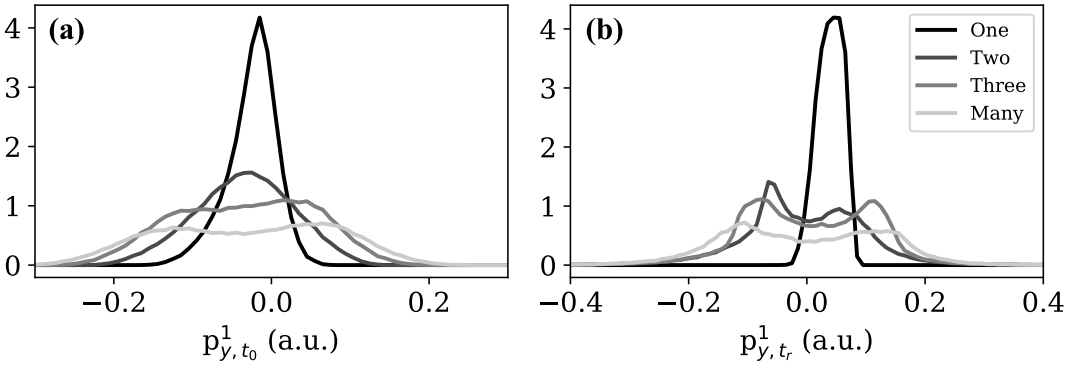

Figure 7.6 | Momentum distributions (a) $P(p^1_{y,t_0})$ and (b) $P(p^1_{y,t_r})$ for the field intensity 2×10^{15} W cm^{-2} with the magnetic field switched-on, plotted for different numbers of returns.

Moreover, at the larger intensity of 3.8×10^{15} W cm^{-2} electron 1 exits the field-lowered Coulomb barrier closer to the nucleus. Indeed, the average distance of electron 1 from the nucleus at the time electron 1 tunnel-ionises is 2.4 a.u. at 3.8×10^{15} W cm^{-2} compared to roughly 3.5 a.u. at 2×10^{15} W cm^{-2} with $\chi = 0$ and $\chi = 0.05$, see Table 7.2. This is consistent with the width of $P(p^1_{y,t_r})$ being significantly smaller than the width of $P(p^1_{y,t_0})$ at 3.8×10^{15} W cm^{-2}. That is, the Coulomb potential of the ion has a large effect on electron 1 from the time electron 1 tunnel-ionises onwards. This is not the case for the smaller intensities of 2×10^{15} W cm^{-2} with $\chi = 0$ and $\chi = 0.05$ where the widths of the distributions $P(p^1_{y,t_0})$ and $P(p^1_{y,t_r})$ are similar.

7.3.4 Glancing Angles in Recollisions

It is shown in the previous section that effectively the only force that could result in a change of the momenta of the two electrons between the final time and the time shortly after recollision is due to the electric field. Between the time shortly after

Table 7.2 | Average distance from the nucleus of electron 1 at the time electron 1 tunnel-ionises, $\langle r^1_{t_0} \rangle$.

	$2.0^\dagger$ $(\chi = 0)$	$2.0^\dagger$ $(\chi = 0$ M.F. off$)$	$2.0^\dagger$ $(\chi = 0.05)$	$3.8^\dagger$ $(\chi = 0)$
$\langle r^1_{t_0} \rangle$ (a.u.)	3.5	3.5	3.7	2.4

† Intensity in units of $\times 10^{15}$ W cm^{-2}

recollision takes place and the asymptotic time, the electric field mainly affects the x-component and not the y-component of the momentum of electron 1. Moreover, at the smaller intensities considered, in the time interval following recollision, the electric field does not significantly affect the magnitude of the x-component of the electron 1 momentum – this component is mainly determined by the vector potential at the recollision time. Given the above, it is enough to find how the momentum of electron 1 (roughly equal to the x-component) and its y-component change from just before to just after the time of recollision due to the recollision itself. This will therefore provide an understanding of the features seen in the distribution $P^{\text{DI}}_{1,\text{asym}}(\phi)$ (Fig. 7.1).

A measure of the strength of a recollision is the collision angle θ, defined as

$$\cos\theta = \frac{\mathbf{p}_{1,\text{bef}} \cdot \mathbf{p}_{1,\text{aft}}}{(|\mathbf{p}_{1,\text{bef}}||\mathbf{p}_{1,\text{aft}}|)}. \tag{7.4}$$

That is, θ, is the angle between the momentum of electron 1 just before and just after the time of recollision. The momentum just before the time of recollision is roughly along the x-axis (polarisation axis). Thus, θ is the angle of the momentum of electron 1 after the time of recollision with respect to the x-axis. $\theta = 180^\circ$ corresponds to a "head on" collision and complete backscattering. $\theta = 0^\circ$ corresponds to forward scattering and thus to almost no change due to the recollision.

Fig. 7.7 shows the probability for electron 1 to escape with a final angle, ϕ, and a scattering angle, θ, for each laser field considered in this work. It is shown that very strong recollisions, i.e., $\theta = 180^\circ$, take place only when electron 1 escapes with a momentum that has a very small y-component, i.e., ϕ is around 90°. How-

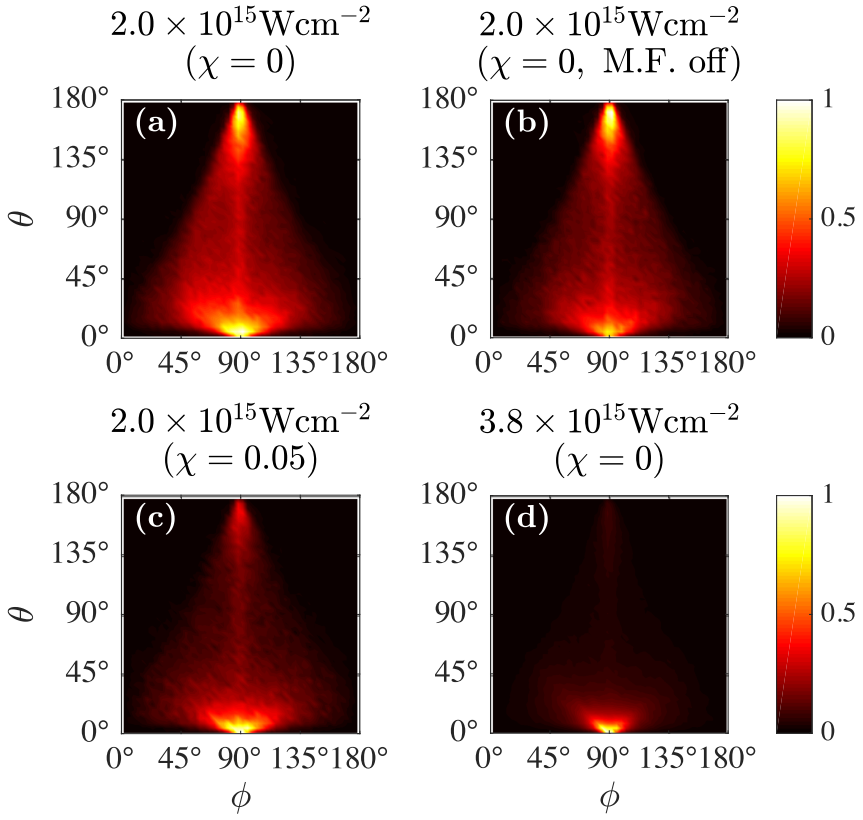

Figure 7.7 | Double differential probability of electron 1 to have a scattering angle θ and a final angle ϕ at (a) $2{\times}10^{15}$ W cm^{-2}, (b) $2{\times}10^{15}$ W cm^{-2} with the magnetic field switched-off, (c) $2{\times}10^{15}$ W cm^{-2} with $\chi = 0.05$ and (d) $3.8{\times}10^{15}$ W cm^{-2}.

ever, even when electron 1 escapes with ϕ around $90°$, it is more likely that a weak recollision takes place, i.e., $\theta = 0°$, rather than a strong one with $\theta = 180°$. Moreover, when electron 1 ionises with momenta that have larger y-components with $\phi \in [45°, 90°]$ and $\phi \in [90°, 135°]$ the scattering angles θ are on average smaller than $90°$. That is, in most cases, electron 1 ionises at glancing angles θ following recollision. Moreover, a comparison of the values of θ at $2{\times}10^{15}$ W cm^{-2} and at $3.8{\times}10^{15}$ W cm^{-2}, see Fig. 7.7(a) and (d), clearly shows that overall the recollision is stronger at the smaller intensity. In addition, a comparison of the values of θ at $2{\times}10^{15}$ W cm^{-2} and at $2{\times}10^{15}$ W cm^{-2} with $\chi = 0.05$, see Fig. 7.7(a) and (c), clearly shows that overall the recollision is stronger when $\chi = 0$. Thus, electron 1 escapes at glancing angles following recollision.

7.3.5 Asymmetric Transverse Recollision Position

To explain how the y-component of the momentum of electron 1 changes from just before to just after the time of recollision, due to the recollision itself, the case where the magnetic field is switched-off at 2×10^{15} W cm^{-2} will be considered first. It is found that doubly-ionised events are equally likely to have positive or negative y-component of the momentum and of the position of electron 1 just before the time of recollision, see Fig. 7.4(b2) an (c2). Moreover, the y-component of the final momentum of electron 1 is positive (negative) depending on whether the y-component of the position of electron 1 is negative (positive) just before the time of recollision. The reason is that electron 1 ionises at glancing angles. The direction of the Coulomb attraction of electron 1 from the nucleus just before the time of recollision determines whether just after the time of recollision, as well as at asymptotically large times, the y-component of the momentum of electron 1 is positive or negative. Indeed, looking at the distance in the y-direction of electron 1 from the nucleus, at the time just before the recollision, r^1_{y,t_r}, it can be seen that doubly-ionised events with $r^1_{y,t_r} > 0$ give rise to negative values of $P^{\rm DI}_{\rm 1,asym}$, while doubly-ionised events with $r^1_{y,t_r} < 0$ give rise to positive values of $P^{\rm DI}_{\rm 1,asym}$ and cancel each other out.

However, when the magnetic field is switched-on at 2×10^{15} W cm^{-2}, most (59%) doubly-ionised events have $r^1_{y,t_r} < 0$ just before the time of recollision. This is due to non-dipole recollision gated ionisation, since out of these latter events 61% have both $p^1_{y,t_r} > 0$ just before the time of recollision and $p^1_{y,t_0} < 0$ at the initial time that electron 1 tunnel-ionises. The shift towards negative values in the transverse y-component of the position of electron 1 just before the time of recollision is shown in Fig. 7.4(c1), (c3) at 2×10^{15} W cm^{-2} with $\chi = 0$ and $\chi = 0.05$, respectively, and in (c4) at 3.8×10^{15} W cm^{-2}. As for the case when the magnetic field is switched-off, when the magnetic field is switched-on electron 1 ionises at glancing angles. Therefore, doubly-ionised events with $r^1_{y,t_r} > 0$ give rise to negative values of $P^{\rm DI}_{\rm 1,asym}$ and doubly-ionised events with $r^1_{y,t_r} < 0$ give rise to positive values of $P^{\rm DI}_{\rm 1,asym}$. However, the latter events are 59% of all doubly-ionised events and thus overall $P^{\rm DI}_{\rm 1,asym}$ has positive values.

From the above it also follows that a small width of $P(p^1_{y,t_r})$ affects only doubly-ionised events with small y-components of the electron 1 final momenta. On the other hand, a large width of $P(p^1_{y,t_r})$ just before the time of recollision affects doubly-ionised events with y-components of the electron 1 final momenta ranging from small to large. However, doubly-ionised events with large y-components of the electron 1 momenta correspond to smaller ϕ in $P^{\mathrm{DI}}_{1,\mathrm{asym}}$. Indeed, this is clear in Fig. 7.8 when comparing the distribution of the y-component of the final momentum of electron 1 in the smaller ϕ of 27° with the one in the larger ϕ of 81°. The large y-components of the momenta of electron 1 are a result of the recollision. This is the case since for each intensity, $P(p^1_{y,t_r})$ are similar for all ϕ bins, see Fig. 7.8. $P(p^1_{y,t_r})$ is depicted in Fig. 7.4(b1), (b3) and (b4) for three different laser fields.

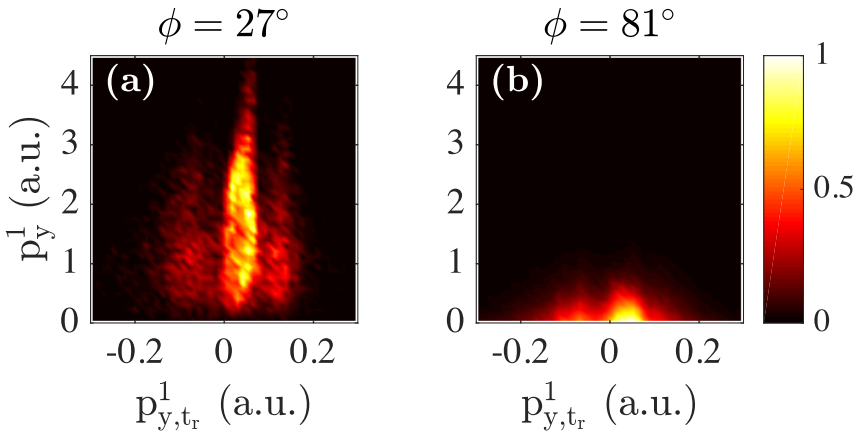

Figure 7.8 | Double differential probability of the tunnelling electron to have a y-component of the momentum equal to p^1_{y,t_r} at the time of recollision and equal to p^1_y at the asymptotic time for two different ϕs at 2.0×10^{15} W cm^{-2}. ϕ is binned in intervals of 18°.

Most doubly-ionised events have a positive y-component of the momentum of electron 1 just before the time of recollision, when magnetic effects are included. Thus, the width of $P(p^1_{y,t_r})$ is also a measure of the shift towards positive y-components of the final momenta of electron 1.

Finally, the probability density of the distributions for the x-component of the momentum of electron 1 are compared at intensities where strong recollisions prevail with intensities where softer collisions occur. The probability density is double-peaked; just before (Fig. 7.9(a)) and just after (Fig. 7.9(b)) the time of recollision, as well as at asymptotically large times (Fig. 7.9(c)) for intensities where stronger

recollisions prevail i.e., near 2.0×10^{15} W cm^{-2}. Whereas, at the higher intensity of 3.8×10^{15} W cm^{-2}, where softer recollisions occur, the probability density is less peaked. Indeed, for strong recollisions, the x-component of the momentum of electron 1 is determined mainly by the vector potential at the time of recollision. However, for soft recollisions this is not quite the case since electron 1 only transfers a small amount of its kinetic energy to electron 2, compared to U_p (Fig. 6.7(a3, b3 and c3)). In addition, for soft recollisions, the time of recollision has a much broader range of values, see Fig. 6.7(a2, b2 and c2).

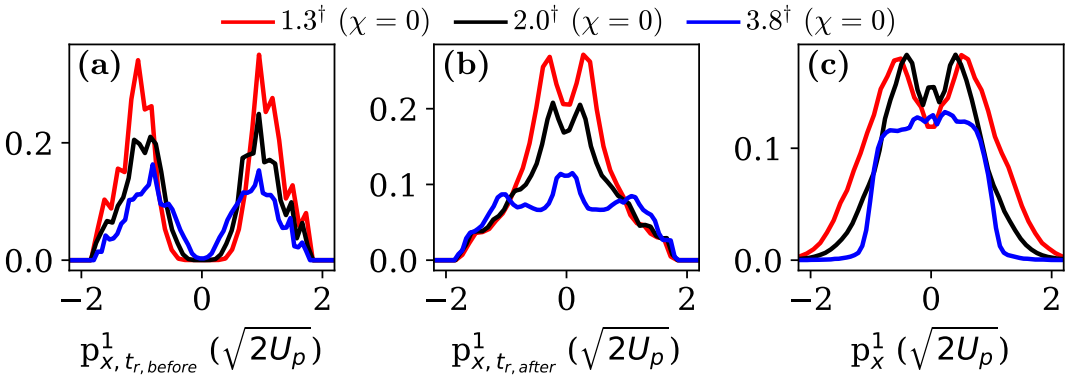

Figure 7.9 | Momentum distributions in the x-direction for electron 1 at a time (a) just before the recollision, $P(p^1_{x,t_{r,\text{before}}})$, (b) just after the recollision, $P(p^1_{x,t_{r,\text{after}}})$ and (c) asymptotically large, $P(p^1_x)$. Plotted for the three different intensities with the magnetic field switched-on i.e., $1.3{\times}10^{15}$ W cm^{-2}, $2{\times}10^{15}$ W cm^{-2} and $3.8{\times}10^{15}$ W cm^{-2}.
†Intensity in units of 10^{15} W cm^{-2}.

Combining the width of the asymmetry of $P(p^1_y)$ with the width of the distribution of the x-component of the momentum of electron 1. It then follows that $P^{\text{DI}}_{1,\text{asym}}(\phi)$ should have higher values over a larger range of ϕ at $2{\times}10^{15}$ W cm^{-2} (stronger recollision) and smaller values at $2{\times}10^{15}$ W cm^{-2} with $\chi = 0.05$ (softer recollision). Indeed, this is the case as shown in Fig. 7.4(d1)-(d4).

7.3.6 Average Sum Electron Momenta in DI

Previously in chapter 6, it was shown that in DI the ratio $\langle p^1_y + p^2_y \rangle_{\text{DI}} / 2 \langle p_y \rangle_{\text{SI}}$ is maximum and roughly equal to eight at intensities $1.3{\times}10^{15}$ W cm^{-2} and $2{\times}10^{15}$ W cm^{-2}, see Fig. 7.10. $\langle p^1_y + p^2_y \rangle$ is the average sum of the two electron momenta along the propagation direction of the laser field, while $\langle p_y \rangle_{\text{SI}}$ is the corresponding average electron momentum in single ionisation. In Fig. 7.10(a),

$\langle p_y^1 + p_y^2 \rangle_{\rm DI} / 2 \langle p_y \rangle_{\rm SI}$ is shown to decrease with increasing intensity, for the intensities considered. Moreover, in Fig. 7.10(b), it is shown that it is $\langle p_y^1 \rangle_{\rm DI}$ of the tunnelling electron that contributes the most to $\langle p_y^1 + p_y^2 \rangle_{\rm DI}$ for the intensities considered. The ratio $\langle p_y^1 \rangle_{\rm DI} / \langle p_y \rangle_{\rm SI}$ has surprisingly large values at intensities smaller than the intensities satisfying the criterion for the onset of magnetic-field effects $\beta_0 \approx 1$ a.u. (Reiss, 2008, 2014). In contrast, $\langle p_y \rangle_{\rm SI}$ increases from 0.0035 a.u. at 0.7×10^{15} W cm^{-2} to 0.028 a.u. at 4.8×10^{15} W cm^{-2}, see Fig. 7.10(a). The small values of the average electron momentum in single ionisation and the increase of this average with intensity are in accord with the effect of the $\mathbf{F}_B$ force. The latter increases with intensity, since the magnetic field increases. The increase of $\langle p_y \rangle_{\rm SI}$ with intensity has been addressed in several experimental and theoretical studies (Smeenk et al., 2011; Chelkowski et al., 2014, 2015; Titi and Drake, 2012; Ivanov, 2015).

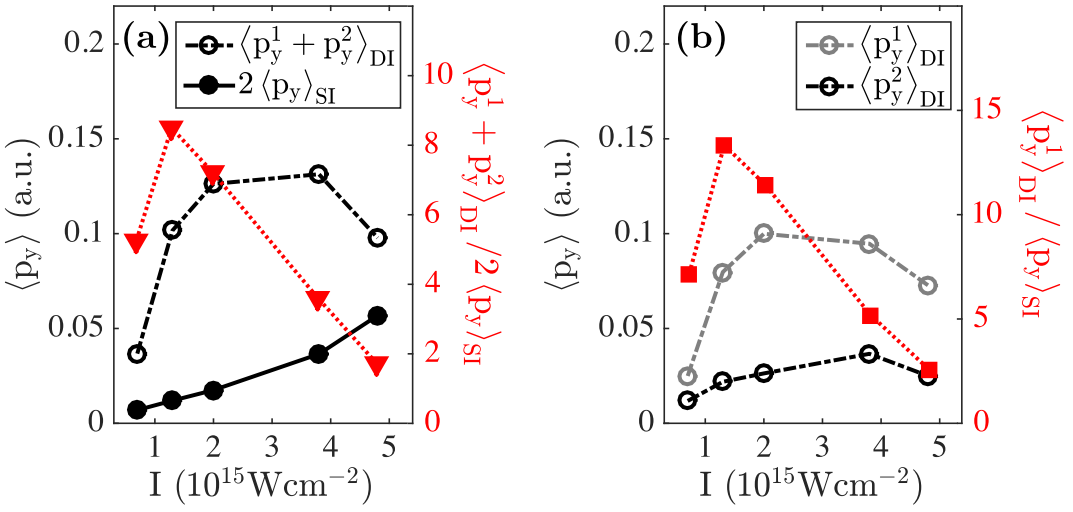

Figure 7.10 | (a) The average sum of the two electron momenta $\langle p_y^1 + p_y^2 \rangle_{\rm DI}$ in DI (black dot-dashed line with open circles), twice the average electron momentum $\langle p_y \rangle_{\rm SI}$ in single ionisation (black solid line with circles) and the ratio $\langle p_y^1 + p_y^2 \rangle_{\rm DI} / \langle p_y \rangle_{\rm SI}$ (red dotted line with triangles) as a function of the intensity of the laser field. (b) The average momentum of the tunnelling electron $\langle p_y^1 \rangle_{\rm DI}$ (grey dot-dashed line with open circles) and the bound electron $\langle p_y^2 \rangle_{\rm DI}$ (black dot-dashed line with circles) in DI and the ratio $\langle p_y^1 \rangle_{\rm DI} / \langle p_y \rangle_{\rm SI}$ (red dotted line with squares) as a function of the intensity of the laser field.

In the following, it will be demonstrated that non dipole recollision gated ionisation accounts for the large values of $\langle p_y^1 \rangle_{\rm DI} / \langle p_y \rangle_{\rm SI}$ and thus for the large average sum of the two electron momenta along the propagation direction of the laser field

at smaller intensities of 1.3-2$\times10^{15}$ W cm^{-2}. To do so, $\langle p_y^i \rangle_{\rm DI}$ is expressed as

$$\langle p_y^i \rangle_{\rm DI} = \int_{0^\circ}^{180^\circ} \langle p_y^i(\phi) \rangle_{\rm DI} \, P_i^{\rm DI}(\phi) d\phi, \tag{7.5}$$

with $i = 1, 2$ for electrons 1 and 2 in double ionisation – a similar expression holds in single ionisation. It has already been shown that non-dipole recollision gated ionisation accounts for the asymmetry in $P_1^{\rm DI}(\phi)$. So now the influence of the magnetic field on $\langle p_y^i(\phi) \rangle_{\rm DI}$ is investigated. To do so, $\langle p_y^1(\phi) \rangle_{\rm DI}$ of the tunnel electron, $\langle p_y^2(\phi) \rangle_{\rm DI}$ of the bound electron and $\langle p_y(\phi) \rangle_{\rm SI}$ are plotted in Fig. 7.11(a), (b) and (c), respectively, at 2$\times10^{15}$ W cm^{-2} with linearly polarised light and with the magnetic field switched-on and off. It is shown that the magnitude of the average electron momentum increases as a function of ϕ, both in double and in single ionisation. This is evident mostly for ϕ around 0° and 180°. Moreover, it is clearly seen that the magnetic field has no influence on any of the average electron momenta considered and that $\langle p_y^i(\phi) \rangle_{\rm DI} = \langle p_y^i(180^\circ - \phi) \rangle_{\rm DI}$ and $\langle p_y(\phi) \rangle_{\rm SI} = \langle p_y(180^\circ - \phi) \rangle_{\rm SI}$. This is expected when the magnetic field is switched-off, since there is no preferred direction of electron escape on the plane that is perpendicular to the polarisation direction (x-axis) of the laser field. Similar results hold at 1.3$\times10^{15}$ W cm^{-2} and at 3.8$\times10^{15}$ W cm^{-2}.

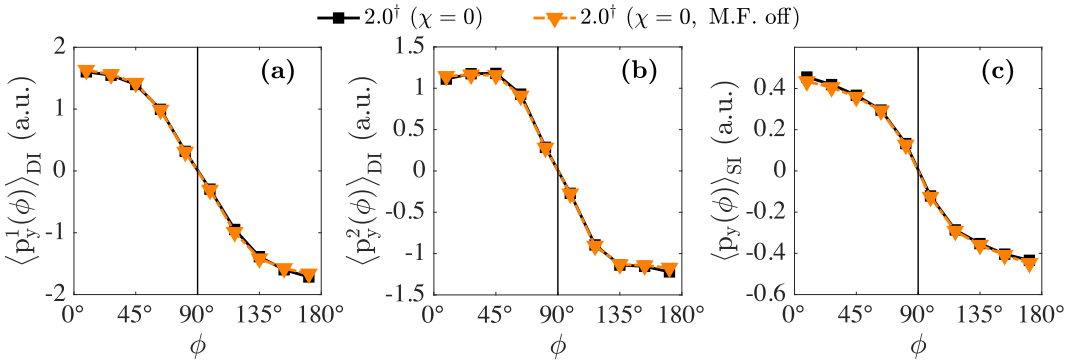

Figure 7.11 | (a) $\langle p_y^1 \rangle_{\rm DI}$ of the tunnelling electron, (b) $\langle p_y^2 \rangle_{\rm DI}$ of the initially bound electron and (c) $\langle p_y \rangle_{\rm SI}$ in single ionisation are plotted as a function of ϕ at 2$\times10^{15}$ W cm^{-2} with the magnetic field switched-on and off. ϕ is binned in intervals of 18°.
†Intensity in units of 10^{15} W cm^{-2}.

It is also found that the effect of the magnetic field on $\langle p_y^1(\phi) \rangle_{\rm DI}$ is very small

even at a more differential level. Specifically, the dependence of $\langle p_y^1(t)\rangle_{\text{DI}}$ on time, for a given angle ϕ, is very similar both with the magnetic field switched-on and off, as shown in Fig. 7.12. The only difference is a small oscillation due to the magnetic field. It is noted that $\langle p_y^1(\phi, t\to\infty)\rangle_{\text{DI}} = \langle p_y^1(\phi)\rangle_{\text{DI}}$. Similar results hold for the bound electron.

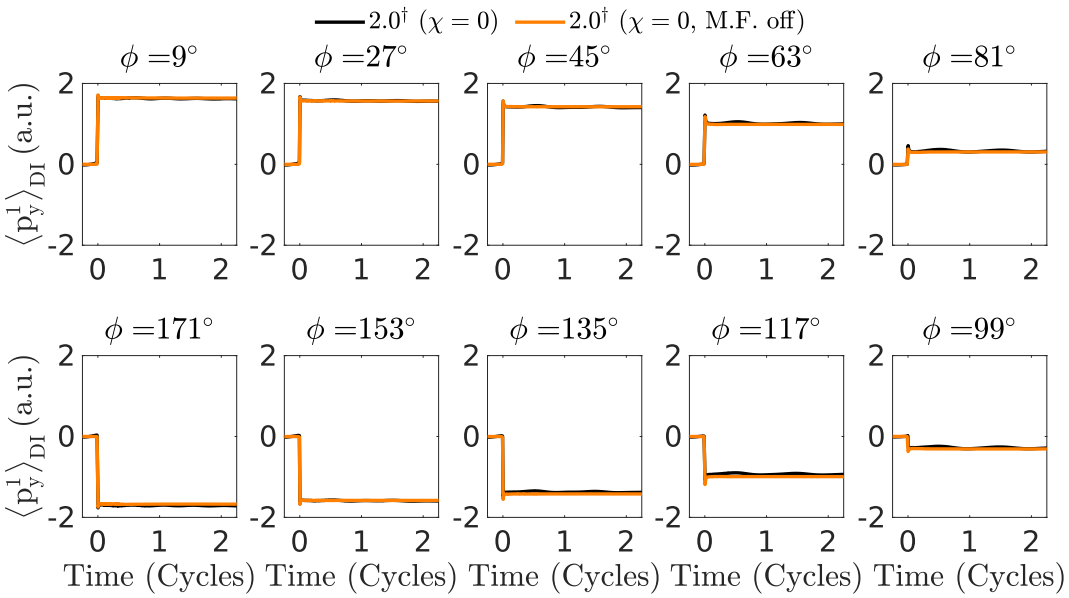

Figure 7.12 | Average momentum of electron 1 in the y-direction, $\langle p_y^1(t)\rangle_{\text{DI}}$, as a function of the time. Time zero is is chosen to as the recollision time of each double ionising event. Each panel represents DI events with an angle ϕ that falls into a given bin of width $\Delta\phi = 18°$, e.g., $\phi = 81°$ corresponds to events that had an angle $72° < \phi < 90°$.
†Intensity in units of 10^{15} W cm^{-2}.

Using equation 7.5, it is now possible to explain why $\langle p_y^1\rangle_{\text{DI}}$ is much larger than $\langle p_y\rangle_{\text{SI}}$ at intensities around 2×10^{15} W cm^{-2}. When the magnetic field is switched-on, $\langle p_y^1(\phi)\rangle_{\text{DI}}$ does not change but $P^{\text{DI}}_{1,\text{asym}}(\phi)$ does. $P^{\text{DI}}_{1,\text{asym}}(\phi)$ is much wider than $P^{\text{SI}}_{\text{asym}}(\phi)$ and $P^{\text{DI}}_{2,\text{asym}}(\phi)$ and has higher values at 2×10^{15} W cm^{-2} rather than at 3.8×10^{15} W cm^{-2}. The higher values of $P^{\text{DI}}_{1,\text{asym}}(\phi)$ over a wider range of ϕ compared to $P^{\text{SI}}_{\text{asym}}(\phi)$ and $P^{\text{DI}}_{2,\text{asym}}(\phi)$ result in smaller ϕ, and thus larger $\langle p_y^1(\phi)\rangle_{\text{DI}}$ (Fig. 7.11), having a significant weight in equation 7.5.

7.4 Conclusion

By fully accounting for non-dipole effects in double ionisation, it is shown that the recollision and the magnetic field act together as a gate. This gate *selects* a distri-

bution of the y-component of the tunnelling electron's initial momentum, $P(p^1_{y,t_0})$, which is shifted towards negative values; negative values in the y-axis are opposite to the propagation direction of the laser field. The term non-dipole recollision-gated ionisation was adopted to describe this effect. The asymmetry in $P(p^1_{y,t_0})$, caused by non-dipole recollision-gating, maps in time to an asymmetry of the transverse electron 1 momentum just before the time of recollision, i.e., to an asymmetry in $P(p^1_{y,t_r})$. That is, the y-component of the momentum of the tunnelling electron, $P(p^1_{y,t_r})$, is shifted towards positive values just before the time of recollision. In addition, the asymmetry in $P(p^1_{y,t_0})$ maps in time to an asymmetry of the y-position of electron 1 just before the time of recollision $P(r^1_{y,t_r})$, where $P(r^1_{y,t_r})$ is shifted towards negative values just before the time of recollision. The above asymmetries combined with the tunnelling electron escaping at glancing angles following a recollision give rise to an asymmetry in $P^{\mathrm{DI}}_1(\phi)$ with respect to $\phi = 90°$ – the probability distribution of electron 1 to escape with an angle ϕ.

The asymmetry in $P^{\mathrm{DI}}_1(\phi)$ is more significant, i.e., higher values of $P^{\mathrm{DI}}_{1,\mathrm{asym}}(\phi)$ over a wider range of ϕ, in double ionisation compared to single ionisation. Moreover, higher values of $P^{\mathrm{DI}}_{1,\mathrm{asym}}(\phi)$ over a wider range of ϕ result from larger widths of $P(p^1_{y,t_r})$ just before the time of recollision. The latter width depends on the intensity and the ellipticity of the laser pulse and this is related to Coulomb focusing. Also, it is the asymmetry in $P^{\mathrm{DI}}_1(\phi)$ over a wide range of ϕ that accounts for the large values of the average transverse electron 1 momentum and thus of the large average sum of the two electron momenta at smaller intensities. Even though not as pronounced, these features of the probability distribution $P^{\mathrm{DI}}_1(\phi)$ of the tunnelling electron are also present in an experimentally accessible observable. Namely, the probability distribution for electron 1 or 2 to escape with an angle ϕ. This observable effect of the non-dipole recollision-gated ionisation can be measured by future experiments.

Finally, this work shows that magnetic field effects cause an offset of the transverse momentum and position of the recolliding electron just before recollision takes place and that these asymmetries lead to asymmetries in observables that are experimentally accessible. It is conjectured that this is a general phenomenon not

restricted to magnetic field effects. That is, these observable asymmetries will be present in any process that has two delayed steps and allows an electron to gain an offset before recollision takes place. For example, in a pump-probe experiment the delay of the probe relative to the pump could have such an effect. Similarly, two-colour laser fields with different polarisation axes could be an interesting platform to study non-linear gating effects. The difficulty is finding an observable that is not already dominated by a lower order effect. For example, for the linearly-polarised laser fields discussed in this chapter, the electric field acts in the x-direction. The force due to the electric field overshadows any effects caused by the magnetic component of the Lorentz force in the same direction. However, in the y-direction there is no such contribution from the electric field and therefore the effect of the magnetic field can be observed.

Chapter 8

Conclusion

This thesis has explored the broad topic of electron collisions with atoms and molecules, that occur in either field-free or strongly-driven environments. In the context of this work the two different regimes corresponded, approximately, to scattering at either low or high energies. Part I focussed on electron-molecule collisions at low to intermediate energies, in the absence of external fields. Whereas, part II investigated electron-atom collisions, in the context of non-sequential double ionisation which occurs in strongly-driven systems.

Two contrasting approaches were employed. Firstly, a fully-quantum *ab initio* R-matrix method for low to intermediate energy scattering and secondly, a semiclassical Monte-Carlo trajectory method for high energy scattering. In each case, the theory was chosen to optimise its tractability, accuracy and predictive power for the system under study. As mentioned in chapter 1, there is often a trade-off between the physical insight afforded by semiclassical techniques and the brute-force accuracy of fully-quantum *ab initio* methods. Personally, I believe that the ideal scenario is to use both approaches in tandem, building on each others strengths. That is the accuracy of a calculation can be targeted using high-level quantum calculations and the theory can be elucidated by classical arguments. For example, Maxwell et al. (2017) use a theory that combines quantum mechanics with classical trajectories. In doing so, they are able to understand which types of classical orbits contribute to the different quantum interference patterns they obtain. Similarly, Bauer (2005) directly compares a fully numerical solution of the TDSE with classical trajectories

in order to understand the contribution of different pathways to the photoelectron spectra.

In chapter 3, benchmark cross-section data were produced for electron impact electronic excitation of molecular hydrogen, using one of the largest molecular R-matrix calculations to date. The calculations used an R-matrix radius of 100 a_0 and an asymptotic boundary of 300 a_0. Furthermore, this was the first calculation to utilise a B-spline only continuum which consisted of 75 BTOs per angular symmetry and a triply-augmented basis set (tAVTZ) that was capable of accurately describing the first ten electronic excited states (see Fig. 3.2). These technical advances were made possible by the recently developed UKRMol+ codes (Mašín et al., 2020) which significantly improved the representation of the continuum for larger R-matrix radii calculations. Based on the findings of this work, suggestions were put forward to revise the previously recommended data, to bring them in line with the theoretical calculations.

The work presented in chapter 3 only considered excitation from the ground electronic state. However, excitations from intermediate or metastable states are also of interest to the scientific community e.g., see work carried out by Sartori et al. (1998), Celiberto et al. (2001) and Laricchiuta et al. (2004). Moreover, the UKRMol+ codes are already setup to calculate superelastic cross-sections. Therefore, it is hoped that future work can extend the calculations presented in this thesis to provide accurate superelastic collisions.

In chapter 4, the mixed Rydberg-like and valence states of nitric oxide were investigated. The RMPS method was employed to substantially improve the target PECs compared to standard CASCI approaches. By using MOs optimised from the previous geometry and a suitable set of PCOs, the $C\ ^2\Pi$ and $D\ ^2\Sigma^+$ states regained their Rydberg-like character at small bond lengths. However, the vertical excitation energies are still roughly 2 eV too high compared to the reference data of Gilmore (1965). Nevertheless, it is hoped that this work can still serve as a starting point for more in-depth studies of NO and mixed Rydberg-like and valence state molecules in general. It would be interesting to see how the target model developed in this

thesis would affect future scattering calculations.

At the end of chapters 3 and 4, various ways to improve the R-matrix calculations were discussed. Comparing the two projects, it would appear that the biggest improvement stands to be gained by increasing the efficiency of the calculations. This requires further optimisation of the UKRMol+ code in general, as well as more specific changes to the memory and CPU-usage of the integrals code. Both for H_2 and NO the computational cost was a large factor in determining the accuracy and scale of calculation achievable. For example, it was not possible to carry out RMPS calculations for H_2, using the accurate target model described earlier, due to the memory consumption of the integrals code. The full calculation without RMPS used 1.5 Tb of RAM which was the maximum amount available for the hardware used in this project. The situation is worse for NO, where a much simpler target model would be required in order to run a full scattering calculation.

In addition to this, it is beneficial to discuss a more general point about the future of R-matrix calculations for electron-molecule collisions. Calculations are becoming more demanding than ever, and the need for accurate scattering data is continuing to increase. The RMPS method presents the most realistic opportunity of providing accurate data for electron-molecule collisions where either convergence or intermediate scattering energies are required. However, RMPS alone is not a viable option for larger molecules as they suffer from unfavourable scaling laws. Therefore, a combined approach using the partitioned R-matrix approach should be sought in future. To date, only a handful of electron-molecule studies have considered the partitioned R-matrix approach (Tennyson, 2004; Halmová et al., 2008; Dora et al., 2009) and of these studies only Halmová et al. (2008) also used it in combination with the RMPS method. Given recent software and hardware developments, it would be desirable to create a generalised approach, insofar as possible, that is capable of applying RMPS and the partitioned R-matrix method to polyatomic molecules.

In chapters 6 and 7, electron collisions with atoms were studied in the context of non-sequential double ionisation, namely, He and Xe. NSDI occurs in strongly-

driven systems and it can be accurately described by the intuitive three-step model (Corkum, 1993). For this work a semiclassical Monte-Carlo technique was employed to investigate the effect of the magnetic field on single and double ionisation observables. Historically, most theoretical studies were carried out in the dipole approximation because magnetic-field effects were thought to be negligible. However, in chapter 6, by accounting for the full potential of the laser field, it was found that the magnetic-field had a non-negligible impact on the ionisation observables. For instance, the average sum of the electron momenta along the propagation direction of the laser field, $\left\langle p_y^1 + p_y^2 \right\rangle_{\mathrm{DI}}$, had much larger values than expected due to the interaction of the electrons with the magnetic field. Furthermore, this behaviour was observed at intensities significantly lower than those previously accepted to mark the onset of magnetic-field effects. It was found that the effect was largest for NSDI originating from strong recollisions.

In the following chapter, chapter 7, the investigation was extended to uncover the mechanism behind the unexpected increase in $\left\langle p_y^1 + p_y^2 \right\rangle_{\mathrm{DI}}$. It was shown that the magnetic field and the recollision act as a gate. NSDI is a non-linear process and it is extremely dependent on the initial conditions. The magnetic field imposes a small bias on the initial conditions that lead to double ionisation and through a series of knock-on effects this bias is amplified. By the time the recollision takes place there is a strong asymmetry in the spatial distribution of the initially tunnelling electron. Due to the combined interaction of the Coulomb potential and laser field, this asymmetry manifests as an asymmetry in the transverse asymptotic y-momentum. This could be observed experimentally by measuring the double ionisation asymmetry, $P_{\mathrm{asym}}^{\mathrm{DI}}$.

It was found that the biggest contribution to the asymmetry, $P_{\mathrm{asym}}^{\mathrm{DI}}$, came from the asymmetry of the initially tunnelling electron, $P_{\mathrm{1,asym}}^{\mathrm{DI}}$. Moreover, that the leading contribution to the asymmetry is a result of the specific combination of glancing angle collisions with small asymmetries caused by the magnetic field at the time of recollision. This effect was studied across a range of targets, intensities and with different values of ellipticity. It is conjectured that this gating mechanism is

a general phenomenon and that it is not restricted to magnetic fields. In fact, these observable asymmetries should be present in any process that has two delayed steps and allows an electron to gain an offset before recollision takes place.

For future studies, there are a couple of directions that could be of interest. The 3D-SMND code is one of the first codes that is capable of fully accounting for magnetic-field effects, the Coulomb potential and two active electrons in three dimensions. There could be many unexplored and, as yet, unexplained phenomena waiting to be discovered. Furthermore, without too much software development, this code could readily be extended to explore more exotic laser fields such as; two colour lasers, counter-propagating beams and pump-probe pulses (Hartung et al., 2019; Kerbstadt et al., 2019). Again, here there is potential for a vast array of unexplored phenomena and even perhaps the opportunity to observe effects similar to the recollision gating observed in this work. In fact, even without moving to more exotic laser fields there is still much more work to carry out using standard laser fields, such as the effects of a carrier-envelope phase on shorter pulses.

Secondly, whilst molecules typically stretch the limits of validity for semiclassical methods, a variant of the 3D-SMD model has been used successfully used to describe molecules (Emmanouilidou et al., 2012; Chen et al., 2016; Vilà et al., 2019). However, magnetic field effects have not yet been studied for such systems. Therefore this would be an interesting direction for future work.

In the work presented in chapters 6 and 7 it was not possible to carry out a detailed investigation into the effects of intensity averaging over the focal volume. Whilst it is not expected that focal averaging would change the observed behaviour, it is expected to change the intensity at which it occurs. Therefore, for accurate comparison to experiment this effect should be studied in future work.

On a final note, from the work presented in this thesis it is clear that no one theoretical approach is capable of describing the vast array of physics that encompass electron collisions with atoms and molecules, or indeed any area of physics. This is an unsurprising result but nevertheless it is important to acknowledge the strengths and weaknesses of different theoretical techniques and the ranges of va-

lidity in which they are applied. That is, it is important to understand how different theoretical approaches complement one another, rather than deciding which one is ultimate. In this work two vastly different approaches have been used to solve a similar problem but at completely different ends of the energy spectrum. Interestingly, the scientific community is often divided on which approach is best, if any. Theories are sometimes split into arbitrary categories based on; whether they are analytic or numerical; or whether they are classical, semiclassical or fully *ab initio* etc. Personally, I find that this often overlooks the merits of a given model in favour of its technical prowess. In my opinion the most important feature of a theory should be its range of validity. Assuming that the model is valid for the system under study, then it becomes an matter of deciding what question needs to be answered. If it is only the answer that is required, and perhaps it is required to a given degree of accuracy then numerical, fully-quantum methods can be most suitable. However, if it is a question of understanding the underlying process and/or mechanisms behind a given observable then more classical approaches can be beneficial. Ultimately, the community is also governed by what is achievable. Perhaps the experimental conditions fall outside of the semiclassical domain e.g., at very low scattering energies, or perhaps a full numerical solution of the TDSE is not computationally possible.

Quantum mechanics has brought forward some of the most accurate predictions ever made but humans are innately driven to make classical models in order to develop understanding. Therefore, I believe a pragmatic approach is required that combines as many appropriate theories as possible, meaning that for an ideal case the problem would be solved by a range of complementary theories.

Bibliography

R. Abrines and I. C. Percival. Classical theory of charge transfer and ionization of hydrogen atoms by protons. *Proc. Phys. Soc.*, 88:861–872, 1966. doi:10.1088/0370-1328/88/4/306.

A. F. Al-Refaie and J. Tennyson. A parallel algorithm for Hamiltonian matrix construction in electron–molecule collision calculations: MPI-SCATCI. *Comput. Phys. Commun.*, 221:53–62, 2017. doi:10.1016/j.cpc.2017.07.023.

K. Amini, J. Biegert, F. Calegari, A. Chacón, M. F. Ciappina, A. Dauphin, D. K. Efimov, C. Figueira de Morisson Faria, K. Giergiel, P. Gniewek, A. S. Landsman, M. Lesiuk, M. Mandrysz, A. S. Maxwell, R. Moszyński, L. Ortmann, J. Antonio Pérez-Hernández, A. Picón, E. Pisanty, J. Prauzner-Bechcicki, K. Sacha, N. Suárez, A. Zaïr, J. Zakrzewski, and M. Lewenstein. Symphony on strong field approximation. *Reports Prog. Phys.*, 82:116001, 2019. doi:10.1088/1361-6633/ab2bb1.

M. V. Ammosov, N. B. Delone, and V. P. Krainov. Tunnel ionization of complex atoms and of atomic ions in an alternating electromagnetic field. *Sov. Phys. JETP*, 64:1191–1194, 1986. doi:10.1117/12.938695.

K. Anzai, H. Kato, M. Hoshino, H. Tanaka, Y. Itikawa, L. Campbell, M. J. Brunger, S. J. Buckman, H. Cho, F. Blanco, G. Garcia, P. Limão-Vieira, and O. Ingólfsson. Cross section data sets for electron collisions with H_2, O_2, CO, CO_2, N_2O and H_2O. *Eur. Phys. J. D*, 66:36, 2012. doi:10.1140/epjd/e2011-20630-1.

K. Baluja, P. Burke, and L. Morgan. R-matrix propagation program for solving

coupled second-order differential equations. *Comput. Phys. Commun.*, 27:299–307, 1982. doi:10.1016/0010-4655(82)90177-1.

K. L. Baluja, C. J. Noble, and J. Tennyson. Electronic excitation of the b $^3\Sigma_u^+$ state of H_2 using the R-matrix method. *J. Phys. B: At. Mol. Phys.*, 18:L851–L855, 1985.

K. L. Baluja, N. J. Mason, L. A. Morgan, and J. Tennyson. Electron scattering from ClO using the R-matrix method. *J. Phys. B: At. Mol. Opt. Phys.*, 33:L677–L684, 2000.

K. Bartschat. Computational methods for electron–atom collisions in plasma applications. *J. Phys. D. Appl. Phys.*, 46:334004, 2013. doi:10.1088/0022-3727/46/33/334004.

K. Bartschat and M. J. Kushner. Electron collisions with atoms, ions, molecules, and surfaces: Fundamental science empowering advances in technology. *Proc. Natl. Acad. Sci.*, 113:7026–7034, 2016. doi:10.1073/pnas.1606132113.

K. Bartschat, I. Bray, P. G. Burke, and M. P. Scott. Benchmark calculations for e–H scattering between the n=2 and n=3 thresholds. *J. Phys. B At. Mol. Opt. Phys.*, 29:5493–5503, 1996a. doi:10.1088/0953-4075/29/22/023.

K. Bartschat, E. T. Hudson, M. P. Scott, P. G. Burke, and V. M. Burke. Electron-atom scattering at low and intermediate energies using a pseudo-state/ R-matrix basis. *J. Phys. B At. Mol. Opt. Phys.*, 29:115–123, 1996b. doi:10.1088/0953-4075/29/1/015.

K. Bartschat, A. S. Kheifets, D. V. Fursa, and I. Bray. Benchmark calculations for electron impact ionization and ionization-excitation of magnesium. *J. Phys. B At. Mol. Opt. Phys.*, 43:165205, 2010. doi:10.1088/0953-4075/43/16/165205.

D. Bauer. Emergence of classical orbits in few-cycle above-threshold ionization of atomic hydrogen. *Phys. Rev. Lett.*, 94:1–4, 2005. doi:10.1103/PhysRevLett.94.113001.

A. Becker, R. Dörner, and R. Moshammer. Multiple fragmentation of atoms in femtosecond laser pulses. *J. Phys. B At. Mol. Opt. Phys.*, 38:S753–S772, 2005. doi:10.1088/0953-4075/38/9/021.

W. Becker, A. Lohr, and M. Kleber. Light at the end of the tunnel: two- and three-step models in intense-field laser-atom physics. *Quantum Semiclassical Opt. J. Eur. Opt. Soc. Part B*, 7:423–448, 1995. doi:10.1088/1355-5111/7/3/017.

V. R. Bhardwaj, S. A. Aseyev, M. Mehendale, G. L. Yudin, D. M. Villeneuve, D. M. Rayner, M. Y. Ivanov, and P. B. Corkum. Few Cycle Dynamics of Multiphoton Double Ionization. *Phys. Rev. Lett.*, 86:3522–3525, 2001. doi:10.1103/PhysRevLett.86.3522.

C. Bloch. Une formulation unifiée de la théorie des réactions nucléaires. *Nucl. Phys.*, 4:503–528, 1957. doi:10.1016/0029-5582(87)90058-7.

M. Born and R. Oppenheimer. Zur Quantentheorie der Molekeln. *Ann. Phys.*, 389: 457–484, 1927. doi:10.1002/andp.19273892002.

T. Brabec, M. Ivanov, and P. Corkum. Coulomb focusing in intense field atomic processes. *Phys. Rev. A*, 54:R2551–R2554, 1996. doi:10.1103/PhysRevA.54.R2551.

S. E. Branchett, J. Tennyson, and L. A. Morgan. Electronic excitation of molecular hydrogen using the R-matrix method. *J. Phys. B At. Mol. Opt. Phys.*, 23:4625–4639, 1990a.

S. E. Branchett, J. Tennyson, and L. A. Morgan. Electronic excitation of molecular hydrogen using the R-matrix method. *J. Phys. B: At. Mol. Opt. Phys.*, 23:4625–4639, 1990b.

S. E. Branchett, J. Tennyson, and L. A. Morgan. Differential cross sections for electronic excitation of molecular hydrogen using the R-matrix method. *J. Phys. B At. Mol. Opt. Phys.*, 24:3479–3490, 1991.

I. Bray and A. T. Stelbovics. Convergent close-coupling calculations of electron-hydrogen scattering. *Phys. Rev. A*, 46:6995–7011, 1992. doi:10.1103/PhysRevA.46.6995.

I. Bray, K. McNamara, and D. V. Fursa. Calculation of electron-impact ionization of Mg and Al^+. *Phys. Rev. A*, 92:022705, 2015. doi:10.1103/PhysRevA.92.022705.

W. J. Brigg, J. Tennyson, and M. Plummer. R-matrix calculations of low-energy electron collisions with methane. *J. Phys. B At. Mol. Opt. Phys.*, 47:185203, 2014. doi:10.1088/0953-4075/47/18/185203.

A. C. Brown, G. S. Armstrong, J. Benda, D. D. Clarke, J. Wragg, K. R. Hamilton, Z. Mašín, J. D. Gorfinkiel, and H. W. van der Hart. RMT: R-matrix with time-dependence. Solving the semi-relativistic, time-dependent Schrödinger equation for general, multielectron atoms and molecules in intense, ultrashort, arbitrarily polarized laser pulses. *Comput. Phys. Commun.*, 250:107062, 2020. doi:10.1016/j.cpc.2019.107062.

B. D. Bruner, H. Soifer, D. Shafir, V. Serbinenko, O. Smirnova, and N. Dudovich. Multidimensional high harmonic spectroscopy. *J. Phys. B At. Mol. Opt. Phys.*, 48:174006, 2015. doi:10.1088/0953-4075/48/17/174006.

M. J. Brunger, L. Campbell, D. C. Cartwright, A. G. Middleton, B. Mojarrabi, and P. J. O. Teubner. Electron-impact excitation of Rydberg and valence electronic states of nitric oxide: I. Differential cross sections. *J. Phys. B At. Mol. Opt. Phys.*, 33:783–808, 2000a. doi:10.1088/0953-4075/33/4/314.

M. J. Brunger, L. Campbell, D. C. Cartwright, A. G. Middleton, B. Mojarrabi, and P. J. O. Teubner. Electron-impact excitation of Rydberg and valence electronic states of nitric oxide: II. Integral cross sections. *J. Phys. B At. Mol. Opt. Phys.*, 33:809–819, 2000b. doi:10.1088/0953-4075/33/4/315.

P. Burke, C. Noble, and P. Scott. R-matrix theory of electron scattering at intermediate energies. *Proc. R. Soc. London. A. Math. Phys. Sci.*, 410:289–310, 1987. doi:10.1098/rspa.1987.0040.

P. G. Burke. *R-Matrix Theory of Atomic Collisions*, volume 61 of *Springer Series on Atomic, Optical, and Plasma Physics*. Springer Berlin Heidelberg, Berlin, Heidelberg, 2011. ISBN 978-3-642-15930-5. doi:10.1007/978-3-642-15931-2.

P. G. Burke, A. Hibbert, and W. D. Robb. Electron scattering by complex atoms. *J. Phys. B At. Mol. Opt. Phys.*, 4:153–161, 1971. doi:10.1088/0022-3700/4/2/002.

J. M. Carr, P. G. Galiatsatos, J. D. Gorfinkiel, A. G. Harvey, M. A. Lysaght, D. Madden, Z. Mašín, M. Plummer, J. Tennyson, and H. N. Varambhia. UKRmol: a low-energy electron- and positron-molecule scattering suite. *Eur. Phys. J. D*, 66: 58, 2012. doi:10.1140/epjd/e2011-20653-6.

D. C. Cartwright, M. J. Brunger, L. Campbell, B. Mojarrabi, and P. J. O. Teubner. Nitric oxide excited under auroral conditions: Excited state densities and band emissions. *J. Geophys. Res. Sp. Phys.*, 105:20857–20867, 2000. doi:10.1029/1999JA000333.

L. Castillejo, I. C. Percival, and M. J. Seaton. On the theory of elastic collisions between electrons and hydrogen atoms. *Proc. R. Soc. London. Ser. A. Math. Phys. Sci.*, 254:259–272, 1960. doi:10.1098/rspa.1960.0019.

R. Celiberto and T. N. Rescigno. Dependence of electron-impact excitation cross sections on the initial vibrational quantum number in H_2 and D_2 molecules: $X\ ^1\Sigma_g^+ \rightarrow B\ ^1\Sigma_u^+$ and $X\ ^1\Sigma_g^+ \rightarrow C\ ^1\Pi_u$ transitions. *Phys. Rev. A*, 47:1939–1945, 1993. doi:10.1103/PhysRevA.47.1939.

R. Celiberto, R. K. Janev, A. Laricchiuta, M. Capitelli, J. M. Wadehra, and D. E. Atems. Cross section data for electron-impact inelastic processes of vibrationally excited molecules of hydrogen and its isotopes. *At. Data Nucl. Data Tables*, 77: 161–213, 2001. doi:10.1006/adnd.2000.0850.

S. Chelkowski, A. D. Bandrauk, and P. B. Corkum. Photon Momentum Sharing between an Electron and an Ion in Photoionization: From One-Photon (Photoelectric Effect) to Multiphoton Absorption. *Phys. Rev. Lett.*, 113:263005, 2014. doi:10.1103/PhysRevLett.113.263005.

S. Chelkowski, A. D. Bandrauk, and P. B. Corkum. Photon-momentum transfer in multiphoton ionization and in time-resolved holography with photoelectrons. *Phys. Rev. A*, 92:2–6, 2015. doi:10.1103/PhysRevA.92.051401.

A. Chen, H. Price, A. Staudte, and A. Emmanouilidou. Frustrated double ionization in two-electron triatomic molecules. *Phys. Rev. A*, 94:043408, 2016. doi:10.1103/PhysRevA.94.043408.

A. Chen, M. Kübel, B. Bergues, M. F. Kling, and A. Emmanouilidou. Nonsequential double ionization with near-single cycle laser pulses. *Sci. Rep.*, 7: 7488, 2017. doi:10.1038/s41598-017-07635-5.

J. Chen, J. Liu, L. B. Fu, and W. M. Zheng. Interpretation of momentum distribution of recoil ions from laser-induced nonsequential double ionization by semiclassical rescattering model. *Phys. Rev. A*, 63:011404, 2000. doi:10.1103/PhysRevA.63.011404.

C. C. Chirilă, N. J. Kylstra, R. M. Potvliege, and C. J. Joachain. Nondipole effects in photon emission by laser-driven ions. *Phys. Rev. A*, 66:063411, 2002. doi:10.1103/PhysRevA.66.063411.

H.-K. Chung, B. J. Braams, K. Bartschat, A. G. Császár, G. W. F. Drake, T. Kirchner, V. Kokoouline, and J. Tennyson. Uncertainty Estimates for Theoretical Atomic and Molecular Data. *J. Phys. D: Appl. Phys.*, 49(36):363002, 2016. doi:10.1088/0022-3727/49/36/363002.

D. D. A. Clarke, H. W. van der Hart, and A. C. Brown. Extreme-ultraviolet-initiated high-order harmonic generation in Ar^+. *Phys. Rev. A*, 97:023413, 2018. doi:10.1103/PhysRevA.97.023413.

D. Comtois, D. Zeidler, H. Pépin, J. C. Kieffer, D. M. Villeneuve, and P. B. Corkum. Observation of Coulomb focusing in tunnelling ionization of noble gases. *J. Phys. B At. Mol. Opt. Phys.*, 38:1923–1933, 2005. doi:10.1088/0953-4075/38/12/008.

P. B. Corkum. Plasma perspective on strong field multiphoton ionization. *Phys. Rev. Lett.*, 71:1994–1997, 1993. doi:10.1103/PhysRevLett.71.1994.

F. J. da Paixão, M. A. P. Lima, and V. McKoy. Elastic e-NO collisions. *Phys. Rev. A*, 53:1400–1406, 1996. doi:10.1103/PhysRevA.53.1400.

D. Darby-Lewis, Z. Mašín, and J. Tennyson. R-matrix calculations of electron impact electronic excitation of BeH. *J. Phys. B At. Mol. Opt. Phys.*, 50:175201, 2017. doi:10.1088/1361-6455/aa8161.

D. Darby-Lewis, J. Tennyson, K. D. Lawson, S. N. Yurchenko, M. F. Stamp, A. Shaw, S. Brezinsek, and JET Contributors. Synthetic spectra of BeH, BeD and BeT for emission modelling in JET plasmas. *J. Phys. B: At. Mol. Opt. Phys.*, 51:185701, 2018. doi:10.1088/1361-6455/aad6d0.

R. De Vivie and S. D. Peyerimhoff. Theoretical spectroscopy of the NO radical. I. Potential curves and lifetimes of excited states. *J. Chem. Phys.*, 89:3028–3043, 1988. doi:10.1063/1.454958.

H. Deutsch, K. Becker, S. Matt, and T. Märk. Theoretical determination of absolute electron-impact ionization cross sections of molecules. *Int. J. Mass Spectrom.*, 197:37–69, 2000. doi:10.1016/S1387-3806(99)00257-2.

A. Dora, J. Tennyson, L. Bryjko, and T. van Mourik. R-matrix calculation of low-energy electron collisions with uracil. *J. Chem. Phys.*, 130:164307, 2009. doi:10.1063/1.3119667.

D. Dundas, K. T. Taylor, J. S. Parker, and E. S. Smyth. Double-ionization dynamics of laser-driven helium. *J. Phys. B At. Mol. Opt. Phys.*, 32:L231–L238, 1999. doi:10.1088/0953-4075/32/9/107.

T. H. Dunning. Gaussian basis sets for use in correlated molecular calculations. I. The atoms boron through neon and hydrogen. *J. Chem. Phys.*, 90:1007–1023, 1989. doi:10.1063/1.456153.

J. H. Eberly, J. Javanainen, and Q. Su. High-order harmonic production in multiphoton ionization. *J. Opt. Soc. Am. B*, 6:1289, 1989. doi:10.1364/JOSAB.6.001289.

M. Y. Emelin and M. Y. Ryabikin. Atomic photoionization and dynamical stabilization with subrelativistically intense high-frequency light: Magnetic-field effects revisited. *Phys. Rev. A*, 89:013418, 2014. doi:10.1103/PhysRevA.89.013418.

A. Emmanouilidou. Recoil collisions as a portal to field-assisted ionization at near-uv frequencies in the strong-field double ionization of helium. *Phys. Rev. A*, 78: 2–5, 2008. doi:10.1103/PhysRevA.78.023411.

A. Emmanouilidou and T. Meltzer. Recollision as a probe of magnetic-field effects in nonsequential double ionization. *Phys. Rev. A*, 95:033405, 2017. doi:10.1103/PhysRevA.95.033405.

A. Emmanouilidou and A. Staudte. Intensity dependence of strong-field double-ionization mechanisms: From field-assisted recollision ionization to recollision-assisted field ionization. *Phys. Rev. A*, 80:1–7, 2009. doi:10.1103/PhysRevA.80.053415.

A. Emmanouilidou, J. S. Parker, L. R. Moore, and K. T. Taylor. Direct versus delayed pathways in strong-field non-sequential double ionization. *New J. Phys.*, 13:043001, 2011. doi:10.1088/1367-2630/13/4/043001.

A. Emmanouilidou, C. Lazarou, A. Staudte, and U. Eichmann. Routes to formation of highly excited neutral atoms in the breakup of strongly driven H_2. *Phys. Rev. A*, 85:011402, 2012. doi:10.1103/PhysRevA.85.011402.

A. Emmanouilidou, T. Meltzer, and P. B. Corkum. Non-dipole recollision-gated double ionization and observable effects. *J. Phys. B At. Mol. Opt. Phys.*, 50: 225602, 2017. doi:10.1088/1361-6455/aa90e9.

F. H. M. Faisal. Multiple absorption of laser photons by atoms. *J. Phys. B At. Mol. Opt. Phys.*, 6:L89–L92, 1973. doi:10.1088/0022-3700/6/4/011.

R. Fandreyer, P. G. Burke, L. A. Morgan, and C. J. Gillan. Low-energy electron scattering by HBr. *J. Phys. B At. Mol. Opt. Phys.*, 26:3625–3637, 1993. doi:10.1088/0953-4075/26/20/021.

J. Feist, S. Nagele, R. Pazourek, E. Persson, B. I. Schneider, L. A. Collins, and J. Burgdörfer. Nonsequential two-photon double ionization of helium. *Phys. Rev. A*, 77:043420, 2008. doi:10.1103/PhysRevA.77.043420.

B. Feuerstein, R. Moshammer, D. Fischer, A. Dorn, C. D. Schröter, J. Deipenwisch, J. R. Crespo Lopez-Urrutia, C. Höhr, P. Neumayer, J. Ullrich, H. Rottke, C. Trump, M. Wittmann, G. Korn, and W. Sandner. Separation of recollision mechanisms in nonsequential strong field double ionization of Ar: The role of excitation tunneling. *Phys. Rev. Lett.*, 87:043003, 2001. doi:10.1103/PhysRevLett.87.043003.

D. N. Fittinghoff. Polarization dependence of tunneling ionization of helium and neon by 120-fs pulses at 614 nm. *Phys. Rev. A*, 49:2174–2177, 1994.

L. B. Fu, J. Liu, J. Chen, and S. G. Chen. Classical collisional trajectories as the source of strong-field double ionization of helium in the knee regime. *Phys. Rev. A*, 63:1–7, 2001. doi:10.1103/PhysRevA.63.043416.

M. M. Fujimoto and M. T. Lee. Elastic and absorption cross sections for electron-nitric oxide collisions. *J. Phys. B At. Mol. Opt. Phys.*, 33:4759–4768, 2000. doi:10.1103/PhysRevA.65.062702.

M. Gailitis. New forms of asymptotic expansions for wavefunctions of charged-particle scattering. *J. Phys. B At. Mol. Opt. Phys.*, 9:843–854, 1976. doi:10.1088/0022-3700/9/5/027.

F. R. Gilmore. Potential energy curves for N_2, NO, O_2 and corresponding ions. *J. Quant. Spectrosc. Radiat. Transf.*, 5:369–390, 1965. doi:10.1016/0022-4073(65)90072-5.

H. Goldstein. *Classical Mechanics*. Addison-wesley, 2nd edition, 1980. ISBN 0-201-029189.

J. D. Gorfinkiel and S. Ptasinska. Electron scattering from molecules and molecular aggregates of biological relevance. *J. Phys. B At. Mol. Opt. Phys.*, 50:182001, 2017. doi:10.1088/1361-6455/aa8572.

J. D. Gorfinkiel and J. Tennyson. Electron-H_3^+ collisions at intermediate energies. *J. Phys. B At. Mol. Opt. Phys.*, 37:L343–L350, 2004. doi:10.1088/0953-4075/37/20/L01.

J. D. Gorfinkiel and J. Tennyson. Electron impact ionization of small molecules at intermediate energies: The molecular R-matrix with pseudostates method. *J. Phys. B At. Mol. Opt. Phys.*, 38:1607–1622, 2005. doi:10.1088/0953-4075/38/11/003.

R. Grobe and J. H. Eberly. Photoelectron spectra for a two-electron system in a strong laser field. *Phys. Rev. Lett.*, 68:2905–2908, 1992. doi:10.1103/PhysRevLett.68.2905.

J. Grochmalicki, M. Lewenstein, and K. Rzaewski. Stabilization of atoms in superintense laser fields: Is it real? *Phys. Rev. Lett.*, 66:1038–1041, 1991. doi:10.1103/PhysRevLett.66.1038.

G. Halmová and J. Tennyson. Resonances in Electron-Impact Electron Detachment of C_2^-. *Phys. Rev. Lett.*, 100:213202, 2008. doi:10.1103/PhysRevLett.100.213202.

G. Halmová, J. D. Gorfinkiel, and J. Tennyson. Low and intermediate energy electron collisions with the C_2^- molecular anion. *J. Phys. B At. Mol. Opt. Phys.*, 41: 155201, 2008. doi:10.1088/0953-4075/41/15/155201.

L. R. Hargreaves, S. Bhari, B. Adjari, X. Liu, R. Laher, M. C. Zammit, J. S. Savage, D. V. Fursa, I. Bray, and M. A. Khakoo. Differential cross sections for excitation

of H_2 by low-energy electron impact. *J. Phys. B At. Mol. Opt. Phys.*, 50:225203, 2017. doi:10.1088/1361-6455/aa9048.

A. Hartung, S. Eckart, S. Brennecke, J. Rist, D. Trabert, K. Fehre, M. Richter, H. Sann, S. Zeller, K. Henrichs, G. Kastirke, J. Hoehl, A. Kalinin, M. S. Schöffler, T. Jahnke, L. P. H. Schmidt, M. Lein, M. Kunitski, and R. Dörner. Magnetic fields alter strong-field ionization. *Nat. Phys.*, 15:1222–1226, 2019. doi:10.1038/s41567-019-0653-y.

O. Hassouneh, A. C. Brown, and H. W. van der Hart. Harmonic generation by noble-gas atoms in the near-IR regime using *ab initio* time-dependent R-matrix theory. *Phys. Rev. A*, 90:043418, 2014. doi:10.1103/PhysRevA.90.043418.

A. U. Hazi. Impact-parameter method for electronic excitation of molecules by electron impact. *Phys. Rev. A*, 23:2232–2240, 1981. doi:10.1103/PhysRevA.23.2232.

W. M. Huo. The Schwinger Variational Method. In W. M. Huo and F. A. Gianturco, editors, *Comput. Methods Electron—Molecule Collisions*, pages 327–355. Springer US, Boston, MA, 1995. ISBN 978-1-4757-9797-8. doi:10.1007/978-1-4757-9797-8_15.

I. A. Ivanov. Relativistic calculation of the electron-momentum shift in tunneling ionization. *Phys. Rev. A*, 91:1–5, 2015. doi:10.1103/PhysRevA.91.043410.

A. Jain. Total (elastic+absorption) cross sections for e-CH_4 collisions in a spherical model at 0.10–500 eV. *Phys. Rev. A*, 34:3707–3722, 1986. doi:10.1103/PhysRevA.34.3707.

M. Jones and J. Tennyson. On the use of pseudostates to calculate molecular polarizabilities. *J. Phys. B At. Mol. Opt. Phys.*, 43:045101, 2010. doi:10.1088/0953-4075/43/4/045101.

K. N. Joshipura, S. Gangopadhyay, and B. G. Vaishnav. Electron scattering and ionization of NO, N_2O, NO_2, NO_3 and N_2O_5 molecules: theoretical cross sec-

tions. *J. Phys. B At. Mol. Opt. Phys.*, 40:199–210, 2007. doi:10.1088/0953-4075/40/1/018.

M. H. Kalos and P. A. Whitlock. *Monte Carlo Methods*. Wiley-VCH, 2nd edition, 2008. ISBN 978-3-527-40760-6.

S. Kaur, K. L. Baluja, and J. Tennyson. Electron–impact study of NeF using the R-matrix method. *Phys. Rev. A*, 77:032718, 2008.

C. H. Keitel and P. L. Knight. Monte Carlo classical simulations of ionization and harmonic generation in the relativistic domain. *Phys. Rev. A*, 51:1420–1430, 1995. doi:10.1103/PhysRevA.51.1420.

L. V. Keldysh. Ionization in the field of a string electromagnetic wave. *J. Exp. Theor. Phys.*, 20:1307–1314, 1965. doi:10.1234/12345678.

R. A. Kendall, T. H. Dunning, and R. J. Harrison. Electron affinities of the first-row atoms revisited. Systematic basis sets and wave functions. *J. Chem. Phys.*, 96: 6796–6806, 1992. doi:10.1063/1.462569.

S. Kerbstadt, K. Eickhoff, T. Bayer, and M. Wollenhaupt. Control of free electron wave packets by polarization-tailored ultrashort bichromatic laser fields. *Adv. Phys. X*, 4:1672583, 2019. doi:10.1080/23746149.2019.1672583.

S. P. Khare, M. K. Sharma, and S. Tomar. Electron impact ionization of methane. *J. Phys. B At. Mol. Opt. Phys.*, 32:3147–3156, 1999. doi:10.1088/0953-4075/32/13/305.

Y.-K. Kim and M. E. Rudd. Binary-encounter-dipole model for electron-impact ionization. *Phys. Rev. A*, 50:3954–3967, 1994. doi:10.1103/PhysRevA.50.3954.

A. Kirrander, H. H. Fielding, and C. Jungen. Excitation, dynamics, and control of rotationally autoionizing Rydberg states of H_2. *J. Chem. Phys.*, 127:164301, 2007. doi:10.1063/1.2798764.

P. Knowles and N. Handy. A new determinant-based full configuration interaction method. *Chem. Phys. Lett.*, 111:315–321, 1984. doi:10.1016/0009-2614(84)85513-X.

W. Kolos, K. Szalewicz, and H. J. Monkhorst. New Born–Oppenheimer potential energy curve and vibrational energies for the electronic ground state of the hydrogen molecule. *J. Chem. Phys.*, 84:3278–3283, 1986. doi:10.1063/1.450258.

R. Kopold, W. Becker, H. Rottke, and W. Sandner. Routes to nonsequential double ionization. *Phys. Rev. Lett.*, 85:3781–3784, 2000. doi:10.1103/PhysRevLett.85.3781.

J. L. Krause, K. J. Schafer, and K. C. Kulander. High-order harmonic generation from atoms and ions in the high intensity regime. *Phys. Rev. Lett.*, 68:3535–3538, 1992. doi:10.1103/PhysRevLett.68.3535.

F. Krausz and M. Ivanov. Attosecond physics. *Rev. Mod. Phys.*, 81:163–234, 2009. doi:10.1103/RevModPhys.81.163.

M. Kübel, C. Burger, N. G. Kling, T. Pischke, L. Beaufore, I. Ben-Itzhak, G. G. Paulus, J. Ullrich, T. Pfeifer, R. Moshammer, M. F. Kling, and B. Bergues. Complete characterization of single-cycle double ionization of argon from the nonsequential to the sequential ionization regime. *Phys. Rev. A*, 93:053422, 2016. doi:10.1103/PhysRevA.93.053422.

L. D. Landau and E. M. Lifshitz. *Quantum Mechanics*. Pergamon Press, 2nd edition, 1965.

N. F. Lane. The theory of electron-molecule collisions. *Rev. Mod. Phys.*, 52:29–119, 1980.

M. Lange, J. Matsumoto, J. Lower, S. Buckman, O. Zatsarinny, K. Bartschat, I. Bray, and D. V. Fursa. Benchmark experiment and theory for near-threshold excitation of helium by electron impact. *J. Phys. B At. Mol. Opt. Phys.*, 39:4179–4190, 2006. doi:10.1088/0953-4075/39/20/016.

V. Laporta, R. Celiberto, and J. M. Wadehra. Theoretical vibrational-excitation cross sections and rate coefficients for electron-impact resonant collisions involving rovibrationally excited N_2 and NO molecules. *Plasma Sources Sci. Technol.*, 21:055018, 2012. doi:10.1088/0963-0252/21/5/055018.

A. Laricchiuta, R. Celiberto, and R. K. Janev. Electron-impact-induced allowed transitions between triplet states of H_2. *Phys. Rev. A*, 69:022706, 2004. doi:10.1103/PhysRevA.69.022706.

A. Laricchiuta, R. Celiberto, M. Capitelli, and G. Colonna. Calculation of Electron-Scattering Cross Sections Relevant for Hypersonic Plasma Modeling. *Plasma Process. Polym.*, 14:1600131, 2017. doi:10.1002/ppap.201600131.

M.-T. Lee and I. Iga. Elastic and total cross sections for electron scattering by nitrogen molecule in the intermediate energy range. *J. Phys. B At. Mol. Opt. Phys.*, 32:453–462, 1999. doi:10.1088/0953-4075/32/2/024.

J. G. Leopold and I. C. Percival. Microwave Ionization and Excitation of Rydberg Atoms. *Phys. Rev. Lett.*, 41:944–947, 1978. doi:10.1103/PhysRevLett.41.944.

M. Lewenstein, P. Balcou, M. Y. Ivanov, A. L'Huillier, and P. B. Corkum. Theory of high-harmonic generation by low-frequency laser fields. *Phys. Rev. A*, 49: 2117–2132, 1994. doi:10.1103/PhysRevA.49.2117.

J. C. Light and R. B. Walker. An R-matrix approach to the solution of coupled equations for atom–molecule reactive scattering. *J. Chem. Phys.*, 65:4272–4282, 1976. doi:10.1063/1.432836.

M. A. P. Lima, T. L. Gibson, W. M. Huo, and V. McKoy. Cross sections for electron impact excitation of the $b\ ^3\Sigma_u$ state of H_2 : an application of the Schwinger multichannel variational method. *J. Phys. B At. Mol. Phys.*, 18:L865–L870, 1985. doi:10.1088/0022-3700/18/24/007.

D. A. Little and J. Tennyson. An R-matrix study of singlet and triplet continuum states of N_2. *J. Phys. B: At. Mol. Opt. Phys.*, 47:105204, 2014.

X. Liu and C. Figueira de Morisson Faria. Nonsequential Double Ionization with Few-Cycle Laser Pulses. *Phys. Rev. Lett.*, 92:133006, 2004. doi:10.1103/PhysRevLett.92.133006.

X. Liu, D. E. Shemansky, S. M. Ahmed, G. K. James, and J. M. Ajello. Electron-impact excitation and emission cross sections of the H_2 Lyman and Werner Systems. *J. Geophys. Res. Sp. Phys.*, 103:26739–26758, 1998. doi:10.1029/98ja02721.

X. Liu, D. E. Shemansky, H. Abgrall, E. Roueff, S. M. Ahmed, and J. M. Ajello. Electron impact excitation of H_2: Resonance excitation of $B\,^1\Sigma_u^+(J_j = 2, v_j = 0)$ and effective excitation function of EF $^1\Sigma_g^+$. *J. Phys. B At. Mol. Opt. Phys.*, 36: 173–196, 2003. doi:10.1088/0953-4075/36/2/301.

A. Ludwig, J. Maurer, B. W. Mayer, C. R. Phillips, L. Gallmann, and U. Keller. Breakdown of the Dipole Approximation in Strong-Field Ionization. *Phys. Rev. Lett.*, 113:243001, 2014. doi:10.1103/PhysRevLett.113.243001.

B. P. Marinković, V. Pejčev, D. M. Filipović, D. Šević, A. R. Milosavljević, S. Milisavljević, M. S. Rabasović, D. Pavlović, and J. B. Maljković. Cross section data for electron collisions in plasma physics. *J. Phys. Conf. Ser.*, 86:012006, 2007. doi:10.1088/1742-6596/86/1/012006.

Z. Mašín, J. D. Gorfinkiel, D. B. Jones, S. M. Bellm, and M. J. Brunger. Elastic and inelastic cross sections for low-energy electron collisions with pyrimidine. *J. Chem. Phys.*, 136:144310, 2012. doi:10.1063/1.3702629.

Z. Mašín, J. Benda, J. D. Gorfinkiel, A. G. Harvey, and J. Tennyson. UKRmol+: A suite for modelling electronic processes in molecules interacting with electrons, positrons and photons using the R-matrix method. *Comput. Phys. Commun.*, 249: 107092, 2020. doi:10.1016/j.cpc.2019.107092.

A. S. Maxwell, A. Al-Jawahiry, T. Das, and C. F. d. Morisson Faria. Coulomb-corrected quantum interference in above-threshold ionization: Working to-

wards multitrajectory electron holography. *Phys. Rev. A*, 96:023420, 2017. doi:10.1103/PhysRevA.96.023420.

T. Meltzer, J. Tennyson, Z. Mašín, M. C. Zammit, L. H. Scarlett, D. V. Fursa, and I. Bray. Benchmark calculations of electron impact electronic excitation of the hydrogen molecule. *J. Phys. B At. Mol. Opt. Phys.*, 53:145204, 2020. doi:10.1088/1361-6455/ab8c58.

D. B. Milosevic, G. G. Paulus, D. Bauer, and W. Becker. Above-threshold ionization by few-cycle pulses. *J. Phys. B At. Mol. Opt. Phys.*, 39:R203, 2006. doi:10.1088/0953-4075/39/14/R01.

R. S. Minns, J. R. R. Verlet, L. J. Watkins, and H. H. Fielding. Observation and control of dissociating and autoionizing Rydberg electron wave packets in NO. *J. Chem. Phys.*, 119:5842–5847, 2003. doi:10.1063/1.1603218.

L. A. Morgan, J. Tennyson, and C. J. Gillan. The UK molecular R-matrix codes. *Comput. Phys. Commun.*, 114:120–128, 1998.

M. A. Morrison. Near-Threshold Electron-Molecule Scattering. In *Adv. At. Mol. Phys.*, volume 24, pages 51–156. Academic Press, jan 1988. doi:10.1016/S0065-2199(08)60230-4.

L. T. Murray. Lightning NO_x and Impacts on Air Quality. *Curr. Pollut. Reports*, 2: 115–133, 2016. doi:10.1007/s40726-016-0031-7.

J. Muse, H. Silva, M. C. Lopes, and M. A. Khakoo. Low energy elastic scattering of electrons from H_2 and N_2. *J. Phys. B At. Mol. Opt. Phys.*, 41:095203, 2008. doi:10.1088/0953-4075/41/9/095203.

T. Nagano and T. Yoshimura. Bioimaging of Nitric Oxide. *Chem. Rev.*, 102:1235–1270, 2002. doi:10.1021/cr010152s.

C. J. Noble and R. Nesbet. CFASYM, a program for the calculation of the asymptotic solutions of the coupled equations of electron collision theory. *Comput. Phys. Commun.*, 33:399–411, 1984. doi:10.1016/0010-4655(84)90145-0.

D. W. Norcross and N. T. Padial. The multipole-extracted adiabatic-nuclei approximation for electron-molecule collisions. *Phys. Rev. A*, 25:226–238, 1982. doi:10.1103/PhysRevA.25.226.

S. Palaniyappan, A. DiChiara, E. Chowdhury, A. Falkowski, G. Ongadi, E. L. Huskins, and B. C. Walker. Ultrastrong Field Ionization of $Ne^{n+}(n \leq 8)$: Rescattering and the Role of the Magnetic Field. *Phys. Rev. Lett.*, 94:243003, 2005. doi:10.1103/PhysRevLett.94.243003.

J. S. Parker, B. J. S. Doherty, K. J. Meharg, and K. T. Taylor. Time delay between singly and doubly ionizing wavepackets in laser-driven helium. *J. Phys. B At. Mol. Opt. Phys.*, 36:L393–L400, 2003. doi:10.1088/0953-4075/36/21/L04.

J. S. Parker, B. J. S. Doherty, K. T. Taylor, K. D. Schultz, C. I. Blaga, and L. F. Dimauro. High-energy cutoff in the spectrum of strong-field nonsequential double ionization. *Phys. Rev. Lett.*, 96:7–10, 2006. doi:10.1103/PhysRevLett.96.133001.

L. C. Pitchford, L. L. Alves, K. Bartschat, S. F. Biagi, M.-C. Bordage, I. Bray, C. E. Brion, M. J. Brunger, L. Campbell, A. Chachereau, B. Chaudhury, L. G. Christophorou, E. Carbone, N. A. Dyatko, C. M. Franck, D. V. Fursa, R. K. Gangwar, V. Guerra, P. Haefliger, G. J. M. Hagelaar, A. Hoesl, Y. Itikawa, I. V. Kochetov, R. P. McEachran, W. L. Morgan, A. P. Napartovich, V. Puech, M. Rabie, L. Sharma, R. Srivastava, A. D. Stauffer, J. Tennyson, J. de Urquijo, J. van Dijk, L. A. Viehland, M. C. Zammit, O. Zatsarinny, and S. Pancheshnyi. LXCat: an Open-Access, Web-Based Platform for Data Needed for Modeling Low Temperature Plasmas. *Plasma Proc. Polymers*, 14:1600098, 2017. doi:10.1002/ppap.201600098.

R. Polák and J. Fišer. On the behavior of the low-lying $^2\Sigma^+$ electronic states of NO. *Chem. Phys. Lett.*, 377:564–570, 2003. doi:10.1016/S0009-2614(03)01179-5.

R. Polák and J. Fišer. A comparative icMRCI study of some NO^+, NO and NO^- electronic ground state properties. *Chem. Phys.*, 303:73–83, 2004. doi:10.1016/j.chemphys.2004.04.027.

S. V. Popruzhenko, P. A. Korneev, S. P. Goreslavski, and W. Becker. Laser-Induced Recollision Phenomena: Interference Resonances at Channel Closings. *Phys. Rev. Lett.*, 89:023001, 2002. doi:10.1103/PhysRevLett.89.023001.

K. Regeta, M. Allan, Z. Mašín, and J. D. Gorfinkiel. Absolute cross sections for electronic excitation of pyrimidine by electron impact. *J. Chem. Phys.*, 144: 24302, 2016. doi:10.1063/1.4939077.

H. R. Reiss. Effect of an intense electromagnetic field on a weakly bound system. *Phys. Rev. A*, 22:1786–1813, 1980. doi:10.1103/PhysRevA.22.1786.

H. R. Reiss. Limits on tunneling theories of strong-field ionization. *Phys. Rev. Lett.*, 101:1–4, 2008. doi:10.1103/PhysRevLett.101.043002.

H. R. Reiss. The tunneling model of laser-induced ionization and its failure at low frequencies. *J. Phys. B At. Mol. Opt. Phys.*, 47:2–3, 2014. doi:10.1088/0953-4075/47/20/204006.

T. N. Rescigno, C. W. McCurdy, A. E. Orel, and B. H. Lengsfield. The Complex Kohn Variational Method. In W. M. Huo and F. A. Gianturco, editors, *Comput. Methods Electron—Molecule Collisions*, pages 1–44. Springer US, Boston, MA, 1995. ISBN 978-1-4757-9797-8. doi:10.1007/978-1-4757-9797-8_1.

A. Rohatgi. Webplotdigitizer, 2017.

A. Rudenko, V. L. B. de Jesus, T. Ergler, K. Zrost, B. Feuerstein, C. D. Schröter, R. Moshammer, and J. Ullrich. Correlated Two-Electron Momentum Spectra for Strong-Field Nonsequential Double Ionization of He at 800 nm. *Phys. Rev. Lett.*, 99:263003, 2007. doi:10.1103/PhysRevLett.99.263003.

C. Ruiz, L. Plaja, L. Roso, and A. Becker. Ab initio Calculation of the Double Ionization of Helium in a Few-Cycle Laser Pulse Beyond the One-Dimensional Approximation. *Phys. Rev. Lett.*, 96:053001, 2006. doi:10.1103/PhysRevLett.96.053001.

N. Sanna and F. Gianturco. Differential cross sections for electron/positron scattering from polyatomic molecules. *Comput. Phys. Commun.*, 114:142–167, 1998. doi:10.1016/S0010-4655(98)00091-5.

C. S. Sartori, F. J. da Paixão, and M. A. P. Lima. Transitions between excited electronic states of H_2 molecules by electron impact. *Phys. Rev. A*, 58:2857–2863, 1998. doi:10.1103/PhysRevA.58.2857.

L. H. Scarlett, J. K. Tapley, D. V. Fursa, M. C. Zammit, J. S. Savage, and I. Bray. Low-energy electron-impact dissociative excitation of molecular hydrogen and its isotopologues. *Phys. Rev. A*, 96:62708, 2017. doi:10.1103/PhysRevA.96.062708.

L. H. Scarlett, J. K. Tapley, D. V. Fursa, M. C. Zammit, J. S. Savage, and I. Bray. Electron-impact dissociation of molecular hydrogen into neutral fragments. *Eur. Phys. J. D*, 72:34, 2018. doi:10.1140/epjd/e2017-80649-8.

L. H. Scarlett, J. S. Savage, D. V. Fursa, M. C. Zammit, and I. Bray. Electron-Impact Dissociation of Vibrationally-Excited Molecular Hydrogen into Neutral Fragments. *Atoms*, 7:75, 2019a. doi:10.3390/atoms7030075.

L. H. Scarlett, J. K. Tapley, J. S. Savage, D. V. Fursa, M. C. Zammit, and I. Bray. Vibrational excitation of the H_2 $X\ ^1\Sigma_g^+$ state via electron-impact excitation and radiative cascade. *Plasma Sources Sci. Technol.*, 28:025004, 2019b. doi:10.1088/1361-6595/ab005b.

L. H. Scarlett, J. S. Savage, D. V. Fursa, I. Bray, and M. C. Zammit. Electron-scattering on molecular hydrogen: convergent close-coupling approach. *Eur. Phys. J. D*, 74:36, 2020. doi:10.1140/epjd/e2020-100549-0.

L. H. Scarlett, D. V. Fursa, M. C. Zammit, I. Bray, Yu. Ralchenko, and K. Davie. *Atom. Data Nucl. Data Tables*, 2020, submitted.

R. S. Schappe, R. J. Edgell, and E. Urban. Electron-impact excitation of nitric oxide $(A\ ^2\Sigma^+ - X\ ^2\Pi)$. *Phys. Rev. A*, 65:10, 2002. doi:10.1103/PhysRevA.65.042701.

M. W. Schmidt and K. Ruedenberg. Effective convergence to complete orbital bases and to the atomic Hartree–Fock limit through systematic sequences of Gaussian primitives. *J. Chem. Phys.*, 71:3951–3962, 1979. doi:10.1063/1.438165.

B. I. Schneider and L. A. Collins. Electronic excitation of the $b\,^3\Sigma_u$ state of H_2 by electron impact in the linear algebraic approach. *J. Phys. B At. Mol. Opt. Phys.*, 18:L857–L863, 1985. doi:10.1088/0022-3700/18/24/006.

H. Shi and A. L. East. Improved results for the excited states of nitric oxide, including the B/C avoided crossing. *J. Chem. Phys.*, 125:104311, 2006. doi:10.1063/1.2336214.

N. I. Shvetsov-Shilovski, M. Lein, L. B. Madsen, E. Räsänen, C. Lemell, J. Burgdörfer, D. G. Arbó, and K. Tőkési. Semiclassical two-step model for strong-field ionization. *Phys. Rev. A*, 94:013415, 2016. doi:10.1103/PhysRevA.94.013415.

C. T. L. Smeenk, L. Arissian, B. Zhou, A. Mysyrowicz, D. M. Villeneuve, A. Staudte, and P. B. Corkum. Partitioning of the Linear Photon Momentum in Multiphoton Ionization. *Phys. Rev. Lett.*, 106:193002, 2011. doi:10.1103/PhysRevLett.106.193002.

M.-Y. Song, J.-S. Yoon, H. Cho, G. P. Karwasz, V. Kokoouline, Y. Nakamura, and J. Tennyson. Cross Sections for Electron Collisions with NO, N_2O, and NO_2. *J. Phys. Chem. Ref. Data*, 48:043104, 2019. doi:10.1063/1.5114722.

G. Staszewska and L. Wolniewicz. Transition Moments among 3Σ and 3Π States of the H2 Molecule. *J. Mol. Spectrosc.*, 198:416–420, 1999. doi:10.1006/jmsp.1999.7975.

G. Staszewska and L. Wolniewicz. Adiabatic Energies of Excited $^1\Sigma_u$ States of the Hydrogen Molecule. *J. Mol. Spectrosc.*, 212:208–212, 2002. doi:10.1006/jmsp.2002.8546.

A. Staudte, C. Ruiz, M. Schöffler, S. Schössler, D. Zeidler, T. Weber, M. Meckel, D. M. Villeneuve, P. B. Corkum, A. Becker, and R. Dörner. Binary and recoil collisions in strong field double ionization of helium. *Phys. Rev. Lett.*, 99:1–4, 2007. doi:10.1103/PhysRevLett.99.263002.

D. T. Stibbe and J. Tennyson. Ab initio calculations of vibrationally resolved resonances in electron collisions with H_2, HD and D_2. *Phys. Rev. Lett.*, 79:4116–4119, 1997.

D. T. Stibbe and J. Tennyson. Near-threshold electron impact dissociation of H_2 within the adiabatic nuclei approximation. *New J. Phys.*, 1:1–9, 1998. doi:10.1088/1367-2630/1/1/002.

E. Stiefel and P. Kustaanheimo. Perturbation theory of Kepler motion based on spinor regularization. *J. Reine Angew. Math.*, 218:204–219, 1965. doi:10.1515/crll.1965.218.204.

A. Szabo and N. S. Ostlund. *Modern Quantum Chemistry: Introduction to Advanced Electronic Structure Theory*. Dover Publications, 1989. ISBN 0486691861.

V. Szebehely. *Theory of Orbits*. Academic Press, 1967.

H. Tanaka, M. J. Brunger, L. Campbell, H. Kato, M. Hoshino, and A. R. P. Rau. Scaled plane-wave Born cross sections for atoms and molecules. *Rev. Mod. Phys.*, 88:025004, 2016. doi:10.1103/RevModPhys.88.025004.

J. K. Tapley, L. H. Scarlett, J. S. Savage, D. V. Fursa, M. C. Zammit, and I. Bray. Electron-impact dissociative excitation cross sections for singlet states of molecular hydrogen. *Phys. Rev. A*, 98:032701, 2018a. doi:10.1103/PhysRevA.98.032701.

J. K. Tapley, L. H. Scarlett, J. S. Savage, M. C. Zammit, D. V. Fursa, and I. Bray. Vibrationally resolved electron-impact excitation cross sections for singlet states

of molecular hydrogen. *J. Phys. B At. Mol. Opt. Phys.*, 51:144007, 2018b. doi:10.1088/1361-6455/aac8fa.

H. Tawara, Y. Itikawa, H. Nishimura, and M. Yoshino. Cross Sections and Related Data for Electron Collisions with Hydrogen Molecules and Molecular Ions. *J. Phys. Chem. Ref. Data*, 19:617–636, 1990. doi:10.1063/1.555856.

K. T. Taylor, J. S. Parker, D. Dundas, and K. J. Meharg. Theory of laser-driven double-ionization of atoms at Ti:sapphire laser wavelengths. *J. Mod. Op.*, 54: 1959–1983, 2007. doi:10.1080/09500340701483154.

J. Tennyson. A new algorithm for Hamiltonian matrix construction in electron - molecule collision calculations. *J. Phys. B At. Mol. Opt. Phys.*, 29:1817–1828, 1996a. doi:10.1088/0953-4075/29/9/024.

J. Tennyson. R-matrix calculation of Rydberg states of CO. *J. Phys. B: At. Mol. Opt. Phys.*, 29:6185–6201, 1996b.

J. Tennyson. Phase factors in electron-molecule collision calculations. *Comput. Phys. Commun.*, 100:26–30, 1997. doi:10.1016/S0010-4655(96)00144-0.

J. Tennyson. Partitioned R-matrix theory for molecules. *J. Phys. B At. Mol. Opt. Phys.*, 37:1061–1071, 2004. doi:10.1088/0953-4075/37/5/009.

J. Tennyson. Electron–molecule collision calculations using the R-matrix method. *Phys. Rep.*, 491:29–76, 2010. doi:10.1016/j.physrep.2010.02.001.

J. Tennyson and C. J. Noble. Low-energy electron scattering by the NO molecule. *J. Phys. B At. Mol. Opt. Phys.*, 19:4025–4033, 1986. doi:10.1088/0022-3700/19/23/020.

A. S. Titi and G. W. F. Drake. Quantum theory of longitudinal momentum transfer in above-threshold ionization. *Phys. Rev. A*, 85:12–15, 2012. doi:10.1103/PhysRevA.85.041404.

D. Tong. *Applications of Quantum Mechanics*. 2017.

C. S. Trevisan and J. Tennyson. Calculated rates for the electron impact dissociation of molecular hydrogen: mixed isotopomers and scaling laws. *Plasma Phys. Control. Fusion*, 44:2217–2230, 2002.

C. S. Trevisan, K. Houfek, Z. Zhang, A. E. Orel, C. W. McCurdy, and T. N. Rescigno. Nonlocal model of dissociative electron attachment and vibrational excitation of NO. *Phys. Rev. A*, 71:1–12, 2005. doi:10.1103/PhysRevA.71.052714.

A. Vilà, G. P. Katsoulis, and A. Emmanouilidou. Sub-cycle attosecond control in frustrated double ionization of molecules. *J. Phys. B At. Mol. Opt. Phys.*, 52: 015604, 2019. doi:10.1088/1361-6455/aaf012.

B. Walker, B. Sheehy, L. F. Dimauro, P. Agostini, K. J. Schafer, and K. C. Kulander. Precision measurement of strong field double ionization of helium. *Phys. Rev. Lett.*, 73:1227–1230, 1994. doi:10.1103/PhysRevLett.73.1227.

M. W. Walser, C. H. Keitel, A. Scrinzi, and T. Brabec. High harmonic generation beyond the electric dipole approximation. *Phys. Rev. Lett.*, 85:5082–5, 2000. doi:10.1103/PhysRevLett.85.5082.

P. Wang, A. M. Sayler, K. D. Carnes, B. D. Esry, and I. Ben-Itzhak. Disentangling the volume effect through intensity-difference spectra: application to laser-induced dissociation of H_2^+. *Opt. Lett.*, 30:664, 2005. doi:10.1364/OL.30.000664.

H.-J. Werner, P. J. Knowles, G. Knizia, F. R. Manby, and M. Schütz. Molpro: a general-purpose quantum chemistry program package. *Wiley Interdiscip. Rev. Comput. Mol. Sci.*, 2:242–253, 2012. doi:10.1002/wcms.82.

L. Wolniewicz and K. Dressler. Adiabatic potential curves and nonadiabatic coupling functions for the first five excited $^1\Sigma_g^+$ states of the hydrogen molecule. *J. Chem. Phys.*, 100:444–451, 1994. doi:10.1063/1.466957.

L. Wolniewicz and G. Staszewska. Excited $^1\Pi_u$ states and the $^1\Pi_u \rightarrow X\ ^1\Sigma_g^+$

transition moments of the hydrogen molecule. *J. Mol. Spectrosc.*, 220:45–51, 2003. doi:10.1016/S0022-2852(03)00121-8.

B. Wolter, M. G. Pullen, M. Baudisch, M. Sclafani, M. Hemmer, A. Senftleben, C. D. Schröter, J. Ullrich, R. Moshammer, and J. Biegert. Strong-field physics with Mid-IR fields. *Phys. Rev. X*, 5:1–16, 2015. doi:10.1103/PhysRevX.5.021034.

D. E. Woon and T. H. Dunning. Gaussian basis sets for use in correlated molecular calculations. IV. Calculation of static electrical response properties. *J. Chem. Phys.*, 100:2975–2988, 1994. doi:10.1063/1.466439.

J. Wragg and H. W. van der Hart. Spin and spatial dynamics in electron-impact scattering off S-wave He using R-matrix-with-time-dependence theory. *Phys. Rev. A*, 94:032706, 2016. doi:10.1103/PhysRevA.94.032706.

J. Wragg, J. S. Parker, and H. W. van der Hart. Double ionization in R-matrix theory using a two-electron outer region. *Phys. Rev. A*, 92:022504, 2015. doi:10.1103/PhysRevA.92.022504.

J. Wrkich, D. Mathews, I. Kanik, S. Trajmar, and M. A. Khakoo. Differential cross-sections for the electron impact excitation of the $B\ ^1\Sigma_u^+$, $c\ ^3\Pi_u$, $a\ ^3\Sigma_g^+$, $C\ ^1\Pi_u$, $EF\ ^1\Sigma_g^+$ and $e\ ^3\Sigma_u^+$ states of molecular hydrogen. *J. Phys. B At. Mol. Opt. Phys.*, 35:4695–4709, 2002. doi:10.1088/0953-4075/35/22/311.

E. Yakaboylu, M. Klaiber, H. Bauke, K. Z. Hatsagortsyan, and C. H. Keitel. Relativistic features and time delay of laser-induced tunnel ionization. *Phys. Rev. A*, 88:063421, 2013. doi:10.1103/PhysRevA.88.063421.

T.-M. Yan and D. Bauer. Sub-barrier Coulomb effects on the interference pattern in tunneling-ionization photoelectron spectra. *Phys. Rev. A*, 86:053403, 2012. doi:10.1103/PhysRevA.86.053403.

J.-S. Yoon, M.-Y. Song, J.-M. Han, S. H. Hwang, W.-S. Chang, B. Lee, and

Y. Itikawa. Cross Sections for Electron Collisions with Hydrogen Molecules. *J. Phys. Chem. Ref. Data*, 37:913–931, 2008. doi:10.1063/1.2838023.

G. L. Yudin and M. Y. Ivanov. Physics of correlated double ionization of atoms in intense laser fields: Quasistatic tunneling limit. *Phys. Rev. A*, 63:033404, 2001. doi:10.1103/PhysRevA.63.033404.

M. C. Zammit, D. V. Fursa, and I. Bray. Electron scattering from the molecular hydrogen ion and its isotopologues. *Phys. Rev. A*, 90:022711, 2014. doi:10.1103/PhysRevA.90.022711.

M. C. Zammit, D. V. Fursa, J. S. Savage, and I. Bray. Electron-and positron-molecule scattering: development of the molecular convergent close-coupling method. *J. Phys. B At. Mol. Opt. Phys.*, 50:123001, 2017a. doi:10.1088/1361-6455/aa6e74.

M. C. Zammit, J. S. Savage, D. V. Fursa, and I. Bray. Electron-impact excitation of molecular hydrogen. *Phys. Rev. A*, 95:022708, 2017b. doi:10.1103/PhysRevA.95.022708.

O. Zatsarinny, K. Bartschat, S. Gedeon, V. Gedeon, and V. Lazur. Low-energy electron scattering from Ca atoms and photodetachment of Ca^-. *Phys. Rev. A*, 74:052708, 2006. doi:10.1103/PhysRevA.74.052708.

M. Zawadzki, R. Wright, G. Dolmat, M. F. Martin, B. Diaz, L. Hargreaves, D. Coleman, D. V. Fursa, M. C. Zammit, L. H. Scarlett, J. K. Tapley, J. S. Savage, I. Bray, and M. A. Khakoo. Low-energy electron scattering from molecular hydrogen: Excitation of the $X\ ^1\Sigma_g^+$ to $b\ ^3\Sigma_u^+$ transition. *Phys. Rev. A*, 98:062704, 2018. doi:10.1103/PhysRevA.98.062704.

M. Zawadzki, M. A. Khakoo, L. Voorneman, L. Ratkovic, Z. Mašín, K. Houfek, A. Dora, and J. Tennyson. Low Energy Inelastic Electron Scattering from Carbon Monoxide: I. Excitation of the a $^3\Pi$, a' $^3\Sigma^+$ and A $^1\Pi$ Electronic States. *J. Phys. B: At. Mol. Opt. Phys.*, 53:165201, 2020. doi:10.1088/1361-6455/ab95ef.

R. Zhang, A. Faure, and J. Tennyson. Electron and positron collisions with polar molecules: studies with the benchmark water molecule. *Phys. Scr.*, 80:015301, 2009.

R. Zhang, K. L. Baluja, J. Franz, and J. Tennyson. Positron collisions with molecular hydrogen: cross sections and annihilation parameters calculated using the R-matrix with pseudo-states method. *J. Phys. B At. Mol. Opt. Phys.*, 44:035203, 2011a. doi:10.1088/0953-4075/44/3/035203.

R. Zhang, P. G. Galiatsatos, and J. Tennyson. Positron collisions with acetylene calculated using the R-matrix with pseudo-states method. *J. Phys. B At. Mol. Opt. Phys.*, 44:195203, 2011b. doi:10.1088/0953-4075/44/19/195203.